

AD-A076 567

ARMAMENT DEVELOPMENT AND TEST CENTER EGLIN AFB FL  
PROCEEDINGS OF THE BIENNIAL GUIDANCE TEST SYMPOSIUM (9TH) HELD --ETC(U)  
OCT 79

F/G 17/7

UNCLASSIFIED ADTC-TR-79-11-VOL-1

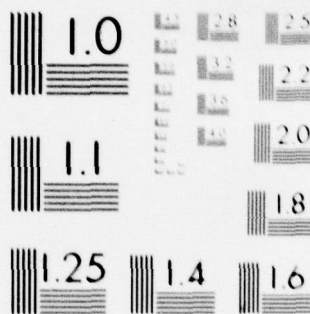
NL

1 OF 5

AD  
A076567





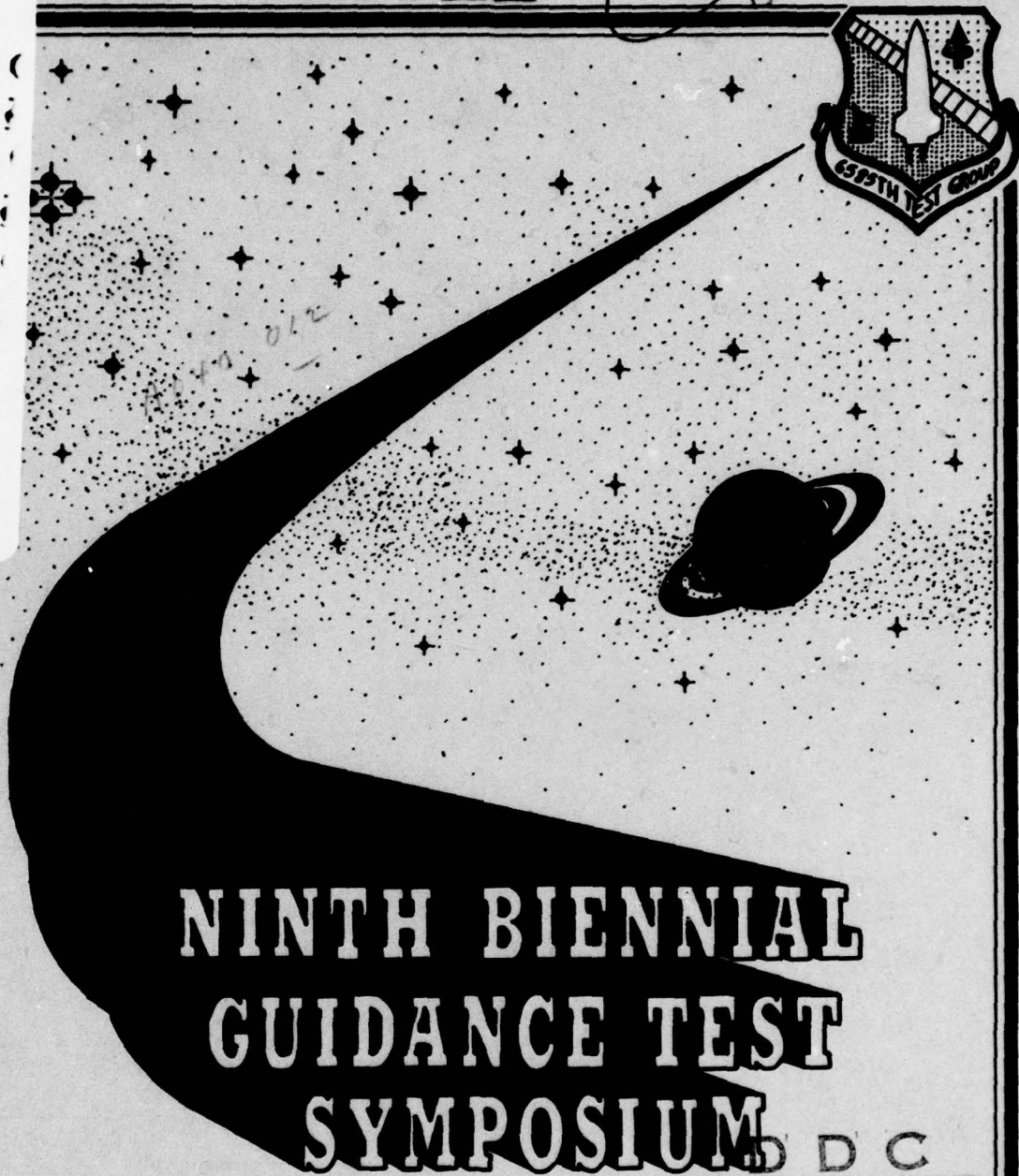


MICROCOPY RESOLUTION TEST CHART  
NATIONAL BUREAU OF STANDARDS-1963-A

LEVEL II

VOLUME 1  
ADTC TR-79-11

AD A 076567

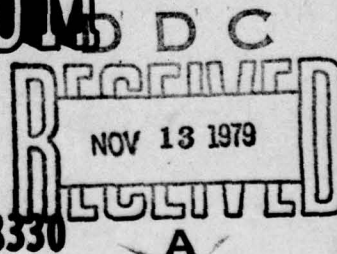


# NINTH BIENNIAL GUIDANCE TEST SYMPOSIUM

DDC FILE COPY

10-12 OCTOBER, 1979

HOLLOMAN AFB, NEW MEXICO 88330



APPROVED FOR PUBLIC RELEASE:  
DISTRIBUTION UNLIMITED

79 11 09 071

UNCLASSIFIED

SECURITY CLASSIFICATION OF THIS PAGE (When Data Entered)

REPORT DOCUMENTATION PAGE		READ INSTRUCTIONS BEFORE COMPLETING FORM
1. REPORT NUMBER ADTC-TR-79-11 (Volume I) ✓	2. GOVT ACCESSION NO.	3. RECIPIENT'S CATALOG NUMBER
4. TITLE (and Subtitle) NINTH BIENNIAL GUIDANCE TEST SYMPOSIUM PROCEEDINGS		5. TYPE OF REPORT & PERIOD COVERED Symposium Proceedings
		6. PERFORMING ORG. REPORT NUMBER
7. AUTHOR(s) As indicated on individual papers.		8. CONTRACT OR GRANT NUMBER(s)
9. PERFORMING ORGANIZATION NAME AND ADDRESS 6585th Test Group/GD ✓ Holloman AFB, New Mexico 88330 389 490		10. PROGRAM ELEMENT, PROJECT, TASK AREA & WORK UNIT NUMBERS
11. CONTROLLING OFFICE NAME AND ADDRESS 6585th Test Group/GD Holloman AFB, New Mexico 88330		12. REPORT DATE October 1979
		13. NUMBER OF PAGES
14. MONITORING AGENCY NAME & ADDRESS (if different from Controlling Office)		15. SECURITY CLASS. (of this report) UNCLASSIFIED
		15a. DECLASSIFICATION/DOWNGRADING SCHEDULE
16. DISTRIBUTION STATEMENT (of this Report)  <div style="border: 1px solid black; padding: 5px; width: fit-content;"> <b>DISTRIBUTION STATEMENT A</b>            Approved for public release            Distribution Unlimited         </div>		
17. DISTRIBUTION STATEMENT (of the abstract entered in Block 20, if different from Report)  <div style="float: right; border: 1px solid black; padding: 5px;">             D D C              RECEIVED              NOV 13 1979              RECEIVED              A           </div>		
18. SUPPLEMENTARY NOTES		
19. KEY WORDS (Continue on reverse side if necessary and identify by block number)  Test and Evaluation, Gyroscopes, Accelerometers, Inertial Guidance, Navigators, Modeling, GPS, Space Shuttle		
20. ABSTRACT (Continue on reverse side if necessary and identify by block number) These proceedings contain papers included in the Ninth Biennial Guidance Test Symposium. This symposium, hosted by the Central Inertial Guidance Test Facility, is directed toward the exchange of information, stimulation of new ideas, and discussion of recent developments in the field of guidance testing. The papers presented include such topics as the Global Positioning System, the Space Shuttle, Aircraft Inertial Navigators, Component Evaluation, Advanced Guidance Methodology, Missile Guidance Systems and Analysis Techniques. The		

DD FORM 1 JAN 73 1473

UNCLASSIFIED

SECURITY CLASSIFICATION OF THIS PAGE (When Data Entered)



**UNCLASSIFIED**

SECURITY CLASSIFICATION OF THIS PAGE(When Data Entered)

**Block 20 (Cont'd)**

included papers were those presented in the unclassified sessions of the symposium. Papers presented in the classified portions of the meeting are being published as Volume II.

**UNCLASSIFIED**

SECURITY CLASSIFICATION OF THIS PAGE(When Data Entered)

11 Oct 79

14

ADTC-TR-79-11-VOL-1

Volume I

12 389

6

PROCEEDINGS OF THE  
BIENNIAL GUIDANCE TEST SYMPOSIUM (9th)

Held at

HEADQUARTERS 6585TH TEST GROUP  
ARMAMENT DEVELOPMENT TEST CENTER,  
HOLLOMAN AIR FORCE BASE, NEW MEXICO

10-12 October 1979  
Volume I.

Accession For	
NTIS GRA&I	<input checked="checked" type="checkbox"/>
DDC TAB	<input type="checkbox"/>
Unannounced	<input type="checkbox"/>
Justification	
By	
Distribution/	
Availability Codes	
Dist	Avail and/or special
A	

Hosted by

CENTRAL INERTIAL GUIDANCE TEST FACILITY,

10-12 OCTOBER 1979

404 038

elt

## FOREWORD

The Ninth Biennial Guidance Test Symposium was held at Holloman Air Force Base, New Mexico 10-12 October 1979. These symposia are hosted by the Central Inertial Guidance Test Facility (CIGTF). These meetings bring together approximately 450 people from industry, educational institutions, foreign governments, the Department of Defense and other Government agencies. The goal is to provide a forum for the exchange of technical information and the stimulation of new ideas related to the testing of aided and unaided inertial guidance systems and components.

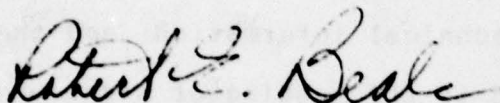
Many excellent papers were received for presentation at this meeting, but due to the time available only a portion of those submitted could be included.

The paper selection committee, headed by Dr. F. F. Kuhn of the Central Inertial Guidance Test Facility, included Col R. E. Clark, Aeronautical Systems Division; Col O. Tedeschi, Air Force Armament Laboratory; Col D. Henderson, Space and Missile Systems Organization; Dr. H. Sorenson, University of California at San Diego; Major T. Swartz, HQ USAF; Mr. D. Dickman (Ret), formerly of HQ USAF; Col L. Sugerman, USAF (Ret), Physical Science Laboratory, New Mexico State University; Mr. F. Guenthner, Consultant to Space and Missile Systems Organization; Mr. T. Sanders, Naval Air Development Center; and Dr. H. Pastrick, Office of the Under Secretary of Defense.



In addition to those listed above and the contributing authors, a large number of people contributed to the success of this meeting and I wish to express my appreciation to each for his efforts. Special thanks go to our symposium manager, Mr. G. Mozer.

This document is published only for the exchange and stimulation of ideas. Its publication does not constitute Air Force approval of the documents' findings or conclusions.



ROBERT E. BEALE, Colonel, USAF  
Deputy Commander, 6585th Test Group



#### ABSTRACT

These proceedings contain papers included in the Ninth Biennial Guidance Test Symposium. This symposium, hosted by the Central Inertial Guidance Test Facility, is directed toward the exchange of information, stimulation of new ideas and discussion of recent developments in the field of guidance testing. The papers presented include such topics as the Global Positioning System, the Space Shuttle, Aircraft Inertial Navigators, Component Evaluation, Advanced Guidance Methodology, Missile Guidance Systems and Analysis Techniques. The included papers were those presented in the unclassified sessions of the symposium. Papers presented in the classified portions of the meeting are being published as Volume II.

## PROCEEDINGS

### SESSION I - GPS & SPACE SHUTTLE

GLOBAL POSITIONING SYSTEM EVALUATOR (GPSE) - J. G. Pennett and T. F. Bowlds

A DYNAMIC INTEGRATED TEST FOR THE SPACE SHUTTLE - Richard W. Weissberg and Steven Brody

DETECTION OF ANOMALOUS GUIDANCE SYSTEM PERFORMANCE USING FLY-2 AND GPS MEASUREMENTS - Edward M. Duiven, Larry M. Hawthorne, Kevin S. Tait and C. Julian Vahlberg

### SESSION II - INERTIAL COMPONENTS TESTING

MODELS FOR G-SENSITIVE TRENDING (GST) RELATED TO FLOTATION FLUID BEHAVIOR - N. Barbour and M. Weinberg

CENTRIFUGE TESTING OF A LASER GYRO, PROCEDURES AND RESULTS - Robert Thede and Robert Kim

ACCELEROMETER SCALE FACTOR AND LINEARITY CALIBRATION USING A LASER INTERFEROMETER - Paul Klingenstein and William Lange

### SESSION III - INERTIAL NAVIGATION & COMPONENTS

EVALUATION OF AN FM/CW RANGE MEASUREMENT SYSTEM FOR VTOL LANDING - Dean G. Krenz, David R. Colvin, Stanley K. Miyashiro and Francis E. Morris

SPECTRAL NOISE PERFORMANCE OF A HIGH ACCURACY DRY TUNED GYROSCOPE AND THE NASA STANDARD REDUNDANT DRY ROTOR INERTIAL REFERENCE UNIT (DRIRU II) - K. N. Green, E. M. Oshika and R. L. Van Alstine

### SESSION IV - SYSTEMS TESTING & MODELING

COMBINED ENVIRONMENTAL TESTING OF THE AGM-86 INERTIAL NAVIGATION ELEMENT FOR CRUISE MISSILE - Barry Hardison

CALIBRATION AND ALIGNMENT PERFORMANCE EVALUATION OF THE ROCKWELL ASP-IMU TEST BED, TECHNIQUES AND RESULTS - V. D. Henderson

SESSION IV - SYSTEMS TESTING & MODELING, Continued

3D SCENE MODELING: A FLEXIBLE APPROACH TO REFERENCE  
MAP GENERATION - E. M. Rounds and A. T. Zavodny

SESSION V - ADVANCED GUIDANCE METHODOLOGY

PROPOSED USE OF RETRO ROCKETS FOR OPTIMIZING ANALYSIS  
OF INERTIAL GUIDANCE SYSTEM ERRORS IN 100-G SLED TESTS -  
Norman L. Ingold

PROGRESS AND PLANS FOR THE DEVELOPMENT OF AN ADVANCED  
GUIDANCE TEST LABORATORY - W. J. Whitesell and Major T. R.  
Hooten

STRAPDOWN SYSTEM PERFORMANCE IMPROVEMENT BY ROTATING  
THE INERTIAL INSTRUMENTS - J. C. Pinson

BACK-UP PAPER

MEASUREMENT OF AN ACCELEROMETER SECOND ORDER ERROR  
COEFFICIENT THROUGH A LINEAR VIBRATOR MECHANIZATION -  
Leo A. Keller, Jr.

AN EVALUATION OF SENSOR FAULT DETECTION AND IDENTIFICATION  
ALGORITHMS FOR IMPROVED UTILIZATION OF TETRAD CONFIGURED  
STRAPDOWN INS - Ronald J. Hruby, William S. Bjorkman, and Ralph  
A. Carestia



TITLE: GLOBAL POSITIONING SYSTEM  
EVALUATOR (GPSE)

AUTHORS: J. G. PENNETT  
T. F. BOWLDS

AFAL/RWA-4  
WRIGHT-PATTERSON AFB, OH 45433

10

## GPS EVALUATOR

By: J.G. Pennett

Abstract - This paper presents a general overview of the capabilities of the Global Positioning System User Equipment Evaluator (GPSE) at Wright-Patterson AFB, Ohio. The GPSE is capable of electrically simulating the flight conditions a typical GPS receiver would expect. The effects of errors are all controlled and repeatable for each simulation. The GPSE is also capable of jamming valid satellite signals with various signal formats. The simulation is controlled by a PDP 11/70 which makes the evaluator adaptable to user equipment requirements. The effects of the user's IMU errors, clock drift, antenna pattern, and jamming immunity are all calculated by the 11/70 which then controls the various satellite, jammer, and data signals seen by the user equipment. The duration of a flight simulation is theoretically unlimited; however, equipment specifications limit present flight time to 10 hours. The present system is configured for aircraft flight simulation; however, vehicle parameter software can be changed to simulate ships, tanks, or missiles.

Capt Gary Pennett  
AFAL/RWA-4  
Wright-Patterson AFB, OH 45433  
Phone: AV7856849  
(513-255-6849)

## GLOBAL POSITIONING SYSTEM EVALUATOR (GPSE)

### Introduction

The Global Positioning System (GPS) is a proposed worldwide navigation system consisting of a 24 satellite reference grid. Reception of any four properly positioned satellites will provide a triangulation type reference point to a navigation user equipment (UE). The proposed system of 24 satellites will not be available until mid to late 1980's. There are presently 10 to 15 user's receivers under test or development. The options for testing of present UE is either field testing with the four developmental satellites in orbit or by simulation. A GPS Evaluator was developed by the Air Force Avionics Laboratory in Ohio for the express purpose of simulating a fully operational GPS environment. This paper will describe the functions and limitations of the GPSE.

### Considerations

Before embarking on a description of GPSE, a brief tutorial on the necessary electrical signals for navigation and simulation considerations will be covered.

The precise navigational capability of GPS is inherent in the pseudo random or pseudo range codes transmitted by each of the 24 satellites. All satellites are synchronized via a ground station to a very precise GPS time. The precision of the time and code rate determines the lower bound on navigation performance. Each satellite has a dedicated 10MHz linear pseudo range code that repeats approximately every 8 days. Additionally, each satellite has a dedicated 1MHz code that repeats every millisecond. The 10MHz code is called the precise code or P-code and the 1MHz code is the clear acquisition or C/A code. The P and C/A codes are transmitted in a QPSK format on a 1227.6MHz carrier and the P-code is transmitted in a BPSK format with a 1575.42MHz carrier. The separation of frequencies allows the receiver to compare arrival times of the P-codes and thus calculate ionospheric delay for use in the navigation solution. The 1575.42 MHz carrier is the L1 frequency and the 1227.6 MHz carrier is the L2 frequency.

A 50 BPS data rate is modulated on both the L1 and L2 codes. The data consists of a handover word (HOW), ephemeris, satellite clock bias, satellite health, and a satellite almanac. The HOW is a message usually received on the C/A code and provides the receiver with information necessary to aid in the acquisition of the P-code. The satellite ephemeris is updated by the ground station after the satellite has been tracked over a portion of its orbit by other ground stations. The satellite clock bias is provided to the satellite by the ground station based on the ground station's integration of the satellite's L1 and L2 codes, and tracking information. Since all satellites are in a 12 hour orbit, and due to the positioning of those orbits, all satellites will pass within sight of a central ground station,



at least once during a 24 hour period, thus allowing for one reference clock at the ground station that will be used to synchronize all 24 satellites. This reduces position errors caused by clock bias to a minimum. The satellite health word tells the user whether the information transmitted by a particular satellite is reliable. This message is also provided to the satellite via ground station monitoring. Finally, the satellite almanac allows the receiver to lock on to one satellite and decode the position of all other satellites in orbit (1). In addition to providing useful information, the data storage capability of the UE is reduced as the satellite can provide necessary navigation information.

Precise navigation is accomplished when the UE receives signals from four properly spaced satellites. The geometry of the satellites regulates the precision at which the UE can determine its position. For example, four satellites in close proximity of each other provide poor geometry, whereas one satellite overhead and three satellites spaced  $120^\circ$  apart on the horizon provide good geometry. The four satellites are necessary to solve four equations with the four unknowns of delay of signal from each satellite. Based on the absolute delay of the codes from each satellite, clock bias, and satellite position from ephemeris the receiver can calculate its position. The UE can also navigate with less than four satellites in a degraded mode by receiving position reference from another source such as a barometric altimeter.

The GPS system is a stand-alone navigation system; however, other navigation instruments such as an inertial measurement unit (IMU) can be used to aid in satellite acquisition, reacquisition, and tracking in a high dynamic maneuver. A GPS Evaluator must therefore provide corresponding inertial simulation to the UE along with satellite signals to stimulate navigational responses from the UE under test. In a real world environment there are undesired signals that accompany the desired signals, either as Radio Frequency Interference (RFI) or intentional jamming. The GPSE therefore must provide these extraneous signals as part of a simulation.

The next section is a description of the GPSE system and how various portions of the system are used to simulate the GPS environment.

### System Description

The GPSE is a totally self-contained evaluation facility. It generates the required satellite RF signals, and sensor inputs for real time flight simulation and analyzes the performance of the UE on each flight after it is flown. The facility consists of three rooms and is laid out as shown in Figure 1. The simulation equipment consists of two major subsystems, the data processor (DP) and the simulation hardware.

The data processor consists of an off-the-shelf PDP 11/70 computer, four magnetic tape units, an RP05 disk, line printer, and CRT displays. The functions of the DP will be described in detail in the software section of this paper (2).



### Simulation Hardware

The simulation hardware equipment shown in Figure 1 is controlled via the software in the DP. The interconnection of the various assemblies is shown in Figure 2. The DP communicates with the Unit Device Controller Assembly (UDCA) during a real time simulation (3).

Unit Device Controller Assembly (UDCA). The UDCA serves two main functions in the GPSE. During a real time simulation the UDCA acts as a communications processor and as a maintenance tool in the off-line mode. In a real time simulation the UDCA transmits and receives commands from the DP and in-turn times and formats these commands for the various simulation hardware assemblies. In the maintenance mode the CRT terminal connected to the UDCA allows the technicians to address individual assemblies.

The UDCA contains no operating system as does the DP and is therefore programmed in assembly language. Since assembly language is rather awkward without an operating system, the DP is used to edit and compile programs for the UDCA. Programs compiled on the DP are recorded on cassettes which are then read by the cassette unit integral to the UDCA CRT terminal.

The present configuration of the UDCA as a message processor during real time has room for future expansion of hardware capabilities. One of these such expansions under development at AFAL is automatic switching of satellite PN codes and antenna port selection (4). It is also conceivable that additional satellite signal generation hardware can be added to provide the UE with access to 6-10 satellites simultaneously. Each satellite signal is generated in a separate satellite signal RF generator.

Satellite Signal Generator Assembly (SSGA). The satellite signal generators consist of five separate satellite signal RF modules. The SSGA can provide five satellite signals simultaneously for the user equipment. The normal mode, however, is four satellite signal generators on line and a fifth generator as a spare. The spare channel can be configured for the next expected satellite to be used by the UE.

The SSG's consist of a baseband unit which generates the L1 and L2 codes and an RF section which uses the baseband signals to modulate the BPSK or QPSK format. The baseband units are also provided with the 50BPS data via the 11/70 through the 11/04 device controller. This allows the navigation message to be updated in real time and for the spare channel to be switched to a new satellite as necessary. The carrier frequency for each modulator and the L1 and L2 codes must be delayed and doppler shifted by the appropriate amount to simulate user and satellite range and motion. The Dynamic Frequency Synthesizer provides the required delays and frequency shifts.

Dynamic Frequency Synthesizer Assembly (DFSA). The DFSA is a five channel hardware digital integrator, allowing one integration for each satellite channel. The output of the integrator is used as a reference for a phase lock loop to drive the various clocks and modulators in the SSGA. The DFSA provides fine frequency resolution over a wide frequency range necessary to simulate satellite and user vehicle dynamics.

The UDCA, by command from the DP, loads a digital register which is the input for jerk, acceleration, and velocity to the integrator which then provides position in terms of delay and doppler frequency to the SSCA. The ionospheric differential delay between L1 and L2 frequency is accomplished by loading a differential delay value in the L2 velocity integrator prior to clocking the L2 P and C/A code generators.

The DFSA is used as a reference to the phase lock loops to provide precise computer controlled, repeatable scenarios. The total accumulated range error after a 10 hour mission is on the order of .1 meter absolute position ambiguity. Since the expected accuracy of most user sets is on the order of 10 meter range ambiguity, the GPSE introduces very little uncertainty to the truth model (5).

Jammer Generator Assembly (JGA). The Jammer Generators, five total, are controlled based on a particular scenario programmed in the DP. The DP, through the UDCA, turns the jammers on or off, attenuates the jammer power based on antenna pattern selected, path loss, shifts frequency of the jammer for a frequency hop simulation, or accepts up to three external jammer sources for future threats and investigations.

The RF interference investigation is accomplished in the same manner as jamming tests; however, RF interference sources are used on the external inputs to the jammer ports. The external ports can also be used to test multipath effects by splitting a particular satellite signal and providing a delayed version to an external jammer port. The multipath satellite signal will then be attenuated by the particular antenna pattern.

Satellite Signal Combiner/Noise Generator Assembly (SSC/NGA). The SSC/NG combines the satellite signals, jammer signals, and excess noise prior to supplying the RF signals to the UE via the bulkhead between the RF screen rooms. The signal combination is based on the type of antennas the UE is planning to use or is using in actual operation. The GPSE has four separate ports to simulate a high performance four beam steered antenna. It also has one port with all four satellites combined to simulate an omni-directional type antenna. The antenna sidelobe and main beam attenuation is controlled via the DP selected scenario through the UDCA.

In/Out Controller Unit (I/O CU). The I/O CU provides all sensor interfaces to the UE other than the RF signals. These signals include a serial MIL-STD-1553A data bus, IRIG time, 5MHz clock, and altimeter synchro. The 1553 serial data bus is primarily for half duplex serial direct memory access (DMA) with the UDCA. The UDCA in turn provides DMA data from the UE to the DP which generates IMU signals and barometric altimeter simulation. The DP also records antenna pointing commands generated by the UE for post-flight processing.

Functional Test Assembly (FTA). The FTA performs two major functions during the real-time simulations. The front panel of the FTA has LED's associated with the assemblies previously discussed to visually identify the malfunction of any of these assemblies. A second set of LED's is used during the startup of a real-time simulation to synchronize the GPSE to the UE.



The ultimate accuracy of the GPSE is determined by the timing differences between the UE and GPSE. In order to minimize timing differences the GPSE provides a clock signal to the UE. The UE is transmitting data via the 1553 data bus which is in-turn received and processed by the GPSE. The synchronization lights on the FTA allow the operators to a null timing bias between the GPSE and UE. Once the timing bias has been adjusted manually at real-time startup the GPSE software automatically maintains the proper timing.

#### GPSE Software

The GPSE facility is entirely self-contained in that it can generate real-time flight simulations for the UE and analyze the results of the flight. In this section the GPSE DP software is described and its interface to the various GPSE subsystems through the UDCA are indicated when applicable.

The GPSE software is divided into three distinct segments. Each segment is a stand-alone program except for data tapes that are used in each successive segment. The three segments will be described individually in the sequence in which they are used. The three segments are the Pre-Computed Simulation (PCS), Real-Time Simulation (RTS), and Post-Run Analysis (PRA). The relationship of the three segments is shown in Figure 3.

Pre-Compute Segment (PCS). The PCS segment is run prior to the real-time simulation with the DP isolated from the UDC and other GPSE subsystems. This segment precomputes "truth data" for use in the real-time run and stores this information on magnetic tape. The precomputation of truth data is necessary as the complexity of the real-time simulation is such that the DP could not handle all truth and real-time computations in real-time.

The types of truth data that comprise the PCS are divided into sub-routines relating to each particular portion of the flight simulation. The subroutines include a user vehicle trajectory generator, an ideal IMU simulator, an antenna lever arm simulator, satellite constellation selection, satellite ephemeris generator, user satellite geometry calculation, signal path effects, signal derivative, jammer trajectory, user jammer geometry, and jamming path loss calculations. The pre-computed data tapes generated in the PCS are then used in the real-time segment.

Real-Time Segment (RTS). The RTS is the portion of testing when the user's equipment is subjected to navigation sensor inputs from the various GPSE subsystems, e.g., errors are introduced. The UDCA receives commands from the DP which in-turn is using the pre-computed data tape and a real-time disc file as a data base. The pre-computed tape contains the truth models developed in the PCS and the disc file contains the parameters for the error model subroutines.

The RTS subroutines are: IMU error simulator, altimeter error, user clock drift, satellite data block formatter, antenna pattern simulator, jammer signal control, and GPSE synchronization. The RTS generates a post-run data tape that contains the values of the corrupted truth model for use

in the post-run analysis. The post-run data tape also records GPSE subsystem health and user equipment antenna pointing commands. The UE position and velocity is being recorded during real-time on the UE's instrumentation tape. The UE's instrumentation tape is time-tagged with IRIG time as are the GPSE pre-computed and post-run data tapes. These three tapes are used in the post-run analysis.

Post-Run Analysis (PRA). The PRA segment operates in non-real-time as does the PCS. Also, the DP is again isolated from the UDCA and UE. The PRA reads the truth data from the pre-computed tape, the real-time simulation from the post-run data tape and the UE instrumentation tape, and correlates the data with respect to a common data base and computes UE navigation errors.

### Conclusion

The software control of simulation hardware allows the GPSE to test developmental concepts. For example, since the software generates the antenna sidelobe attenuation effects the actual antenna hardware need not exist prior to GPSE testing. Similarly, various parameters for clocks and IMU's may be investigated without the need for actual hardware.

The GPSE provides an alternate to field testing of GPS user's equipment with the advantage of repeatability and convenience. The present and future GPS UE are complex systems requiring a rigorous, controlled method of testing to verify all modes of operation. The software control of the simulation hardware enables the GPSE to adapt to future requirements with a minimum of modification.

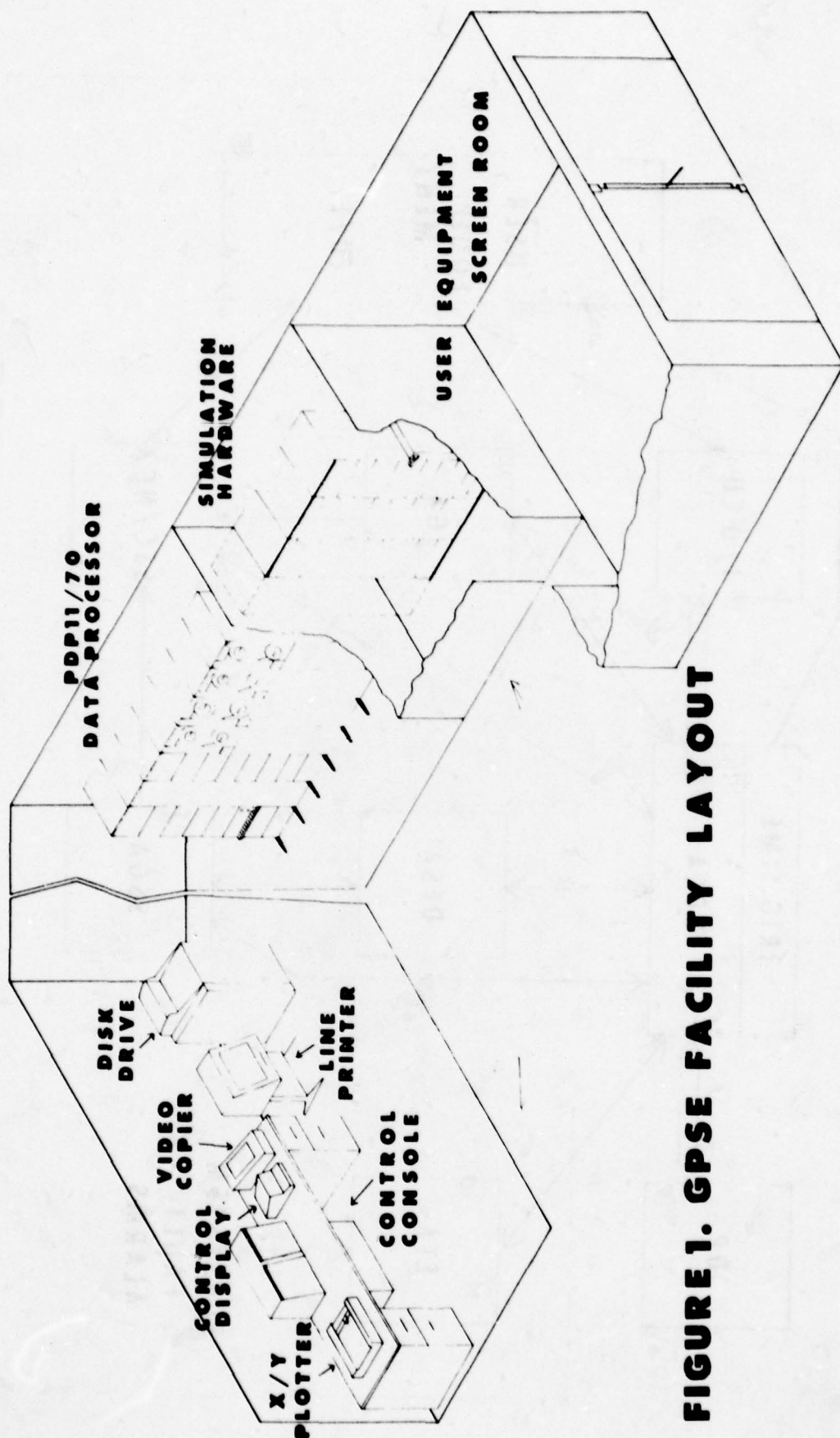


**FIGURE 1. GPSE FACILITY LAYOUT**



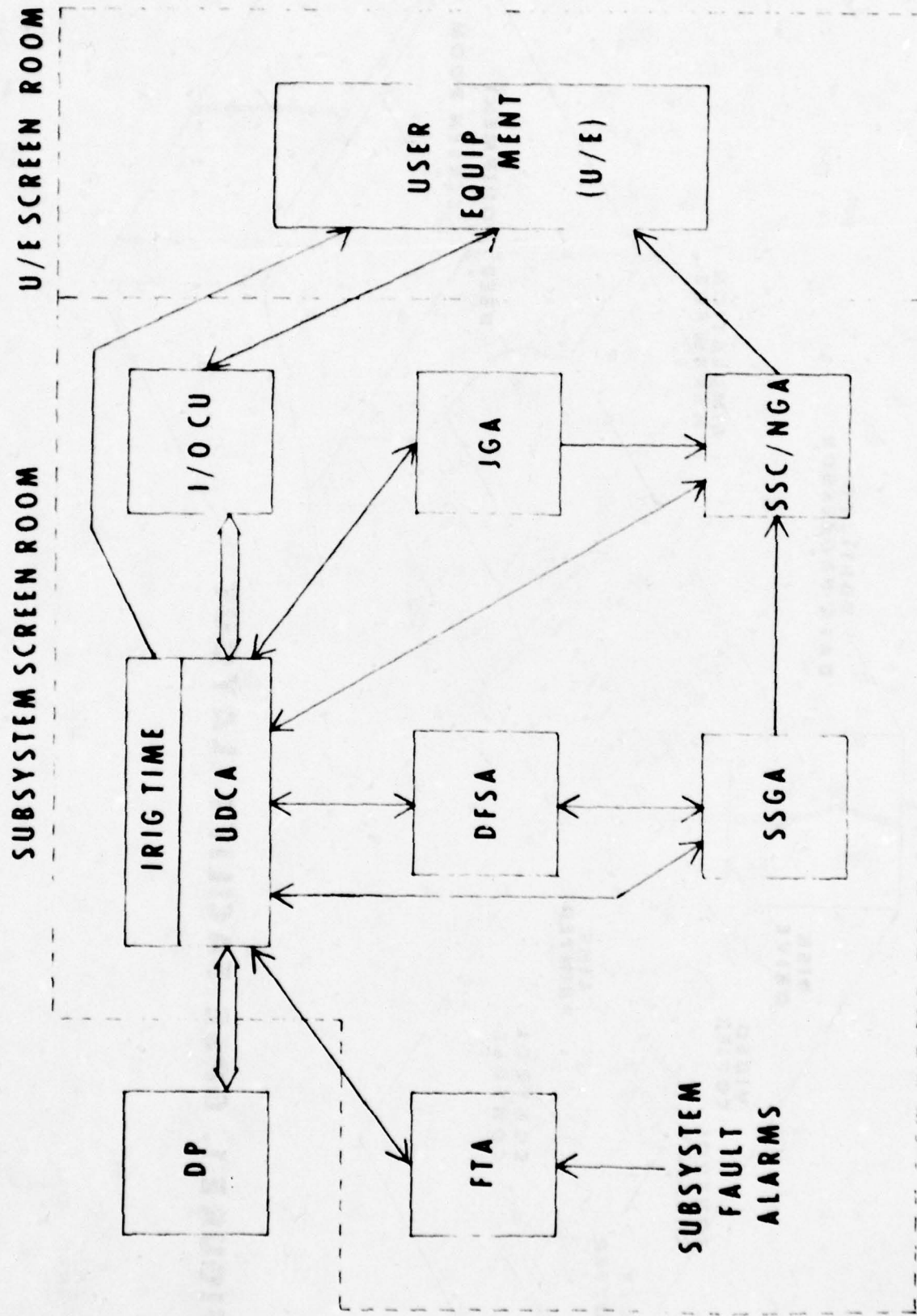


**FIGURE 2. GPSE SUBSYSTEM INTERCONNECTIONS**

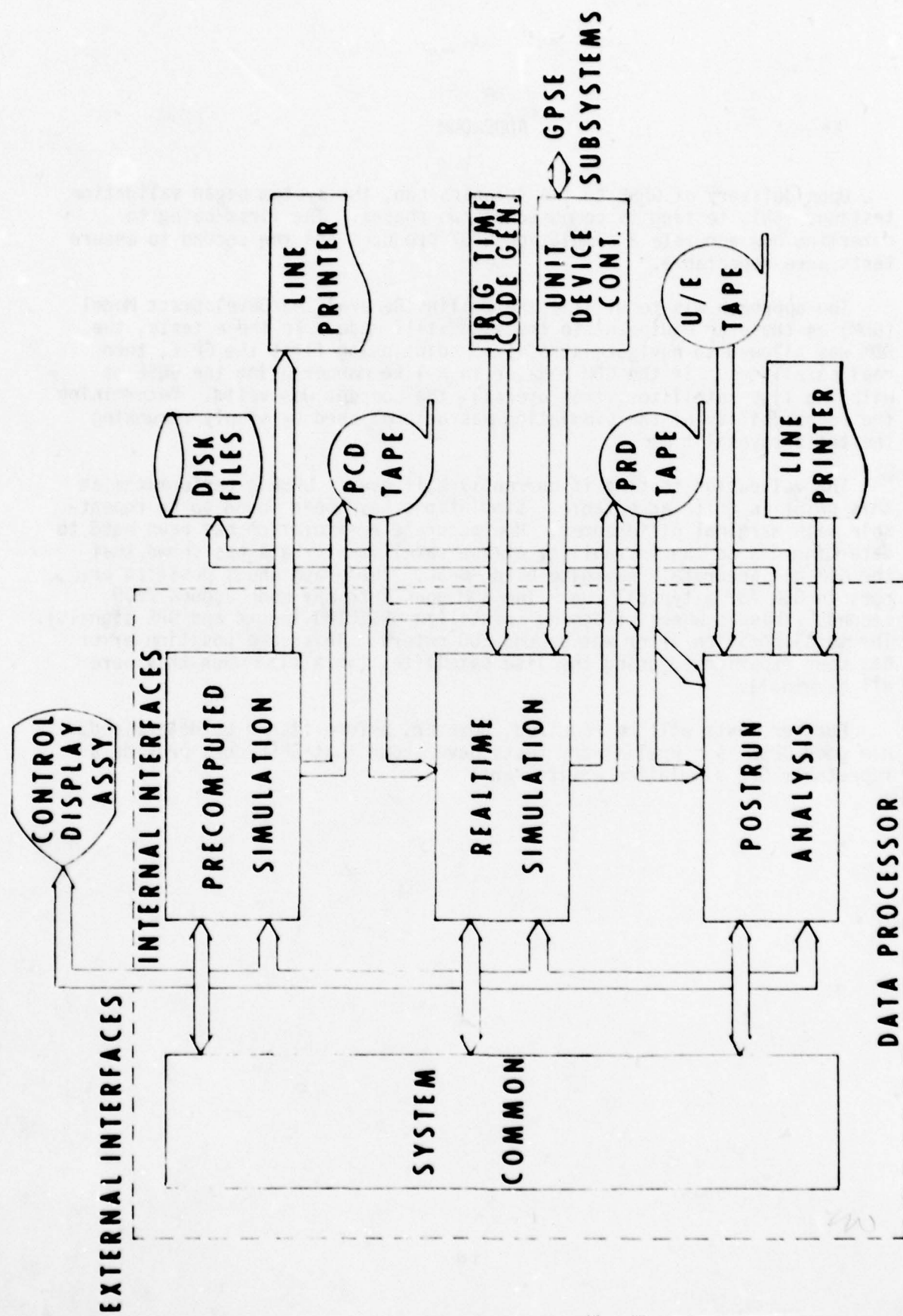


**FIGURE 3. GPSE SOFTWARE RELATIONSHIPS**



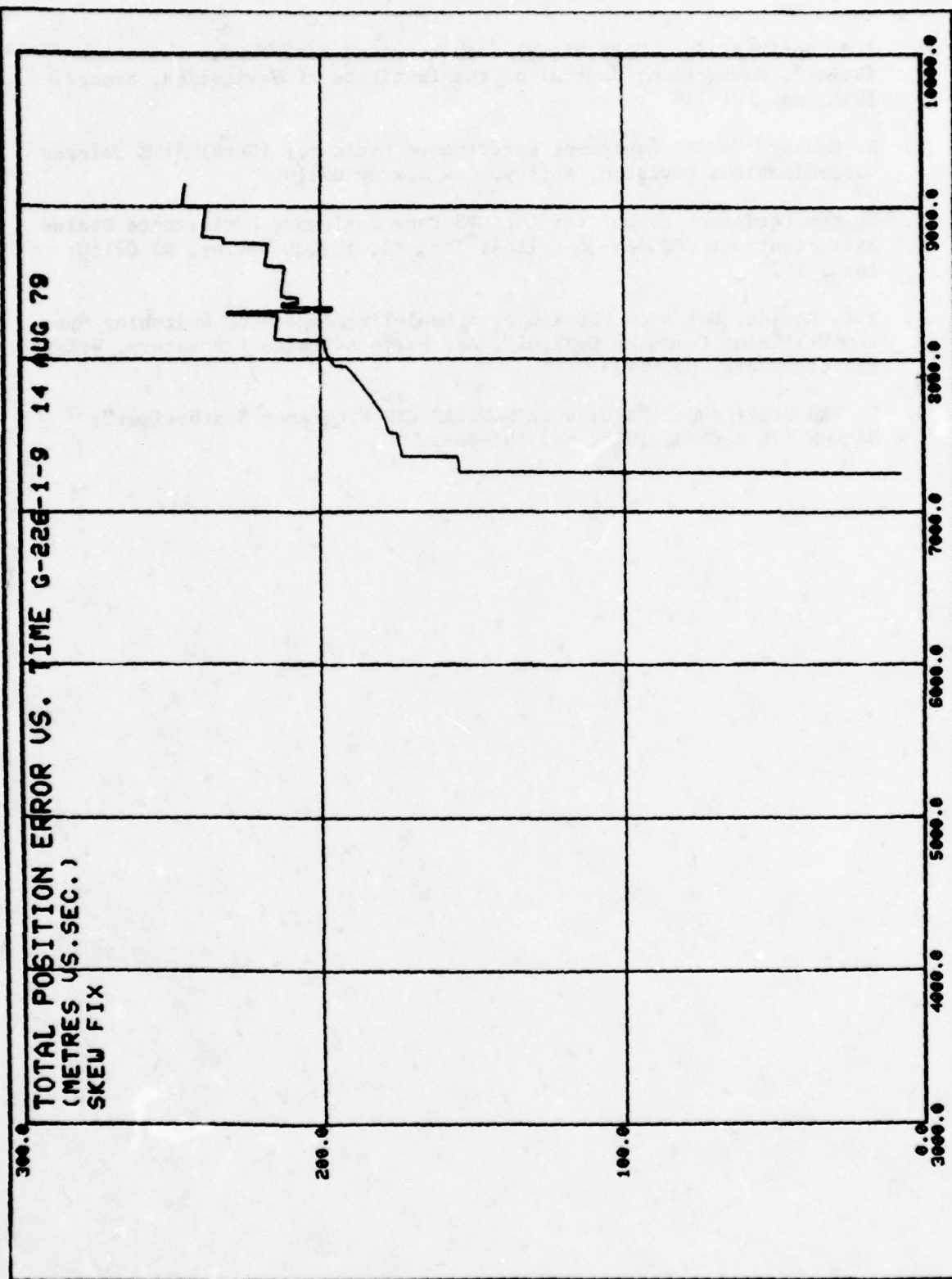
## ADDENDUM

Upon delivery of GPSE to the Avionics Lab, the system began validation testing. This testing is composed of two phases. The first being to determine how accurate a simulation GPSE produces and the second to ensure tests were repeatable.

The approach was to utilize the Collins Generalized Development Model (GDM) as the user equipment in the standstill mode. In these tests, the GDM was allowed to navigate at a fixed point using first the GPSE, then real satellites. If the GDM behaved in a like manner using the GPSE as with the live satellites, then overall, the concept was valid. Determining the repeatability of the simulation was accomplished by simply rerunning the tests several times.

The validation testing is currently half over. GPSE's performance at this point is quite acceptable. Simulations have been found to be repeatable with marginal differences. How accurate a simulation has been hard to determine due to the instability of the satellites. Data has shown that the GDM can accurately navigate using GPSE. The graph shows position errors in GDM for a typical run. The GDM goes into nav mode around 7200 seconds (this is where it begins to utilize GPSE IMU inputs and GPS signals). The total position error was around 200 meters. This same position error has been experienced using the live satellites (at a time when they were all marginal).

Further tests will be required, however, before it can be determined how good GPSE is. Preliminary tests have shown that GPSE does provide a repeatable GPS simulation environment.



#### BIBLIOGRAPHY

1. J.J. Spilker, Jr., "GPS Signal Structure and Performance Characteristics", Navigation: Journal of the Institute of Navigation, Summer 1978, pp. 121-146.
2. B. Cooper, "A GPS Equipment Performance Evaluator (GPSE)", ITT Defense Communications Division, Nutley, New Jersey 07110.
3. System/Equipment Manual for the GPS User Equipment Performance Evaluator, Contract #F33615-76-C-1164, Item #2, ITTDCD Nutley, NJ 07110: April 1979.
4. T.F. Bowlds, Notes on "Design of a Real-Time Automated Switching System Utilizing Computer Control", Air Force Avionics Laboratory, Wright-Patterson AFB, OH 45433.
5. P. Van Broekhoven, "A Dynamic NAVSTAR GPS Frequency Synthesizer", NAECON '76 Record, 1976, pp. 857-863.

**TITLE:       A DYNAMIC INTEGRATED  
TEST FOR THE SPACE  
SHUTTLE**

**AUTHORS:     RICHARD W. WEISSBERG  
STEVEN BRODY**

**INTERMETRICS, INCORPORATED  
Cambridge, Massachusetts**



## TABLE OF CONTENTS

	PAGE
1 Introduction	1
1.1 The Space Transportation System	1
1.2 Motivation Behind the DIT	5
1.3 A Brief Overview	5
2 Ground Rules and Constraints	7
3 The DIT Movie	9
3.1 The Simdata Tape	9
3.2 Obtaining Simdata	13
3.3 Transmitting the Simdata to the Vehicle	13
3.4 The DIT and Time	17
4 Modifying the Flight Software for the DIT	17
4.1 Injection of Simdata	17
4.2 Other DIT Patches to the Flight Software	19
5 Vehicle and Personnel Safety	20
6 Evaluation of Test Results	22
7 Progress to Date	23
8 Applying the DIT Concept to Other Systems	24

## A DYNAMIC INTEGRATED TEST FOR THE SPACE SHUTTLE

### 1 Introduction

#### 1.1 The Space Transportation System

The Space Transportation System (STS) is planned to be the workhorse of NASA and DOD in the 1980's and beyond. Illustrated in Figure 1, it consists of the Space Shuttle Orbiter spacecraft with its three main engines, an external tank housing the main engine propellants, and two solid rocket boosters. The Space Division of Rockwell

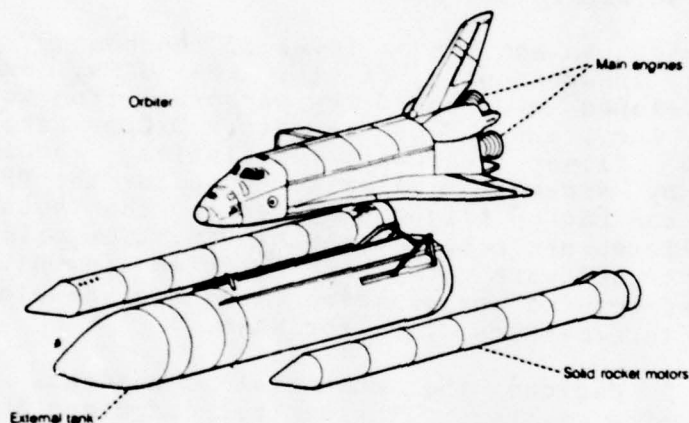


FIGURE 1 Configuration of Space Transportation System

International is prime contractor to NASA for the Space Shuttle Orbiter as well as for total integration of the STS. At present, the orbiter spacecraft containing the crew and payload bay is the only component that reaches orbit. After completing its mission, the shuttle then returns to earth, landing as an airplane.

Central to the operation of the STS are the five on-board IBM AP-101 flight computers which monitor and control the vehicle's flight operations. In fact, the shuttle has been designed as a digitally controlled spacecraft; that is, there are no direct mechanical linkages by which the crew can manipulate the aerosurfaces or cause the various propulsion subsystems to fire. The vehicle is unstable in most flight modes and generally requires continuous control by the computers to maintain stability within rigid boundaries. In certain flight modes the crew does have the option to select either the automatic mode for guidance, navigation, and control (GN&C) of the vehicle, which essentially allows the computers to do all the flying,

or the manual mode of flight, whereby the crew flies the vehicle by hands-on manipulation of the controls. However, if manual flight is selected, the commands issued by the crew to the aerosurfaces and the engines must still pass through and be issued by the computers. Hence, the reliance on the computers is absolute.

The five flight computers, called general purpose computers or GPCs, are organized into a redundant set of four GPCs which form the primary flight system (PFS) plus a single GPC used as the backup flight system (BFS). IBM has responsibility not only for the flight computer hardware but also for the software which runs in the four PFS GPCs. This code, written by IBM to implement Rockwell specified requirements, is loaded identically into each of the four redundant computers. During flight operations, inter-computer communication insures self-consistency and synchronization within the PFS.

To provide an additional level of redundancy, a fifth GPC operates independently of the PFS GPCs, executing software developed and coded by personnel from Rockwell, Intermetrics, Inc., and the Charles Stark Draper Laboratory. This backup flight software satisfies requirements established by Rockwell similar to those for the PFS. The crew engages the backup flight computer in the event that critical failures are detected in the PFS. The primary and backup flight software are both written in HAL/S, a high-order structured programming language developed and supported by Intermetrics, Inc. for NASA.

Figure 2 depicts the essential components of the orbiter avionics system. The central computers interface with the various subsystems through 19 serial data buses. Eight of these connect with the flight forward and flight aft multiplexer/demultiplexer (MDM) units which in turn serve as the conduit for signals going to and from such devices as 1) the master timing unit (MTU) which serves as the accurate time source for the GPCs; 2) sensors which provide velocity and attitude information such as the inertial measurement unit (IMU), the accelerometer assembly (AA), and the rate gyro assembly (RGA); 3) external navigation aids ("navaids") such as the tactical air navigation system (TACAN), microwave landing system (MLS), radar altimeter (RA), air data system (ADS), and star tracker (ST); 4) propulsion subsystems such as the reaction control system (RCS), the orbital maneuvering system (OMS), and the main engines; 5) the vehicle aerosurfaces such as elevons, rudder, speedbrake, and body flap; and 6) the cockpit switches and controls and dedicated display units (DDU) which provide to the crew information such as shuttle velocity, altitude, attitude, and other flight critical parameters.



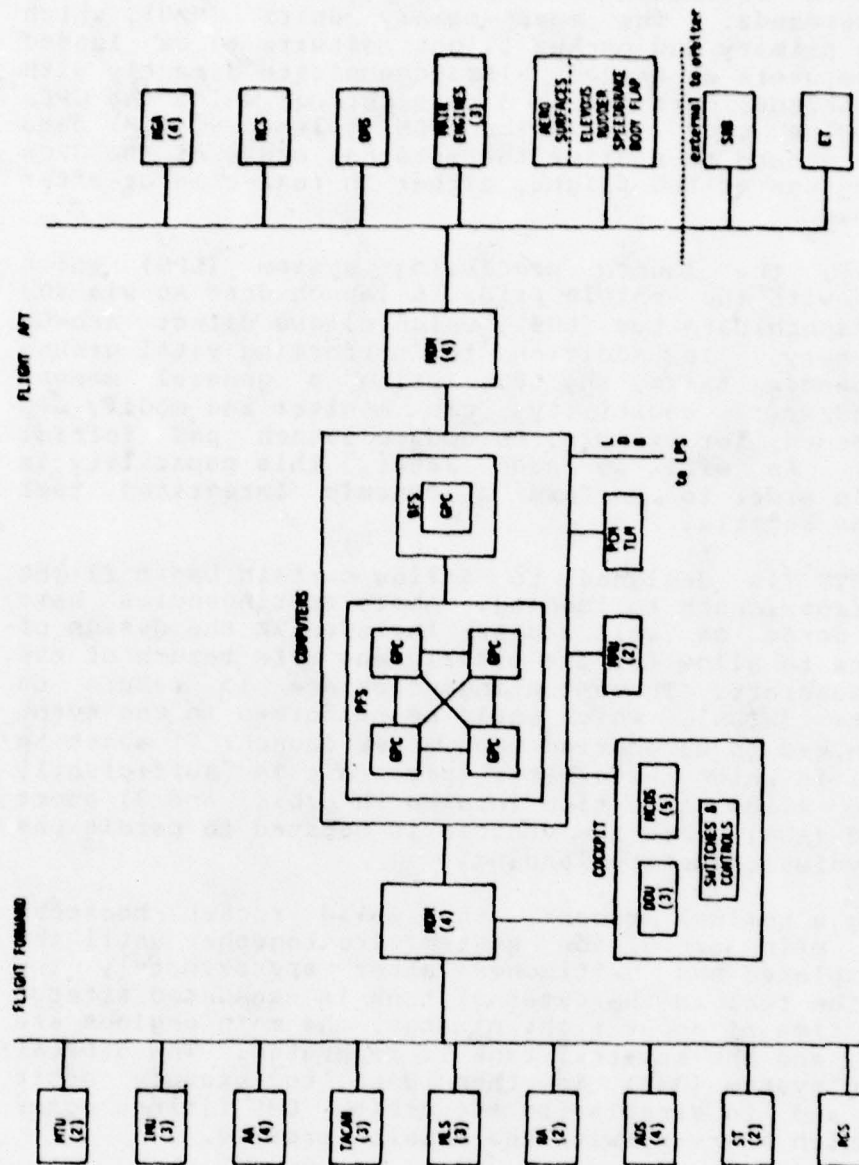


FIGURE 2 Orbiter Avionics Subsystems

Other data buses connect the GPCs with the multi-function CRT display systems (MCDS) which present a variety of GN&C and system status information to the crew, and allow them extensive interaction with the GPCs via keyboard commands. The mass memory units (MMU), which contain the primary and backup flight software to be loaded into the computers as needed, also communicate directly with the GPCs. Another data bus is a port through which the GPCs transmit pulse code modulation (PCM) telemetry (TLM) data used by the ground to monitor the internal state of the GPCs and the progress of the flight, either in real-time or after the mission.

Finally, the launch processing system (LPS) which interfaces with the vehicle prior to launch does so via the umbilical launch data bus (LDB), which allows direct access to GPC memory. In addition to performing vital ground launch sequencing tasks, the LPS, using a general memory (GMEM) read/write capability, can monitor and modify GPC core, if needed; for example, to update launch pad initial conditions. As will be seen later, this capability is essential in order to perform a dynamic integrated test (DIT) of the shuttle.

The STS is designed to follow certain basic flight sequences from launch to landing. Abort contingencies have been considered as well and are included in the design of the software to allow for the orderly and safe return of the orbiter spacecraft. These contingencies are 1) return to launch site (RTLS), which would be performed in the event the mission had to be aborted soon after launch; 2) abort to orbit (ATO) in which the orbiter spacecraft is sufficiently healthy to allow insertion into earth orbit; and 3) abort once around (AOA) where the vehicle is boosted to permit one orbital revolution before landing.

During a nominal ascent, the solid rocket boosters (SRB) and main propulsion system fire together until the SRBs are depleted and jettisoned after approximately two minutes. The fuel in the external tank is exhausted after a total burn time of about eight minutes, the main engines are shut down, and the external tank is separated. The orbital maneuvering system (OMS) is then used to execute orbit insertion and to circularize the orbit. OMS firings occur at times which may vary with the mission profile.

After earth orbit operations are complete, the OMS is once again used for the deorbit burn to begin a nominal descent. The orbiter coasts for about 30 minutes to atmospheric entry. Approximately another 30 minutes places the shuttle on the runway having transitioned through several guidance phases and performed the requisite landing

maneuvers. The shuttle makes a dead-stick landing as a glider; it was not designed to allow a go-around capability.

### 1.2 Motivation Behind the DIT

The various subsystems -- computers, flight software, navigation instruments, environment sensors, engines, etc. -- are subjected to rigorous checkout and verification procedures, at least to the fullest extent possible in a testbed environment. Then they are shipped to Kennedy Space Center (KSC), Florida, for final integration into the shuttle vehicle. But it is not until these subsystems are received and fitted to the vehicle at KSC that the Space Transportation System exists which will carry a crew into orbit. Clearly, just as checkout and verification of each of the component subsystems is vital, so is it necessary to verify the final integrated configuration. The complete hardware-software data paths which are utilized in flight simply do not exist until the vehicle is put together. The integrated test is necessary to verify the integrity of these paths: that proper connections have been made, that correct polarity is maintained, and that no unexpected interference is generated.

The concept of the integrated test is complicated by the fact that the vehicle is not static -- the software and hardware configuration changes during the course of a mission as the software is moded through various sequences. Thus a valid integrated test is necessarily a dynamic integrated test, which checks out hardware-software data paths in a vehicle which is sequenced through the events of a flight profile.

### 1.3 A Brief Overview

A mechanism conceived by Intermetrics, Inc., has been developed for realizing this DIT concept. In essence, a simulated flight sensor profile is transmitted over the umbilical launch data bus and injected into the flight software in such a manner that the grounded vehicle believes it is flying. The vehicle is sequenced through nominal flight phases and deceived to detect the environment, position, velocity, and attitude it would detect on a nominal mission.

In fact, it is not the hardware sensors which are stimulated; the sensors do detect their earth-fixed environment, or in some cases, the constant output of a test set. Rather it is locations in the software which are



changed by the DIT. Instead of accessing locations written to by the sensors, the shuttle navigation software accesses locations containing injected simulated data. The navigation software thus runs open loop, in the sense that it is the "canned profile" which is "flown," and flight control commands cannot affect this profile as they would in real flight.

It is the intent of the DIT to exercise as much as possible the complete hardware-software data paths from sensors to effectors. Toward this end, the DIT design permits a choice between two similar but somewhat different data injection techniques for each sensor. Nominal data flow from sensors through applications programs to effectors is schematically represented in Figure 3a. The two data injection modes, known as substitution and combining, are illustrated in Figures 3b and 3c. In the substitution mode, the real sensor data are processed by the input routines but do not influence the GN&C applications calculations nor the commands sent to the effectors. In the combining mode, the real sensor data are added to the simulated sensor data, and it is the resultant combined values which drive the applications routines and effectors. The combining mode allows a more complete verification of the data paths during a DIT, but does involve added complications which are discussed later.

A few selected nominal profiles are chosen to be "canned" for the DIT; no attempt is made at exhaustive testing of all possible profiles. The selected nominal trajectories serve to mode the software through its various sequences and facilitate verification of hardware-software interfaces and interactions. The various aerosurfaces, engine gimbals, and other effectors on the vehicle are moved (except where prohibited for safety reasons) much as they would be for a real flight.

The rest of this paper examines in some detail the design and implementation of the dynamic integrated test for the Space Shuttle. The ground rules and constraints upon which the design was formulated are presented in Section 2. The concept of the DIT is expanded in Section 3, along with a discussion of the simulated sensor data (simdata), how it is obtained, and how it is transmitted to the GPCs for processing during a DIT. In Section 4, the interaction of the simdata with the flight software is examined, and the software modifications required to implement the DIT concept are presented. Concerns of vehicle and personnel safety during a DIT are discussed in Section 5, along with the techniques developed to ensure a safe checkout of the STS. Section 6 is about test evaluation. The progress made to date in DIT development and testing is the subject of Section 7, and finally, in Section 8 we present some



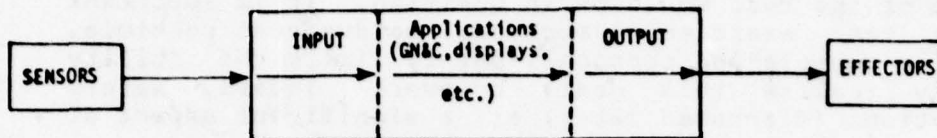


FIGURE 3a Nominal Data Flow

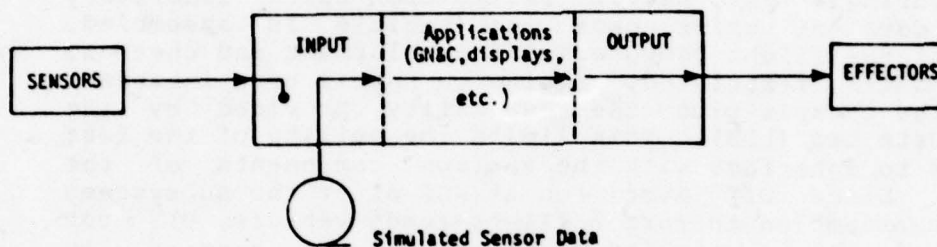


FIGURE 3b Simdata Substitution Mode

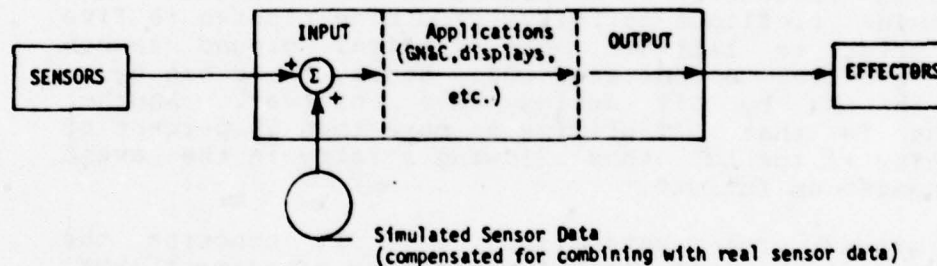


FIGURE 3c Simdata Combining Mode

suggestions concerning the application of the DIT concept to other avionics systems.

## 2 Ground Rules and Constraints

Certain ground rules were established during the initial design phase of DIT, some to satisfy practical constraints imposed by the existing STS design and development plan, and others to insure that the intent of DIT would not be lost during implementation. Included in the latter category is the design goal to minimize the

impact DIT has on the flight software, both in GPC memory requirements imposed by DIT modifications to the software, and in additional execution time (i.e., duty-cycle) resulting from these modifications. If the DIT-modified software were not very similar to the flight software, the relevance of the test would be in question. It is important that the test exercise as much real hardware as possible. Concern for vehicle and personnel safety limits the ability to fully realize this goal, however. Indeed, safety considerations (discussed later) are a significant aspect of the DIT.

The ability to halt and restart the GPCs at specific points during a test, heavily relied upon during laboratory testing, does not exist once the vehicle is assembled. Control of the flight computers for development and checkout becomes quite restricted, relying on normal crew interface through the cockpit plus the capability provided by the launch data bus (LDB). This limits the ability of the test engineers to interface with the various components of the shuttle. Since DIT must run at KSC after the subsystems have been assembled to form a flight-ready vehicle, DIT must operate under the constraint that once it has started, it must complete without interruption.

Certain restrictions are placed on the use of the LDB. During nominal preflight activity, from nine minutes to five seconds prior to lift-off, the critical ground launch sequence requires a dedicated LDB. Hence, there can be no usage of the LDB by DIT during this interval. Another constraint is that DIT utilize no more than 50 percent of the capacity of the LDB, thus allowing a retry in the event of a transmission failure.

A ground rule established for DIT concerns the preservation of the integrity of redundancy management (RM), the software function which selects from among the redundant sensors the set of variables to be accessed by the applications software. The DIT design allows the RM to execute based on inputs from the real sensor hardware, allowing comparisons and fault detection to take place exactly as in real flight. It is only after RM is executed that DIT-supplied simulated sensor data is injected and accessed by the applications routines.

The DIT design necessarily needed to be flexible enough to support development at Rockwell's Flight Systems laboratory (FSL) and NASA's Shuttle Avionics Integration Laboratory (SAIL). The availability of shuttle hardware, simulators, and other support equipment varies substantially at these facilities; so the DIT was designed to be as independent of specific equipment as possible.

Finally, it is a design goal to allow as much crew participation as possible, including manual keying in of commands to effect the transitions of the software through the various GN&C flight modes. In the spirit of flexibility, however, it was desired to be able to automatically issue these commands to the software via the LDB-transmitted simdata if a crew were not available, or if it was found that time criticality of certain events precluded manual key-ins. In either case, the preflight activities for DIT closely follow the standard items to be followed in a real flight, including full cockpit and subsystems checklists.

### 3 The DIT Movie

In some ways, the running of a DIT is analogous to the showing of a motion picture. A reel of movie film is a series of snapshots which are correlated linearly with time so as to create a dynamically flowing image when projected. For a DIT, "snapshots" of sensor data are stored on the simdata tape and correlated linearly with time in an analogous manner. As the movie projector projects each snapshot on the screen in timed succession, so does the launch processing system transmit simdata frames over the LDB to be injected into the flight software.

#### 3.1 The Simdata Tape

The simdata tape, a standard nine-track magnetic tape, is the medium on which the DIT canned sensor profile is stored. It contains four files of data: three of initialization data (not discussed here), and a fourth which contains the frames of simulated sensor data -- simdata -- to be dynamically injected into the flight software during execution of the DIT. Although every frame contains exactly 64 16-bit words, there are actually two types of frames; high-rate, which are refreshed every 160 milliseconds, and low-rate, which are refreshed every 480 milliseconds. Furthermore there are three types of low-rate data, as will be discussed shortly. The frames are arranged on file four of the tape as shown in Figure 4.

The high-rate frame, shown in Figure 5, represents a snapshot of navigation sensor and vehicle status information. Each piece of data has its unique place in the frame template, even though not every sensor is utilized for every DIT. An ascent trajectory requires no tacan or microwave landing system, for example; nor does a descent employ the solid rocket boosters. In any case, the DIT



Time (seconds) with respect to DIT start when frame becomes active	L	H	H	H	L	H	H	H	L	H	H	H	L	H	H
	.000	.000	.160	.320	.480	.480	.640	.800	.960	.960	1.120	1.280	1.440	1.440	1.600
	1	2	3	4	5	6	7	8	9	10	11	12	13	14	15

Each  
frame  
64  
words

L - Low rate frame refreshed every 480 milliseconds  
H - High rate frame refreshed every 160 milliseconds

FIGURE 4 Arrangement of Simdata Frames

WORD NUMBER	1	IMU VELOCITY
	13	TACAN
	17	MICROWAVE LANDING SYSTEM
	23	RADAR ALTIMETER
	25	RATE GYRO ASSEMBLY
	31	ACCELEROMETER ASSEMBLY
	38	SRB RATE GYRO ASSEMBLY
	43	IMU ATTITUDE
	51	SRB CHAMBER PRESSURE
	55	TACAN CHANNEL ID
	56	SPARE
	61	DATA GOOD FLAGS
	62	SELECTED IMU NUMBER AND MILS UPDATE INDICATOR
	63	CHECKSUM
	64	FRAME NUMBER

FIGURE 5 Simdata High-rate Frame

software can uniquely identify each piece of data by its position within the frame, and the data (along with low-rate data, described below) is sufficient to drive the vehicle,

There are three types of low-rate simdata: one which is sensor data refreshed every 480 milliseconds much as high-rate data is refreshed every 160 milliseconds, a second type which provides a more generalized capability to set the value of any parameter in the GPC memory, and a third type for simulating crew inputs. As of this writing, the only type-1 data, and thus the only data refreshed in every low-rate frame, is that associated with the air data sensor.

WORD #	CONTENTS
1	Triplet #1 Destination Address
2	Triplet #1 MASK
3	Triplet #1 Data
4	Triplet #2 Destination Address
5	Triplet #2 MASK
6	Triplet #2 Data
7	
8	
9	
.	.
.	.
.	.
.	.
49	Triplet #17 Destination Address
50	Triplet #17 MASK
51	Triplet #17 Data
52	Auto-Crew-Indicator = 0
53	Selected ADTA Static Pressure
54	
55	Selected ADTA Center Pressure
56	
57	Selected ADTA Lower Pressure
58	
59	Selected ADTA Upper Pressure
60	
61	Selected ADTA Total Temperature
62	
63	Sumcheck
64	Frame Number

FIGURE 6 Simdata Low-rate Frame With Type-2 Data

The second type of low-rate data is used to communicate the "occurrence" of various asynchronous events such as

detection of weight on landing gear. As shown in Figure 6, each type-2 datum is organized in the low-rate frame as an ordered triplet of 16-bit words: a GPC address, a mask indicating which bits are to be set, and a data word indicating the values of the bits to be set. Up to 17 triplets may be transmitted in a single low-rate frame. If the auto-crew flag in word 52 of the low-rate frame is set, the DIT software knows to interpret words two through 47 as type-3 data, which gets copied into the same software buffer which would be filled if a crew member were actually keying in commands (see Figure 7).

WORD #	CONTENTS
1	Address of Input Crew Data Buffer
2 • • • •  • • • • 47	Crew Data
48 49 50 51	Spare
52	Auto Crew Indicator
53 54	Selected ADTA Static Pressure
55 56	Selected ADTA Center Pressure
57 58	Selected ADTA Lower Pressure
59 60	Selected ADTA Upper Pressure
61 62	Selected ADTA Total Temperature
63 64	Suncheck Frame Number

FIGURE 7 Simdata Low-rate Frame With Type-3 Data



### 3.2 Obtaining Simdata

A motion picture is made by photographing the real world with a movie camera. An analogous procedure is utilized to generate simdata for a DIT: "snapshots" are taken from the GPC during a closed loop digital simulation in an avionics laboratory.

In facilities such as Rockwell's Flight Systems Laboratory (FSL) and NASA's Shuttle Avionics Integration Laboratory (SAIL), mechanisms have been developed for simulating the shuttle and its environment. As mentioned earlier, the GPC communicates with the world through 19 serial data buses. All sensor inputs and all effector commands are conveyed on these buses. In the laboratories, as part of the flight software verification process (independent of DIT), realistic closed loop simulations are run by connecting these buses to the shuttle and environment models. The software is effectively led to believe that it is flying. (Unfortunately, a similar procedure cannot be performed on a flight-ready vehicle at KSC. Hence the need for a DIT!)

Simdata is obtained from such a simulation by the procedure illustrated in Figure 8. First, before the simulation, a table driven program is implanted in the flight software to transmit data (a maximum of 128 16-bit words) over the GPC telemetry channel every 40 milliseconds. The table contains the addresses of all the data necessary to generate a simdata tape file 4, both high-rate and low-rate frames. The simulation is then run, and the traffic on the telemetry bus is recorded on tape. This "modified telemetry" tape is then processed by another support program known as SIMGEN, which generates a simdata tape.

### 3.3 Transmitting the Simdata to the Vehicle

Discussed here is the procedure developed for moving simdata from the tape into the GPC over the launch data bus. Central to the mechanism is that the launch processing system has the capacity to transmit a 128-word data packet to the GPC every 120 milliseconds. This operation, called the GMEM Write, is a standard LPS capability, and is a logical choice for transmitting simdata to the vehicle.

In addition to using the GMEM Write operation, these other constraints had to be considered in developing the

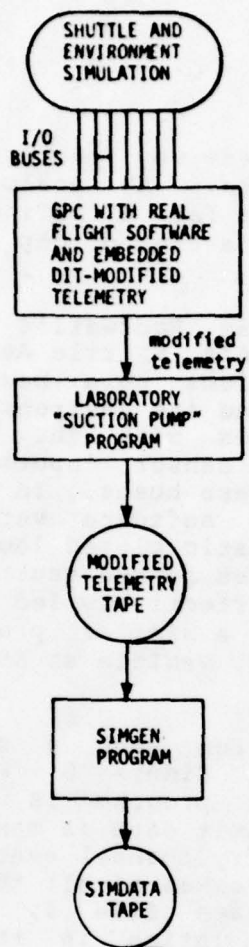


FIGURE 8 Generating a Simdata Tape

procedure:

- The DIT should utilize no more than 50 percent of the capacity of the LDB.
- Three high-rate frames and one low-rate frame (each frame 64 words) must be transmitted every 480 milliseconds.
- Data should not be refreshed too early or too late.

- Time synchronization must be maintained among the LPS, the GPC, and the simdata.

The mechanism which evolved from these constraints is depicted in Figures 9 and 10. A DIT patch, really a program in itself known as the GPCCP (GPC Control Program), is embedded in the flight software to receive and process the transmitted simdata. The LPS and the GPCCP each maintain two 128-word buffers, each of which holds two simdata frames; either two high-rate, or one low-rate and one high-rate. The frames are transmitted in pairs over the LDB according to the timing diagram in Figure 10, and double buffering assures that data is not overwritten while it is being read.

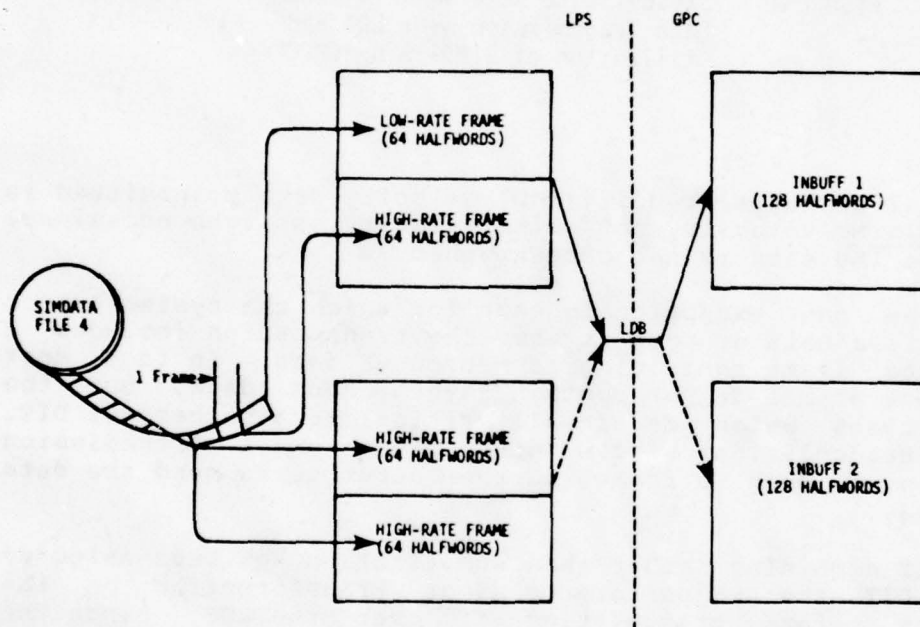


FIGURE 9 DIT Buffers in GPC and LPS

Each transmission has a 240 millisecond window which allows for a second attempt to transmit if the first should fail. Normally, if a successful transmission is not made before the window closes, the data which would have been sent is thrown away since it is critical to maintain GMT synchronization. The system is actually quite robust in that it does remain stable through occasional data dropouts; the GPCCP simply turns off the data good flags associated with the various sensors whenever data dropouts occur. The



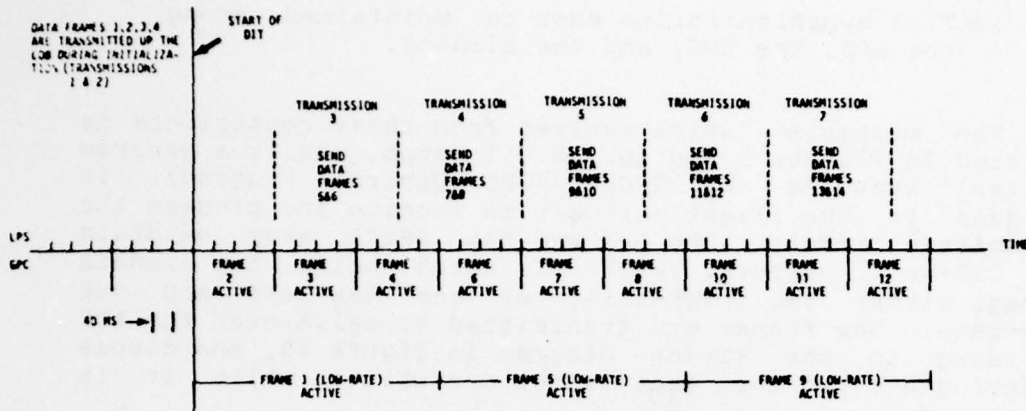


FIGURE 10 Steady State Relationship Between Data Transmission over LDB and Utilization of SIMDATA by GPCCP

inertial measurement unit (IMU) velocity data transmitted is accumulated velocity, not delta velocity, so even occasional missing IMU data is not catastrophic.

The one exceptional case for which the system cannot tolerate a data dropout is when the transmission includes a low-rate frame containing asynchronous data. In fact, most low-rate frames do not contain asynchronous data, but the few frames which do are all critical to a successful DIT. If a transmission window does close on a transmission containing such a frame, further attempts to send the data are made.

If combining rather than substitution has been selected for a DIT, the LPS performs a minor transformation on the simdata before transmitting it over the LDB. Since the simdata are added to corresponding real sensor data (representing the earth-fixed environment or test set data) by the GPCCP, the sensor values must be offset appropriately before they are transmitted. The LPS calculates these offsets and performs the necessary subtraction.

For most sensors, this offsetting procedure represents a trivial calculation, since the quantity subtracted is constant, representing the static output of a test set. However, the IMU represents a special case, for even in a ground environment its outputs are dynamic, reflecting the rotation of the earth. Thus the LPS DIT control program must incorporate a "ground nominal" IMU model to predict the changing values of IMU gimbal angles and accumulated

velocities during the course of a test. When combining is selected for the IMU, these predicted values are generated in real time and subtracted appropriately from the simdata IMU values before transmission over the LDB.

### 3.4 The DIT and Time

The DIT on the vehicle takes place in the time frame of the digital simulation from which the simdata for that DIT was generated. All clocks involved in the test, both in the LPS and on the vehicle, are necessarily initialized so the time of DIT start (see Figure 10) is within a few milliseconds of the corresponding time during the digital simulation. This requirement arises from the fact that time -- GMT -- is one of the inputs which drive the shuttle navigation software. It is, for example, an integral part of the procedure which performs the transformation from the earth-fixed reference frame to the inertial frame used by navigation.

## 4 Modifying the Flight Software for the DIT

### 4.1 Injection of Simdata

The normal (i.e., not modified for DIT) data flow from the sensor subsystem outputs through the MDM's into the flight software is depicted in Figure 11. Associated with each sensor/navaid subsystem is a part of the flight software known as the SOP (subsystem operating program) responsible for transforming the incoming, redundant, raw subsystem outputs into selected, scaled and biased data which can be used by the applications software (e.g., navigation). It is the SOPs which for the DIT are modified to access the simulated trajectory data instead of the ground environment data they would otherwise read.

As mentioned earlier, high-rate simdata is refreshed in the GPC every 160 milliseconds. This is performed by a program (discussed below) known as the GPCCP (GPC Control Program) which executes every 160 milliseconds. The mechanism used to make a SOP access simulated trajectory data is to have the SOP reference a DIT buffer known as SIMBUFF instead of the flight software location normally referenced. It is this buffer the GPCCP refreshes every 160 milliseconds. It does this by extracting data, which has been transmitted by the LPS, from the appropriate LDB input buffer.

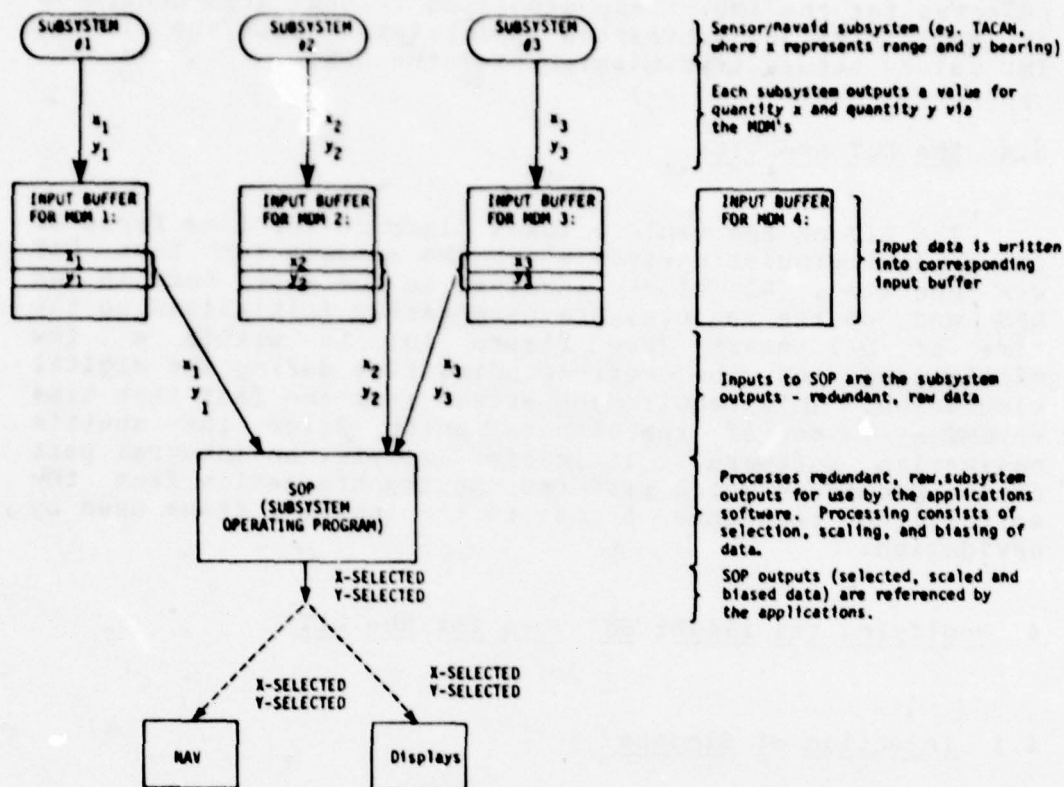


FIGURE 11 Nominal Sensor/Navaid Data Flow

The decision on where to make the data injection patch was based primarily on two factors. First, it is much easier to patch a variable to reference simdata at the one place it is set in the SOP than at the several places it is referenced by the applications software. Second, although the shuttle subsystems are redundant sets, because of LDB capacity constraints it is the selected value rather than the redundant values for a given quantity which are injected. In Figure 11, for example, X\_SELECTED is injected rather than X1, X2, and X3.



#### 4.2 Other DIT Patches to the Flight Software

Some other flight software patches besides the data injection patches in the SOPs are also necessary for DIT. The largest patch is the GPCCP, which has already been introduced. Its functions include the following:

- Knowing which of the three high-rate frames in the input buffers contains the "current" data, and when to process the low-rate frame.
- Processing the low-rate frame asynchronous and auto-crew data.
- Processing input data and writing it to SIMBUFF. Processing may include 1) expansion from single to double precision, 2) combination (addition) of compensated simdata with real sensor data, and 3) conversion from one format to another, as from gimbal angles to quaternions, for example.
- Setting data validity indicators to indicate invalid data when there is no new data with which to update SIMBUFF because of a transmission failure on the LDB.

Another set of patches is necessary for initialization of the DIT. For example, a patch is needed to start the GPCCP at the appropriate GMT. For ascent, a patch is necessary to delay the start of navigation by four seconds to prevent navigation from executing before the simdata which drives it has begun to arrive over the LDB. (The LDB is not available to DIT before T minus four seconds.) Data as well as code needs to be patched: initialization data such as simulation launch site co-ordinates have to be properly set.

For a descent DIT, initialization is more complex than for ascent, because normally a flight begins on the ground. The descent DIT is initialized by overwriting the flight software GN&C common data base so that when the descent software is started on the ground, it believes the vehicle is in orbit, having just flown a nominal ascent trajectory. The process is further complicated by the fact that in order to exactly synchronize the position, velocity, and attitude with GMT, the navigation and attitude states must be set to the simulation initial conditions and "frozen" until the moment of DIT start. Once the DIT starts, however, the

navigation and attitude states are propagated normally, based on simdata.

Still another set of patches is concerned with flight sequences such as solid rocket booster (SRB) ignition, SRB separation, main engine cutoff, external tank separation, and orbital insertion. Each of these sequences involves critically timed interactions with various external subsystems such as the main engines or external tank. Since actual firing of pyros is infeasible for DIT, simulators must be substituted for subsystems whose operation would be hazardous. If a simulator is not available, the software must be modified to sequence correctly without feedbacks it would normally need. However, these DIT sequence patches are designed, in the spirit of the ground rules discussed earlier, such that if the necessary feedbacks are in fact available, the patches can be "turned off" to allow the software to function as it normally would. These patches especially facilitate DIT development in the laboratory, where simulators frequently are not available.

The patches discussed thus far represent (with the exception of inhibits of hazardous outputs, discussed in Section 5) the categories in which most DIT patches may be classified: data injection, GPCCP, initialization, and sequencing. In addition, there are various miscellaneous patches which do not fit conveniently into any of these categories. One example is a patch to schedule the LDB processor, which, not surprisingly, is not normally scheduled by the descent software. Another example is a patch to cause the cockpit displays, some of which would indicate an earth fixed environment during a DIT, to reflect the simdata instead. A final example is a patch which allows the time-consuming IMU gyrocompass alignment procedure to be bypassed in order to facilitate the development process in the laboratory (this patch is not employed on the vehicle, however).

## 5 Vehicle and Personnel Safety

The desire to have DIT emulate a flight must be weighed against the possibility of events occurring which might damage the vehicle or endanger personnel. The aerosurfaces must not be commanded to move so they strike obstructions such as test stands or fuel lines which may be a part of the ground environment. Certainly DIT testing must not cause the engines to fire! Equally catastrophic would be to allow the solid rocket boosters (SRB) or external tank to separate from the orbiter as they do during ascent.

As a result of these concerns, an inhibit methodology using a twofold approach was adopted. First, whenever possible, the hardware action which would be hazardous if permitted to occur is inhibited by physical means such as disabling a circuit via a circuit breaker. Second, a software technique is used to prevent hazardous commands from even being issued to the hardware. This software method may consist of either intercepting and nulling a command, as in the case of an engine fire command, or reducing a command to a safe level. An example of the latter case is the reduction of a rudder movement command from 10 degrees to five degrees if allowing the full rudder travel would cause it to hit an obstruction.

The software inhibit technique has been developed so the test conductors can select, prior to a DIT, those commands which must be inhibited, choosing from a set of possible hazardous commands established during DIT development. (In fact the initial condition of the DIT is all potentially hazardous commands inhibited, and the test conductors select which commands to "uninhibit.") This allows a flexibility to adjust to various hardware configurations; if an SRB simulator is available, for example, it is not necessary to inhibit the SRB ignition commands.

Even though potentially hazardous signals are prevented from ever leaving the GPC's input/output processor, it is important to verify that such commands would have been issued if the inhibit techniques were not applied. This verification is performed by analysis of telemetry data which reflects the state of the commands prior to application of the inhibit code.

Vehicle instability questions have been raised concerning the execution of DIT with the shuttle attached to fixed supports. It has been suggested that the rate gyros and accelerometers, by the degree of their sensitivity, will detect the movement of the effectors during a DIT. This may cause the vehicle to become unstable if the inputs of these sensors are allowed to propagate through the applications software and drive the effectors. It was decided, therefore, that during DIT, to eliminate this potential hazard, the substitution mode rather than the combining mode should be elected for these sensors.



## 6 Evaluation of Test Results

A DIT is evaluated in much the same manner as a real flight -- by analyzing the standard telemetry, monitoring the cockpit displays, and observing the movement of the vehicle hardware. During a successful DIT, the vehicle should be observed to sequence through the nominal events and GN&C modes associated with the particular flight scenario being simulated.

As would be expected, a set of variables considered sufficient to evaluate a flight is a part of the standard flight telemetry. The closed loop simulated flight (from which simdata is extracted) is also evaluated by analysis of these parameters, extracted from the telemetry recorded during a simulation run. In a like manner, the DIT may be evaluated by comparing similarly obtained data with the corresponding simulation data.

Equally significant verification data comes from the cockpit, which is to be manned by either the astronauts who will fly the first shuttle mission, or a similarly experienced crew. The cockpit displays provide extensive information to the crew which enables them to monitor the progress of the flight. Of key importance are the caution and warning, and fault annunciation capabilities of the computers, through which the crew receives indication of any subsystem malfunction detected by the GPCs. Any such malfunctions or other discrepancies during DIT are noted for post-test analysis.

The LPS represents another monitoring station where DIT engineers may follow the progress of the test. In particular, the flow of simdata from the LPS to the GPCs is monitored, and any transmission failures are noted. Also, parameters which are not displayed in the cockpit may be examined from the LPS; GPC duty-cycle, for example. Finally, correlation can be made between observed movement of the vehicle aerosurfaces and flight control and aerosurface position feedbacks observed on displays.

Although DIT is baselined to fly a nominal mission scenario, it may be possible to perform some failure mode analysis by intentionally failing certain redundant shuttle components to verify expected results. It might be of interest, for example, to verify that the shuttle avionics system recovers adequately from the loss of one or more GPCs or MDMs at a critical point in the flight profile.

## 7 Progress to Date

The purpose of DIT is to check out the integrated vehicle at KSC. Toward this end, development has been taking place during the past three years, primarily in the Flight Systems Laboratory (FSL) and the Shuttle Avionics Integration Laboratory (SAIL) mentioned earlier. The feasibility of the DIT concept was demonstrated in early 1978 in the FSL using the flight software developed for the shuttle approach and landing tests. Since that time, the orbital flight test (OFT) DIT has been evolving along with the OFT flight software. What follows is a summary of key milestones which have been demonstrated as of the time of this writing.

Perhaps the most basic and singularly most important achievement is that simdata will drive the vehicle. By transmitting simdata over the LDB in the laboratory, nominal ascent and descent trajectories have been executed, with GN&C functions behaving as they should. Using only the umbilical cord as a data conduit, the vehicle can be led to believe it is flying. Some of the more specific ideas demonstrated by this success are these:

- Data to drive the simulated flight can be obtained by modifying the normal telemetry during a closed loop digital simulation.
- Simulated sensor data may be transmitted over the LDB in steady state without loss of synchronization.
- The system can be initialized to fly both ascent and descent DITs.

Finally, a side benefit which has arisen during this developmental phase of DIT has been the detection of flight software discrepancies. In attempting to make the developing flight software fly, DIT has, from time to time, been one of the first to rigorously exercise certain software modules. Although DIT has no place in the formal software verification process per se, as a heavy user of the immature software, it has sometimes been able to play a productive role in the debugging process.

## 8 Applying the DIT Concept to Other Systems

The shuttle is the first completely digitally controlled manned spacecraft, and as such, it introduces a new level of complexity in avionics systems. All flight control is effected via serial data buses; there are no direct mechanical connections to aerosurfaces. Without the general purpose computers, the vehicle is aerodynamically unstable at high speeds.

And the shuttle is only the beginning. As vehicle complexity and subsystems interactions continue to increase, the need increases to perform fully integrated systems tests which are as close to real flight as possible. The need is compounded by the fact that it has become infeasible in some cases to flight-test a vehicle unmanned, as could be done with Apollo's Saturn V launch vehicle.

The Dynamic Integrated Test, which is now considered to be a necessary element of Space Shuttle flight readiness verification, was retrofitted to the vehicle. As space transportation evolves, it seems logical that with the experience we have now, rather than retrofitting a DIT after a vehicle design has been solidified, the DIT might be built in from the start.

First, the DIT would be designed into the flight software. For example, the umbilical cord data handling routines might be active -- invokable -- throughout an entire flight, not just during the prelaunch sequence. Next, a mechanism for receiving simdata and injecting it into sensor processing modules could also be built in. (Of course, considerable thought would have to be given to a new problem this would introduce: assuring that the flight software is "protected" from the DIT software.) Certainly a safing technique for inhibiting hazardous commands would have to be developed. Finally, it would probably be a good idea for the telemetry software to be designed to accommodate the DIT, both in generating simdata and in monitoring the progress of the test itself.

Second, the vehicle hardware could also be designed with a DIT in mind. A hazardous commands inhibit capability, for example, would complement the software inhibit capability.

Third, in addition to the vehicle and the flight software, the various support facilities and equipment would be set up with the idea that a DIT would be one of the activities they would be expected to support. Certainly the



launch processing or other vehicle interface system would have the capability to initialize the vehicle for a DIT and support the actual transmission of data. Likewise, the various support hardware -- engine simulators and navigation sensor test sets, for example -- would be prepared to support a DIT.

#### ACKNOWLEDGEMENTS

The authors gratefully acknowledge the hard work of all the members of the DIT team.

This paper is based upon work performed for Rockwell International Space Division on Purchase Order M8W8XMS-483151R issued under Contract No. NAS9-14000 between Rockwell and the National Aeronautics and Space Administration.

TITLE: DETECTION OF ANOMALOUS  
GUIDANCE SYSTEM PERFORMANCE  
USING FLY-2 AND GPS  
MEASUREMENTS

AUTHORS: EDWARD M. DUIVEN  
LARRY M. HAWTHORNE  
KEVIN S. TAIT  
C. JULIAN VAHLBERG

THE ANALYTIC SCIENCES CORPORATION  
Six Jacob Way  
Reading, Massachusetts 01867



DETECTION OF  
ANOMALOUS GUIDANCE SYSTEM PERFORMANCE  
USING FLY-2 AND GPS MEASUREMENTS

by

Edward M. Duiven  
Larry M. Hawthorne  
Kevin S. Tait  
C. Julian Vahlberg

The Analytic Sciences Corporation  
Reading, Massachusetts 01867

ABSTRACT

Evaluation of Minuteman III guidance system performance may be significantly enhanced as a result of the Global Positioning System-Receiver Test Program (GPS-RTP). Although initially conceived as a demonstration of GPS receiver performance (i.e., post-boost update capability), the GPS-RTP will provide precise range and range-rate measurements to supplement the radar tracking data available during missile flight tests. The GPS measurements may provide significant insights into the guidance system error characteristics including anomalous instrument performance. Included in this paper are an overview of the GPS-RTP, an assessment of the instrument error coefficient characterization achievable using GPS-RTP measurements, and an overview of the post-flight data processing capability being developed by TASC.

## INTRODUCTION

The demonstration of Minuteman III weapon system performance has, historically, been accomplished by the post-flight processing of NS-20\* telemetry and Western Test Range radar measurement data. As the weapon system matured, the goal of post-mission data analysis has shifted, to some extent, from weapon system performance projection to characterization of the NS-20 instrument errors in the operational environment. This includes the detection of anomalous guidance system performance. In order to achieve the new goal it became necessary to upgrade the range instrumentation quality to a level not achievable using radars alone. This resulted in the FLY-2 flight test program described in Ref. 1. Although superior to the single IMU versus radar approach, the FLY-2 concept suffered from the lack of a precise, independent source of trajectory data. As a consequence the Global Positioning System/Receiver Test Program (GPS/RTP) was initiated. For these flights, scheduled in late 1979 and early 1980, a GPS receiver will be carried on the missile along with two IMUs.

The unique features of the FLY-2/GPS† concept (see Fig. 1) are twofold. First, the test missiles will carry two IMUs. The primary IMU will be the weapon system's NS-20. This being the same unit used to generate the navigation data from which guidance commands are developed. In addition to the primary IMU, a secondary system (also an NS-20) will be contained in the Ballistic Receiver Evaluation Wafer and Spacer (BREWS). The BREWS is an additional missile section inserted between the primary guidance set and the reentry vehicles. The azimuthal alignment of the platforms, with respect to the target, will be different for the two IMUs, their orientation having been selected to enhance guidance coefficient recovery. On the test flights integrated specific force measurements (velocity data) will be collected from each of the IMUs, time tagged,‡ and transmitted, via a telemetry unit within the BREWS, to the ground for post-flight processing.

The second unique feature of the FLY-2/GPS concept is that a GPS receiver is to be carried within the BREWS. The receiver has been designed to operate in a highly dynamic environment such as that associated with the boost phase of a ballistic

\*The NS-20 is the Inertial Measurement Unit (IMU) used for guidance of the Minuteman III missile.

†The names GPS-RTP demonstration and FLY-2/GPS are used interchangeably in this paper.

‡Time tagging of the velocity data is required to minimize the impact of quantization on measurement accuracy.

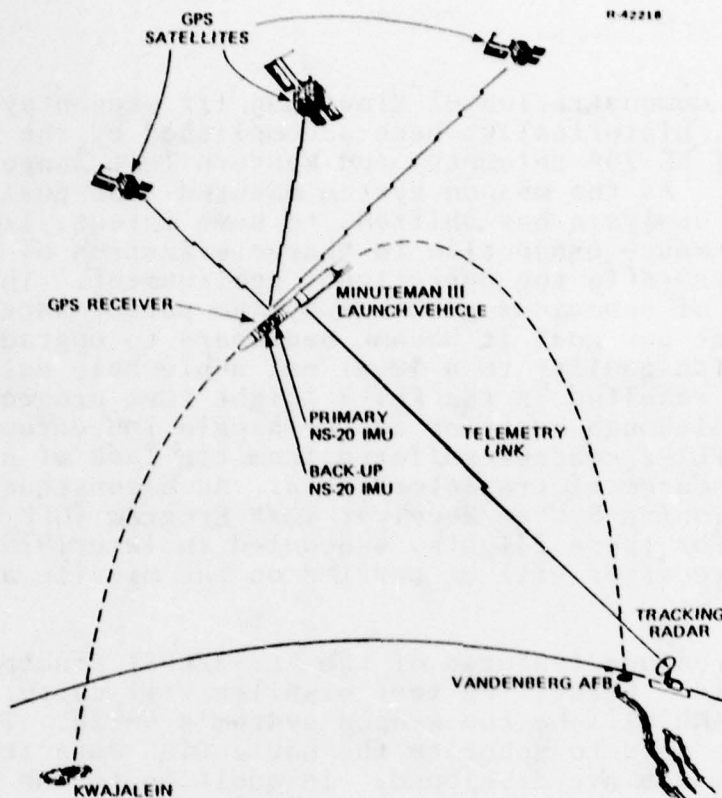


Figure 1 The FLY-2/GPS Concept

missile. During the ascent phase of missile flight range and range-rate measurements, between the missile antenna and selected satellites, will be determined by the GPS receiver, time synchronized with the IMU velocity data, and transmitted to the ground using the BREWS telemetry unit.

The velocity data from the two IMUs and the GPS range and range-rate measurements will be processed, post-flight, using an improved version of the Post Flight Analyzer described in Ref. 1. Figure 2 shows functionally the flow of data through the processor software. The Post Flight Analyzer consists of five major stages as shown on the left of the figure. Of most interest in achieving the goals of TASC's activities in support of the GPS demonstration program are the estimation process and the shift analysis routines. The estimation process consists of a sequential (Kalman) filter that is used to estimate such measures of system performance as missile position and velocity errors at reentry vehicle deployment, initial platform azimuth misalignment, and instrument error coefficients. The shift analysis portion of the processor is used to detect anomalous gui-





assessment, error model characterization, and instrument coefficient shift detection. The results of the data processing portion of this step will, it is anticipated, answer numerous questions relative to Minuteman III system-level performance and the characterization of NS-20 instrument-level error sources.

The following sections of this paper describe the methodology and simulation tools used to project GPS-RTP performance, the results of a number of studies which were undertaken in order to assess the value of FLY-2/GPS measurements for instrument error characterization, and the structure of the Post Flight Analyzer to be used for the processing of GPS-RTP measurement data. A brief discussion of the Minuteman III guidance system error model as well as error models used to describe the GPS space segment characteristics, the GPS receiver characteristics, and the radar error characteristics are also presented herein.

#### STUDY METHODOLOGY

The full FLY-2/GPS measurement system consists of the secondary IMU, the WTR radars, the missile GPS receiver, and the GPS space vehicles, together with the associated post-flight data processing. The purpose of this study is to analyze the performance of this measurement system, rather than evaluate Minuteman III weapon system performance itself.

The methodology used for evaluation of GPS-RTP measurement system performance is summarized in Fig. 3. There are three steps involved in the generation of the projected performance. The first step in the process is the GPS segment simulation, identified as the NESA\* module in Fig. 3. This step is necessary for two reasons.

- To develop a time history of GPS satellite orbital positions and velocities so that the GPS/missile geometry is accounted for in the filter and system evaluation process
- To generate the GPS satellite position, velocity, and clock calibration error covariances necessary for analysis of total system performance.

The upper half of Fig. 3 (the FILTER module) represents the second step, the recursive solution of the filter covariance propagation and update equations. These equations are solved once for a specific GPS satellite geometry, missile flight trajectory, and

\*Navigation Error Sensitivity Analysis.

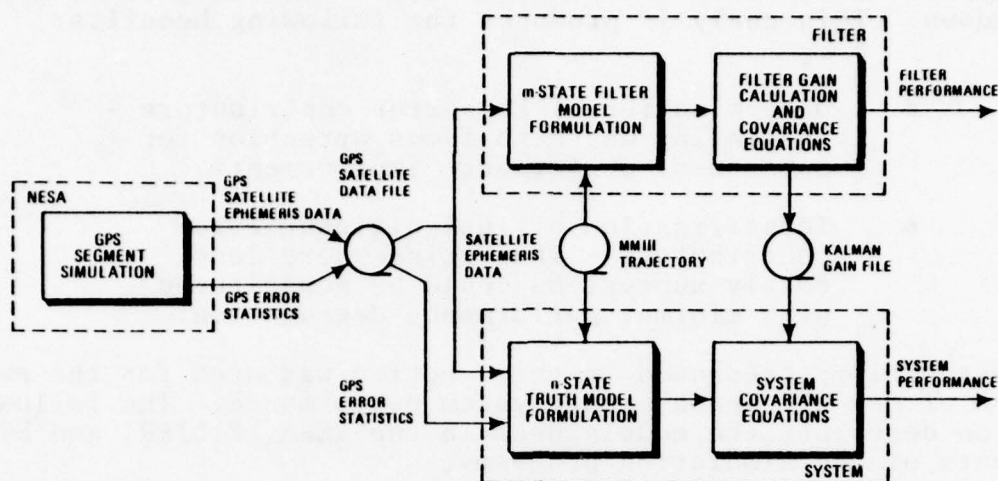


Figure 3 GPS/User Satellite Performance Projection Methodology

measurement schedule. It is important to note that only the GPS satellite position and velocity time histories and not the associated GPS error covariances are supplied to this portion of the evaluation process. Thus, only the GPS satellite/missile geometry and not the GPS satellite tracking error covariances are used in the filter computations (i.e., the data processing algorithms assume that the GPS satellites are tracked perfectly). The outputs of the FILTER module are the time histories of the filter-indicated performance and the Kalman filter gain matrices.\* The latter are stored on tape and constitute a "gain file."

The third step of the process, depicted by the SYSTEM module in the lower half of Fig. 3, encompasses the recursive solution of the linear system error covariance equations. These equations are solved repeatedly to produce an error budget, the same gain file being used each time. In individual error budget runs, elements of the input matrices corresponding to specific error sources (e.g., missile guidance system, GPS tracking errors, etc.) are set to non-zero values, with all other elements set to zero. The output time history of the system error covariance matrix is a statistical measure of the contribution from that particular error source or small group of error sources to the total system error. When all of the error contributors have been evaluated, the overall measurement system performance projection

\*Reference 3 contains a detailed discussion of the Kalman filter.



can be calculated from the detailed error-source-by-error-source breakdown. This analysis produces the following benefits:

- Determination of key error contributors - indicating where to focus attention for subsequent performance improvements.
- Identification of insignificant error contributors - indicating where less costly subsystems could be substituted with minimal performance degradation.

The methodology presented in this section was used for the evaluation of GPS-RTP measurement system performance. The following section describes the models used in the NESA, FILTER, and SYSTEM elements of the simulation programs.

#### SIMULATION DESCRIPTION

The FLY-2/GPS covariance simulations determine the Kalman filter estimation error covariance matrix based upon a sequence of measurements. There are three sets of error measurements associated with the GPS-RTP. The first is the difference between the two IMU velocity measurements. The second set of error measurements are those associated with the WTR radars. The third set of error measurements are those associated with the GPS system. These are the radar-to-missile range and range-rate measurements.

The full set of error sources for the FLY-2/GPS simulations are those associated with the two IMUs, the radar and the GPS satellites. Table 1 lists the full set of error sources associated with each of the IMUs. Table 1 also lists the error sources that are included in the Filter Model and Truth (i.e., system) Model formulations (they include the same states).

In Table 2 are listed the error sources associated with the WTR error measurements, for the Full Model as well as the Truth and Filter Models. The error sources associated with the GPS satellite, propagation delays, and missile receiver are given in Table 3 for the Full Model as well as the Truth and Filter Models. The uncertainties in the satellite position, velocity, etc., are provided by the NESA program. The NESA program simulates the GPS satellite ground tracking process, and determines the estimation error covariance for the GPS satellite. In the NESA simulation the solar radiation force and gravitation constant errors drive the position and velocity errors. The propagation errors, and carrier and code loop errors listed in Table 3 are presently modeled as white measurement noise sources in the simulation and are not estimated.

**TABLE 1**  
**IMU ERROR MODEL SUMMARY**

T-3541

ERROR OR ERROR SOURCE NAME	NUMBER OF STATES		
	FULL MODEL	TRUTH MODEL	FILTER MODEL
<b>PRIMARY</b>			
Position Errors	3	3	3
Velocity Errors	3	3	3
Alignment Errors	3	3	3
Initial Alignment Errors	3	3	3
<b>PRIMARY - MEW</b>			
Differential Position Errors	3	3	3
Differential Velocity Errors	3	3	3
Differential Alignment Errors	3	3	3
Differential Initial Alignment Errors	3	3	3
<b>PRIMARY IMU INSTRUMENT ERRORS SOURCES</b>			
<u>Accelerometers</u>			
Uncorrelated Bias	3	3	3
Scale Factor	3	-	-
Input $g^2$ Nonlinearity	3	-	-
Input $g^3$ Nonlinearity	3	-	-
Input Axis Misalignments	6	-	-
Cross-Axis Nonlinearity	3	-	-
<u>Q-Matrix Calibration Errors</u>	9	9	9
<u>Platform Compliance Errors</u>	27	-	-
<u>Gyros</u>			
Bias	3	3	3
Mass Unbalance	4	2	2
Anisoelasticity	6	3	3
Gyro $g^4$ Coefficients	8	3	3
Temperature Dependent Drift	3	-	-
<b>MEW IMU INSTRUMENT ERROR SOURCES</b>			
<u>Accelerometers</u>			
Uncorrelated Bias	3	3	3
Scale Factor	3	-	-
Input $g^2$ Nonlinearity	3	-	-
Input $g^3$ Nonlinearity	3	-	-
Input Axis Misalignments	6	-	-
Cross-Axis Nonlinearity	3	-	-
<u>Q-Matrix Calibration Errors</u>	9	9	9
<u>Platform Compliance Errors</u>	27	-	-
<u>Gyros</u>			
Bias	3	3	3
Mass Unbalance	4	2	2
Anisoelasticity	6	3	3
Gyro $g^4$ Coefficients	8	3	3
Temperature Dependent Drift	3	-	-
<b>TOTAL NUMBER OF STATES</b>	<b>186</b>	<b>70</b>	<b>70</b>

TABLE 2

## RADAR ERROR MODEL SUMMARY

ERROR OR ERROR SOURCE NAME	NUMBER OF STATES		
	FULL MODEL	TRUTH MODEL	FILTER MODEL
• <u>Range</u>			
• <u>Range Measurement Errors</u>			
Bias Error	1	1	1
Scale Factor Error	1	1	1
Random Error	1	1	1
Measurement Noise	1	1	1
• <u>A Priori Errors</u>			
Radar Position	0	0	0
• <u>Range Rate</u>			
• <u>Range-Rate Measurement Errors</u>			
Bias Error	1	1	1
Scale Factor	1	1	1
Random Error	1	1	1
Measurement Noise	1	1	1
• <u>A Priori Errors</u>			
Radar Position	0	0	0

TABLE 3

## GPS ERROR MODEL SUMMARY

ERROR OR ERROR SOURCE NAME	NUMBER OF STATES		
	FULL MODEL	TRUTH MODEL	FILTER MODEL
• <u>Satellite Errors</u>			
Position	3	3	0
Velocity	3	3	0
Solar Radiation Force	1	1	0
Gravitation Constant	1	1	0
Satellite Clock	3	3	0
• <u>Propagation Errors</u>	2	0	0
• <u>Receiver Errors</u>			
Missile Clock	5	3	3
Carrier and Code Loop	2	0	0



## PERFORMANCE ASSESSMENT

TASC's FLY-2/GPS performance evaluation software has been used to develop preliminary system performance projections. Three study areas of interest were addressed:

- Recovery of initial alignment and RV deployment errors
- Recovery of guidance system instrument error coefficients
- Detection of instrument error coefficient shifts using the GLR test

The results are compared with previous projections for the FLY-2 program without GPS tracking.

A reduced-order filter was modeled in which the satellite ephemeris and clock errors are not estimated, but are included in the performance evaluation via a "truth model". The reduced-order filter performance was also compared with the results of an "optimal" filter in which the satellite error sources are modeled and estimated. The launch time was chosen so that four GPS satellites are visible through deployment. The effect of a loss of one or more satellites is also discussed.

The first study area assessed improvement to the estimation of azimuth alignment at launch, and of position and velocity at deployment, that may be expected with the GPS receiver on board. The results are presented as rms estimation uncertainties normalized by projected performance of the FLY-2 test program which had only velocity difference and radar tracking data (Table 4). The projections indicate that position and velocity estimation errors at deployment will be an order of magnitude smaller than with the FLY-2 system alone. The recovery of initial azimuth errors will be improved by a factor of two using GPS tracking data. The results also show that the reduced-order filter will be effective in guidance error recovery at the cost of a small loss in position accuracy.

The effect of variable satellite availability was also assessed. Relative to the performance with four satellites visible, the loss of one satellite produced position errors about 40% larger and velocity errors some 20% greater. With only two satellites visible, position error uncertainty increased by as much as an order of magnitude in the level axes and a factor of three in the vertical direction. Velocity errors were somewhat less affected increasing by factors of six and three respectively. There was no appreciable loss of initial azimuth recovery in either case.

TABLE 4  
RECOVERY OF INITIAL AZIMUTH AND DEPLOYMENT ERRORS

TRACKING SYSTEM	NORMALIZED ESTIMATION ERRORS				INITIAL AZIMUTH RECOVERY RATIO*
	FILTER MODEL	POSITION	VELOCITY	TIME (sec)	
FLY-2 with Radar	Full Order	1.0	1.0	180	0.60
		1.0	1.0	400	
FLY-2 with Radar and GPS	Full Order	0.43	0.06	180	0.37
		0.12	0.04	400	
FLY-2 with Radar and GPS	Reduced Order	0.66	0.06	180	0.37
		0.22	0.05	400	

\* Recovery ratio is the ratio of final rms estimation uncertainty to initial uncertainty.

Guidance system error coefficient estimation was addressed in the second study area. The FLY-2 test program provided estimates of certain guidance error coefficients in flight. This coefficient recovery was particularly good for the more observable errors such as the gyro  $g^2$ - and  $g^4$ -sensitive terms. The enhanced recovery of these guidance error coefficients with the addition of GPS tracking is displayed in Table 5. Overall the improvement is not large with the recovery of gyro  $g^4$ -terms decreasing by at most 25%. The results quoted are for the optimal filter, but use of the reduced order filter changes the recovery ratios by only a few percent. Thus, neglect of the satellite errors will not impact error coefficient estimation.

The detection of coefficient shifts was evaluated in the third study area. Figures 4 and 5 display graphically the projected performance of the GLR test in detecting jumps in selected guidance error coefficients. These projections are based on a detection threshold corresponding to a 5% false alarm probability, and indicate the shift magnitude that would be required in the specified coefficient (as a function of time) in order to have a 50% probability of detection. As a rule of thumb, to obtain a 90% probability of detection the size of the required jump should be doubled. The figures also show the improvement in detection due to the addition of GPS tracking measurements to the basic FLY-2 system.

TABLE 5  
GUIDANCE ERROR COEFFICIENT RECOVERY

GUIDANCE ERROR COEFFICIENT		RECOVERY RATIOS FOR EACH SYSTEM			
		FLY-2/RADAR		FLY-2/GPS	
		PRIMARY	MEW	PRIMARY	MEW
Gyro $g^2$ -terms	$\delta B_2$	-	-	-	0.70
	$\delta B_1$	0.76	0.54	0.70	0.51
	$\delta E_1$	0.60	0.33	0.48	0.25
Gyro $g^4$ -terms	$P_1$	0.34	0.22	0.20	0.15
	$J_1$	0.66	0.56	0.43	0.37

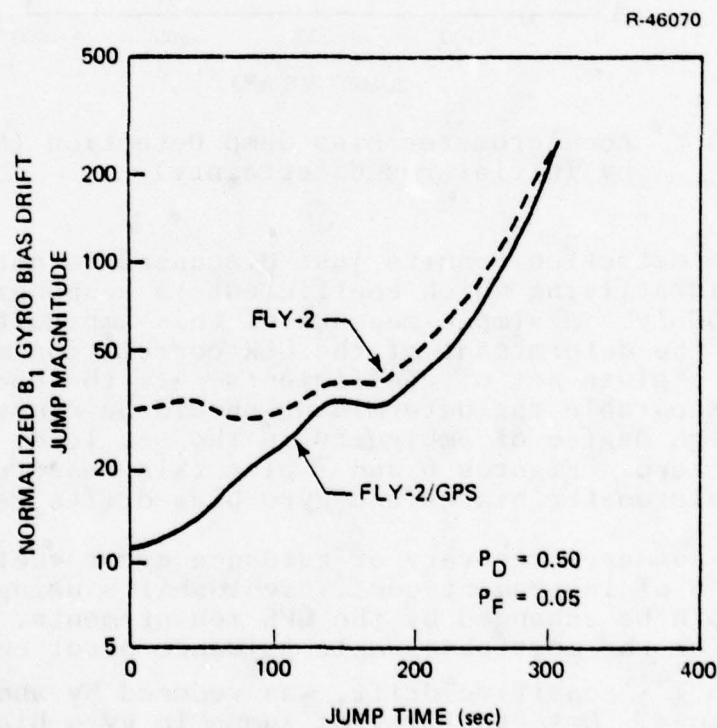


Figure 4 Gyro Bias Drift Jump Detection (Normalized by Initial rms Uncertainty)



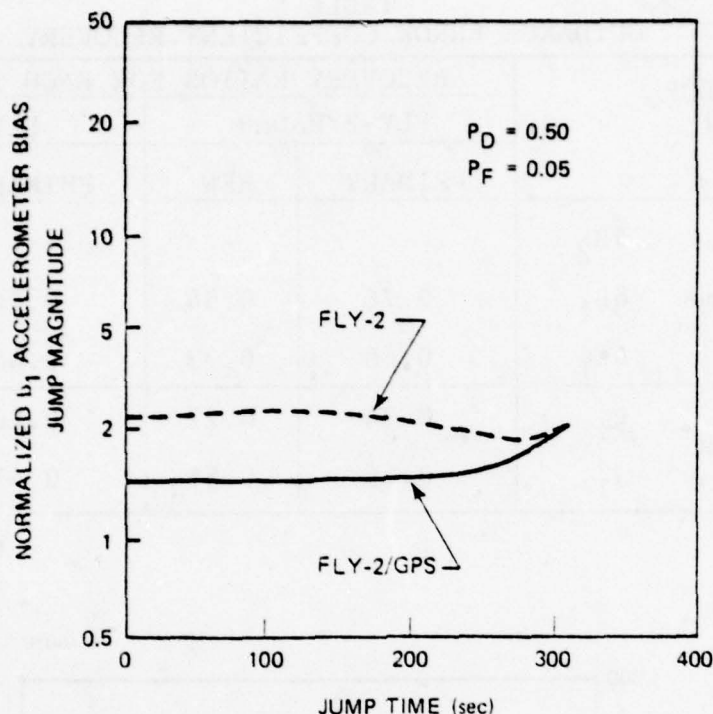


Figure 5 Accelerometer Bias Jump Detection (Normalized by Initial rms Uncertainty)

The detection results just discussed do not address the problem of identifying which coefficient is responsible for an observed anomaly. A simple measure of this ambiguity is obtained by plotting the determinant of the GLR correlation matrix associated with a given set of coefficients. If the coefficients are highly separable the determinant should be close to one, whereas a high degree of ambiguity in the set leads to a determinant near zero. Figures 6 and 7 plot this measure for the primary accelerometer biases and gyro bias drifts respectively.

In summary, recovery of guidance error coefficients, and detection of instrument coefficient shifts using the GLR test will both be enhanced by the GPS measurements. Estimation error for the most observable guidance error coefficients, such as gyro  $g^4$ -sensitive drift, was reduced by about 30% in the simulations. Detectability of jumps in gyro bias drift and accelerometer bias also improved by about a factor of two in terms of the jump magnitude required for detection. In addition, jump identification and coefficient separability should be significantly better, especially for PIGA biases.

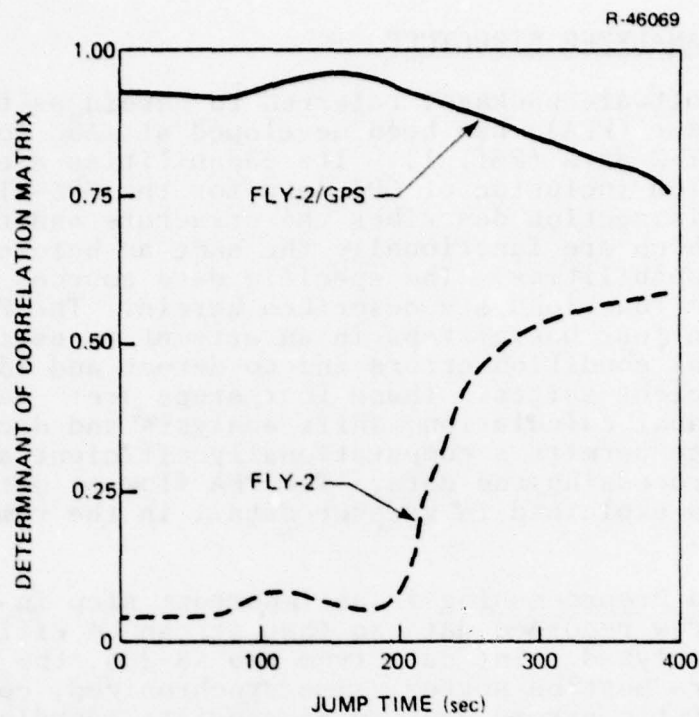


Figure 6 Primary Accelerometer Bias Separability

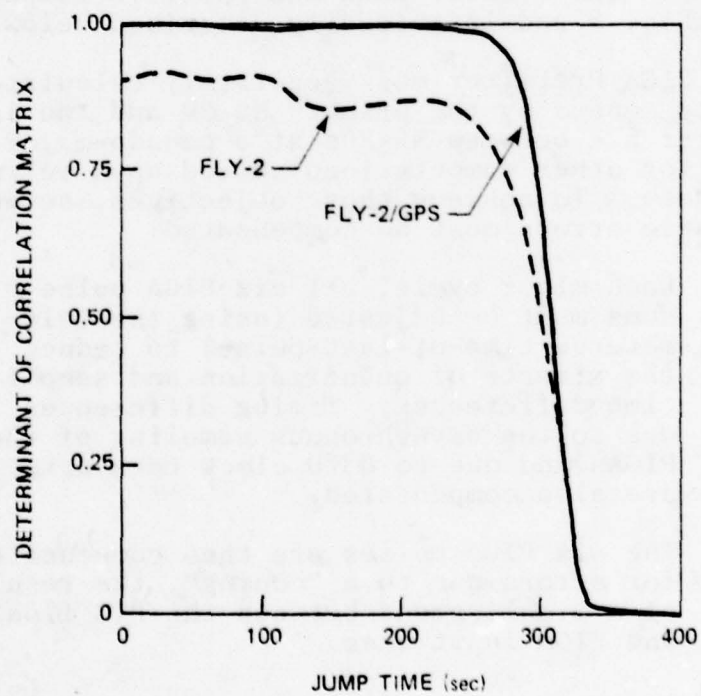


Figure 7 Primary Gyro Bias Separability

## POST FLIGHT ANALYZER STRUCTURE

A software package, referred to herein as the Post Flight Analyzer (PFA), has been developed at TASC for the processing of FLY-2 data (Ref. 1). Its capabilities are being expanded to allow inclusion of GPS data for the GPS-RTP test flights. This section describes the structure and the elements of the PFA which are functionally the same as before, but with some added capabilities. The specific data sources for each of the major PFA functions are described herein. The PFA processes FLY-2 data in four basic steps in an attempt to estimate guidance system initial condition errors and to detect and identify guidance coefficient shifts. These four steps are: data preprocessing, residual calculation, shift analysis and decision making. This structure permits a computationally efficient and orderly manner for processing the data. The PFA flow of data is shown in Fig. 2 and explained in greater detail in the remainder of this chapter.

Data Preprocessing is an important step in the preparation of the raw recorded data so that it can be efficiently and accurately analyzed. The data from two NS-20s, the GPS, and several radars must be sorted, time synchronized, compensated for deterministic errors, put in appropriate coordinate frames for comparison, and combined such that all relevant data at the high raw data rate is reduced to a more appropriate rate for the analysis tools. The flow of data and specific computer programs are shown in Fig. 8 and individually described below.

The PIGA Prefilter must accurately calculate the specific velocity sensed by the primary NS-20 and the indicated-velocity difference between NS-20s at a pseudo-major cycle rate (appropriate for other computations) based upon telemetered minor-cycle data. To achieve those objectives, seven categories of deterministic errors must be compensated.

- Each minor cycle, all six PIGA pulse sums must be adjusted (using the telemetered time-of-last-pulse) to reduce the effects of quantization and sample time differences. Timing differences due to the asynchronous sampling of the PIGAs and due to D37D clock rate drift are also compensated.
- The six PIGA pulses are then compensated for errors due to a "coning", the results of a misalignment between the PIG float and PIGA input axes.



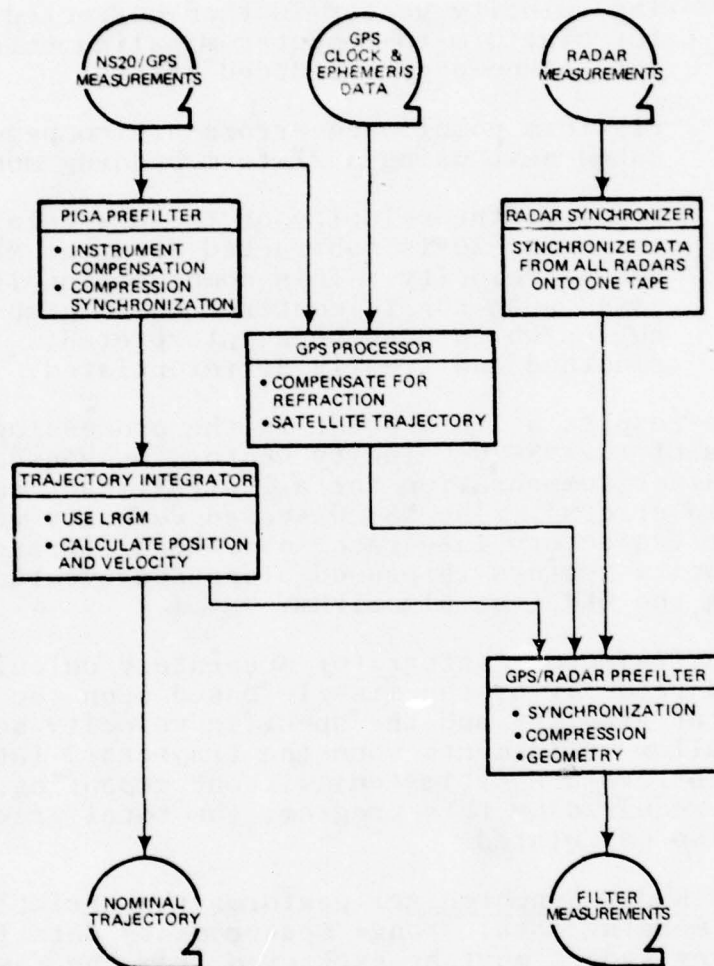


Figure 8 Data Flow for Preprocessing Steps

- The minor PIGA pulses are then passed through a 15-point (on each side) symmetric digital low-pass filter to remove the residual random errors resulting from quantization and timing uncertainties.

- The PIGA pulses are compensated for bias and nonlinearity ( $F_{II}$ ) errors and then transformed into a velocity vector in NS-20 computational coordinates (using  $Q'$  and  $\Delta\alpha$ ).
- The velocity vector is then corrected for platform-to-computer misalignments due to known gyro induced drifts.
- Platform compliance errors are compensated next using a 27-term bending model.
- Finally, the velocity of the MEW relative to the NS-20 is subtracted from the MEW sensed velocity. This compensation is based upon the telemetered NS-20 gimbal angles which have been interpreted, smoothed and finally differentiated.

The results at this point in the processing are two measurements of the NS-20 velocity vector, as sensed by the two platforms (after compensation for all significant calibratable/compensatable errors). The NS-20 sensed velocity vector is provided to the trajectory integrator and the difference between the two velocity vectors is passed along and eventually interpreted using the GLR test algorithm.

The Trajectory Integrator accurately calculates the position and velocity of the missile based upon the best available model for gravity\* and the specific velocity sensed by the NS-20. To allow refinements upon the trajectory (as bad data is removed and errors are estimated) without repeating the long integration required by this program, the total gravity gradient matrix is also calculated.

The Radar Synchronizer performs the strictly clerical function of merging data: range measurements data from the ten or so tracking radars must be extracted from the raw data tapes, put in common engineering units and time synchronized. The result is a single sequential file containing all available radar data.

The GPS Processor must compensate the GPS measurements for all deterministic error sources and calculate the best estimate of each satellite's position (in NS-20 coordinates) at the

\*The WGS-72 gravity model in combination with the DMAAC Launch Region Gravity Model (LRGM) for Vandenberg AFB is used.

time of each available range or range-rate measurement. The satellite position is calculated at each desired time using the best estimate of "Block 11" (Ref. 4) data as provided by GPS Joint Program Office (JPO). Next the range and range-rate data must be compensated for clock and propagation delays. The clock errors are corrected using the best estimate of "Block 1" (Ref. 4) data. This data will also be provided by the GPS JPO. The measurements are also compensated for ionospheric and tropospheric delays using the best data available during the flight test.

The GPS/RADAR Prefilter determines the difference between the measured radar and/or GPS ranges and computed ranges calculated using the NS-20-indicated position time history generated with the Trajectory Integrator versus either the radar coordinates or the satellite position as appropriate. (Range-rate measurements are used similarly where available.) The large uncertainty in each measurement is then reduced by averaging all range and range-rate differences (from each radar or satellite) over the entire pseudo-major cycle interval. The geometry of each measurement is also calculated so that the estimator can properly weight the one-dimensional range and range-rate difference measurements in the estimation of three-dimensional position and velocity.

The residual calculations take the sequence of range and range-rate differences (GPS and/or radar) and velocity difference (between NS-20s) measurements and calculate the best estimate of NS-20 guidance coefficient, GPS, and radar errors based upon a priori error statistics. The basic flow of data is shown in Fig. 9. The residual calculations are divided into two separate programs for computational efficiency since they will be repeated several times as bad data is edited out and as different error models are tried. The Gain Calculation requires the straightforward, although lengthy, computation of Kalman gains based on the nominal trajectory, the system error model (Appendix B), and the measurement sequence.

The Residual Calculator uses the gains to interpret the measurements from the data preprocessor. During preliminary data editing, the relatively simple residual calculations can be made many times using the same set of gains without significant loss of accuracy. The more lengthy gain calculations can then be repeated only after most of the bad data has been removed or whenever the error model is changed.

The primary jump detection, and identification is performed by the Generalized Likelihood Ratio (GLR) test on the filter residuals as described in Ref. 1. As in the residual (i.e., filter) calculations, the GLR test computations are divided into two routines, as shown in Fig. 9. One calculates the



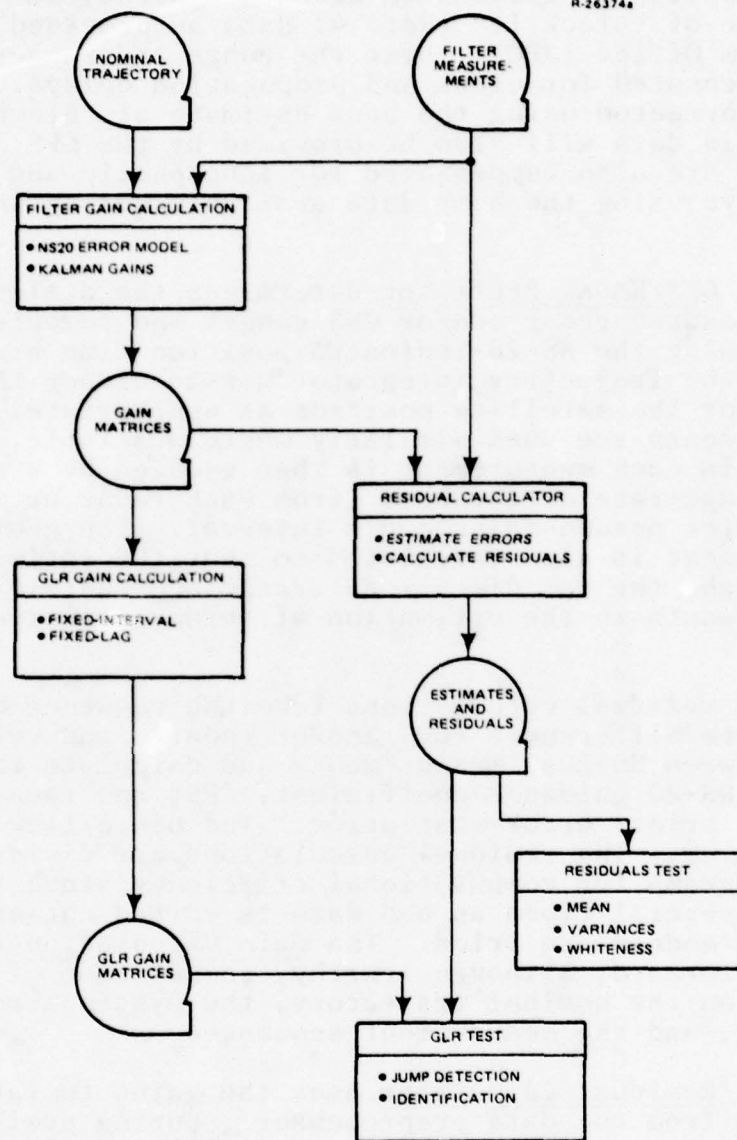


Figure 9 Data Flow for Residual Calculation and Evaluation

GLR gain matrices and the other performs the GLR test on the data. (The GLR gain matrices only need to be recomputed when the filter gain matrices are recomputed.) The GLR Test routines use the gain matrices to determine whether the filter residuals are consistent with the model. In the event of a jump detection, the time and identity of the parameter(s) which changed (jumped)

are estimated using the techniques discussed in Ref. 1. These jump estimates can then be used to change the model and the residual calculations can be repeated.

Various Residual Tests are performed on both the filter and smoother outputs. If the models are correct the residuals will be a zero mean and uncorrelated random sequence and have the variance predicted by the model. Thus, the sample mean and variance calculations provide some clues as to the nature of modeling errors. These tests provide a "quick-look" capability to help identify missions with possible parameter jumps.

In addition, two forms of Smoother may be used. The Fixed-Point Smoother allows the computationally efficient estimation of a limited number of smoothed states at selected times. This is particularly attractive if only certain candidate states are suspected to be time-varying. Fixed-Interval Smoothing allows the smoothed estimation of all parameters but requires more computations. Both have a place, however, in the search for unmodeled parameter changes.

#### SUMMARY

TASC is presently preparing to process Minuteman III telemetry, radar, and GPS measurement data on the forthcoming GPS-RTP flight tests. The purpose of the processing effort is to: (1) estimate position and velocity errors at deployment and initial platform alignment errors, (2) determine guidance system instrument error coefficients, and (3) detect and identify anomalous guidance system performance. This paper describes the results of a study to assess the performance of the GPS-RTP measurement system. The performance is compared to that of the FLY-2 flight test program described in Ref. 1. The major findings of the study are:

- The incorporation of GPS measurements will significantly enhance the estimation of deployment errors and initial azimuth alignment error
- The estimation of instrument error coefficients may be improved to some extent, using the GPS-RTP data
- Detection and identification of anomalous guidance system performance may be significantly enhanced by the introduction of the GPS measurements.

### ACKNOWLEDGEMENT

The work described in this paper was performed for the Air Force Space and Missile Systems Organization under Contract Number F04704-79-C-0055. The authors wish to express their appreciation to Major Gaylord Green, Capt. Ken Wernle and Capt. Ken Jackson of the Minuteman Project Office for their guidance and support. In addition, the technical support provided by Marvin K. Peach, Donald F. Piette, and John W. VanderMeer of TASC is greatly appreciated. Discussions with personnel from TRW and Rockwell International/ Autonetics Group have also been beneficial in the generation of this paper.

### REFERENCES

1. Duiven, E.M., et al., "A New Technique for Detecting Guidance Coefficient Instabilities," Proc. of the 8th Biennial Guidance Test Symposium, (Holloman Air Force Base) May 1977.
2. Duiven, E.M., "Predicted Global Positioning System User Performance," Proc. of the 7th Biennial Guidance Test Symposium, (Holloman Air Force Base) April 1975.
3. Gelb, A., Ed., Applied Optimal Estimation, M.I.T. Press, 1974.



TITLE:        MODELS FOR g-SENSITIVE  
              TRENDING (GST) RELATED  
              TO FLOTATION FLUID  
              BEHAVIOR

AUTHORS:     N. BARBOUR  
              M. WEINBERG

THE CHARLES STARK DRAPER LABORATORY, INC.  
555 Technology Square  
Cambridge, Massachusetts 02139

#### ACKNOWLEDGMENT

This report was prepared by The Charles Stark Draper Laboratory, Inc., under Contract F04704-78-C-0002 with the Space and Missile Systems Organization of the Air Force Systems Command.

Publication of this report does not constitute approval by the U.S. Air Force of the findings or conclusions contained herein. It is published for the exchange and stimulation of ideas.

## TABLE OF CONTENTS

<u>Section</u>	<u>Page</u>
1. INTRODUCTION. . . . .	1
2. TYPICALLY OBSERVED GST SIGNATURES . . . . .	5
3. GENERAL EQUATIONS OF MASS TRANSPORT . . . . .	7
4. BULK FLUID MOTION . . . . .	11
4.1 INTRODUCTION. . . . .	11
4.2 FLUID DENSITY GRADIENT MODELS . . . . .	11
4.2.1 Linear Density Gradient . . . . .	12
4.2.2 Discontinuous Density Gradient (Migrating Mass Unbalance Model). . . . .	15
4.3 NAVIGATION MODELS . . . . .	17
4.3.1 The Multi-Mass Navigation Model . . . . .	18
4.3.2 The Point Mass Navigation Model . . . . .	19
5. SEDIMENTATION . . . . .	23
5.1 INTRODUCTION. . . . .	23
5.1.1 True Sedimenters. . . . .	23
5.1.2 Partial Sedimenters . . . . .	24
5.1.3 Non-Sedimenters . . . . .	24
5.2 TRUE SEDIMENTERS. . . . .	24
5.2.1 True Sedimenters in the Damping Gap . . . . .	24
5.2.2 True Sedimenters in the End Gap . . . . .	27
5.3 PARTIAL SEDIMENTERS . . . . .	29
5.4 ADDITIONAL OBSERVATIONS . . . . .	32



# TABLE OF CONTENTS (Continued)

<u>Section</u>	<u>Page</u>
6. FLUID STRIPPING AND CENTRIFUGE CONDITIONING. . . . .	33
6.1 INTRODUCTION . . . . .	33
6.2 DIFFUSION DURING CENTRIFUGE CONDITIONING . . . . .	33
7. THERMOGRAVITATIONAL DIFFUSION (TGD). . . . .	37
7.1 INTRODUCTION . . . . .	37
7.2 APPLICATION OF THERMAL DIFFUSION COLUMN THEORY . . . .	38
7.2.1 Cartesian Solution of the Unsteady Transport Equation.	39
7.2.2 Polar Solution of the Unsteady Transport Equation. . .	50
7.2.3 Additional Comments on TGD . . . . .	51
7.3 CONCLUDING REMARKS ON TGD MODELING . . . . .	53
8. CONCLUSIONS AND RECOMMENDATIONS. . . . .	55
8.1 CONCLUSIONS. . . . .	55
8.2 RECOMMENDATIONS . . . . .	59
APPENDIX A ONE DIMENSIONAL UNSTEADY PARTIAL SEDIMENTATION .	63
APPENDIX B SOLUTION OF UNSTEADY TRANSPORT EQUATION WHEN $1-c_1 \neq 1$ . . . . .	67
NOMENCLATURE . . . . .	73
REFERENCES. . . . .	75

# LIST OF ILLUSTRATIONS

<u>Figure</u>	<u>Page</u>
1. Viscous torque due to circumferential bulk flow . . . . .	13
2. The concentrated migrating mass model . . . . .	16
3. The multimass navigational model. . . . .	18
4. The point mass navigational model . . . . .	20
5. Damping gap contamination in ppm by volume required to cause 1 meru/g in TGG, based on viscous drag mechanism. .	26
6. Sedimenting contaminant in the end gap . . . . .	28
7. Parabolic bulk flow and diffusion during centrifuge conditioning. . . . .	34
8. Mechanism of thermogravitational diffusion (TGD). . . . .	37
9. Application of classical TD column theory to a gyro . . .	40
10. Convection in the end gap . . . . .	41
11. Steady-state concentration difference due to TGD in TGG damping gap . . . . .	45
12. Steady-state concentration difference due to TGD in TGG end gaps. . . . .	46
13. Time constant for TGD in the TGG damping gap. . . . .	48
14. Time constant for TGD in the TGG end gaps . . . . .	49
15. Relative importance of thermal diffusion and convection .	52

# LIST OF TABLES

<u>Table</u>	<u>Page</u>
1. Correlation between linear density gradient model and observed GST effect . . . . .	14
2. Effect of fill-introduced particulates on TGG . . . . .	25
3. Ratio of fractional mass equilibrium concentration $(c_1)_{x_1} / (c_1)_{x_0}$ at opposite ends of the TGG damping gap $(x_1 - x_0 = 6 \text{ cm})$ . . . . .	30
4. Time constants for equilibrium partial sedimentation from top to bottom of damping gap (6 cm) . . . . .	31
5. Time of ordinary diffusion across TGG damping and end gaps. . . . .	34
6. Applicability of speculated mechanisms. . . . .	56



## SECTION 1

### INTRODUCTION

A phenomenon of current study in floated inertial instruments, is Gravity Sensitive Trending (GST). Typically, after a change in orientation of an instrument, the acceleration dependent instrument coefficients vary as an apparent mass unbalance shift. Several physical mechanisms have been proffered to explain GST (see Reference 1), all of which fall into two broad categories; either flotation fluid or float sources.

Float sources of GST are as follows:

- (1) Float center of gravity shift due to
  - (a) Partially filled void (or bubble)
  - (b) Epoxy viscoelasticity
  - (c) Residual solvent
  - (d) Float creep
- (2) Float center of buoyancy shift due to
  - (a) Epoxy viscoelasticity
  - (b) Float creep

Float creep is currently discounted as a GST source because float assembly induced stresses are much higher than gravity induced stresses, and because gravity independent unbalance ramps are small. The gyro test results described in Reference 1, in which the unit was stored at various temperatures, also suggest discounting float sources, because at low temperatures little trending was observed. This observation

indicates fluid sources, all of which depend upon viscosity which is more temperature dependent than the float parameters. (The partially filled void model is an exception since viscosity is important). However, float sources cannot be conclusively discounted until further test data are obtained. Float sources are not discussed further in this report, which concentrates on the fluid sources.

Motion of the flotation fluid, due to density gradients in the fluid, has been suggested as the fluid source of GST. This report attempts to document the physical and analytical models of flotation fluid behavior in an acceleration field.

There are several postulated physical mechanisms whereby density gradients are built, all of which depend upon the existence of either or both of the following:

(1) Contamination

Contaminants may be introduced by imperfect cleaning techniques, or during fill, or deterioration (incompatibility) during storage or operation. The contaminants may be solid, liquid or gaseous and may be insoluble, soluble, dissolving or precipitating. Their densities may be quite different from that of the fluid.

(2) Multiple Telomer Fluids

If the flotation fluid is not unimolecular, it consists of multiple telomers which are blended to give the fluid its required density and viscosity. The range of telomer molecular weights is strongly suspect as a GST source. For example, Third-Generation Gyros (TGGs) are filled with chlorotrifluoroethylene (CTFE), while other units are filled with bromotrifluoroethylene (BTFE); the approximate difference in molecular weight between the lightest and heaviest CTFE molecules is 500 gm/(gm-mol).

Generally, it has been convenient in the past to make assumptions concerning the nature of an existing density gradient (from whatever

mechanism) and to use these assumptions in predicting the error torques. However, the postulated physical mechanisms which predict the building of a density gradient cannot always be separated from the torque producing mechanism. A brief description of the mechanisms of density gradient and torque production are given below. Note that all the mechanisms may occur simultaneously, and that it is possible for one to predominate and mask the effects of the others.

(1) Sedimentation

An acceleration field will produce a sinking or rising motion of elements\* whose densities are respectively greater than or less than that of the fluid. Density gradients occur when the elements localize in preferential areas rather than become uniformly dispersed throughout the fluid. The torque production is caused by a viscous drag transmitted to the float from the element motion in the fluid, or by a pendulosity effect if the element is adjacent to the float surface. If the elements are small enough so that Brownian motion (diffusion) becomes important, then there is a remixing effect of varying importance (see Section 5).

The case of voids (or cavities) which may appear in the TGG fluid at decreased temperatures (due to incomplete bellows compensation) also lies in this category. At operating temperature these voids disappear over a period of several hours, and are responsible for the very large ramps observed during initial operation. These voids are not considered responsible for the accepted GST phenomena in the TGG although they cause g-insensitive unbalance trends.

(2) Thermogravitational Diffusion (TGD)

A temperature gradient across the fluid enables thermal diffusion to separate lighter from heavier contaminants and/or fluid constituents. In the presence of an acceleration

---

\*Here, element refers to either a contaminant (particulate, liquid or gas) or a fluid constituent.



field, fluid convection enables the lighter species to collect at different locations from the heavier species. Torque production is due to the bulk fluid flow driven by the density gradient. At the same time, the TGD mechanism is also producing an effective mass motion, which should be included in reorientation considerations.

(3) Built-in Density Gradient

If the fluid is not unimolecular (or narrow cut), a fluid inhomogeneity may be poured in during fill. This may occur if the fluid is initially inhomogeneous before fill, or may arise as a direct consequence of the fill procedure (e.g., the more volatile molecules evaporate during the fill process (fluid stripping)). Torque production is caused by the bulk fluid flow driven by the built-in density gradient.

Section 2 of this report discusses typically observed GST signatures. In Section 3 a general analytical description of the equations of mass transport applied to the flotation fluid is presented. Section 4 reviews the analytical models predicting the duration and magnitude of the torques exerted on the float by density gradient driven fluid bulk motion. A discussion of system navigation models also appears in Section 4. Analytical models describing sedimentation, centrifuge conditioning of a built-in density gradient, and TGD are given in Sections 5 through 7. Conclusions and recommendations based on the analyses, are discussed in Section 8.

As an instructional aid, the examples are calculated for the TGG, a floated gas-bearing instrument which was designed at CSDL and is being manufactured at Northrop Precision Products Division.

## SECTION 2

### TYPICALLY OBSERVED GST SIGNATURES

GST is typically noticed after a change in orientation of an instrument which has been maintained in a fixed orientation during a period of time preceeding the orientation change. During the time following this orientation change, the acceleration dependent instrument coefficients vary as an apparent mass unbalance shift. Typically observed GST signatures (see References 1, 2 and 3) can be characterized by the following six descriptions:

- (1) The unbalance eventually moves into alignment with the g-vector (vertical).
- (2) For an  $180^\circ$  storage reorientation the unbalance changes along the new vertical axis only.
- (3) For a  $90^\circ$  storage reorientation either
  - (a) the unbalance changes primarily along the new vertical axis, or
  - (b) the unbalance changes along both the new vertical and new horizontal axes.
- (4) Centrifuging the instrument with wheel off indicates that the equilibrium unbalance (bound magnitude) is independent of g-level.
- (5) Centrifuging the instrument with wheel off indicates that either

- (a) the time-to-bound (time to reach an equilibrium unbalance for a given orientation) is inversely proportional to  $g$ -level (PIGA, another gyro), or
- (b) the time-to-bound is inversely proportional to  $g^n$  where  $0 < n < 1$  (another gyro, TGGs 0002, 222X).
- (6) The time-to-bound is essentially independent of the equilibrium unbalance magnitude.

It is interesting to note that characteristics 3(a) and 3(b) are both observed for the TGG, but only 3(b) for other instruments. Characteristic 6 is derived from the fact that no correlation is observed in the test data between time-to-bound and bound magnitudes.

Test values of times-to-bound and bound magnitudes vary from instrument to instrument. Typically, the times-to-bound range from 10 to 100  $g$  days and the bound magnitudes range from approximately 0 to 0.10 deg/h/ $g$ . Values of bound magnitudes much larger than typical have also been observed. Generally, the longer the test period the larger the time constant of the trend. This is attributed to the several different time constants of the mechanisms governing the fluid motion and diffusion effects (Sections 5 through 7). The simultaneous existence of fluid sources possessing different time constants is assumed responsible for characteristic 5(b).

In the TGG, observed times-to-bound are approximately \*  $g$  days to \*  $g$  days for bound magnitudes of approximately \* through \* meru/ $g$ . These values are based upon MPMS and ASP system data, MX (0002, 0006, and 0015) and prototype units MPMS (221X, 222X).

\* For deleted information please refer to the authors.



### SECTION 3

#### GENERAL EQUATIONS OF MASS TRANSPORT

A complete solution to the phenomenon of mass transport of the flotation fluid requires a combined solution of the equations of bulk fluid motion, bulk fluid continuity, and mass diffusion. The general solution of these equations is not available. A numerical technique for solving a more simplified version has been outlined in Reference 4, and is currently being developed. However, it is advantageous to examine cases which allow simplification of the equations and hence a more readily achievable solution.

One assumption requires that the flotation fluid be a two component (binary) mixture. Although this is not generally true, except for a monomolecular fluid with one contaminant, or a true binary fluid, it permits useful insight into the speculated physical mechanism for GST.

The general equations of the binary fluid are developed as follows. Neglecting compressibility effects, the vector equation of bulk fluid motion is

$$\rho \frac{D}{Dt} (\underline{v}) = - \nabla p + \rho \underline{g} + \mu \nabla^2 \underline{v} \quad (3.1)$$

which is the Navier-Stokes equation, and where  $\underline{v} = (v_x, v_y, v_z)$ .

The continuity equation of the bulk (or barycentric) flow is

$$\frac{D}{Dt} (\rho) + \rho \nabla \cdot \underline{v} = 0 \quad (3.2)$$

which, for component 1 of a two-component fluid, can be expressed as  
(see Reference 4)

$$\rho \frac{\partial c_1}{\partial t} + \rho \underline{v} \cdot \nabla c_1 = - \nabla \cdot \underline{J}_1 \quad (3.3)$$

where  $c_1$  is the fractional mass concentration, and  $\underline{J}_1 = (J_{1x}, J_{1y}, J_{1z})$  is mass flux of component 1 with respect to the bulk flow.

The equation for  $\underline{J}_1$  is

$$\underline{J}_1 = \rho D \left[ \nabla c_1 - \alpha \frac{c_1 c_2}{T} \nabla T + s c_1 \nabla p \right] \quad (3.4)$$

where  $c_1 + c_2 = 1$  for a two component fluid, so that the continuity equation for  $c_2$  is unnecessary. The first term on the right hand side of equation (3.4) represents the effect of ordinary diffusion due to the concentration gradient, the second term represents thermal diffusion across a temperature gradient, and the third term represents transport due to a sedimenting (pressure gradient) force. Section 5 discusses the case where either sedimentation or ordinary diffusion dominate, and Section 6 discusses the case of dominant thermal diffusion.

A constitutive relationship to determine density variation with time is required. As a first approximation the density  $\rho$  is assumed to be the weighted average of the two components

$$\frac{1}{\rho} = \frac{c_1}{\rho_{10}} + \frac{c_2}{\rho_{20}} \quad (3.5)$$

where  $\rho_{10}$  and  $\rho_{20}$  are the densities of components 1 and 2 representing before mixing. Since  $c_1 + c_2 = 1$  equation (3.5) can be rewritten as

$$\frac{1}{\rho} = c_1 \left( \frac{1}{\rho_{10}} - \frac{1}{\rho_{20}} \right) + \frac{1}{\rho_{20}} \quad (3.6)$$

Differentiating with respect to time

$$\frac{1}{\rho^2} \frac{\partial \rho}{\partial t} = \frac{\partial c_1}{\partial t} \left[ \frac{1}{\rho_{20}} - \frac{1}{\rho_{10}} \right] \quad (3.7)$$

Equations (3.1) through (3.7) produce nine equations which, in theory, can be solved for the nine variables,  $p$ ,  $\rho$ ,  $c_1$ ,  $J_1$ , and  $\underline{v}$  if  $\rho_{10}$ ,  $\rho_{20}$ ,  $\mu$ ,  $g$ ,  $D$ ,  $\alpha$ , and the temperature distribution are known. (Note that for the TGG, Rayleigh number calculations indicate that convection does not affect the temperature distribution.) Once  $\rho$  and  $\underline{v}$  are known it is relatively simple to calculate the magnitude and times of the buoyancy force and viscous drag effects on the float. Without simplification it is currently not possible to solve these nine equations. Previous approaches to the GST problem have been based upon assumptions of the nature of the equilibrium density gradient (i.e., after prolonged storage). These assumptions are then used to calculate bound magnitudes and times-to-bound of the GST, and preclude the simultaneous solution of equations (3.1) through (3.7). A review of these past approaches is presented in the next section. The basic technique has been to ignore the mechanism whereby density gradients are developed and to estimate the bulk fluid motion arising from a change in orientation (i.e., develop a basic solution of the Navier-Stokes equations).

The solution of some special case simplifications now follows in Sections 4 through 7. The end gaps as well as the damping gap are studied.

Note that flocculation, coagulation, and electric boundary layer effects are not included in the discussed models. Flocculation and coagulation have been observed in CTFE and are discussed at several points.



## SECTION 4

### BULK FLUID MOTION

#### 4.1 INTRODUCTION

If the density gradient production mechanisms are ignored and an equilibrium density gradient assumed then, after a change in orientation, the realignment of the density gradient along the  $g$  direction by bulk flow is responsible for GST torques exerted on the float. There are two possible causes of these error torques:

- (1) viscous drag effects, and
- (2) buoyancy force effects.

However, the analysis of Reference 5 shows that, for the typical range of eccentricities of centers of rotation and buoyancy, the buoyancy force effect is at least an order of magnitude less than the viscous drag effect. Several theories have been postulated to predict the bulk fluid motion in the damping gap and the corresponding viscous drag effect on the float. These theories assume a density distribution and are essentially solutions of the Navier-Stokes and continuity equations (see Section 3). The theories are discussed briefly and their shortcomings indicated. Also discussed are system navigation models.

#### 4.2 FLUID DENSITY GRADIENT MODELS

Two related models which assume fluid density distributions (a linear gradient and a concentrated non-homogeneity) are discussed. These models reveal the basic torque producing mechanism, but offer no insight into the origins of the distributions.

#### 4.2.1 Linear Density Gradient (see References 1, 3, and 5)

If the density gradient is assumed linear in the  $g$  direction, then the density  $\rho$  at any point in the damping gap can be expressed as

$$\rho = \rho_0 (1 - k \sin \theta) \quad (4.1)$$

where  $k$  is the fluid density variation factor. If convection from the temperature difference across the gap is neglected, then after a  $90^\circ$  storage axis reorientation there will be a circumferential rotation (hoop flow) of the fluid (see Figure 1). The maximum viscous drag torque  $(M_{VD})_{\max}$ , which represents a bound magnitude is (see Reference 5):

$$(M_{VD})_{\max} = \frac{1}{2} \rho_0 V h k g \quad (4.2)$$

and the time constant for the motion after the  $90^\circ$  reorientation is (see Reference 1)

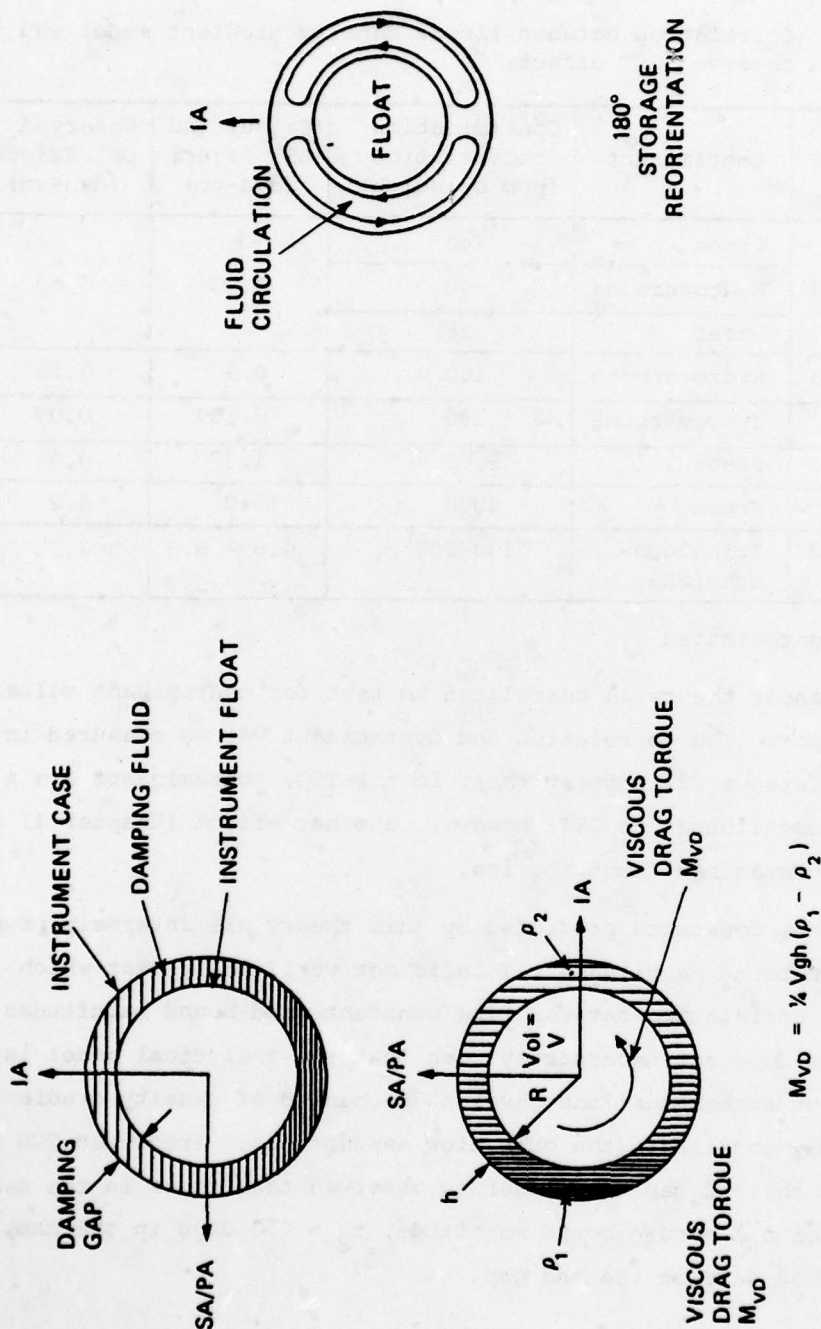
$$t_c = \frac{V r \mu}{2h (M_{VD})_{\max}} \quad (4.3)$$

After a  $180^\circ$  reorientation the viscous drag torque will be zero (see Figure 1) and the time constant for the density gradient realignment is (see Reference 3)

$$t_c = \frac{V r \mu k_v}{2h (M_{VD})_{\max}} \quad (4.4)$$

where  $k_v$  is an empirical vertical settling factor. However, this model gives small initial effect mass velocities along  $g$  after  $180^\circ$  reorientation. Tests indicate relatively large velocities along  $g$ , a contradiction.

Based upon measured values of fluid contamination in several instruments, values of the density difference amplitude  $k$  were assumed



FLUID CIRCULATION IN FLUID-DENSITY GRADIENT MODEL FOR 180° REORIENTATIONS

Figure 1. Viscous torque due to circumferential bulk flow.

INSTRUMENT OUTPUT-AXIS ERROR TORQUE DUE TO FLUID-DENSITY DIFFERENCE



for prediction of the GST bound magnitude (see References 1 and 6). A comparison of theory with test extracted from References 1 and 6 is shown in Table 1 below.

Table 1. Correlation between linear density gradient model and observed GST effect.

Instrument	Contaminant	Contamination Concentration (ppm by weight)	Calculated GST Effect (dyn-cm)	Observed GST Effect (dyn-cm)
25 IRIG Mod 3	Freon	140	0.80	0.60
	Hydrocarbons	40		
	Water	25		
25 IRIG Mod 3	Hydrocarbons	100	0.9	0.56
13 IRIG	Hydrocarbons	180	0.109	0.07
16 PM PIP*	Freon	5000	1.37	0.3
Vial*	Freon	4000	10.0	4.2
25 IRIG Mod 3	Trichloro-ethylene	500-900	4.6 - 8.3	2.2

\*Purposely contaminated

The simple linear theory is correlated to test for contaminant values of roughly 100 ppm. The correlation and contaminant values measured in TGGs (see Reference 22) suggest that, in the TGG, contaminants are a significant contributor to GST; however, another effect (Chapter 1) is masking the contaminant contribution.

The time constants predicted by this theory are inversely proportional to the bound magnitudes. This is not verified by test which indicates no correlation between time constants and bound magnitudes. However, this does not necessarily mean that the analytical model is incorrect, but rather that the physical mechanism of density gradient production may invalidate the bulk flow assumptions. Predicted TGG time constants in the end gap are closer to observed than those in the damping gap, e.g., for a 1 meru/g bound magnitude,  $t_c = 750$  days in the damping gap and  $t_c = 50$  days in the end gap.

A summary of the shortcomings of this theory follows:

- (1) Requires assumptions of the density gradient;
- (2)  $180^\circ$  storage reorientations cannot be predicted unless assumptions are made concerning the bulk flow paths (i.e., three-dimensional flow rather than two-dimensional as discussed);
- (3) Can only predict bound magnitudes after a  $90^\circ$  storage reorientation;
- (4) Time-to-bound depends upon unbalance;
- (5) Poor correlation with observed times-to-bound.

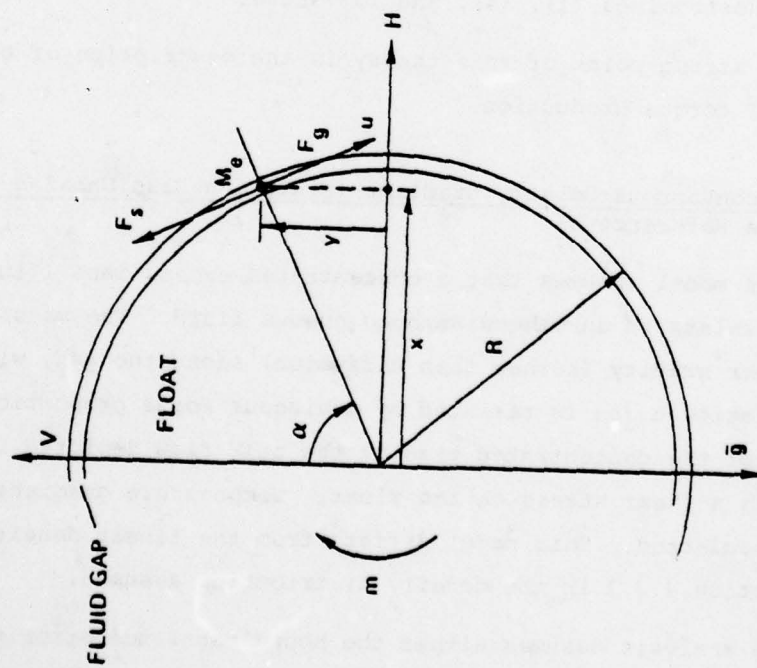
The above analysis has neglected the effect of convection due to the temperature difference across the gap. A first order approximation, in which the density gradient realigned itself with the  $g$  vector along the convection paths, was presented in Reference 7. Apart from requiring assumptions concerning the convection paths, this method also possessed shortcomings (1), (4), and (5) above.

The strong point of this theory is the description of the basic mechanism of torque production.

#### 4.2.2 Discontinuous Density Gradient (Migrating Mass Unbalance Model), (see Reference 8)

This model assumes that a concentrated excess mass (fluid inhomogeneity) exists in an otherwise homogeneous fluid. The mass is assumed to move under gravity (rather than diffusion) along the gap, with a tangential velocity  $u$  and is resisted by a viscous force proportional to  $u$ . The motion of the concentrated mass is the bulk flow depicted in Figure 2, which exerts a shear stress on the float. Temperature gradient effects have been neglected. This model differs from the linear density variation of section 4.2.1 in the density distribution assumed.

The analysis assumes either the bound magnitude error torque, or the excess mass, or the time constant to predict the remaining two. The time constant is inversely proportional to the bound magnitude, a shortcoming



# CONCENTRATED EXCESS MASS IN FLUID GAP

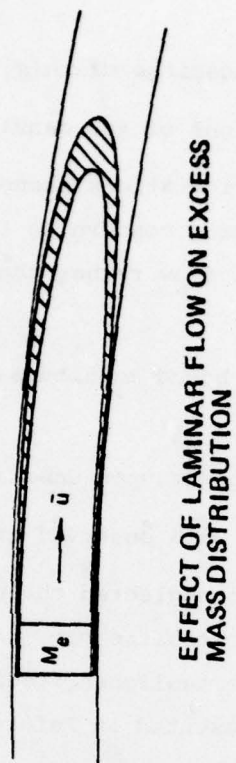


Figure 2. The concentrated migrating mass model.



which is previously discussed in Section 4.2.1. In the damping gap there is poor correlation with observed time constants, e.g., for the TGG in a 1g acceleration field the time constant is predicted to be 833 days for a bound magnitude of 1 meru, and 166.6 days for a bound magnitude of 5 meru. Application of this analysis to the end gap gives better correlation with observed time constants, e.g., for the TGG in a 1g acceleration field the time constant is predicted to be 27 days for a bound magnitude of 1 meru, and 5.4 days for a bound magnitude of 5 meru.

A difficulty encountered with this analysis and that of the linear density gradient is the case of  $180^\circ$  storage reorientation. The concentrated excess mass which was originally at the bottom is now at the top of the vertical axis. Test data have shown that horizontal axis unbalance remains virtually unchanged with time. To achieve this the model requires the mass to split into two practically equal halves which move in similar flow paths on opposite sides of the float. The simplest of these flow paths is circumferential flow around the float, but a more complex flow path with both axial and circumferential velocity components may exist.

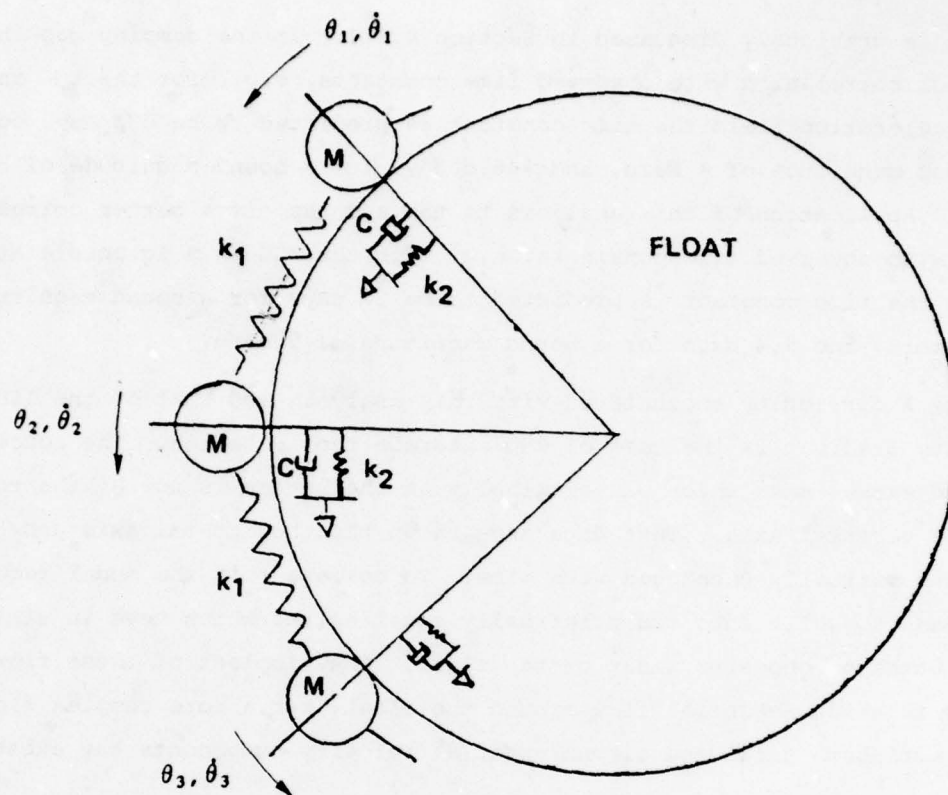
A summary of the shortcomings of this theory is:

- (1) Requires knowledge of the unbalance or time constant;
- (2) Cannot predict  $180^\circ$  reorientations unless mass is divided;
- (3) Time-to-bound depends upon unbalance;
- (4) Poor correlation with observed times-to-bound.

The strong point of this theory is the description of the basic mechanism of torque production.

#### 4.3 NAVIGATION MODELS

An important class of models which requires no knowledge of the GST mechanisms is the class designated Navigation Models. These models are formulated so as to agree qualitatively with the test observations of GST, and are aimed for use at the system level. It should be noted that the migrating mass unbalance (MMU) model of Section 4.2.2 has also been proposed as a Navigation Model.



$$k_1 R [(\theta_3 - \theta_2) - (\theta_2 - \theta_1)] - k_2 R \theta_2 - C \dot{\theta}_2 = M \ddot{\theta}_2 R$$

Figure 3. The multimass navigational model.

#### 4.3.1 The Multi-Mass Navigation Model (see Reference 9)

It is suggested that the density inhomogeneities be modeled as a series of masses as shown in Figure 3. The masses  $M$  are connected to one another by the rotational springs  $k_1$ . Rotational damping constant  $C$  damps the mass motion with respect to the float and case. The second set of rotational springs  $k_2$  are included to simplify the analytic burden. By fixing the masses to a given area around the float, linear models might be used advantageously. To satisfy the observed result that unbalance does not depend on gravity magnitude, and that time constant is inversely proportional to gravity, the spring stiffness would be considered proportional to gravity.

AD-A076 567

ARMAMENT DEVELOPMENT AND TEST CENTER EGLIN AFB FL  
PROCEEDINGS OF THE BIENNIAL GUIDANCE TEST SYMPOSIUM (9TH) HELD --ETC(U)  
OCT 79

F/G 17/7

UNCLASSIFIED ADTC-TR-79-11-VOL-1

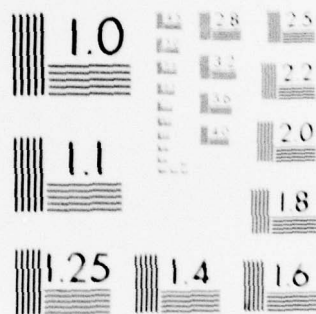
NL

2 OF 5

AD  
A076567







MICROCOPY RESOLUTION TEST CHART  
NATIONAL BUREAU OF STANDARDS-1963-A

It is emphasized that the model is suggested only because it agrees qualitatively with observed data. The actual parameter values, as well as the number of masses, should be determined from test. Since point mass models are a subset of the multi-mass model, any testing designed to study the multi-mass model is also applicable to the MMU. Before fitting data, analytic study of the proposed model's behavior is required.

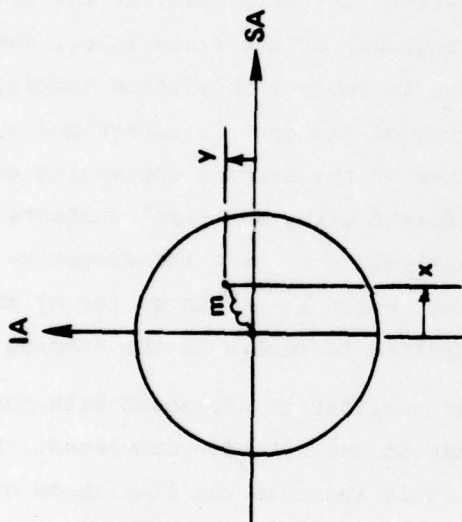
#### 4.3.2 The Point Mass Navigation Model (see Reference 10)

This is an analytically and physically simpler model than the multi-mass. A point mass is located within the gyro case, at the center of gravity of the heavier region (or regions) of the fluid (i.e., due to density inhomogeneities). Its movement is subject to viscous damping and its motion from the geometric center of the gyro is restrained by a spring (see Figure 4). Different values of the damping and spring constants can be introduced to allow different gains and time constants for the motion of the point mass. This analysis does have the advantage that any splitting of the fluid heavier region is accounted for by the fact that the point mass is not constrained to remain in the damping gap.

The point mass model also gives qualitative agreement with observed GST data, although quantitative evaluation has not been completed. As with the multi-mass model, agreement would indicate the likelihood of some density gradient migrating mass unbalance model being responsible for GST. In order to utilize this model the magnitudes of the spring and damping coefficients must be chosen to match test data. Since GST levels vary from gyro to gyro semi-empirical coefficients must be determined.

The shortcomings of both system navigation models are as follows:

- (1) Can only be used for evaluation;
- (2) Insufficient data to answer OA vertical or zero g;
- (3) Cannot satisfy bound magnitudes changing with time.



(a) POINT MASS GST MODEL

$$\begin{aligned} \ddot{x} &= -\frac{k_x}{c_x} \dot{x} + \frac{1}{c_x} g_x \\ \ddot{y} &= -\frac{k_y}{c_y} \dot{y} + \frac{1}{c_y} g_y \end{aligned} \quad \text{where} \quad \begin{cases} c_x, c_y = \text{DAMPING COEFFICIENTS, APPLICABLE TO MOTION OF } m \text{ ALONG THE SA AND IA RESPECTIVELY} \\ k_x, k_y = \text{SPRING CONSTANTS, APPLICABLE TO MOTION OF } m \text{ ALONG THE SA AND IA RESPECTIVELY AND ARE FUNCTIONS OF } g \text{ AND } g \text{ ORIENTATION} \\ g_x, g_y = \text{COMPONENTS OF } g \text{ ALONG THE SA AND IA RESPECTIVELY, AND} \\ x, y = \text{DISPLACEMENTS OF } m \text{ ALONG THE SA AND IA RESPECTIVELY} \end{cases}$$

(b) EQUATIONS OF MOTION FOR THE POINT MASS

Figure 4. The point mass navigational model.



The point mass model also has the disadvantage that it does not satisfy the g alignment observation for a  $90^\circ$  storage reorientation (characteristic 3(a), Section 2). A model which superimposes the above upon a viscoelastic model, where the mass is only permitted motion along gravity is recommended in Section 8 for use in evaluating navigation systems.

## SECTION 5

### SEDIMENTATION

#### 5.1 INTRODUCTION

If the effect of temperature gradient is neglected then Equation (3.4) becomes

$$\underline{J}_1 = \rho D [\nabla c_1 + s c_1 \nabla p] \quad (5.1)$$

The relative importance of the two terms on the right hand side of Equation (5.1) depends upon the size of the contaminants and fluid constituents. (It should be noted here that the largest telomers of CTFE are approximately  $10^{-3}$  microns). It is convenient to examine Equation (5.1) with reference to the three classes of sedimenters discussed in Reference 11.

##### 5.1.1 True Sedimenters

These may be considered to be greater than approximately 1 micron in size (see Reference 12), and can therefore only be contaminants. In an acceleration field  $\geq 1 g$ , the sedimenting force dominates the Brownian motion of the surrounding molecules. Hence the relative mass transfer equation is

$$\underline{J}_1 = \rho D s c_1 \nabla p \quad (5.2)$$

### 5.1.2 Partial Sedimenters

These may be considered to lie in the colloidal size range of approximately  $10^{-3}$  microns to 1 micron (see Reference 12), and can therefore be either contaminants or fluid constituents or both. The net transport is described by Equation (5.1), where the sedimenting force is opposed by diffusion (Brownian motion) due to the development of a concentration gradient in the  $g$  direction.

### 5.1.3 Non-Sedimenters

These are less than approximately  $10^{-3}$  microns, and can therefore be either contaminants, fluid constituents, or both. The sedimenting forces are so small that the effect of Brownian motion predominates. Hence the relative mass transfer equation is

$$\underline{J}_1 = \rho D \nabla c_1 \quad (5.3)$$

This represents a spreading or remixing motion which results in uniform dispersion throughout the fluid. Only in the most powerful ultracentrifuges will sedimentation be possible. This class will become important if a temperature gradient exists (thermal diffusion).

There is clearly no rigid distinction between the boundaries of the first and second, and second and third classes.

## 5.2 TRUE SEDIMENTERS

### 5.2.1 True Sedimenters in the Damping Gap

The behavior of sedimenting contaminants in the damping gap is discussed in detail in Reference 11. Briefly, Reference 11 qualitatively discusses the motion of contaminants, greater than 1 micron in size, for storage axis reorientations in a  $1g$  acceleration field. Contaminant motion between float and case (i.e., across the damping gap) is seen to be important. Analytical predictions are based upon the assumption of



spherically shaped contaminants, which exert a torque about OA due to either:

- (1) contacting the float surface (pendulosity); or
- (2) moving through the fluid (transmitted viscous drag).

Theoretical results relating to the TGG are reproduced from Reference 11 in Table 2 and Figure 5. Note that the binary fluid assumption is not necessary for true sedimenters, and that the bulk fluid motion is accounted for by the transmitted viscous drag.

Based upon a 5 micron filter size, values of fill introduced contaminant densities causing different decay times (times to bound) are shown in Table 2.

Table 2. Effect of fill-introduced particulates on TGG.

Time to Decay (days)	Approximate Particulate Density (gm/cm <sup>3</sup> )
90	$\rho_p < 0.5$ , $\rho_p > 3.0$
30	$\rho_p > 5.0$
12	$\rho_p > 10.0$
4	$\rho_p > 20.0$

Limitation on the size of fill-introduced liquids or gases is not strictly applicable since fluids may pass through the filter. Furthermore, once inside the instrument, contaminants may combine or separate to form various sizes and distributions. Clearly no size restriction can be placed on contaminants already inside the instrument or that are generated in situ.

Values of the amount of contamination required to produce 1 meru/g error torque in the TGG by the viscous drag mechanism versus contaminant density are shown in Figure 5. The results are independent of contaminant radius.

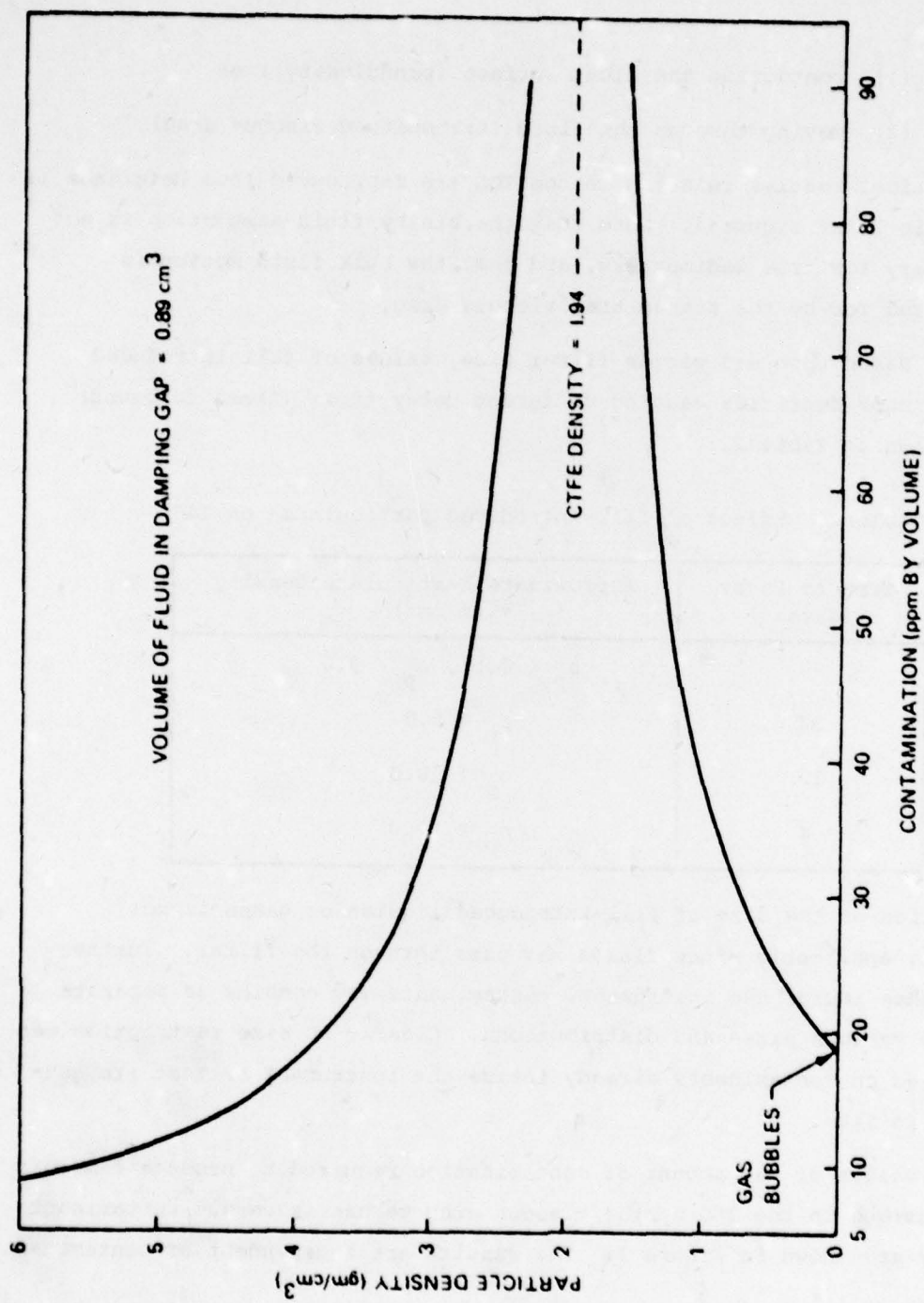


Figure 5. Damping gap contamination in ppm by volume required to cause 1 meru/g in TGG based on viscous drag mechanism.

The mechanism of sedimenting contaminant motion appears to satisfy all the observable characteristics, including some hitherto unexplained test results (see References 11 and 13). There is, however, a need for clarification as to whether the contaminants have crossed the gap onto the float or whether they remain close to the case at the time of torque measurement.

#### 5.2.2 True Sedimenters in the End Gap

The motion of sedimenting contaminants in the end gap, which is not considered in Reference 11, may be necessary to explain some of the observed GST signatures after  $90^\circ$  storage reorientation. The generally accepted signature after  $90^\circ$  reorientation is one in which both vertical and horizontal axes unbalance change with time. However, some test results indicate an unbalance change only along the new vertical axis (i.e., only along g) while the new horizontal axis unbalance remains virtually constant at least for the first ten days or more. (Note, it has never been observed that unbalance changes along only the horizontal axis and not the vertical). An explanation of the phenomenon requires a predominance of sedimenting contaminants in the end gap rather than the damping gap. This is feasible since the volume of fluid in the MX/TGG end gaps is approximately  $1.49 \text{ cm}^3$  (SG end  $\sim 0.65 \text{ cm}^3$ , TG end  $\sim 0.84 \text{ cm}^3$ ) compared with  $0.89 \text{ cm}^3$  in the damping gap.

Similarly to the discussions of Reference 11, consider contaminants that are true sedimenters under gravity. Furthermore, for simplicity, consider only those contaminants which sink under gravity, i.e., which are heavier than the fluid. The following sequence of events, shown in Figure 6 for one contaminant, is indicative of the possible mechanism explaining negligible horizontal axis unbalance after  $90^\circ$  reorientation.



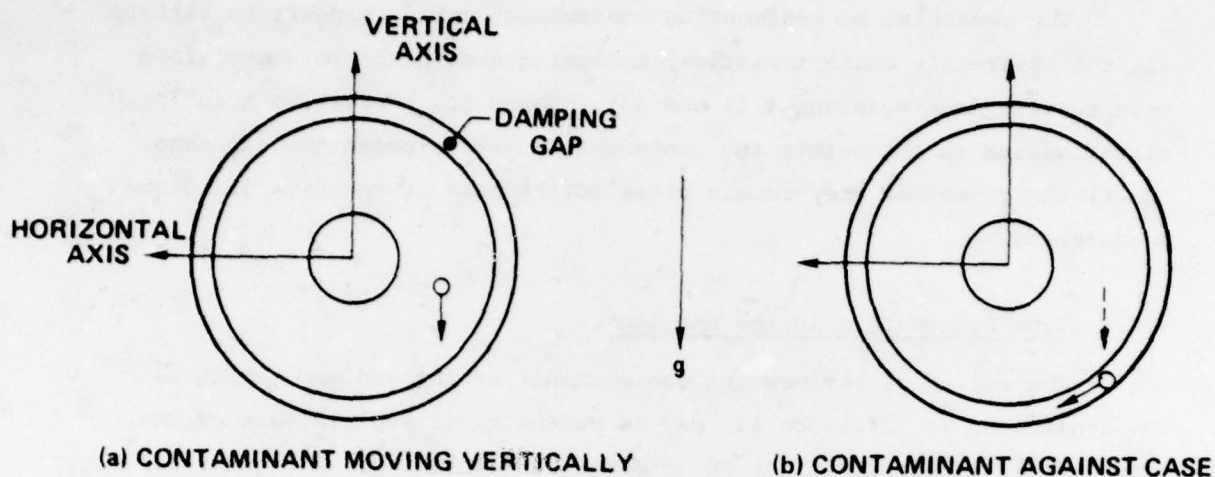


Figure 6. Sedimenting contaminant in the end gap.

Referring to Figure 6(a), the contaminant can travel vertically in the end gap. Thus, there is a significant change with time of the viscous drag moment arm when measuring vertical axis unbalance, but a zero change of the horizontal axis unbalance moment arm. Eventually, the contaminant reaches the case (see Figure 6(b)) and begins to travel down along the case or sticks. For no sticking the viscous drag torque will be measured as a change in both vertical and horizontal axis unbalance. However, it is not possible to ascertain how significant this effect is, due to the fact that the viscous drag acts in the vicinity of the float corner, and not on a plane surface. (At the TG end there is a shoulder 0.005 inch wide, upon which some of the contaminants could end their vertical motion. Their subsequent motion along this surface would contribute to the unbalance of both axes by the float pendulosity mechanism (see Reference 11). This effect could be expected to have some significance.) Note that TGD can also explain this vertical axis unbalance change (see Section 7.3.1).

At room temperature storage bottled CTFE and microscope slides have separated into clear and waxy components. This might indicate a coagulation or flocculation which enables larger particles to form and become true sedimenters. Flocculation has been observed in CTFE samples stored at operating temperature. Thus a sedimentation induced separation of the fluid itself should be considered a GST mechanism.

### 5.3 PARTIAL SEDIMENTERS

The behavior of elements (contaminants or damping fluid constituents) which partially sediment in an acceleration field is described in Reference 11. Briefly, in equilibrium and assuming no bulk flow, a concentration gradient is formed in the  $g$  direction which enables diffusion to counterbalance the sedimenting force. Therefore, at partial sedimentation equilibrium, the net flow is zero so that equation (5.1) becomes

$$\rho D [\nabla c_1 + s c_1 \nabla p] = 0 \quad (5.4)$$

Another way of expressing zero net flow, provided density variations are assumed negligible, is (see Reference 14)

$$c_1 \frac{dx}{dt} = D \frac{dc_1}{dx} \quad (5.5)$$

As a first approximation, the sedimenting force on an element can be equated with the frictional resistance of the damping fluid, so that

$$f \frac{dx}{dt} = v (\rho_p - \rho) g \quad (5.6)$$

where  $\rho$  is taken to be the fluid density. Hence, Equation (5.5) can be written

$$\frac{dc_1}{c_1} = \frac{v}{Df} (\rho_p - \rho) g dx$$

Using Einstein's relation between the ordinary diffusion coefficient and the frictional force,  $f$ , given by Reference 15

$$Df = \frac{RT}{N} \quad (5.8)$$

then Equation (5.7) becomes

$$\frac{dc_1}{c_1} = \frac{VN}{RT} (\rho_p - \rho) g dx \quad (5.9)$$

Assuming that  $V$  and  $\rho_p$  are constant then this can be integrated to give the equilibrium concentration ratio

$$\frac{(c_1)_{x_1}}{(c_1)_{x_0}} = \exp \frac{VN}{RT} (\rho_p - \rho) g (x_1 - x_0) \quad (5.10)$$

Note that the concentration ratio is independent of the element shape. For convenience assume the shape to be spherical of radius  $a$ , then values of the ratio of  $c_1$  at opposite ends of the TGG damping gap are shown in Table 3 for various  $a$  and  $\rho_p$ .

Table 3. Ratio of fractional mass equilibrium concentration  $(c_1)_{x_1} / (c_1)_{x_0}$  at opposite ends of the TGG damping gap ( $x_1 - x_0 = 6$  cm)  $x_1$

a (microns)	$\rho_p$ (gm/cm <sup>3</sup> )							
	0.1	0.5	1.0	1.5	2.0	3.0	5.0	10.0
1.0	(Approximately infinite concentration ratio) True Sedimenters							
$5 \times 10^{-1}$								
$10^{-1}$								
$5 \times 10^{-2}$	$2.18 \times 10^{3.6}$	$3.35 \times 10^{2.2}$	$5.7 \times 10^{2.7}$	$9.8 \times 10^{1.2}$	59.1	$2 \times 10^{1.1}$	$2.3 \times 10^{0.9}$	
$10^{-2}$	2.72	2.18	1.668	1.27	1.033	1.78	5.28	80.2
$5 \times 10^{-3}$	1.13	1.102	1.066	1.03	1.004	1.075	1.23	1.73
$10^{-3}$	1.001	1.0008	1.0005	1.0002	1.00003	1.0006	1.0017	1.004
$5 \times 10^{-4}$	1.0001	1.00009	1.00006	1.00003	1.000004	1.00007	1.0002	1.0005



It is apparent from Table 3 that spherical elements greater than approximately 0.2 microns in size may be considered true sedimenters for this analysis.

A solution of the one-dimensional unsteady partial sedimentation equation (Equation (5.1)) is presented in Appendix A. The time constant  $t_c$  for equilibrium partial sedimentation is shown to be

$$t_c = \frac{L^2}{\pi^2 D} \quad (5.11)$$

where  $t_c$  is the time constant for remixing (uniform dispersion) by ordinary diffusion. This time constant appears again in Section 7. Values of  $t_c$  are shown in Table 4 for various values of  $D$  and  $L = 6$  cm. Also shown are radii  $a$  of spherical elements in CTFE corresponding to the values of  $D$ . These are calculated using Einstein's relation (Equation (5.8)) and the frictional coefficient of spherical elements.

$$f = 6\pi \mu a \quad (5.12)$$

Table 4. Time constants for equilibrium partial sedimentation from top to bottom of TGG damping gap (6 cm).

$D$ (cm /s)	$t_c$	$a$ (microns)
$10^{-5}$	4.2 days	$\sim 10^{-7}$
$10^{-6}$	42.2 days	$\sim 10^{-6}$
$10^{-7}$	422.2 days	$\sim 10^{-5}$
$10^{-9}$	115.7 years	$\sim 10^{-3}$
$10^{-11}$	$\approx \infty$	$\sim 10^{-1}$
$10^{-13}$	$\approx \infty$	$\sim 10$

Only for  $D \approx 10^{-5}$  does the value of  $t_c$  correspond to observed GST time constants. However, based upon the assumption of sphericity, the particle size is too small to exist (since a hydrogen atom is approximately  $10^{-4}$  microns). Since partial sedimenters are expected to be roughly in the size range of  $10^{-3}$  microns to 1 micron, then the values of  $D$  should be roughly in the range of  $10^{-9}$  to  $10^{-12}$   $\text{cm}^2/\text{s}$ . This suggests that if partial sedimentation is occurring (i.e., if diffusion effects and sedimenting effects are of the same order of magnitude) then the time constants are far longer than currently observed for GST. However, it should be noted that partial sedimenters may still cause GST. Although motion by diffusion is very slow, the density variations may induce bulk fluid flows which are discussed in Section 4.

Equation (5.12) holds provided the liquid medium is continuous compared with the element dimension (i.e., Equation (5.12) is not accurate for elements whose sizes are comparable to or less than those of the flotation fluid constituents). Since CTFE telomers are approximately  $10^{-3}$  microns in size, the majority of elements in the partial sedimenter size range satisfy the criterion for Equation (5.12) to hold. A semi-empirical method for obtaining a second estimate of  $D$  is offered. In water, a substance for which much data exists, particle diameters of  $10^{-3}$  microns give  $D$  of the order of  $10^{-5}$ . For CTFE having 3000 times the viscosity of water, a linear relation such as Equation (5.8) gives  $D$  in the  $10^{-8}$  to  $10^{-9}$   $\text{cm}^2/\text{s}$  range. However, since the actual element shapes are unknown, it is not feasible to discount completely the higher values of  $D$  ( $>10^{-9}$ ).

#### 5.4 ADDITIONAL OBSERVATIONS

The projections of Section 5.1 through 5.3 have been based on particles moving across the float, a distance of several inches. The sedimentation equations suggest that particle motion across the damping gap, a distance of 0.005 inch, is also possible. Because of the short distances, the cross-gap motion should result in faster decay time constants. As detailed in Reference 4, the fast transients could explain discrepancies in test data which have been observed in gyro tumble tests.

## SECTION 6

### FLUID STRIPPING AND CENTRIFUGE CONDITIONING

#### 6.1 INTRODUCTION

The phenomenon of fluid stripping is described in Reference 1 as follows:

During the filling of an instrument, a partial vacuum is drawn on the rising fluid filling an instrument. This procedure produces fluid stripping such that lighter viscosity telomers of the damping fluid are preferentially removed from the upper regions of the fluid. The result is a built-in density gradient in the damping fluid along the vertical axis of filling.

A solution to this problem was proposed in Reference 15. Briefly, a fill process performed quickly in a cool, moderate vacuum environment greatly reduces built-in fluid density gradients. A further reduction is achieved by centrifuging the instrument. This reduction is assumed to be due to remixing and diffusion. The analysis presented below suggests that ordinary diffusion across the gap coupled with bulk flow is the primary centrifuge conditioning mechanism.

#### 6.2 DIFFUSION DURING CENTRIFUGE CONDITIONING

During centrifuge conditioning a parabolic flow will occur due to the built-in fluid density gradients. This parabolic flow is shown in Figure 7. Across the interface of the parabolic flow there is a concentration gradient of fluid constituents. Hence it is feasible that diffusion across the interface is the homogenizing mechanism.



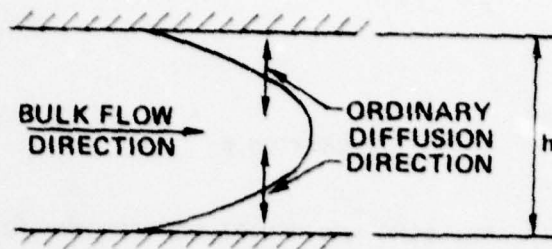


Figure 7. Parabolic bulk flow and diffusion during centrifuge conditioning.

The mean of the square of a molecular displacement in a particular direction  $\overline{x^2}$  is related to the diffusion coefficient by (Reference 12) (equivalent to solving (3.3) and (3.4) with zero barycentric velocity):

$$D = \frac{\overline{x^2}}{2t} \quad (6.1)$$

where  $t$  is the time between successive observations of the  $x$  coordinate. For given values of  $D$ , values of  $t$  in the TGG damping and end gaps are shown in Table 5. Note that this is independent of  $g$ .

Table 5. Time of ordinary diffusion across TGG damping and end gaps.

D	Time		
	Damping Gap $x = 0.0127/2$	SG End Gap $x = 0.0508/2$	TG End Gap $x = 0.0635/2$
$10^{-5}$	2.0 s	32.3 s	50.5 s
$10^{-6}$	20.2 s	322.6 s	504.7 s
$10^{-7}$	201.6 s	0.9 h	1.4 h
$10^{-8}$	0.6 h	8.9 h	14.0 h
$10^{-9}$	5.6 h	3.7 d	5.8 d
$10^{-10}$	2.3 d	37.3 d	58.4 d
$10^{-11}$	23.3 d	373.3 d	584.1 d
$10^{-12}$	233.0 d	10.2 y	16.0 y

Gyroscope centrifuge conditioning, which lasts typically for several cycles of approximately 2 weeks each at between 10 and 40g, has not always been successful in reducing GST bound magnitudes. An investigation of centrifuge conditioning of the TGG at 12g for cycles of 15 to 30 days is presented in Reference 3. The bound magnitude was shown to be attenuated by only approximately 33 percent over 120 g days by the conditioning. Based upon the remixing theory above, this would imply that D is of the order of  $10^{-11}$ . The residual unbalance after conditioning is presumably caused by sedimenting contaminants or TGD. It is also possible that the CTFE constituents are sedimenting in the centrifuge, but there is insufficient evidence at present to enable more than speculation.

More spectacular results have been obtained from size-16 FIGA centrifuge conditioning, where attenuations of an order of magnitude have been achieved at 40g for 2 days (see Reference 16). This success was a result of the very high initial bound magnitude, due to fluid stripping from the drip fill process, which was greatly attenuated by remixing. Changing to a bathtub fill reduced the initial bound magnitude, however, centrifuging achieved the same residuals, as the drip fill units. Accounting for the FIGA's smaller size compared to the TGG, the residual GST in the two devices are similar in magnitudes.

If the effect of diffusion is neglected then the parabolic bulk flow will tend to have a remixing effect similar to that of Figure 2(b). However, this alone cannot account for centrifuge conditioning since a flow reversal would be associated with a g reversal, so that the density gradient would reappear at some later time. This is not observed in test data, although a certain amount of increased unbalance with time has occasionally been observed, but this is more likely to be generated contamination in the fluid.

## SECTION 7

### THERMOGRAVITATIONAL DIFFUSION (TGD)

#### 7.1 INTRODUCTION

The heat flowing outwards from the gyro wheel produces a temperature gradient across the fluid in the damping and end gaps. Fluid convection, up the sides of the hotter float and down the sides of the cooler case, occurs. Furthermore, due to the temperature gradient, thermal diffusion across the gaps (parallel or anti-parallel to the temperature gradient) may occur. Thermal diffusion results in a depletion of an element type in one of the convective streams and an enrichment in the other. Generally, molecules lighter than the average thermally diffuse toward the upward moving hot convection stream, and those heavier than average toward the downward moving stream. The convection streams carry the depleted and enriched species in opposite directions, thereby producing a density gradient along the  $g$  direction. This is shown occurring in the damping gap in Figures 8(a) and 8(b).

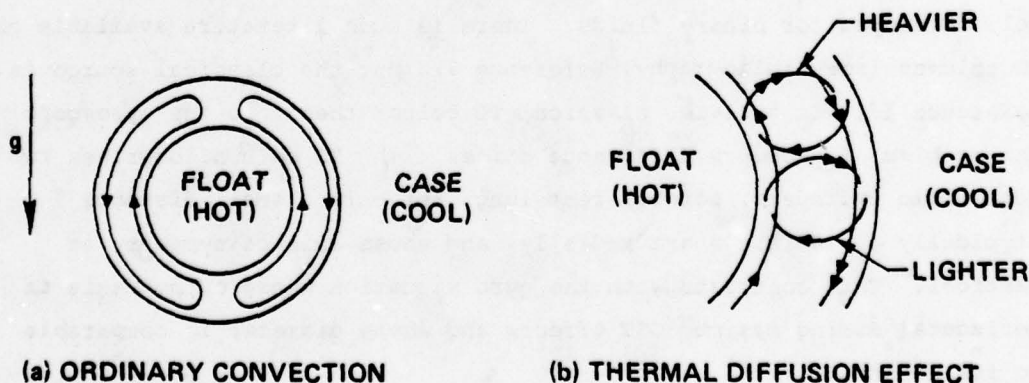


Figure 8. Mechanism of thermogravitational diffusion (TGD).



Small size (less than approximately  $10^{-3}$  microns) soluble and insoluble contaminants and some of the telomers of a multiple telomer flotation fluid are susceptible to this thermal diffusion phenomenon. These elements would generally be the non-sedimenters of Section 5, but may include the smaller less dense partial sedimenters.

The current TGG flotation fluid (CTFE) consists of several telomers, and can be expected to include a certain level of contamination when in the instrument. The complexity of analyzing multiple component fluids has restricted the solution to two component (binary) fluids (see Section 3). Since only non-sedimenters and the smaller and less dense partial sedimenters are susceptible to thermal diffusion, neglecting the sedimenting term in Equation (3.4) leads to

$$\underline{J}_1 = \rho D \left( \gamma c_1 - \frac{\alpha c_1 c_2}{T} \nabla T \right) \quad (7.1)$$

This equation needs to be solved simultaneously with the bulk flow convection, from Equation (3.1).

Float torque production is due to bulk flow driven by the density gradient formed by TGD.

## 7.2 APPLICATION OF THERMAL DIFFUSION COLUMN THEORY

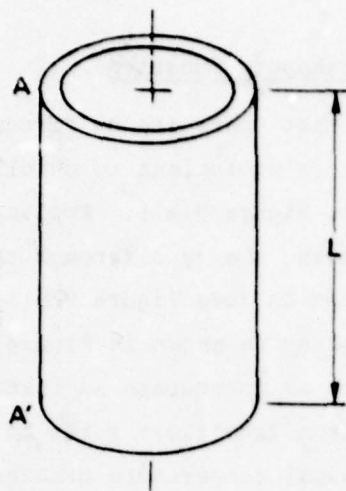
The theory of TGD in a thermal diffusion (TD) column has been well developed for binary fluids. There is much literature available on TD columns (see Bibliography, Reference 7), but the classical source is Reference 17. In applying classical TD column theory to the gyroscope the problem of geometry difference arises. The TD column comprises two concentric cylinders, several feet long, but only a small distance (typically 0.010 in.) apart radially, and whose axis of symmetry is vertical. This contrasts with the gyro situation whose output axis is horizontal during maximum GST effects and whose diameter is comparable to its length.

### 7.2.1 Cartesian Solution of the Unsteady Transport Equation

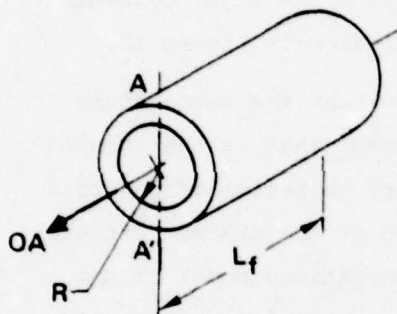
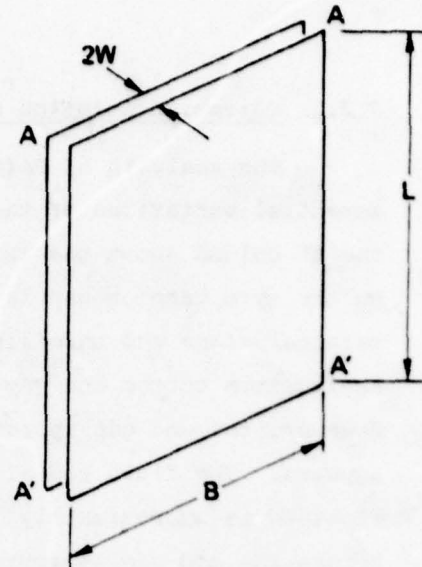
The analysis of Reference 17 assumes that there are no circumferential variations of the TD column. This is equivalent to unrolling the TD column about the axis of symmetry (see Figure 9(a)). Application to the gyro damping gap is equivalent to halving the gyro through the vertical plane and unrolling both halves about OA (see Figure 9(b)). Application to the end gap is a cruder unrolling as shown in Figure 9(c). However, the end gap approximation may not be as inaccurate as initially appears. The fluid radial temperature gradient from float rotor to float OD is approximately  $1^{\circ}\text{F}$ , whereas the axial temperature gradient across the end gap is approximately  $10^{\circ}\text{F}$ . Hence the dominant convection path travels up the float end plate and down the end housing. Only secondary convection effects, due to the radial temperature gradient, pull the dominant path in a horizontal direction. Thus the major concentration difference is developed vertically as indicated in Figure 10.

The assumptions made in Reference 17 are that the temperature dependence of  $\rho$ ,  $\mu$ , and  $D$  can be neglected, except that in the computation of the bulk convection velocity the density variation of  $\rho$  across the annulus is represented as a linear function of the assumed linear temperature gradient across the annulus. A schematized model of the convection process is used. In this model the unrolled upward moving (hotter) and the downward moving (cooler) convection streams are assumed to have equal and opposite constant mean velocities. The total transport of fluid up the annulus is thus zero. However, if the average value of  $c_1$  (say) is larger in the hotter stream than in the cooler, there will be a net transport of  $c_1$  up the tube.

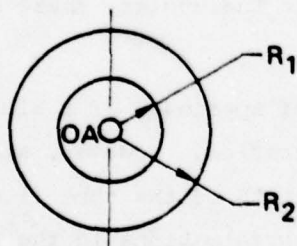
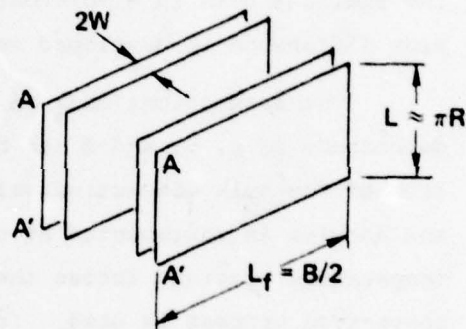
Reference 17 calculates the transport of species 1 of a binary fluid in terms of the fractional molar concentration. However, since the density  $\rho$  is assumed constant along the length of the tube (i.e., is independent of  $z$ ) then the fractional molar concentrations in the analysis of Reference 17 can be replaced by the mass fractions. Thus, from Reference 17, the transport equation for the mass fraction  $c_1$ , of species 1, in a binary fluid, is



(a) UNROLLED TD COLUMN



(b) UNROLLED TD COLUMN



(c) UNROLLED TD COLUMN

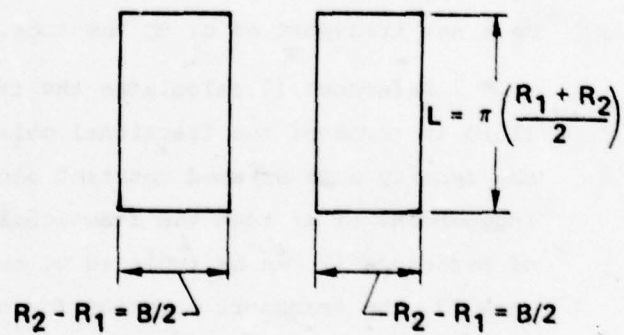
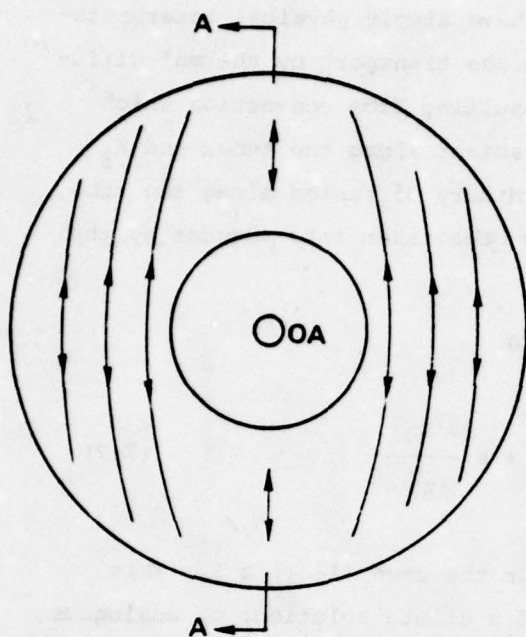
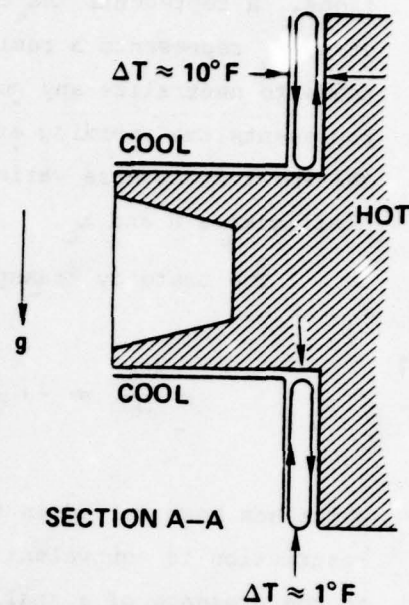


Figure 9. Application of classical TD column theory to a gyro.





(a) CONVECTION PATHS



(b) TEMPERATURE GRADIENTS

Figure 10. Convection in the end gap.

$$\tau_1 = Hc_1 (1-c_1) - K \frac{\partial c_1}{\partial z} \quad (7.2)$$

where

$$H = \frac{\alpha \beta g \rho B (2w)^3 (\Delta T)^2}{6! \mu T} \quad (7.3)$$

and

$$K = K_c + K_d \quad (7.4)$$

where

$$K_c = \frac{\beta^2 g^2 \rho B (2w)^7 (\Delta T)^2}{9! \mu^2 D} \quad (7.5)$$

and

$$K_d = B \rho D (2w) \quad (7.6)$$

and

$$c_1 = c_1(z, t)$$

The three terms  $H$ ,  $K_c$  and  $K_d$  all have simple physical interpretations.  $H$  represents the contribution to the transport by thermal diffusion,  $K_c$  represents a remixing effect resulting from convection which tends to neutralize any concentration gradient along the tube, and  $K_d$  represents the remixing effect due to ordinary diffusion along the tube. The small transverse variation of  $c_1$  has been taken into account by the coefficients  $H$  and  $K_c$ .

The unsteady transport equation is

$$m \frac{\partial c_1}{\partial t} = -H \frac{\partial}{\partial z} [c_1(1-c_1)] + K \frac{\partial^2 c_1}{\partial z^2} \quad (7.7)$$

which has been solved in Reference 17 for the case  $(1-c_1) \approx 1$ . This restriction is equivalent to the case of a dilute solution, or analogous to the presence of a small amount of contaminant in a uni-molecular fluid. The boundary conditions for Equation (7.7) are

$$c_1 = 0 \quad \text{at} \quad z = 0 \quad \text{and} \quad z = L \quad (7.8)$$

$$\text{and} \quad c_1 = Hc_{10} \quad \text{at} \quad t = 0 \quad (7.9)$$

where  $c_{10}$  is the initial constant concentration of species 1.

The steady state solution of Equation (7.7) is

$$\frac{c_1(\infty, z)}{c_{10}} = \left[ \frac{2AL}{e^{2AL} - 1} \right] e^{2Az} \quad (7.10)$$

$$\text{where} \quad A = H/2K \quad (7.11)$$

Since  $AL$  is always rather small in a gyroscope then

$$e^{2AL} \approx 1 + 2AL + 2(AL)^2 \quad (7.12)$$

Therefore, Equation (7.10) becomes for  $z = 0$  and  $z = L$  respectively

$$\frac{c_1(\infty, 0)}{c_{10}} \approx 1 - AL, \quad \frac{c_1(\infty, L)}{c_{10}} \approx 1 + AL \quad (7.13)$$

If  $c_1$  is expressed as  $c_{10} + \Delta c_1$  where  $\Delta c_1 = \Delta c_1(t, z)$  is change in concentration, then for  $z = 0$  and  $z = L$  respectively

$$\frac{\Delta c_1(\infty, 0)}{c_{10}} \approx -AL, \quad \frac{\Delta c_1(\infty, L)}{c_{10}} \approx AL \quad (7.14)$$

For small  $AL$ , the characteristic time  $t_c$  of the first mode of the solution of Equation (7.7) is shown in Reference 17 to be

$$t_c = \frac{2m}{AH \left( 1 + \pi^2 / (AL)^2 \right)} \quad (7.15)$$

In the TGG end and damping gaps  $\pi^2 / (AL)^2 \gg 1$  so that

$$t_c \approx \frac{mL^2}{(K_c + K_d) \pi^2} \quad (7.16)$$

Stipulating that  $1 - c_1 \approx 1$  is unnecessarily restrictive. If  $c_1$  is again expressed as  $c_{10} + \Delta c_1$  then Equation (7.7) becomes

$$m \frac{\partial}{\partial t} (\Delta c_1) = -H (1 - 2c_{10}) \frac{\partial}{\partial z} (\Delta c_1) + K \frac{\partial^2}{\partial z^2} (\Delta c_1) \quad (7.17)$$



where second order terms in  $\Delta c_1$  have been neglected. Equation (7.17) has the same form as Equation (7.7) apart from the first coefficient on the right hand side, and the boundary condition, Equation (7.9) now becomes

$$r_1 = Hc_{10} (1-c_{10}) \text{ at } t = 0 \quad (7.18)$$

Equation (7.17) has been solved in Appendix B using the method of References 18 and 19. The steady-state solutions for small AL at the top and bottom of the column respectively, are

$$\frac{\Delta c_1(\infty, L)}{c_{10}} \approx A (1-c_{10}) L, \quad \frac{\Delta c_1(\infty, 0)}{c_{10}} \approx -A(1-c_{10})L \quad (7.19)$$

and the time constant  $t_c$  for small AL is

$$t_c \approx \frac{mL^2}{(K_c + K_d) \pi^2} \quad (7.20)$$

which is identical to Equation (7.16).

It is no longer necessary for  $c_1$  to be small for Equations (7.19) and (7.20) (or in fact (7.16)) to hold, although the change  $\Delta c_1$  must be small enough that terms in  $(\Delta c_1)^2$  can be neglected.

Note that Equation (7.19) reverts to (7.14) for very small  $c_{10}$ .

Values of the steady-state concentration values predicted by Equation (7.14) are shown versus D in Figures 11 and 12, for the TGG damping and end gaps respectively. (The unrolled paths of Figure 9 are used in the calculations). The difference between the SG and TG end gap predictions are due to the different gap widths (SG ~ 0.020 in., TG ~ 0.025 in.). Note that Equations (7.7) and (7.14) are independent of B (the horizontal dimension). Values of  $\Delta c_1/c_{10}$  from Equation (7.19) can be found by multiplying by the factor  $(1 - c_{10})$ .

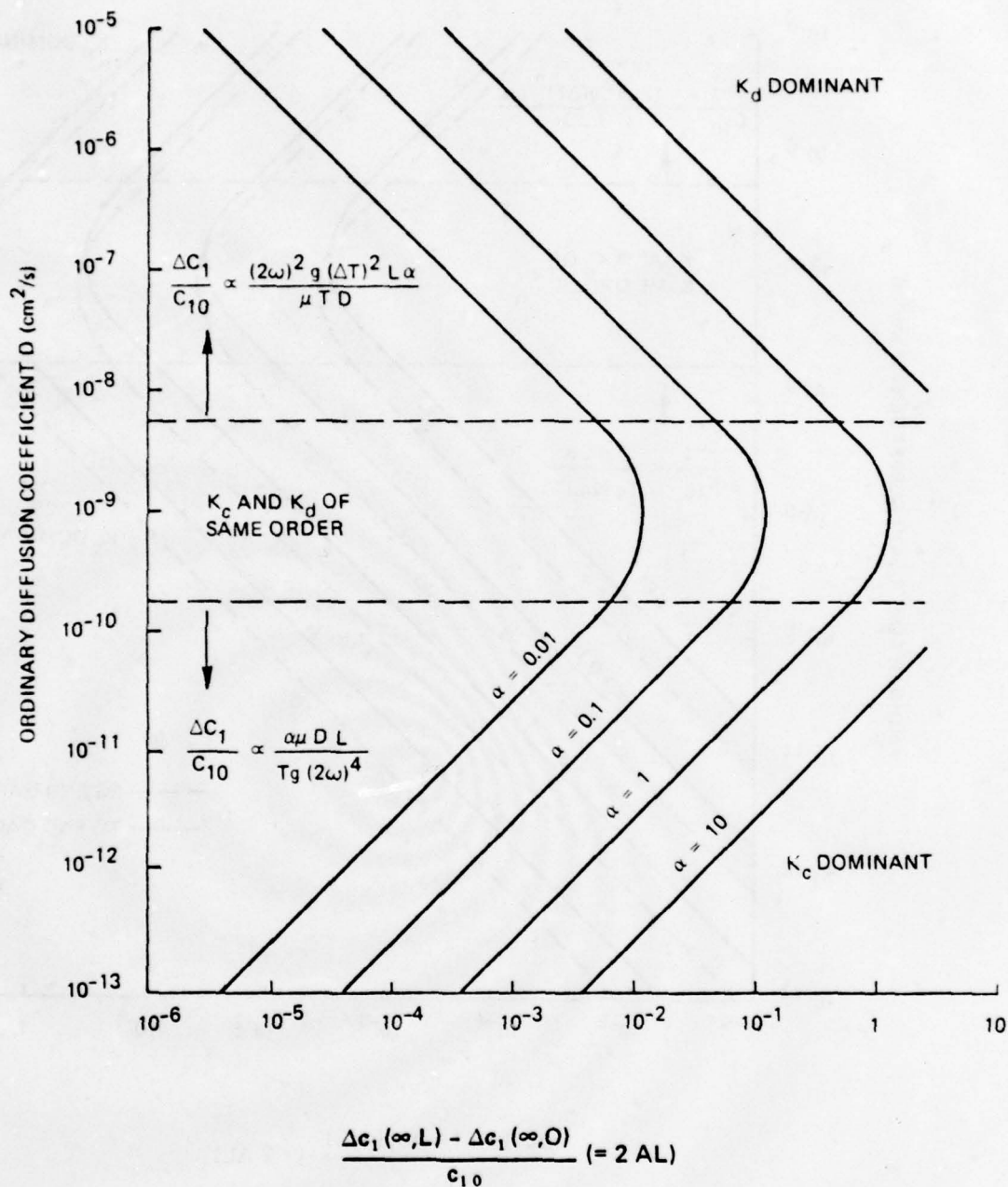
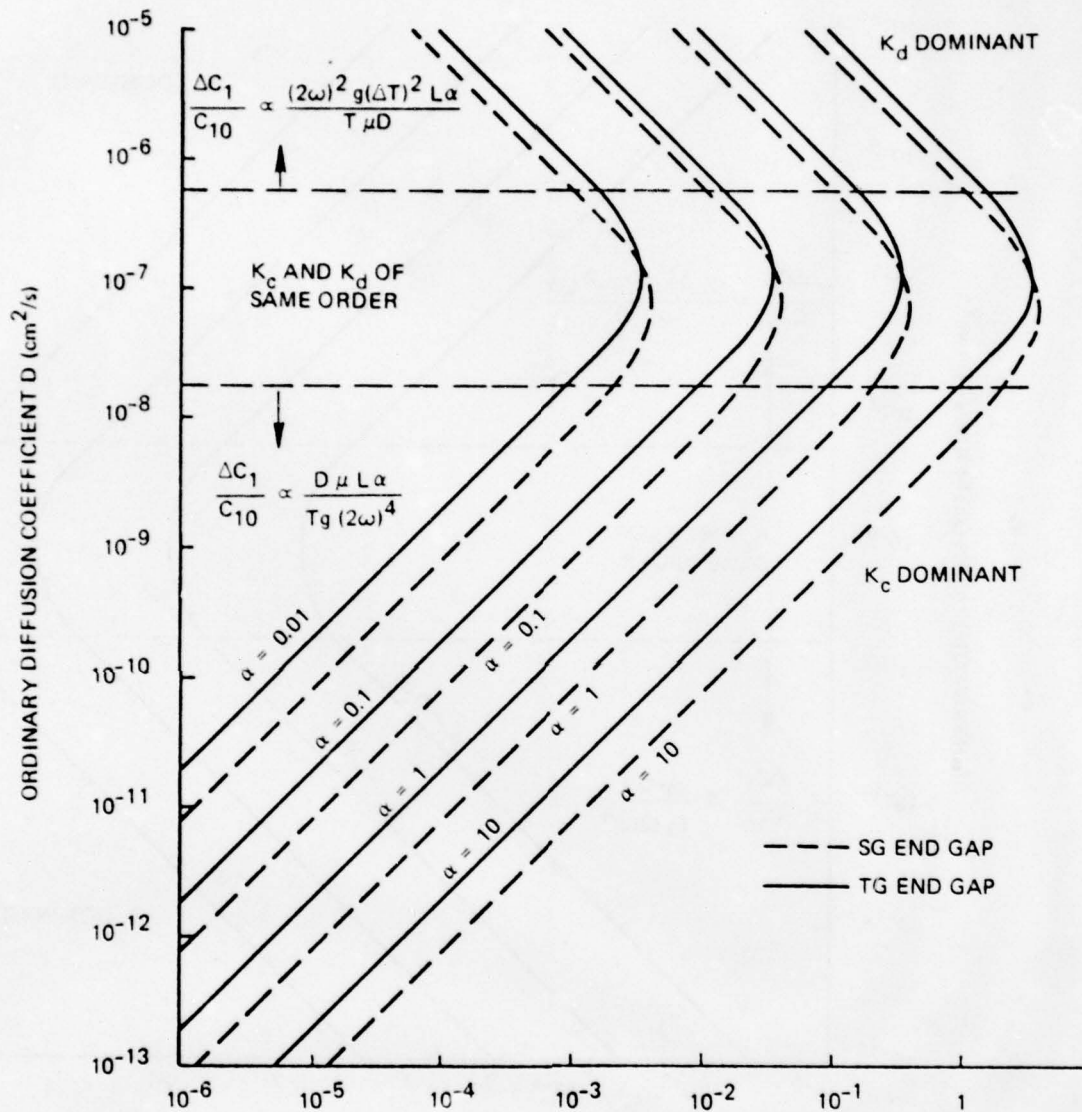


Figure 11. Steady-state concentration difference due to TGD in TGG damping gap.



$$\frac{\Delta c_1(\infty, L) - \Delta c_1(\infty, 0)}{c_{10}} (= 2 AL)$$

Figure 12. Steady-state concentration difference due to TGD in TGG end gaps.



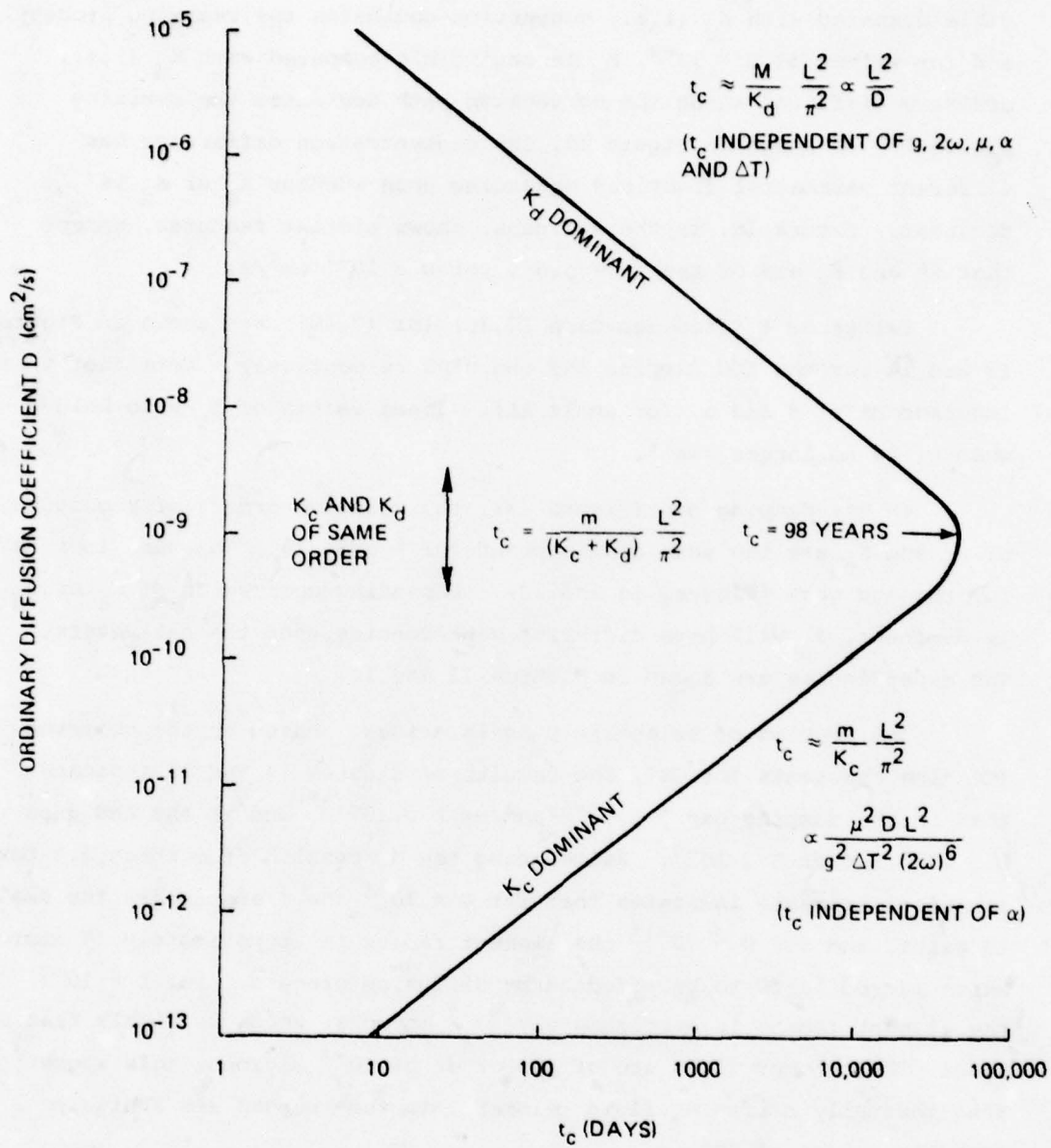
Referring to Figure 11, for values of  $D \approx 10^{-9}$  cm<sup>2</sup>/s,  $K_c$  and  $K_d$  are of the same order. However, for the values of  $D < 10^{-9}$ ,  $K_d$  is negligible compared with  $K_c$  (i.e., convection dominates the remixing process), and for values of  $D > 10^{-9}$ ,  $K_c$  is negligible compared with  $K_d$  (i.e., ordinary diffusion along the convection path dominates the remixing process). As shown in Figure 11, the concentration difference has different parametral functions depending upon whether  $K_c$  or  $K_d$  is dominant. Figure 12, in the end gaps, shows similar features, except that  $K_c$  and  $K_d$  are of the same order for  $D \approx 10^{-7}$  cm<sup>2</sup>/s.

Values of  $t_c$  from Equation (7.16) (or (7.20)) are shown in Figures 13 and 14 for the TGG damping and end gaps respectively. Note that  $t_c$  is independent of  $\beta$  and  $\alpha$  (for small AL). These values of  $t_c$  also hold when  $c_1$  is no longer small.

In the damping gap (Figure 13), the relative orders of magnitude of  $K_c$  and  $K_d$  are the same as discussed for Figure 11. The same is true for the end gaps (Figures 14 and 12). Depending upon which of  $K_c$  or  $K_d$  is dominant,  $t_c$  will have different dependencies upon the parameters. The dependencies are shown in Figures 13 and 14.

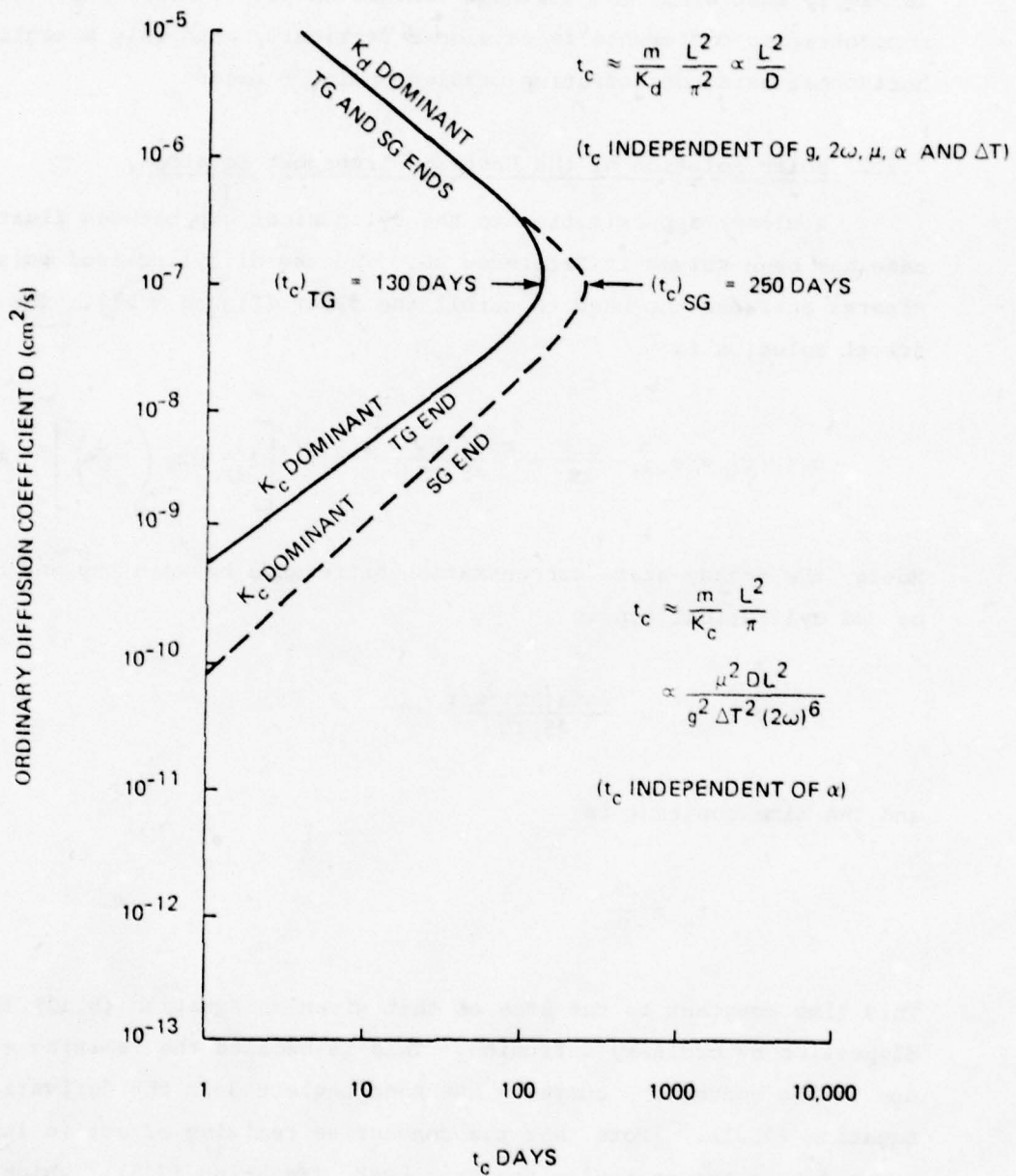
The problem of selecting  $D$  again arises. Based on the observed TGG time constants for GST, the results of Figures 14 and 15 indicate that in the damping gap  $D \approx 10^{-5}$  and/or  $D \approx 10^{-13}$ , and in the end gaps  $D \approx 10^{-5}$  and/or  $D \approx 10^{-9}$ . Reiterating the discussion of Section 5.3 for spherical elements indicates that for  $D = 10^{-5}$  the elements are too small to exist, and for  $D = 10^{-13}$  the element radius is approximately 10 microns, which is too large to be affected by diffusion process. For  $D = 10^{-9}$  the element radius is approximately  $10^{-3}$  microns, which is highly feasible. Since CTFE telomer sizes are of the order of  $10^{-3}$  microns, this suggests that thermally diffusing fluid telomers, in the end gap are a highly probable source of GST.

The discussion of the dominant convection paths in the end gap, at the beginning of this section (see Figure 10), indicates that TGD in



[EQUATIONS 7.16 AND 7.20]

Figure 13. Time constant for TGD in the TGG damping gap.



[EQUATION 7.16 and 7.20]

Figure 14. Time constant for TGD in the TGG end gaps.



the end gaps can explain the phenomenon of only vertical axis unbalance change after a  $90^\circ$  storage reorientation (see Section 2). The explanation is simply that since the dominant convection path is vertical, the major concentration difference is developed vertically with only a negligible horizontal axis concentration gradient being formed.

### 7.2.2 Polar Solution of the Unsteady Transport Equation

A closer approximation to the cylindrical gap between float and case has been solved in Reference 20. The use of cylindrical polar coordinates obviates the need to unroll the float (Figure 9(b)). The cylindrical solution is

$$c_1(\theta, t) = c_{10} - \frac{\alpha \Delta T}{Tw} + \frac{q\beta\alpha(\Delta T)^2 w^2 r}{45\mu TD} \sin \theta \left[ 1 - \exp\left(\frac{-Dt}{r^2}\right) \right] \quad (7.21)$$

Hence, the steady-state concentration difference between top and bottom of the cylindrical gap is

$$c_1(\pi/2, \infty) = \frac{2q\beta\alpha(\Delta T)^2 w^2 r}{45\mu TD} \quad (7.22)$$

and the time constant is

$$t_c = \frac{r^2}{D} \quad (7.23)$$

This time constant is the same as that given in Equation (5.11) for dispersion by ordinary diffusion. This is because the remixing effect due to the convection currents has been neglected in the derivation of Equation (7.21). (Note that the convective remixing effect is incorporated into the cartesian analysis by  $K_c$  (Equation (7.5)), which if neglected, reduces the time constants of Equation (7.16) to that of Equation (7.23)). Hence the solutions given by Equations (7.22) and

(7.23) are only valid for values of  $D$  such that remixing by ordinary diffusion dominates. The results of Section 7.2.1 indicate that this is so at the higher values of  $D$  which, by Einstein's equation, implies elements too small to exist. The polar analysis of Reference 20 may thus be unrealistic.

For  $D = 10^{-7}$ , Equation (7.22) predicts steady-state concentration differences of  $2.74 \alpha \times 10^{-1}$ ,  $5.4 \alpha$ , and  $8.4 \alpha$  in the damping, SG, and TG end gaps respectively, and Equation (7.23) predicts time constants of 590 days and 370 days in the damping and end gaps respectively.

### 7.2.3 Additional Comments on TGD

An indication of the likely significance of TGD can be determined from the height  $h$ , an element travels along the convection path, while thermally diffusing in the direction of the temperature gradient. Using the average convection fluid velocity  $\bar{v}$  resulting from the linear temperature gradient  $\Delta T$  across the gap

$$\bar{v} = \frac{8\alpha g w^3 \Delta T}{24\mu} \quad (7.24)$$

then  $h$  is given in Reference 21 by

$$h = \frac{8\alpha g w^4}{24\mu D_T} \quad (7.25)$$

If thermal diffusion is slow compared with convection then  $h$  will be large compared with the total height of the convection path, so that TGD will be unlikely to produce a density gradient (Figure 15(a)). However, if thermal diffusion is fast compared with convection then  $h$  is small compared with the convection path height. Hence the enrichment and depletion of elements in the convection streams can occur, and TGD can produce a density gradient (Figure 15(b)).

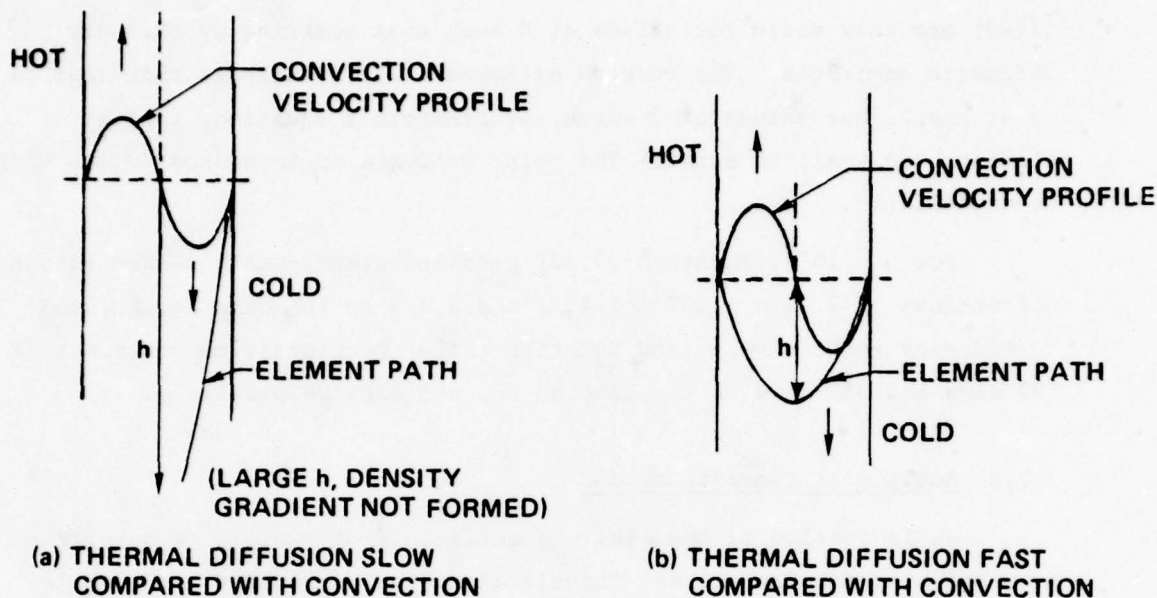


Figure 15. Relative importance of thermal diffusion and convection.

Knowledge of the thermal diffusion factor  $D_T$  is required for accurate calculation of  $h$ . In the TGG values of  $h$  less than the convection path height ( $\approx 6$  cm) occur for  $D_T > 7.1 \times 10^{-13} \text{ cm}^2/(\text{s}^\circ\text{F})$  in the damping gap, and  $D_T > 1.8 \times 10^{-10} \text{ cm}^2/(\text{s}^\circ\text{F})$  in the end gap. Values of  $D_T$  are expected to be well in the range where TGD is important. More generally, the fact that viscosity is in the denominator of Equation (7.25) implies that effective separation is extremely likely in high viscosity fluids, such as CTFE.

If effective separation is feasible, it is interesting to note that concentration gradient increase initially as the square root of the time (see Reference 17). This means that for a time-to-bound of 100 days, a period of operation as short as 1 day will have produced one tenth of the equilibrium concentration difference. Furthermore, this initial rise is independent of the column length, since the rapid increase in the concentration difference occurs only over a small length near each end. Torques arising from bulk fluid motion may be significant well before the equilibrium concentration difference has been attained.



### 7.3 CONCLUDING REMARKS ON TGD MODELING

The application of classical thermal diffusion column theory to the gyroscope introduces approximations of geometry and fluid constituent simplification. The errors arising from these approximations are uncertain. However, a general indication of the effects of TGD and order of magnitude predictions can be expected. The primary prediction uncertainty is the lack of known values for the diffusion coefficient  $D$  and factor  $\alpha$ . It is not possible to determine accurate values of  $D$  and  $\alpha$  for multicomponent fluids, so that reasonable estimates must be used. TGD does satisfy all the signature characteristics (Section 2) of GST where applicable. TGD is not applicable to characteristics 4 and 5 since centrifuging is performed with wheel-off, so that a temperature gradient does not exist.

The theory presented above is restricted to solutions for a very small concentration level (Equations (7.14) and (7.16)), or for a very small concentration change (Equations (7.19) and (7.20)). An extension of the theory to unrestricted concentration levels and differences (binary fluid) has been developed using a finite difference and matrix exponential numerical solution of Equation (7.7). Preliminary results concerning the concentration change with time after a  $180^\circ$  reorientation were presented in Reference 7. This analysis is being incorporated into a more complete numerical model including time dependent bulk mass transport.

It should be noted that in certain cases, where similarity of molecular masses occurs, it is possible for the heavier molecules to thermally diffuse into the warm upward moving convection stream, and for lighter ones to diffuse into the colder stream. Initially then, the heavier molecules collect above the lighter ones. This is unstable and eventually the flow direction is reversed so that the heavier molecules finally collect at the bottom. This behavior is termed the forgotten

effect. The forgotten effect is discernible in a thermal diffusion column, but modeling its effect in a gyro is complicated, and has not yet been attempted.

## SECTION 8

### CONCLUSIONS AND RECOMMENDATIONS

#### 8.1 CONCLUSIONS

The analyses performed herein indicate that the CTFE or BTFE telomers and/or contaminants are highly probable candidates for the source of Gravity Sensitive Trending (GST). The analyses are based on the continuity, Navier-Stokes, diffusion, and constitutive relations for a two component fluid. The two component assumption, the omission of flocculation and electric charge effects, the uncertainty in present knowledge of diffusion coefficients for the flotation fluids, difficulty in modeling the transition from sedimentation to precipitation, and the simplifications required to obtain closed form solutions limit the quantitative accuracy of the results, but should permit order of magnitude estimation.

Sedimentation of contaminants and of fluid components within the fluid and thermogravitational diffusion (TGD) can establish density variations and transfer the position of effective mass unbalances. As summarized in Table 6 which tabulates the applicability of various models in describing observed phenomena, sedimentation can explain many of the experimental observations. Also, CTFE has been observed to sediment and separate in bottled samples and in glass slides, and to flocculate at operating temperatures.



Table 6. Applicability of speculated mechanisms.

Speculated Mechanism Observable Signature Characteristic	Sedimenting Contaminants	TGD	Bulk Flow Models	
			Linear Density Gradient	Migrating Mass Model
Unbalance alignment with $g$	Yes	Yes	Yes	Yes
180° storage reorientation	Yes	Yes	No	No
90° storage reorientation				
Vertical axis unbalance change only	End gap	End gap	No	Possibly
Vertical and horizontal axes unbalance change	Yes	Yes	Horizontal axis bound magnitude only	Yes
Unbalance independent of $g$	Yes	NA*	Yes	Yes
Time-to-bound proportional to $g^{-1}$	Yes	NA*	Yes	Yes
Time-to-bound independent of unbalance	Yes	Yes	No	No
Comments	Highly Probable	Likely to be significant	Time-to-bound depends upon unbalance. Poor correlation with observed time-to-bound.	

\* Requires temperature gradient for model.

Calculations of time constants and comparisons with the thermal diffusion column indicate that TGD is occurring in the end regions of the gyro rather than in the annulus. Because of the narrower gap in the annulus, convective remixing is less important than in the end regions, the effect which accounts for the different time constants.

Bulk flow of the fluid produces the GST torques which are sensed by the float and transfers the effective mass position. If a density gradient exists, specific force will cause the fluid to flow. The resulting shear causes the torques sensed by the gyroscope which are interpreted as GST. Early models (both phenomena understanding and system evaluation) of GST focused upon this bulk fluid motion and are reflected by two entries in Table 6, which assume density distributions without considering their origins and proceed to solve the Navier-Stokes and fluid continuity equations. Assuming that the effective mass is not near the top of the float, and that the effective mass results in an unbalance change of 1 meru (zero to peak) results in time constants of 27 days for the ends and 833 days for the cylindrical annulus. These time constants emphasize the importance of the previously neglected end regions. Because of the complicated flow patterns which are expected when the effective mass is near the top of the float, the simple models such as the linear density gradient and the migrating mass unbalance must be modified to describe the 180 degree storage reversal.

Ordinary diffusion homogenizes the fluid because of the random motion of the particles. If bulk motion is neglected, the time required for a particle to diffuse across the float is very long because of the high fluid viscosity. With bulk motion, diffusion is important because the particle must only cross the damping gap rather than the float, a possible explanation of the success of PIGA centrifuging.

The discussed cases and the experimental observations indicate that several signatures with widely different time constants are possible and are observed. The numerous phenomena and their dependence on prior histories make the use of simple models such as the single mass models of References 1 through 3 and 8 through 10 tenuous for evaluating system performance (evaluation implies use in a simulation). Because of the distributed nature of the sedimentation and the complex gyro float-to-case geometry, it is unlikely that GST can be modeled and compensated in system use.

The conclusion that multiple telomers and/or contamination cause GST has been strengthened by performance improvements in TGGs, in the Pendulous Integrating Gyroscopic Accelerometers (PIGAs) at CSDL, and in CSDL's gravity gradiometer. The importance of liquid and solid contaminants has been strengthened by slide observations at CSDL while the contribution of dissolved gases is considered small because of considerations of float gas leakage (see Reference 24).

Northrop Precision Products Division (PPD) has filled a TGG with a narrow cut of CTFE obtained by distillation of the original fluid which had been used in other TGGs. In GST testing in a 1-gravity field, this unit has shown one to two orders of magnitude improvement over previous units.

CSDL has constructed and tested several PIGAs which have demonstrated very low trending in absolute terms and when converted to the larger TGG float size and angular momentum. The PIG (Pendulous Integrating Gyro) is filled with BTFE, a multiple telomer which is considered similar to CTFE because of its polytelomeric nature. The improved performance of this device is attributed to the great care given to cleaning and qualifying the gyro parts and fill apparatus used in the PIG construction.



The fact that PIGs were improved by cleaning and TGGs by fluid change underline the contributions of at least two mechanisms to GST.

At CSDL, improvements in the gravity gradiometer trending were realized by improved cleaning and inspection (see Reference 25). The gradiometer is filled with monomolecular Freon (with the exception of isotopes) which also reduces the opportunity of contamination since the Freon is also used as a final cleaning agent.

As described in Section 5, contaminants can affect GST differently depending on whether they are true, partial, or nonsedimenters. A qualitative test was run in which liquid contaminants such as Freon, acetone, water, food-colored water, trichloroethane, and hydrocarbons were dropped between glass slides separated by 0.010 inch and filled with CTFE, the TGG fill fluid. Since CTFE becomes waxy at room temperature, a microscope and nearly cross-polarized light could be used to observe the contaminant migration. In storage at room and gyro operating temperatures, the contaminants were observed to sediment with little diffusion; thus, these contaminants could be classified as true sedimenters and are suspected GST candidates. Contaminants in significant quantities are measured in instrument fill and teardown samples.

The hydrogen and helium which fill the gyro floats have been measured to leak at substantial rates (see Reference 24). The fact that PIGAs and narrow-cut TGGs show only small GST in the presence of the gases indicates that certain gases can be classified as nonsedimenting or easily diffusing. Thus, one may conclude that testing must be performed (see Section 8.2, Recommendations) to categorize a fluid and possible contaminants to establish acceptable limits for contaminants.

## 8.2 RECOMMENDATIONS

Based on the aforementioned analysis and conclusions, the following are recommended or have been implemented:

- (1) Continue testing and build of TGGs filled with narrow cut fluid. One unit has been extensively tested for GST. Additional units should be constructed and tested to expand the data base and improve confidence.
- (2) Distillation fill MX units with monomolecular fluid. The monomolecular fluid should reduce fluid effects below those of the narrow cut fluid. Because selective evaporation does not affect the mono-fluid, distillation fills which could reduce the quantity of contamination are feasible. A candidate fluid T-17<sup>-2</sup> has been synthesized at CSDL, and an MX-TGG fill is planned for July 1979. A 25 IRIG filled with another monomolecular fluid has performed well (see References 23 and 26); however, the inherent limitations of that family of gyros does not permit extrapolation to TGG performance levels.
- (3) Tests should be performed to pinpoint the fluid or float as the GST source. The analyses of Sections 3 through 7 indicate that the fluid or its contaminants are probable candidates. Furthermore, because the assembly induced stresses are much higher than the gravity induced stresses and because the gravity independent unbalance ramps are small, deformation of the float structure has been discounted as a GST source. This fact should be experimentally verified. Reference 1 describes 25 IRIG testing where the unit was stored at different temperatures. At low temperatures, little trending was observed. Because all the fluid GST models depend on viscosity (which is more dependent on temperature than the float structural parameters), the trending was attributed to the fluid or an effect exterior to the float. Preliminary testing indicates that this conclusion holds for TGGs.

Although the temperature storage has greatly reduced concern over the float interior being the principal GST source, PPD will add confidence by conducting float pumping tests in July 1979. A previously characterized TGG will be stationed with the output axis horizontal. By switching the suspension capacitors, the float will be driven in a circular orbit about the nominal case center. The float revolution will force fluid across the float in several hours (per PPD and CSDL calculations). If unbalance changes significantly because of the pumping, one can conclude that the fluid or contaminants therein are GST causes.

- (4) TGD should be evaluated by centrifuge testing. Since the predicted unbalance resulting from TGD may be proportional to or inversely proportional to  $g$ , depending on  $D$  (see Figures 11 and 12), centrifuge testing could clarify the contribution of TGD to GST. These results would strengthen any conclusion gained from the narrow cut and monomolecular fills. Centrifuging might also permit long time constant effects to be observed. Centrifuge tests are planned at CSDL and CIGTF for summer 1979.
- (5) Test the sensitivity of GST to temperature difference across the fluid gap. The temperature difference across the gap is an important driver in the diffusion column theory. As in item 4 above, results could identify the role of TGD in GST and would reinforce any conclusions from the instrument fills.
- (6) Models used for system evaluation should reflect the multiple GST effects. Models which result in only a single time constant appear inadequate. A model which superimposes that of Figure 4 (see Reference 10) upon a viscoelastic model where mass is the only permitted motion along gravity is recommended.



- (7) Employ vial testing to expand quantitatively the slide tests. As deduced in the conclusions, and in Section 5, contaminants of different masses will have different GST effects depending on their classification as true, partial, or nonsedimenters. An air bearing torque tester is being used to measure the torque versus time for vials filled with gyro fluids and known large (5000 ppm) amounts of contamination (see Reference 1 and Section 5). These tests will determine the required in situ cleanliness of flotation fluids.
- (8) Perform more detailed simulation. In Section 3, the governing equations are listed. Subsequent sections made simplifying assumptions so that subsets of the original equations were solved. Diffusion, TGD, bulk fluid motion, and particularly sedimentation should be studied in greater detail in simulations which reflect the actual gyroscope geometry.
- (9) Investigate possible fast transients from sedimentation. While sedimentation and bulk flow models describe the long (10 days and longer) decay time for GST, these models also predict faster phenomena with 10-minute to 1-hour decay times. The more rapid transients result because of the short distance between the float and case. Experimental investigation of fast transients should be undertaken for the following reasons:
- (a) Verification or denial of sedimentation models;
  - (b) Possible explanation of previously unexplained gyro behavior; and
  - (c) Performance improvement.

## APPENDIX A

### ONE DIMENSIONAL UNSTEADY PARTIAL SEDIMENTATION

The mass transfer equations of Section 3 are solved with the following assumptions:

- (1) The mass transfer is one dimensional (along x).
- (2) Thermal diffusion and bulk flow may be neglected.
- (3) The weight fraction variations are small.

The mass transfer is then governed by the phenomenological diffusion equation

$$J_x = -\rho D \left[ \frac{\partial c_1}{\partial x} + s c_1 \frac{\partial p}{\partial x} \right] \quad (A.1)$$

where:  $J_x$  = mass flow in x direction

$\rho$  = density

$c_1$  = mass fraction of component 1

$D$  = diffusion coefficient

$s$  = sedimentation coefficient

$\frac{\partial p}{\partial x}$  = pressure gradient in x direction

With no bulk fluid motion and little density variation along the x axis,  $\frac{\partial p}{\partial x}$  and  $s c_1 \frac{\partial p}{\partial x}$  can be regarded as constants. Continuity for component 1 results in:

$$\rho \frac{\partial c_1}{\partial t} = - \frac{\partial J_x}{\partial x} = \rho D \frac{\partial^2 c}{\partial x^2} \quad (\text{A.2})$$

The boundary conditions are:

$$J_x = 0 \quad \text{at} \quad x = \pm L/2$$

$$\int c_1 dx = L c_{\text{ave}} \quad (\text{A.3})$$

At steady-state,  $J_x = 0$  gives

$$c_1 - c_{\text{ave}} = -k_x \quad (\text{A.4})$$

where:  $k = \rho D \frac{\partial c}{\partial x}$

$c_{\text{ave}}$  = average mass fraction

Let the mass fraction be given by:

$$c_1(x,t) - c_{\text{ave}} = \sum_{n=1}^{\infty} C_n \sin \frac{n\pi x}{L} e^{s_n t} - k_x \quad (\text{A.5})$$

where the coefficients  $C_n$  and  $s_n$  will be determined.

The solution Equation (A.5) satisfies the boundary conditions Equation (A.3) for all  $s_n$  and  $C_n$ .

Substitution of Equation (A.5) into Equation (A.2) gives:

$$s_n = -D \left( \frac{n\pi}{L} \right)^2$$

which is the time constant for ordinary diffusion.



For time zero, Equation (A-5) may be written as:

$$c_1(x,0) - c_{ave} + k_x = \sum_{n=1}^{\infty} \sin \frac{n\pi x}{L} C_n \quad (A.6)$$

where  $c_1(x,0)$  is the initial mass fraction distribution.

Multiply both sides of Equation (A.6) by  $\sin n\pi x/L$ , integrate from  $-\frac{L}{2}$  to  $+\frac{L}{2}$ , and invoke orthogonality to obtain the solution

$$c_1(x,t) - c_{ave} = \sum_{n=1}^{\infty} C_n \sin \frac{n\pi x}{L} e^{s_n t} - c_{ave} \frac{\partial p}{\partial x} x \quad (A.7)$$

where:  $s_n = -D \left(\frac{n\pi}{L}\right)^2$

$$C_n = \frac{2}{L} \int_{-L/2}^{L/2} (c_1(x,0) - c_{ave}) \sin \frac{n\pi x}{L} dx$$

where:  $c_1(x,0) - c_{ave}$  is assumed to be representable by Fourier sine series.

## APPENDIX B

### SOLUTION OF UNSTEADY TRANSPORT EQUATION

WHEN  $1 - c_1 \neq 1$

The transport equation for species 1 of a binary fluid is Equation (7.2)

$$\tau_1 = Hc_1(1-c_1) - k \frac{\partial c_1}{\partial z} \quad (\text{B.1})$$

If  $c_1 = c_{10} + \Delta c_1$ , then ignoring terms in  $\Delta c_1^2$

$$\tau_1 = Hc_{10}(1-c_{10}) + H\Delta c_1(1-2c_{10}) - k \frac{\partial(\Delta c_1)}{\partial z} \quad (\text{B.2})$$

The unsteady transport equation for species 1 is Equation (7.7)

$$m \frac{\partial c_1}{\partial t} = -H \frac{\partial}{\partial z} [c(1-c_1)] + K \frac{\partial^2 c_1}{\partial z^2} \quad (\text{B.3})$$

Again writing  $c_1 = c_{10} + \Delta c_1$  and ignoring terms in  $\Delta c_1^2$ , Equation (B.3) becomes

$$m \frac{\partial(\Delta c_1)}{\partial t} = -H(1-2c_{10}) \frac{\partial(\Delta c_1)}{\partial z} + K \frac{\partial^2(\Delta c_1)}{\partial z^2} \quad (\text{B.4})$$

Equation (B.4) has to be solved under the boundary conditions

$$\tau_1 = 0 \text{ at } z = 0 \text{ and } z = L \quad (\text{B.5})$$

and from equation (B.2)

$$\tau_1 = Hc_{10}(1-c_{10}) \text{ at } t = 0 \quad (\text{B.6})$$

Since  $K = H/2A$  (Equation (7.11)), Equation (B.4) can be written

$$m \frac{\partial(\Delta c_1)}{\partial t} = -H(1-2c_{10}) \left[ \frac{\partial(\Delta c_1)}{\partial z} - \frac{1}{2A(1-2c_{10})} \frac{\partial^2(\Delta c_1)}{\partial z^2} \right] \quad (\text{B.7})$$

Conservation of species 1 requires that

$$m \frac{\partial(c_{10} + \Delta c_1)}{\partial t} = - \frac{\partial \tau_1}{\partial z} \quad (\text{B.8})$$

$$m \frac{\partial(\Delta c_1)}{\partial t} = - \frac{\partial \tau_1}{\partial z} \quad (\text{B.9})$$

Differentiating Equation (B.2) with respect to time gives

$$m \frac{\partial \tau_1}{\partial t} = mH(1-2c_{10}) \frac{\partial(\Delta c_1)}{\partial t} - mK \frac{\partial}{\partial t} \frac{\partial(\Delta c_1)}{\partial z} \quad (\text{B.10})$$

Using Equation (B.9)

$$m \frac{\partial \tau_1}{\partial t} = -H(1-2c_{10}) \frac{\partial \tau_1}{\partial z} + K \frac{\partial}{\partial t} \frac{\partial \tau_1}{\partial z} \quad (\text{B.11})$$

or

$$m \frac{\partial \tau_1}{\partial t} = -H(1-2c_{10}) \left[ \frac{\partial \tau_1}{\partial z} - \frac{1}{2A(1-2c_{10})} \frac{\partial^2 \tau_1}{\partial z^2} \right] \quad (\text{B.12})$$



Note that Equation (B.12) for  $\tau_1$  is the same as Equation (B.7) for  $\Delta c_1$ . It is thus simplest to follow Bardeen's method (References 18 and 19), and solve firstly for  $\tau_1$  as a function of  $z$  and  $t$ .

Since Equation (B.12) differs from Bardeen's equation only in the constant coefficients, the particular solution of Equation (B.12) satisfying boundary condition (B.5) can be immediately written down from Bardeen's solution

$$\tau_1^{(n)} = \sin \frac{n\pi z}{L} \exp \left[ A(1-2c_{10})z - \frac{AH(1-2c_{10})^2}{2m} \left( 1 + \frac{n^2\pi^2}{A^2(1-2c_{10})^2L^2} \right) t \right] \quad (B.13)$$

where  $n$  is a positive integer and

$$\tau_1 = \sum a_n \tau_1^{(n)} \quad (B.14)$$

Using boundary condition (B.6) at  $t = 0$  then Equation (B.14) gives

$$Hc_{10}(1-c_{10}) = e^{\frac{A(1-2c_{10})z}{2m}} \sum a_n \sin \left( \frac{n\pi z}{L} \right) \quad (B.15)$$

The Fourier coefficient  $a_n$  can thus be determined from

$$a_n = \frac{2Hc_{10}(1-c_{10})}{L} \int_0^L e^{-\frac{A(1-2c_{10})z}{2m}} \sin \left( \frac{n\pi z}{L} \right) dz \quad (B.16)$$

$$= \frac{2n\pi Hc_{10}(1-c_{10})}{A^2(1-2c_{10})^2L^2} \left[ \frac{1 - (-1)^n e^{-\frac{A(1-2c_{10})L}{2m}}}{1 + n^2\pi^2/A^2(1-2c_{10})^2L^2} \right] \quad (B.17)$$

The expression for  $\Delta c_1$  consists of a steady-state equilibrium concentration and a transient term. The equilibrium term is of the form

$$\Delta c_1^{(e)} = P e^{\frac{2A(1-2c_{10})z}{L}} + Q \quad (B.18)$$

where  $P$  and  $Q$  are constants which may be determined from mass conservation

$$\int_0^L \Delta c_1^{(e)} dz = 0 = \int_0^L \left( P e^{\frac{2A(1-2c_{10})z}{L}} + Q \right) dz \quad (B.19)$$

or

$$QL = \frac{P}{2A(1-2c_{10})} \left[ 1 - e^{\frac{2A(1-2c_{10})L}{L}} \right] \quad (B.20)$$

and from Equation (B.2) using boundary condition (B.5) at  $t = 0$

$$Hc_{10}(1-c_{10}) + H(1-2c_{10})(P+Q) - KP2A(1-2c_{10}) = 0 \quad (B.21)$$

$$Q = \frac{-c_{10}(1-c_{10})}{1-2c_{10}} \quad (B.22)$$

Therefore using (B.20)

$$P = \frac{2AL c_{10}(1-c_{10})}{e^{\frac{2A(1-2c_{10})L}{L}} - 1} \quad (B.23)$$

The transient term for  $\Delta c_1$  can be obtained from Equations (B.9) and (B.14). The final expression for  $\Delta c_1$  is identical to Bardeen's solution except for the constant coefficients, so that the time constant for equilibrium  $t_c$  is obtained from the last term in Equation (B.13) with  $n = 1$

$$t_c = \left[ \frac{AH(1-2c_{10})^2}{2m} \left( 1 + \frac{\pi^2}{A^2(1-2c_{10})^2 L^2} \right) \right]^{-1} \quad (B.24)$$

Since AL is always small in a gyroscope then

$$\frac{\pi^2}{A^2(1-2c_{10})^2 L^2} \gg 1 \quad (B.25)$$

so that

$$t_c = 2m \frac{A}{H} \frac{L^2}{\pi^2} \quad (B.26)$$

$$= \frac{mL^2}{(K_c + K_d) \pi^2} \quad (B.27)$$

Using (B.18), (B.22) and (B.23) the equilibrium concentration change is

$$\Delta c_1(\infty, z) = \left[ \frac{2AL c_{10}(1-c_{10})}{2A(1-2c_{10})L} e^{2A(1-2c_{10})z} - \frac{c_{10}(1-c_{10})}{1-2c_{10}} \right] \quad (B.28)$$

For small AL Equation (B.28) can be expanded retaining first order terms in AL, so that for  $z = L$  and  $z = 0$  respectively

$$\Delta c_1(\infty, L) = AL(1-c_{10}), \quad \Delta c_1(\infty, 0) = -AL(1-c_{10}) \quad (B.29)$$

Therefore, the equilibrium concentration difference from top to bottom is

$$\frac{\Delta c_1(\infty, L) - \Delta c_1(\infty, 0)}{c_{10}} = 2AL (1-c_{10}) \quad (B.30)$$



# NOMENCLATURE

$\alpha$	Thermal diffusion factor (dimensionless)
$a$	Radius of spherical element (cm)
$\beta$	Temperature coefficient of density ( $\text{gm}/(\text{cm}^3\text{-}^\circ\text{F})$ )
$B$	Length (cm)
$c$	Fractional mass concentration (dimensionless)
$D$	Coefficient of ordinary diffusion ( $\text{cm}^2/\text{s}$ )
$D_T$	Coefficient of thermal diffusion ( $\text{cm}^2/(\text{s-}^\circ\text{F})$ )
$f$	Frictional coefficient ( $\text{gm}/\text{s}$ )
$g$	Acceleration due to gravity ( $\text{cm}/\text{s}^2$ )
$h$	Maximum height travelled during thermal diffusion process (cm)
$J$	Mass flux relative to barycentric coordinates ( $\text{gm}/(\text{cm}^2\text{-s})$ )
$k$	Spring constant ( $\text{gm}/\text{s}^2$ )
$\theta$	Angle (rads)
$\mu$	Viscosity ( $\text{gm}/(\text{cm-s})$ )
$m$	Mass per unit length ( $\text{gm}/\text{cm}$ ) = $\rho_2 w_B$
$M_{VD}$	Viscous drag torque (dyn-cm)
$N$	Avogadro's Number ( $6.02 \times 10^{23}/\text{gm-mole}$ )
$\rho$	Density ( $\text{gm}/\text{cm}^3$ )

# NOMENCLATURE (Continued)

$\Delta\rho$	Density difference between top and bottom of density gradient ( $\text{gm}/\text{cm}^3$ )
R	Universal gas constant ( $8.31 \times 10^7 \text{ gm}\cdot\text{cm}^2/(\text{s}^2\cdot\text{K}\cdot\text{mol})$ )
r	Radius (cm)
s	Sedimentation coefficient ( $\text{cm}/(\text{s}^2\cdot\text{cm})$ )
$t_c$	Characteristic time (s)
T	Mean fluid temperature ( $^{\circ}\text{F}$ )
$\Delta T$	Temperature gradient across fluid gap ( $^{\circ}\text{F}$ )
$\tau$	Net transport ( $\text{gm}/\text{s}$ )
2w	Damping gap width (cm)
$\bar{v}$	Average fluid velocity ( $\text{cm}/\text{s}$ )
V	Volume ( $\text{cm}^3$ )
x	Distance (cm)
z	Vertical distance (cm)

## Subscripts

0	Initial
1	Species 1
2	Species 2
p	Element (contaminant or fluid constituent)

Underline denotes vector e.g.  $\underline{J}$

#### REFERENCES

1. Aronson, J., and P. Steranka, Preliminary Findings in HSS Investigation, The Charles Stark Draper Laboratory, Inc. (CSDL) Report R-801, February 1974.
2. Aronson, J., J. Miola, and P. Steranka, Storage Sensitivity Test Using TGG 221X, CSDL Report C-4026, January 1974.
3. Miola, J., P. Steranka, C. Kochakian, and B. Noyes, IR&D Task Accelerometer and Gyro Modeling Interim Report April through December 1975, CSDL Report C-4593, September 1976.
4. Weinberg, M., Proposed Analysis of Hot Storage Sensitivity, CSDL Component Development Department (CDD) Memorandum No. 30H-77-345, September 1977.
5. Publicover J., and G. Ciacco, 25 IRIG Mod 3 Hot Storage Sensitivity Study. Summary of Calculations on Gyro Error Torques Produced by Flotation Fluid Stratification: 1) Viscous Drag Effects; 2) Buoyancy Force Effects, FBM Inertial Components Memorandum Serial No. JP-76, June 1970.
6. Steranka, P., HSS Progress Report, CDD Memorandum 30K-75-024, January 1975.
7. Barbour, N. and M. Weinberg, Predicted Signatures of Storage Sensitivity in Floated Gyros: A Review, CSDL Report P-660, May 1978.



REFERENCES (Continued)

8. Wilkinson, R.H., A Possible Model of Long-Term g-Dependent Transients in Gyros (Hot Storage), CSDL Report C-4248, November 1974.
9. Weinberg, M., Reply to L. Schnee on Proposed HSS Tests, CDD Memorandum No, 30H-77-427, December 1977.
10. Sargent, D., Augmenting the AIRS Error Model, TRW Interoffice Correspondence, 6435 3-78-0007, January 1978.
11. Barbour, N., and P. Steranka, Discussion of g-Sensitive Trending Caused by Sedimenting Contaminants in the Damping Gap, CSDL Report C-5115, September 1978.
12. Daniels, F., and R. Alberty, Physical Chemistry, Wiley and Sons, 1967.
13. Mondshein, L., and P. Steranka, FGII Baseline Slides, CDD Memorandum 30K-78-017, January 1978.
14. Shaw, D.J., Introduction to Colloid and Surface Chemistry, Butterworth and Co. Ltd., London, 1970.
15. Castleman, W., Hot Storage Sensitivity, Honeywell Avionics Division, 1977.
16. 16 PM PIP HSS Centrifuge Test Results, HI-TCL-491, Honeywell Incorporated, July 1973 (Confidential).
17. Jones, R.C. and W.H. Furry, The Separation of Isotopes by Thermal Diffusion, Reviews of Modern Physics, 18, No. 2, April 1946.
18. Bardeen, J., Concentration of Isotopes by Thermal Diffusion: Rate Of Approach to Equilibrium, Physical Review, 57, January 1970.
19. Bardeen, J., Concentration of Isotopes by Thermal Diffusion: Rate of Approach to Equilibrium, Physical Review, 58, 1940.

REFERENCES (Continued)

20. Lewellen, W.S., Analytic Solution for Fluid Stratification in a Gyroscope, Aerospace Corporation Report, TDR-669 (9210-01)-1, December 1965.
21. Rockower, B., Improvements in Brominated Damping Fluids to Reduce Their Thermal Diffusion Susceptibility, MIT Instrumentation Laboratory, Report E-1702, December 1964.
22. Krawczyk, F., Disassembly Report of PPD MPMS/TGG Units Nos. 0002, 0003, 0006, 0008 and 0010, CSDL Report C-4639, April 1976.
23. Weinberg, M., Minutes of T-11 25 IRIG Review (17 October) and Trend Team Meeting (14 October), CSDL Memorandum 30H-78-348, October 1978.
24. Weinberg, M., Analysis of Float Gas Leakage in TGG and IAP/PIGA, CSDL Memorandum 304-79-166, May 14, 1979.
25. Harlan, R.S., M. Trageser, and M. Gerber, Gravity Gradiometer Flotation Fluid Contamination Effects, CSDL Report R-1247, April 1979.
26. Dopico, J., Gyro Fill Study; Interim Report on HSS Tests Performed on Modified 25 IRIG Mod 3 Instruments Filled With Special Fluids, CSDL Memorandum 30K-74-090, March 8, 1979.

TITLE:       CENTRIFUGE TESTING  
              OF A LASER GYRO,  
              PROCEDURES AND RESULTS

AUTHORS:   MR ROBERT THEDE  
             MR ROBERT KIM

CENTRAL INERTIAL GUIDANCE TEST FACILITY  
6585th Test Group/GD  
Holloman Air Force Base, New Mexico 88330



## ABSTRACT

A Honeywell laser gyro model GG1328AC was recently subjected to a series of tests on the 260 inch centrifuge at the Central Inertial Guidance Test Facility, Holloman AFB, New Mexico. For these tests the gyro was securely mounted in a precision cube on the counter-rotating platform of the centrifuge. Power supplies and other required electronics were mounted in the centrifuge control room. Data acquisition and quick-look analysis were provided by a Hewlett-Packard Fourier Analyzer system.

Tests were conducted in both the fixed and the counter-rotating modes. During fixed mode testing the gyro was subjected to constant accelerations in one direction of up to 100g. Several different gyro orientations were used, however, all orientations had the gyro input axis vertical. The input rate to the gyro was therefore the centrifuge rate. These tests were similar to scale factor linearity tests with an acceleration applied to the gyro. The results of these tests showed that the gyro output varied as functions of acceleration and acceleration squared. It was shown that this sensitivity could be caused by an acceleration sensitive misalignment of the gyro input axis relative to the spin axis of the centrifuge. The test orientations used did not permit the separation of tilt caused by centrifuge or gyro mount bending from bending of the gyro input axis within the gyro. Gyro orientations and analysis procedures are suggested which should permit such separation.

Counter-rotating tests were conducted at accelerations up to 50g with the gyro input axis vertical. These tests were essentially bias tests with an acceleration vector rotating around the gyro. The test results showed that the gyro output varied with acceleration and acceleration squared. It was shown that these variations were most likely caused by an acceleration sensitive coning of the gyro input axis relative to the spin axis of the centrifuge. The acceleration sensitive coning angle was of the same magnitude as the acceleration sensitive misalignment observed during the fixed mode tests. It again was not possible to determine if the coning was caused by centrifuge or mount deflections or by deflections within the gyro.

These centrifuge tests show that it is possible to evaluate the performance of a laser gyro in a high g environment. The testing left some questions concerning how much, if any, the gyro IA alignment was affected by the acceleration. Test and analysis procedures however are suggested which should provide answers to these questions.

## 1. INTRODUCTION

The Central Inertial Guidance Test Facility (CIGTF) recently completed a series of laboratory tests on a Honeywell Model 1328AC Laser Gyro. These tests were sponsored by the Air Force Space and Missiles Systems Organization, Los Angeles, California. A primary concern of this test program was to evaluate the performance of the Laser Gyro in a high-g environment. In order to perform this evaluation a series of tests was conducted on the 260 inch radius centrifuge at the CIGTF. Testing was conducted with the counter-rotating platform (CRP) on the centrifuge fixed which caused a constant acceleration to be directed along a given gyro axis, and with the CRP rotating at the same rate but opposite in direction of the centrifuge main arm resulting in a constant acceleration vector rotating around the gyro at centrifuge rate. This paper presents a description of the Honeywell Laser Gyro as well as a description of the instrumentation used to conduct the centrifuge tests. The test procedures used and the results of the tests are then presented. Some additional test orientations are also suggested which should provide answers to some questions which arose as a result of the centrifuge tests.

## 2. GYRO DESCRIPTION

The Honeywell Model 1328AC is a single-axis, ring laser gyro with the block assembly and all control and readout electronics contained in one housing. It is cylindrical with approximate dimensions of six inches in diameter by four inches in height. The unit weighs about four pounds by itself, and about 9.4 pounds including the baseplate heater assembly (supplied by CIGTF).

The block assembly is mechanically dithered to prevent the effects of lockin at low rates. A path length controller (PLC) servos the path length of the optical cavity within the block to compensate for the effects of thermal or mechanical stress on the block. The drawing in Figure 1 shows the position of the PLC relative to the input axis, J-axis and K-axis. The gyro uses a block mounted readout device and readout electronics to produce a series of pulses containing rotation magnitude and direction information.

The performance of the laser gyro can be characterized by its two primary parameters; the scale factor which relates the magnitude of the output to the applied rotational input and the gyro bias which is the output with no input applied.

The support electronics consisted of a power supply to provide all necessary voltages to excite and operate the gyro; a breakout box to access the gyro monitor signals; a dither compensator to avoid dither effects on the data at low input rates; and a dither cutoff protection circuit which would prevent laser damage to the gyro mirrors in case the dither failed.

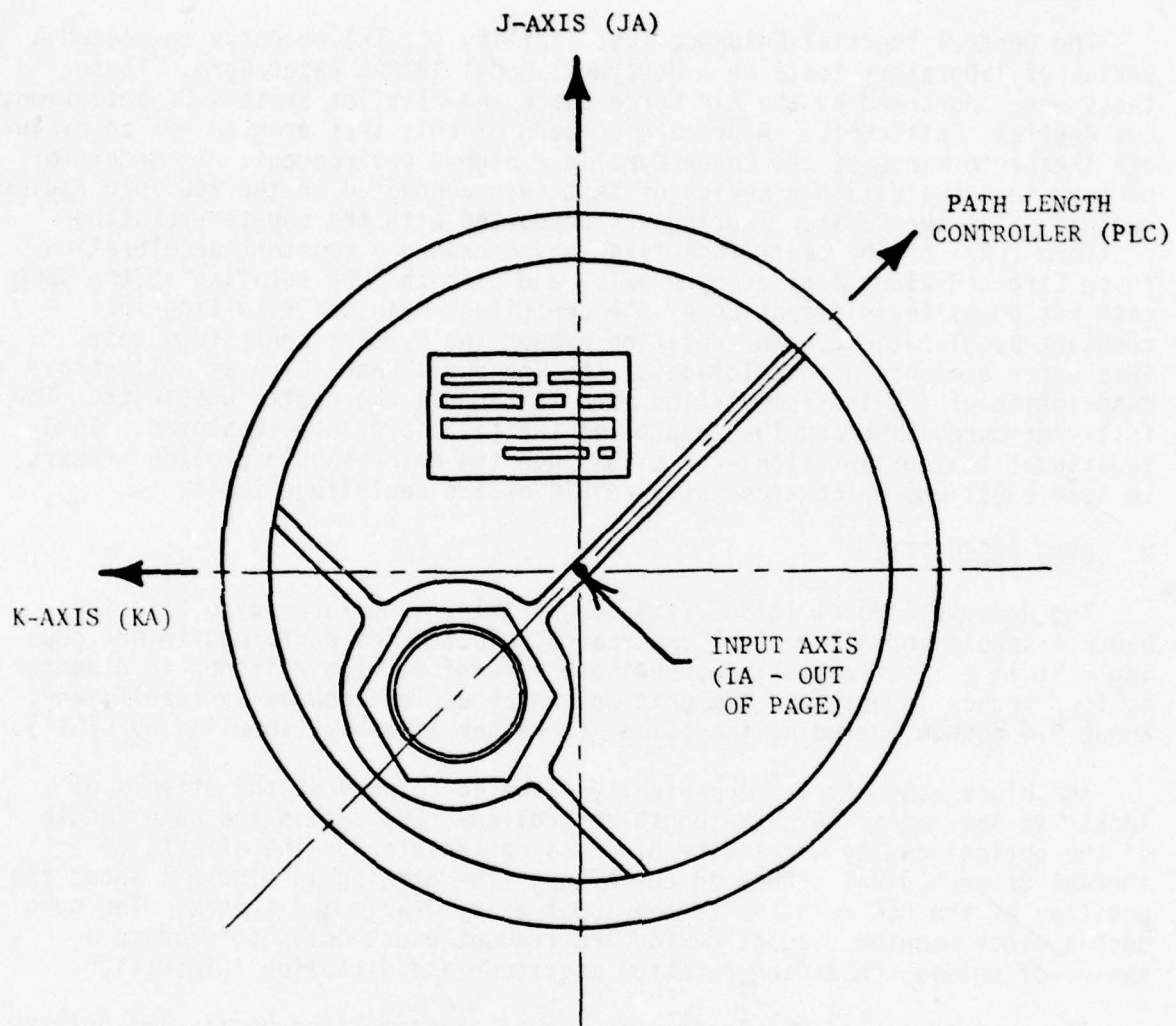


FIGURE 1. TOP VIEW OF GYRO SHOWING IA, JA, KA, AND PLC



### 3. TEST EQUIPMENT

#### 3.1 Centrifuge

The CIGTF 260 inch precision centrifuge with counter-rotating platform (CRP) was used during these centrifuge tests.

In the non-counter-rotating mode, the centrifuge is capable of 100g at a rate of 697.8 degrees/second (116.3 RPM). A radius of 260.50 inches to the center of the CRP accounts for this low rate. This allowed the laser gyro to be oriented with the input axis parallel to the centrifuge spin axis without exceeding the gyro input rate limit (800 degrees/second) at 100g. With a rotational mass of 47 tons and sophisticated control electronics, this centrifuge maintains a rate stability of better than 5 ppm rev-to-rev with an average (over 50 seconds) angular rate stability of 0.2 ppm. The day-to-day rate repeatably is 0.4 ppm and the position accuracy of the main arm is  $\pm 1$  arc-second.

In the counter-rotating mode, the CRP spins at the same rate as the main arm, but in the opposite direction, producing a g-vector of constant magnitude that rotates around the test item at the main arm rate. The centrifuge is capable of 85g counter-rotating with a payload of 30,000 g-pounds and a payload size of up to 50 inches in diameter by 50 inches in height. The CRP has a position accuracy of  $\pm 30$  arc-seconds.

#### 3.2 Gyro Mounting Fixture

During these tests the gyro temperature was controlled at 100 degrees Fahrenheit with an aluminum baseplate with a +28 volt strip heater around its circumference. The temperature was held constant with a proportional temperature controller using a sensing thermistor located in the aluminum disk. The gyro baseplate was mounted on a Mycalex ceramic insulator to thermally isolate the heater from the test fixture.

Figure 2 is an artist's drawing of the 260 inch centrifuge showing the mounting configuration in the bottom of the CRP high-g test cell. The laser gyro (with the baseplate heater assembly) was secured inside a 9-inch precision test cube machined from a solid block of aluminum. This cube was set into a mounting plate and was bolted in place. The mounting plate had a hole machined out in the shape of a six-pointed star, which allowed the cube containing the gyro to be reoriented in several repeatable orientations. The cube and "star plate" were attached to a rigid mount in the bottom of the CRP test cell, placing the gyro along the axis of the CRP.

#### 3.3 Data Acquisition Equipment

A Hewlett-Packard 5451 Fourier Analyzer was used to collect data during centrifuge testing of the laser gyro. The Fourier Analyzer consisted of a HP2100 computer, HP5466A Analog-to-Digital Converter, dual disk drive, magnetic tape unit, graphics terminal, hard copier, paper tape reader, and paper tape punch.

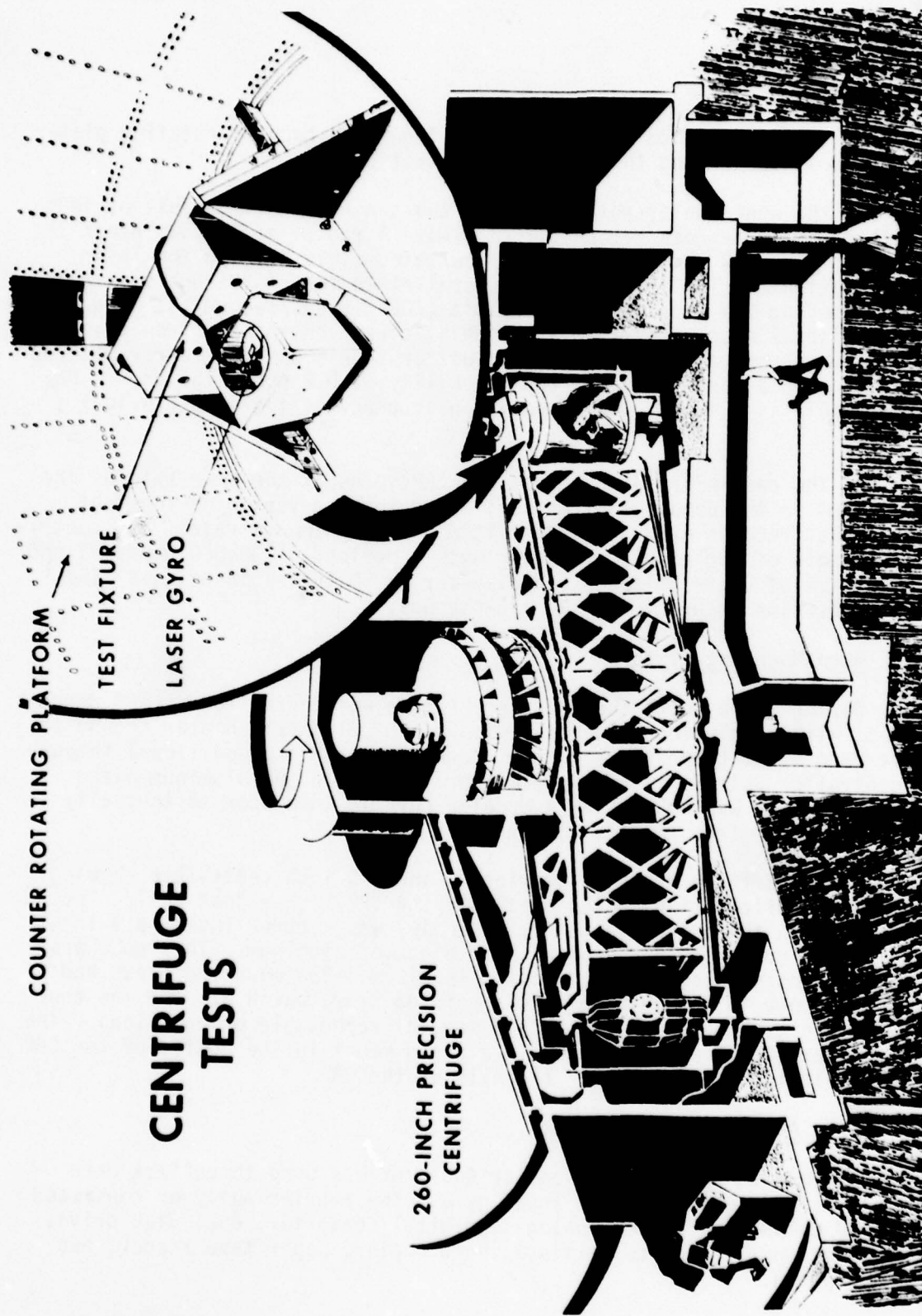


Figure 2. Centrifuge Test Set-Up

Two Hewlett-Packard reversible counters were interfaced with the Fourier Analyzer system. One was used to count the gyro output pulses and the other was used to count pulses from a 1 MHz frequency source to provide a time base during the testing. A drawing of the data acquisition system along with a cutaway view of the test cube is shown in Figure 3.

This data acquisition system allowed data to be recorded on magnetic tape and disk files for later use, and processed and displayed on the graphics terminal for quick-look information. The quick-look capability insured that the laser gyro and test setup were functioning properly and that any anomalies could be discovered and corrected quickly. The data stored on magnetic tape was later transferred onto the CIGTF Hewlett-Packard 3000 computer system for further analysis.

During the tests, the following information was recorded by the data acquisition system: gyro counts, sample interval time, gyro monitor signals and environmental temperatures.

The gyro put out a positive pulse approximately every 3 arc-seconds of counter-clockwise rotation and a negative pulse approximately every 3 arc-seconds of clockwise rotation. These pulses were routed through a pair of line drivers to a Hewlett-Packard K20-5280 reversible counter where they were differenced to determine the direction and magnitude of rotation. The reversible counter used was equipped with a readout on the fly option which allowed samples to be taken without resetting the counter, thus spreading the digital  $\pm 1$  count uncertainty over the entire length of the test and improving the accuracy of the data.

Since data was recorded at 100 rev intervals, the sample interval varied with the input rate (g level). In order to accurately determine the sample time, a 1 MHz clock frequency was put into another Hewlett-Packard K20-5280 reversible counter and the output was sampled along with the gyro counts. This counter also had the readout on the fly option so it was not necessary to reset it for each sample.

The following seven gyro monitor signals and three environmental temperatures were recorded during each sample: path length voltage indicating the position of the path length control transducer, four temperature sensor values indicating the temperature and gradients of the laser block, the discharge current in leg A and leg B of the laser gyro, the temperature of the center and circumference of the baseplate heater, and the temperature of centrifuge test cell. These signals were low pass filtered and multiplexed into the analog-to-digital converter of the Fourier Analyzer. During each sample interval 128 samples were taken of each signal, and the average value was recorded along with the gyro counts and sample interval time.



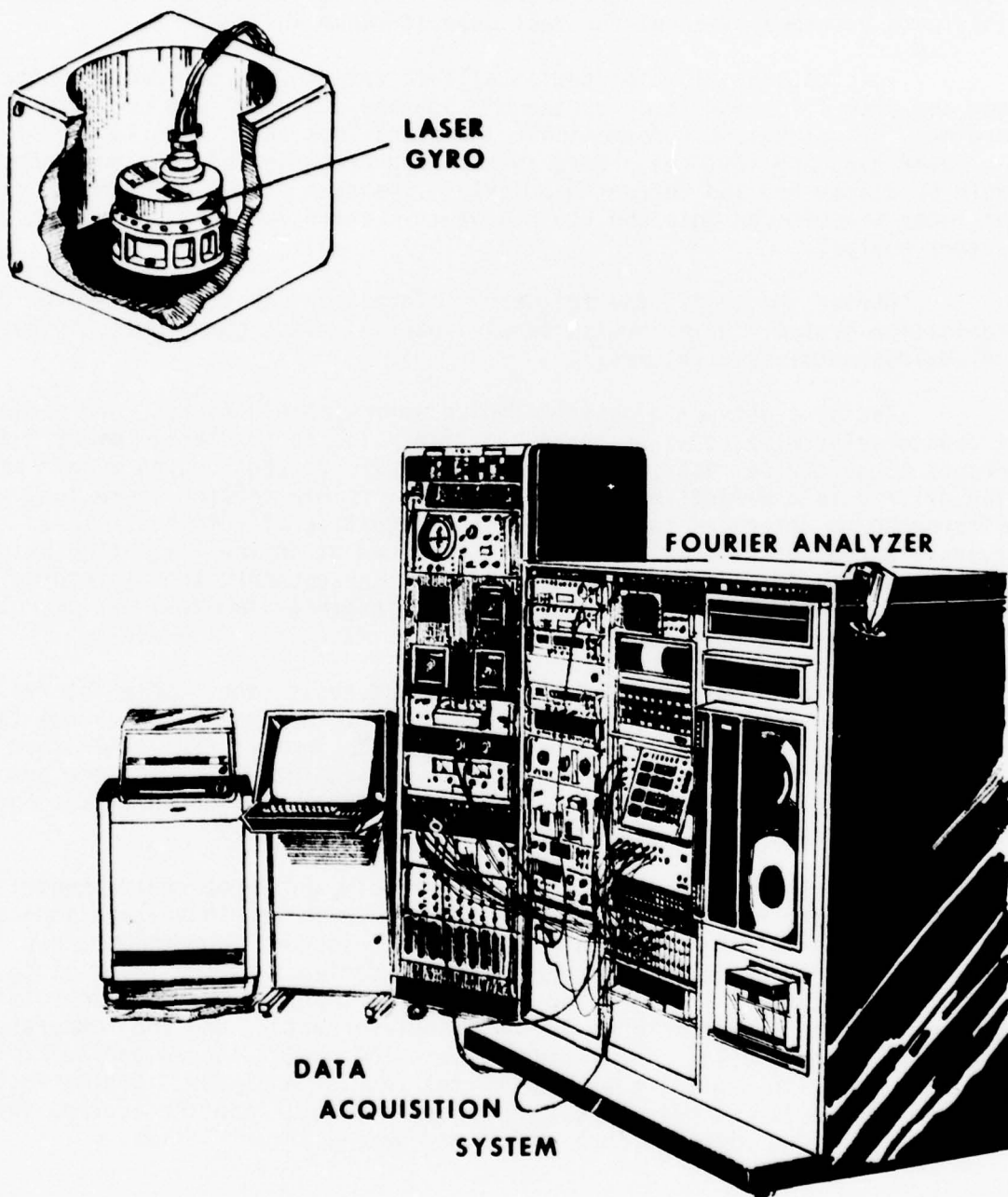


Figure 3. Gyro and Data Acquisition System

#### 4. TEST DESCRIPTION

##### 4.1 Fixed Tests

###### 4.1.1 Test Procedures

Fixed centrifuge tests were run with the CRP mechanically locked down (in the "fixed" position) and the main arm rotated to produce various g levels. With dither off, three 100 rev samples were taken at each g level. Data was taken going up in 10 g increments from 5g to 95g and coming down in 10g increments from 100g to 10g. The gyro had operated continuously several hours prior to each test.

Fixed tests were run in three orientations (see Figures 1 and 4), all IA up: (1) Path Length Controller (PLC) pointing out from the center of the centrifuge (along the negative g vector), (2) PLC pointing in toward the center of the centrifuge (along the positive g vector), and (3) PLC perpendicular to the g vector.

###### 4.1.2 Analysis Procedures

During fixed centrifuge tests conducted with the gyro IA vertical the rate about the gyro IA was equal to the centrifuge rate. This rate ranged from 156 deg/sec at 5g to 697 deg/sec at 100g. Because of this, the fixed centrifuge tests were essentially scale factor linearity tests with an applied acceleration. The first step, therefore, was to determine the gyro scale factor in units of pulses per revolution at each acceleration level. This was given by

$$SF_{P/R} = \frac{N-BT}{R_0} \quad (1)$$

where  $SF_{P/R}$  = gyro scale factor (pulses/rev)

$N$  = number of gyro pulses obtained during  $R$  centrifuge revolutions (pulses)

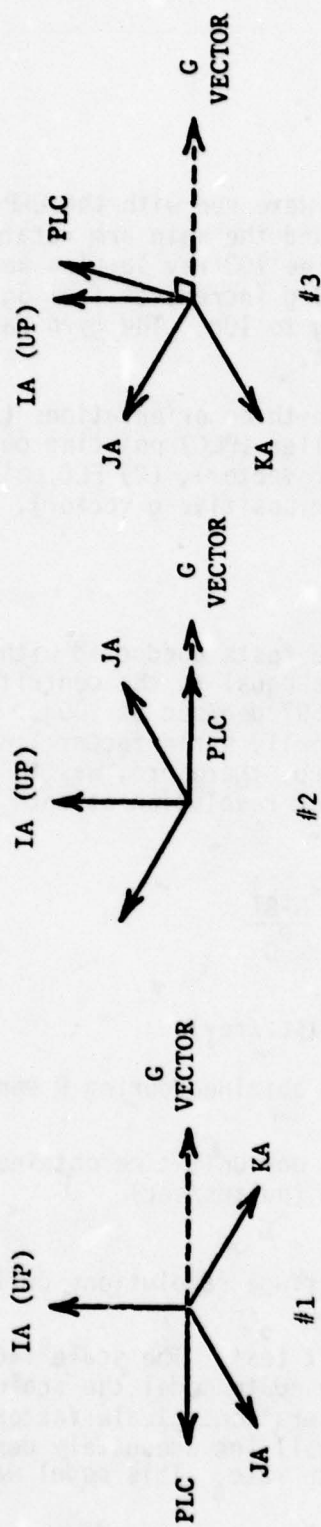
$B$  = number of gyro pulses per unit time obtained when the gyro was not rotating (pulses/sec)

$T$  = sample time (sec)

$R_0$  = total number of centrifuge revolutions during the sample interval (rev)

$B$  was obtained from a recent bias drift test. The scale factors obtained using the above procedures were then used to model the scale factor as functions of centrifuge rate and acceleration. Scale factor linearity tests had shown that a model given by Honeywell Inc adequately described the variation of the gyro scale factor with rate. This model was

# FIXED TEST ORIENTATIONS



8

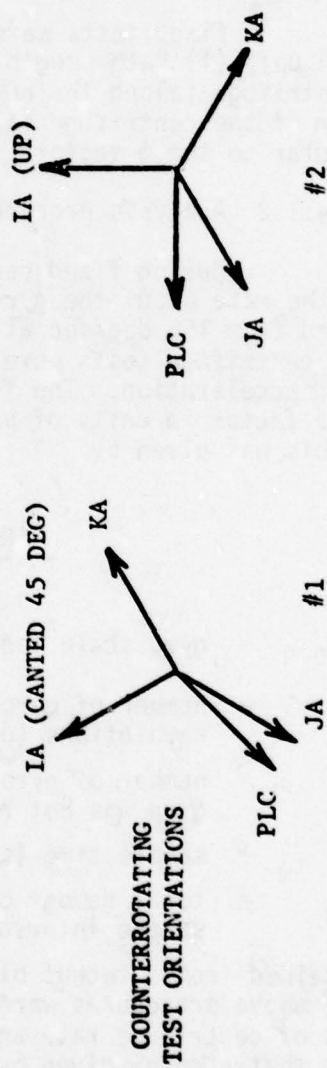


FIGURE 4. GYRO ORIENTATIONS DURING CENTRIFUGE TESTS



$$SF_{P/R} = SF_{\infty} \left[ 1 + \frac{.5\Omega_s^2}{\Omega^2 + \Omega_G^2} \right] \quad (2)$$

where  $SF_{\infty}$  = gyro scale factor at infinite rate (pulses/rev)  
 $\Omega_s$  = scale factor linearity coefficient (deg/sec)  
 $\Omega$  = rate about gyro input axis (deg/sec)  
 $\Omega_G$  = laser gyro parameter given by Honeywell Inc. as 12 deg/sec

An examination of the residuals remaining after performing a least squares fit of the above model to the data revealed the need to expand the model to include acceleration and acceleration squared terms.

$$SF_{P/R} = SF_{\infty} \left[ 1 + \frac{.5\Omega_s^2}{\Omega^2 + \Omega_G^2} \right] + K_1 A + K_2 A^2 \quad (3)$$

where  $K_1$  = variation in scale factor proportional to acceleration (pulses/rev/g)  
 $A$  = centrifuge acceleration (g)  
 $K_2$  = variation in scale factor proportional to the square of acceleration (pulses/rev/g<sup>2</sup>)

The centrifuge acceleration,  $A$ , was given by

$$A = \left( \frac{2\pi}{T} \right)^2 L / 385.48698 \quad (4)$$

where  $L$  = centrifuge radius (inches)

385.48698 = conversion factor from inches per second squared to g (in/sec<sup>2</sup>/g)

After determining that the above model (Equation 3) adequately described the scale factor variation with rate and acceleration, the next step was to investigate the reasons for the acceleration and acceleration squared terms in the model. The scale factor was initially determined using Equation 1 which assumed that the gyro input axis (IA) was perfectly aligned with the centrifuge rotation axis. If the gyro IA was misaligned from the centrifuge rotation axis by an angle  $\phi$ , the number of rotations about the gyro IA would be

$$R = R_0 \cos \phi \quad (5)$$

where  $R$  = number of gyro IA revolutions  
 $R_0$  = number of centrifuge revolutions  
 $\phi$  = misalignment between gyro IA and centrifuge rotation axis

During centrifuge testing  $\phi$  may vary as a function of acceleration caused either by a changing tilt of the gyro on the centrifuge or by bending inside the gyro. The angle,  $\phi$ , can then be given by

$$\phi = \phi_0 + \phi_1 A \quad (6)$$

where  $\phi_0$  = misalignment at zero acceleration (rad)  
 $\phi_1$  = rate of change of misalignment with acceleration (rad/g)  
 $A$  = acceleration (g)

Using this in Equation 1 and combining it with Equation 2 gives

$$SF_{P/R} = \frac{N - BT}{R_0 \cos(\phi_0 + \phi_1 A)} = SF_\infty \left[ 1 + \frac{.5\Omega_s^2}{\Omega^2 + \Omega_G^2} \right] \quad (7)$$

Since the misalignment is not known, the scale factor determination is based on  $R_0$ . The scale factor determined ( $SF_D$ ) from centrifuge tests is therefore given by

$$SF_D = \frac{N - BT}{R_0} = SF_\infty \left[ 1 + \frac{.5\Omega_s^2}{\Omega^2 + \Omega_G^2} \right] \cos(\phi_0 + \phi_1 A) \quad (8)$$

The misalignment will be small; therefore, the cosine can be quite accurately given by the first two terms in the cosine expansion

$$\cos(\phi_0 + \phi_1 A) \approx 1 - \frac{(\phi_0 + \phi_1 A)^2}{2} \quad (9)$$

or

$$\cos(\phi_0 + \phi_1 A) \approx 1 - \frac{1}{2}(\phi_0^2 + 2\phi_0\phi_1 A + \phi_1^2 A^2) \quad (10)$$

The determined scale factor now becomes

$$SF_D = SF_\infty \left[ 1 + \frac{.5\Omega_s^2}{\Omega^2 + \Omega_G^2} \right] (1 - .5\phi_0^2) - .5 SF_\infty \left[ 1 + \frac{.5\Omega_s^2}{\Omega^2 + \Omega_G^2} \right] (2\phi_0\phi_1 A + \phi_1^2 A^2) \quad (11)$$

If  $\phi_0 \ll 1$ ,  $\phi_1 \ll 1$ , and  $\frac{.5\Omega_s^2}{\Omega^2 + 144} \ll 1$ , products of three or more of these terms can be ignored and the above equation can be approximated by

$$SF_D = SF_\infty \left[ 1 + \frac{.5\Omega_s^2}{\Omega^2 + \Omega_G^2} - .5\phi_0^2 \right] - SF_\infty \phi_0 \phi_1 A - .5 SF_\infty \phi_1^2 A^2 \quad (12)$$

This equation therefore predicts that if the gyro IA misalignment angle varies linearly with acceleration, the determined scale factor will be a function of acceleration and acceleration squared. Relating this equation to Equation 3 gives

$$K_1 = - SF_\infty \phi_0 \phi_1 \quad (13)$$

$$K_2 = - .5 SF_\infty \phi_1^2 \quad (14)$$

This requires that if  $SF_\infty$  is positive,  $K_2$  must be negative in order for  $\phi_1$  to be real.

Comparing Equations 12 and 3 shows that the value obtained for  $SF_\infty$  will really be  $SF_\infty (1 - .5\phi_0^2)$ . If  $\phi_0$  is small it will contribute very little to this term. If  $\phi_0$  is 30 arc-sec the error in  $SF_\infty$  will be only .01 part per million.

## 4.2 CRP Tests

### 4.2.1 Test Procedures

Counter-rotating tests were run from 5g to 50g with gyro dither on, and after several hours of continuous gyro operation. Three 100 rev samples were taken at each g level. These tests were conducted in two orientations (see Figures 1 and 4): (1) IA approximately 45 degrees down from vertical, with the PLC also about 45 degrees down from horizontal; (2) IA up and PLC in the horizontal plane.

Since the CRP tests were conducted with dither on, the dither compensator was used to synchronize the sample interval to the dither signal by starting and stopping the data taking interval on the first positive-going dither zero crossing following the 100th revolution of each sample.



The position error between the main arm and the CRP was measured at the start and stop of each interval and the data was compensated according to the difference. This error was obtained by counting 1 MHz clock pulses with a counter that could be reset and stopped. Both the main arm and the CRP have very accurate one-half degree pulses, with the CRP pulses occurring half way between main arm pulses when the CRP is perfectly slaved to the main arm. The main arm one-half degree pulse was used to start the counter and the CRP one-half degree pulse was used to stop it. The output of the counter and the number of main arm one-half degree pulses that had occurred since the last main arm once-per-rev pulse were read at the start and stop of the sample interval. The position error angle was calculated by multiplying the stop and start difference by the rate for the g level of the sample.

#### 4.2.2 Analysis Procedures

The counter-rotating centrifuge tests were essentially fixed position bias drift tests with an acceleration vector rotating around the gyro at centrifuge frequency. The change in gyro bias at each acceleration level caused by centrifuging was therefore determined by

$$\Delta B = \frac{N' - B'}{SF} \quad (15)$$

where  $\Delta B$  = Bias variation as a function of acceleration (deg/hr)

$N'$  = Average number of gyro pulses per second obtained during centrifuging (pulses/sec)

$B'$  = Number of gyro pulses per second obtained at zero centrifuge acceleration (pulses/sec)

SF = Gyro scale factor (arc-sec/pulse)

The CRP position variation from the start to the end of each data sample interval was measured and  $\Delta B$  was corrected for this error. The results of this analysis showed that the bias variation was a function of acceleration and acceleration squared and also of centrifuge direction. Because of the apparent IA misalignment variation with acceleration observed during fixed centrifuge tests, it was felt that a similar misalignment might be occurring during CRP tests. A constant outward tilt of the gyro IA relative to the rotation axis of the centrifuge would cause the gyro IA to move in a cone relative to the earth as the centrifuge rotated. Many sources describe the effects of coning of the IA of a conventional gyro. Reference 1, in reference to a theorem by Goodman and Robinson states,

"This theorem essentially states that if a body undergoes a sequence of rotations in which each axis of the body returns to its initial orientation and an axis in the body has moved in a conical path, there will have been an angular velocity component about that axis ...".

This reference then goes on to show that this motion can be represented as periodic angular oscillations about one space-fixed axis and one body-fixed axis. It then shows that the rate about the coning axis,  $\omega_z$ , is given by

$$\omega_z = \dot{\phi}\dot{\theta} \quad (16)$$

where  $\phi$  = angle about the body-fixed axis

$\dot{\theta}$  = time derivative of the angle about the space-fixed axis

For the coning of the IA of the laser gyro on the centrifuge these two angles are given by

$$\phi = \phi' \sin(\Omega t + \delta) \quad (17)$$

$$\theta = \phi' \cos(\Omega t + \delta) \quad (18)$$

where  $\phi'$  = amplitude of the tilt producing the coning motion

$\Omega$  = centrifuge rate

$t$  = time

$\delta$  = phase angle of the tilt

This gives

$$\omega_z = -\phi'^2 \Omega \sin^2(\Omega t + \delta) \quad (19)$$

$$\omega_z = -.5\phi'^2 \Omega [1 - \cos 2(\Omega t + \delta)] \quad (20)$$

The average rate about the gyro IA over an integral number of revolutions is therefore

$$\bar{\omega}_z = -.5\phi'^2 \Omega \quad (21)$$

The tilt  $\phi'$  will again be assumed to be a function of acceleration:

$$\phi' = \phi_0 + \phi_1 A \quad (22)$$

Substituting this gives

$$\bar{\omega}_z = -.5\Omega(\phi_0^2 + 2\phi_0\phi_1 A + \phi_1^2 A^2) = \Delta B \quad (23)$$

This equation shows that a g-sensitive coning of the input axis would cause a gyro output that was functions of acceleration, acceleration squared and centrifuge rate. This equation was therefore fit to the observed bias variations,  $\Delta B$ , using least squares procedures and  $\phi_0$  and  $\phi_1$  were determined.

## 5. TEST RESULTS

### 5.1 Fixed Centrifuge Tests

The coefficients obtained by fitting Equation 3 to the scale factor data obtained from fixed centrifuge tests are shown in Table I. Also shown are the maximum acceleration level during the test and the standard deviation of the residuals from the fit. The tilt angles ( $\phi_0$  and  $\phi_1$ ) obtained from the acceleration and acceleration-squared coefficients ( $K_1$  and  $K_2$ ) are shown in Table II. It can be seen that the acceleration-sensitive tilt,  $\phi_1$ , is very repeatable at about 5.3 arc-sec/g from test to test and from one orientation to the next. The acceleration insensitive tilt,  $\phi_0$ , is fairly stable within an orientation but varies greatly from one orientation to the next. This is as expected since  $\phi_0$  is the misalignment of the gyro IA with respect to the centrifuge rotation axis at zero centrifuge acceleration. This angle would therefore be expected to change when the gyro was reoriented.

Table III shows the values of scale factor linearity coefficients ( $SF_\infty$  and  $\Omega_s^2$ ) obtained from scale factor linearity tests. Also shown is the standard deviation of the residuals from the fit. These tests were conducted

TABLE III. SCALE FACTOR LINEARITY RESULTS

Date (1978)	Direction	$SF_\infty$ (Pulses/Rev)	$\Omega_s^2$ (Deg/Sec) <sup>2</sup>	$\sigma_{Res}$ (PPM)
22 May	CCW	411879.43	.238	.035
2 Jun	CW	411879.52	.038	.026
8 Jun	CCW	411879.65	.000	.012
8 Jun	CW	411879.62	-.005	.011
19 Jun	CCW	411879.67	-.046	.027
27 Jun	CCW	411879.37	-.125	.021
30 Jun	CW	411879.39	-.091	.018

on the centrifuge by rotating the counter-rotating platform while holding the main arm stationary. The rates used were the same as main arm rates required to reach accelerations from 5 to 100g in 5g increments. A comparison of these coefficients with those obtained during centrifuging (Table I) shows good agreement indicating the  $SF_\infty$  and  $\Omega_s^2$  were not affected by centrifuging. The day-to-day variations in  $\Omega_s^2$  had been observed prior to centrifuging and were later found to be caused by a problem in the gyro electronics. The shift in  $SF_\infty$  from 19 June to 27 June occurred following a repair to the gyro dither circuitry at Honeywell, Inc. None of these variations in  $\Omega_s^2$  and  $SF_\infty$



TABLE I. FIXED CENTRIFUGE TEST RESULTS

Date (1978)	Max G	$SF_{\infty}$ (Cnts/Rev)	$\Omega_s^2$ (Deg/Hr) <sup>2</sup>	$K_1$ (PPM/G)	$K_2$ (PPM/G <sup>2</sup> )	$\sigma_{res}$ (PPM)
PLC Pointing Outward						
17 May	75 CCW	411879.49	.284	.0161	-.000307	.036
17 May	95 CW	411879.50	.296	.0174	-.000357	.072
23 May	75 CW	411879.55	.232	.0136	-.000303	.045
23 May	100 CCW	411879.58	.228	.0192	-.000363	.090
27 Jun	75 CCW	411879.47	-.118	.0130	-.000290	.044
28 Jun	75 CW	411879.49	-.108	.0108	-.000272	.017
Mean		411879.51	.136	.0150	-.000314	
Sigma		.10 PPM	.194	.0031	.000036	
PLC Pointing Inward						
5 Jun	100 CCW	411879.62	.015*	-.0073*	-.000344	.098
6 Jun	100 CW	411879.64	.005*	-.0097	.000328	.073
Mean		411879.63	.010*	-.0085	-.000336	
Sigma		.03 PPM	.007	.0017	.000011	
PLC Pointing Across Arm						
9 Jun	100 CCW	411879.83	-.008*	.0054*	-.000334	.066
14 Jun	95 CW	411879.79	-.060	.0041	-.000323	.042
Mean		411879.81	-.034*	.0047	-.000328	
Sigma		.07 PPM	.037	.0009	.000008	

\*Not significantly different from zero at the 1% significance level.

TABLE II. TILT ANGLES FROM FIXED CENTRIFUGE TESTS

Date (1978)	Max G	$\phi_0$ (Arc Sec)	$\phi_1$ (Arc Sec/G)
PLC Pointing Outward			
17 May	75 CCW	-134	5.12
17 May	95 CW	-135	5.47
23 May	75 CW	-114	5.09
23 May	100 CCW	-147	5.57
27 Jun	75 CCW	-111	4.98
28 Jun	75 CW	-95	4.82
Mean		-123	5.17
Sigma		19	.29
PLC Pointing Inward			
5 Jun	100 CCW	57	5.42
6 Jun	100 CW	78	5.29
Mean		68	5.36
Sigma		15	.09
PLC Pointing Across Arm			
9 Jun	100 CCW	-43	5.34
14 Jun	95 CW	-33	5.25
Mean		-38	5.30
Sigma		7	.06

were therefore caused by centrifuging the gyro. A plot of the residuals from two typical centrifuge tests are shown in Figure 5. These residuals show a definite hysteresis effect, indicating that the coefficients for decreasing acceleration were different than those for increasing acceleration. Because of this the model was then fit separately to increasing acceleration data and to decreasing acceleration data. The coefficients and the misalignment angles obtained from these fits are shown in Tables IV and V. The acceleration sensitive tilt,  $\phi_1$ , was about .9 arc-sec/g greater for increasing acceleration than for decreasing acceleration,  $SF_\infty$  and  $\Omega_s^2$  did not differ significantly from increasing acceleration to decreasing acceleration. The residuals from these fits were small and were caused primarily by scatter within an acceleration level. A plot of the residuals from two of these tests is shown in Figure 6.

The observed acceleration sensitive tilt,  $\phi_1$ , could be caused by a bending within the gyro, movement of the gyro in the mount, movement of the gyro mount on the centrifuge, or a bending of the centrifuge arm. Push tests in which pressure was applied to a dummy gyro within the mount were conducted to determine how much motion of the gyro within the mount could be expected. These results showed a motion of about .5 arc-sec/g. An analytical study of the centrifuge mounting cell and the gyro mount on this cell predicted a tilt of about 1 arc-sec/g. The tilt of the centrifuge arm was not measured during the centrifuge tests and it is therefore not known how much this contributed to the total tilt. It is therefore not known how much of the observed tilt was caused by centrifuge bending and how much, if any, was caused by bending within the gyro. A test using more orientations of the gyro on the centrifuge arm is proposed in Section 6 of this paper. The additional orientations will permit separation of centrifuge tilts from tilts within the gyro mounting cube; however, these tests have not yet been performed.

## 5.2 Counter-Rotating Centrifuge Tests

The bias variation as a function of acceleration obtained from CRP centrifuge tests is presented in Figure 7. These plots show that the bias difference varies as a function of acceleration squared and is also dependent on the direction of the centrifuge. This is predicted by the model presented in Section 4.2.2 (Equation 23). This model was fit to the data and the angles, obtained,  $\phi_0$  and  $\phi_1$  are presented in Table VI.  $\phi_1$  from the orientation which had IA at 45 degrees to the centrifuge rotation axis is not given because the coefficient containing  $\phi_1^2$  was negative, therefore giving meaningless results for  $\phi_1$ . The data from both 45 degree orientations was noisy, causing the standard errors of the coefficients obtained from these tests to be large. There is, therefore, a large uncertainty in the angles obtained from these tests. The values obtained for the acceleration sensitive coning angle of about 6 arc-sec/g agree well with the acceleration sensitive misalignment of 5.3 arc-sec/g obtained from fixed centrifuge tests. The same mechanism is therefore most likely responsible for these tilts. However, it is not known if they are caused primarily by centrifuge errors or by bending



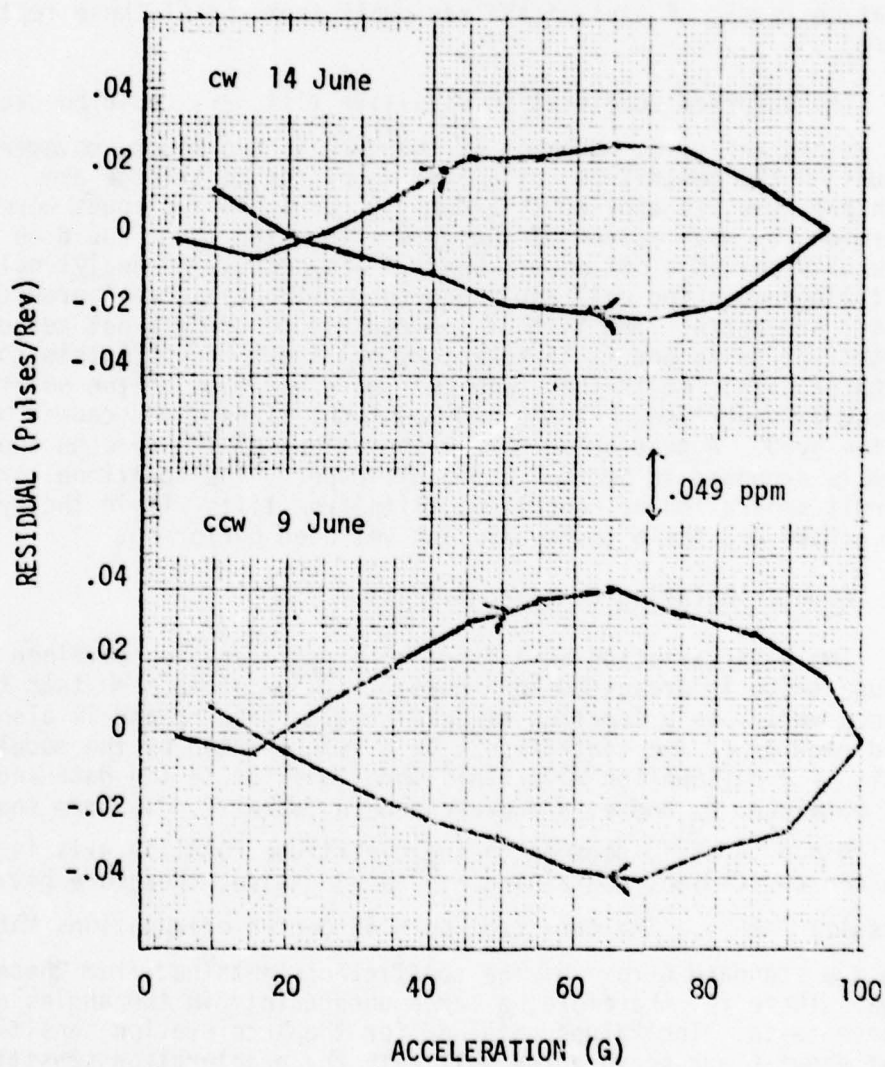


FIGURE 5. CENTRIFUGE TEST RESIDUALS

TABLE IV. COEFFICIENTS FROM INCREASING  $\alpha$  DATA

Date (1978)	Max G	SF <sub>∞</sub> (Cnts/Rev)	$\Omega_S^2$ (Deg/Hr) <sup>2</sup>	$\phi_0$ (Sec)	$\phi_1$ (Sec/G)	$\sigma_{res}$ (PPM)
PLC Pointing Outward						
17 May	75 CCW	411879.40	.293	-187	5.77	.017
17 May	95 CW	411879.36	.309	-206	6.16	.039
23 May	75 CW	411879.55	.232	-133	5.43	.021
23 May	100 CCW	411879.60	.227	-160	5.78	.020
27 Jun	75 CCW	411879.36	-.108	-180	5.84	.021
28 Jun	75 CW	411879.47	-.106	-113	5.03	.010
Mean		411879.46	.141	-163	5.67	
Sigma		.25 PPM	.195	35	.39	
PLC Pointing Inward						
5 Jun	100 CCW	411879.58	.018	- 4	5.94	.014
6 Jun	100 CW	411879.58	.009	15	5.78	.016
Mean		411879.58	.013	6	5.86	
Sigma		0.0 PPM	.006	13	.11	
PLC Pointing Across Arm						
9 Jun	100 CCW	411879.76	-.002*	- 96	5.81	.018
14 Jun	95 CW	411879.73	-.055	- 76	5.62	.015
Mean		411879.74	-.028	- 86	5.71	
Sigma		.05 PPM	.037	14	.13	

\*Not significantly different from zero at the 1% significance level.

TABLE V. COEFFICIENTS FROM DECREASING  $g$  DATA

Date (1978)	Max G	$SF_{\infty}$ (Cnts/Rev)	$\Omega_S^2$ (Deg/Hr) <sup>2</sup>	$\phi_0$ (Sec)	$\phi_1$ (Sec/G)	$\sigma_{res}$ (PPM)
PLC Pointing Outward						
17 May	70 CCW	411879.51	.287	-113	4.88	.014
17 May	90 CW	411879.58	.295	- 82	5.01	.015
23 May	70 CW	411879.59	.227	- 73	4.52	.017
23 May	90 CCW	411879.66	.206	- 94	5.09	.019
27 Jun	70 CCW	411879.47	-.110	- 96	4.76	.021
28 Jun	70 CW	411879.49	-.105	- 95	4.81	.020
Mean		411879.55	.133	- 92	4.84	
Sigma		.18 PPM	.190	14	.20	
PLC Pointing Inward						
5 Jun	90 CCW	411879.67	.009*	129	4.91	.015
6 Jun	90 CW	411879.69	-.002*	142	4.87	.013
Mean		411879.68	.003*	135	4.89	
Sigma		.03 PPM	.008	9	.03	
PLC Pointing Across Arm						
9 Jun	90 CCW	411879.87	-.011	1	5.00	.014
14 Jun	90 CW	411879.83	-.064	10	4.90	.015
Mean		411879.85	-.037	6	4.95	
Sigma		.07 PPM	.037	6	.07	

\*Not significantly different from zero at the 1% significance level.



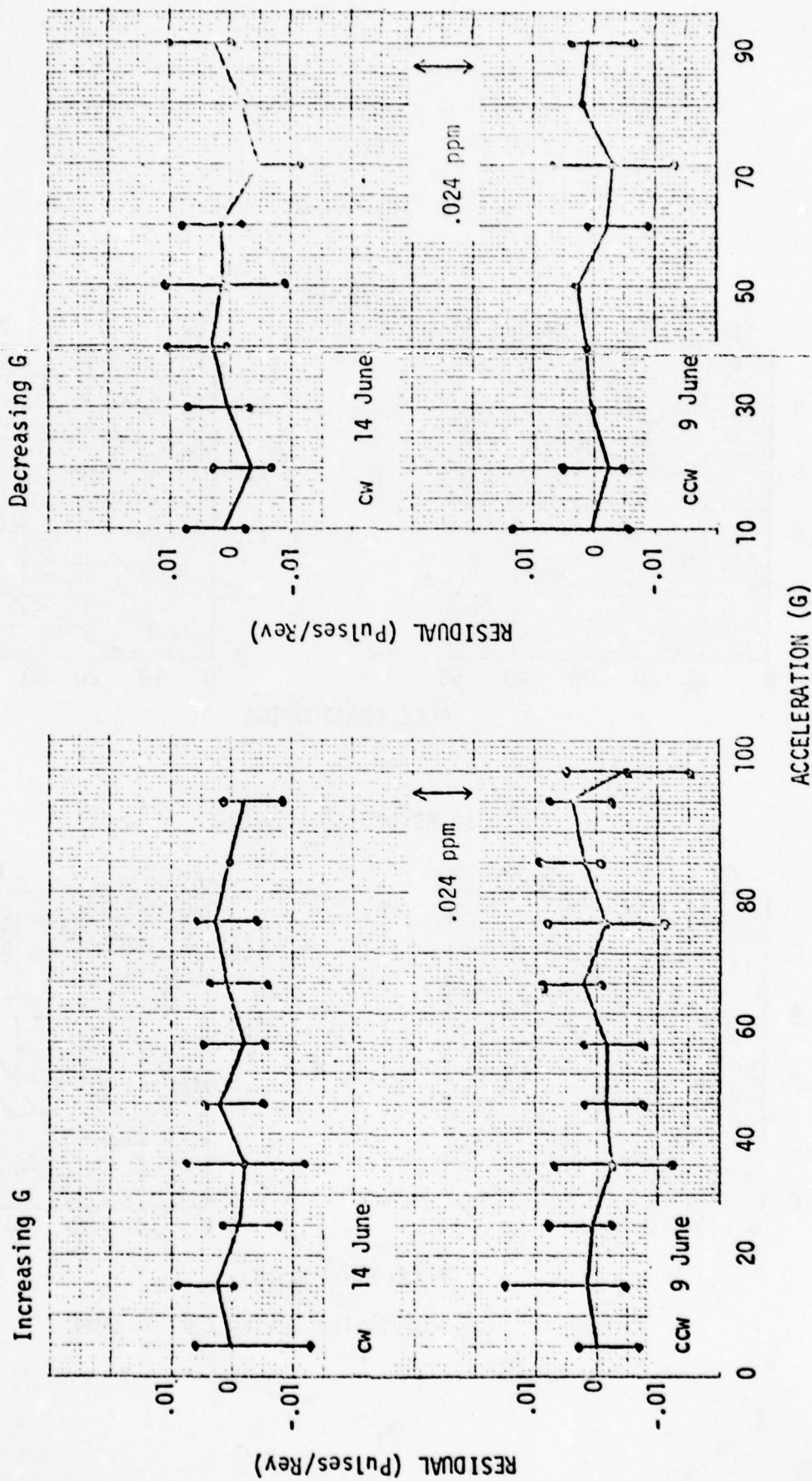


Figure 6. Residuals From Separate Fits To Increasing g and Decreasing g Data

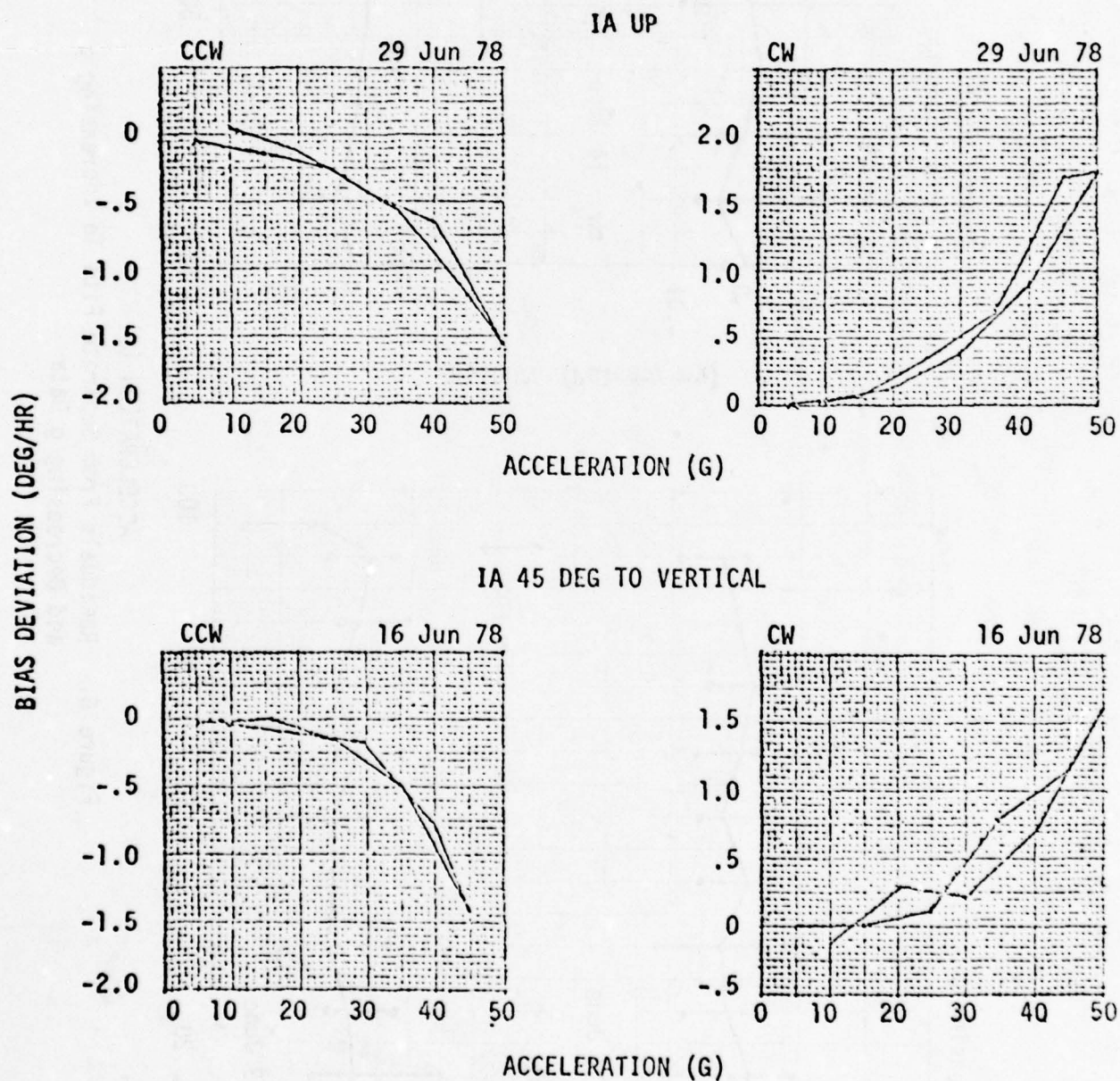


Figure 7. Bias Deviation During CRP Testing

within the gyro.

TABLE VI. CONING ANGLES FROM CRP TESTS

Date (1978)	Orientation	Direction	$\phi_0$ (Arc-Sec)	$\phi_1$ (Arc-Sec/g)
16 June	IA 45 Deg	CCW	144.2	12.5
16 June	IA 45 Deg	CW	60.5	----
29 June	IA Up	CCW	69.4	6.0
29 June	IA Up	CW	53.6	6.5

#### 6. SUGGESTED ADDITIONAL TESTS

It has been shown that apparent gyro bias and scale factor acceleration and acceleration squared sensitivities observed during centrifuge testing could be caused by an acceleration sensitive misalignment of the gyro IA relative to the centrifuge spin axis. From the tests conducted it was not possible to determine if this misalignment was caused by a motion of the gyro IA within the gyro or by a bending of the centrifuge. Procedures will now be developed which will permit a separation of bending within the gyro mounting fixture from bending external to the fixture. Equation 12 which was used to describe the gyro output from fixed centrifuge tests evolved from Equation 8 through a cosine expansion and small angle approximations. The argument of the cosine term in Equation 8 will now be expanded to more fully describe the gyro IA alignment.

$$\phi_0 + \phi_1 A = \phi_T = \phi_{00} + \phi_{0\delta i} + \phi_C A + \phi_{GP} A \cos \phi_{00} + \phi_{GI} A \sin \phi_{00} \quad (24)$$

where

- $\phi_T$  Total angle between the gyro IA and the centrifuge spin axis in a vertical plane along the centrifuge arm, positive outward from the centrifuge spin axis. (rad)
- $\phi_{00}$  Desired angle between the gyro IA and the centrifuge spin axis. (rad)
- $\phi_{0\delta i}$  Acceleration insensitive misalignment between the actual gyro IA and the desired gyro IA alignment.  $i$  references the gyro orientation. (rad)
- $\phi_C$  Acceleration sensitive misalignment of the centrifuge mounting surface with respect to the centrifuge spin axis. (rad/g)
- $\phi_{GP}$  Acceleration sensitive misalignment of the gyro IA from the centrifuge mounting surface caused by acceleration perpen-



dicular to the gyro IA. (rad/g)

$\phi_{GI}$  Acceleration sensitive misalignment of the gyro IA from the centrifuge mounting surface caused by acceleration along the gyro IA. (rad/g)

The cosine of the total angle is now expanded using trig identities.

$$\begin{aligned} \cos \phi_T = & \cos \phi_{00} \cos(\phi_{0\delta i} + \phi_C A + \phi_{GP} A \cos \phi_{00} + \phi_{GI} A \sin \phi_{00}) \\ & - \sin \phi_{00} \sin(\phi_{0\delta i} + \phi_C A + \phi_{GP} A \cos \phi_{00} + \phi_{GI} A \sin \phi_{00}) \end{aligned} \quad (25)$$

All angles except  $\phi_{00}$  are small angles. Series expansions of the sine and cosine will now be employed and any terms involving products of three or more small angles will be ignored.

$$\begin{aligned} \cos \phi_T = & \cos \phi_{00} \left[ 1 - \frac{1}{2}(\phi_{0\delta i}^2 + \phi_C^2 A^2 + \phi_{GP}^2 A^2 \cos^2 \phi_{00} + \phi_{GI}^2 A^2 \sin^2 \phi_{00} \right. \\ & + 2\phi_{0\delta i} \phi_C A + 2\phi_{0\delta i} \phi_{GP} A \cos \phi_{00} + 2\phi_{0\delta i} \phi_{GI} A \sin \phi_{00} \\ & + 2\phi_C \phi_{GP} A^2 \cos \phi_{00} + 2\phi_C \phi_{GI} A^2 \sin \phi_{00} + 2\phi_{GP} \phi_{GI} A^2 \sin \phi_{00} \cos \phi_{00}) \\ & \left. - \sin \phi_{00} [\phi_{0\delta i} + \phi_C A + \phi_{GP} A \cos \phi_{00} + \phi_{GI} A \sin \phi_{00}] \right] \end{aligned} \quad (26)$$

This will now be rewritten lumping together coefficients of A and coefficients of A<sup>2</sup>.

$$\begin{aligned} \cos \phi_T = & (1 - \frac{1}{2}\phi_{0\delta i}^2) \cos \phi_{00} - \phi_{0\delta i} \sin \phi_{00} \\ & + A[(-\phi_C - \phi_{GP} \cos \phi_{00} - \phi_{GI} \sin \phi_{00}) \phi_{0\delta i} \cos \phi_{00} \\ & + (-\phi_C - \phi_{GP} \cos \phi_{00} - \phi_{GI} \sin \phi_{00}) \sin \phi_{00}] \\ & + A^2[-\frac{1}{2}\phi_C^2 - \frac{1}{2}\phi_{GP}^2 \cos^2 \phi_{00} - \frac{1}{2}\phi_{GI}^2 \sin^2 \phi_{00} \\ & - \phi_C \phi_{GP} \cos \phi_{00} - \phi_C \phi_{GI} \sin \phi_{00} - \phi_{GP} \phi_{GI} \sin \phi_{00} \cos \phi_{00}] \cos \phi_{00} \end{aligned} \quad (27)$$

Substituting this for the cosine term in Equation 8 gives

$$SF_D = SF_\infty \left[ 1 + \frac{.5\Omega_S^2}{\Omega^2 + 144} \right] \left[ \left( 1 - \frac{1}{2}\phi_{0\delta i}^2 \right) \cos\phi_{00} - \phi_{0\delta i} \sin\phi_{00} \right] \quad (28)$$

$$+ SF_\infty K_1 A + SF_\infty K_2 A^2$$

where

$$K_1 \approx (-\phi_C - \phi_{GP} \cos\phi_{00} - \phi_{GI} \sin\phi_{00}) \phi_{0\delta i} \cos\phi_{00} \quad (29)$$

$$+ (-\phi_C - \phi_{GP} \cos\phi_{00} - \phi_{GI} \sin\phi_{00}) \sin\phi_{00}$$

$$K_2 \approx \left( -\frac{1}{2}\phi_C^2 - \frac{1}{2}\phi_{GP}^2 \cos^2\phi_{00} - \frac{1}{2}\phi_{GI}^2 \sin^2\phi_{00} \right. \quad (30)$$

$$\left. - \phi_C \phi_{GP} \cos\phi_{00} - \phi_C \phi_{GI} \sin\phi_{00} - \phi_{GP} \phi_{GI} \sin\phi_{00} \cos\phi_{00} \right) \cos\phi_{00}$$

The goal is to separate  $\phi_C$  from  $\phi_{GI}$  and  $\phi_{GP}$  by using several different test orientations, i.e., several different values for  $\phi_{00}$ . Examination of the above equations reveals that all terms contain squares or products of small angles except for the multipliers of  $\sin\phi_{00}$  in the equation for  $K_1$ . This is therefore the most likely term from which to obtain  $\phi_C$ ,  $\phi_{GI}$ , and  $\phi_{GP}$ . This therefore requires that  $\phi_{00}$  cannot be  $0^\circ$  or  $180^\circ$ . Since significant centrifuge rates must be applied about the gyro IA,  $\phi_{00}$  cannot be  $90^\circ$  or  $270^\circ$ . The required orientations will therefore be those at which the gyro IA is at  $45^\circ$  to the centrifuge spin axis. If products of small angles are ignored,  $K_1$  for the four orientations in which the gyro IA is at  $45^\circ$  to the centrifuge spin axis is:

$$K_1(45^\circ) = -.707(\phi_C + .707\phi_{GP} + .707\phi_{GI}) \quad (31)$$

$$K_1(135^\circ) = -.707(\phi_C - .707\phi_{GP} + .707\phi_{GI}) \quad (32)$$

$$K_1(225^\circ) = .707(\phi_C - .707\phi_{GP} - .707\phi_{GI}) \quad (33)$$

$$K_1(315^\circ) = .707(\phi_C + .707\phi_{GP} - .707\phi_{GI}) \quad (34)$$

Only two orientations are required if  $\phi_{GP}$  is not to be separated from  $\phi_{GI}$ . For example adding the  $K_1$ 's from the  $45^\circ$  and the  $225^\circ$  orientations gives

$$\phi_{GP} + \phi_{GI} = -K_1(45^\circ) - K_1(225^\circ) \quad (35)$$

subtracting gives

$$\phi_C = \frac{1}{1.414} [K_1(225^\circ) - K_1(45^\circ)] \quad (36)$$

$\phi_{GP}$  and  $\phi_{GI}$  can be separated if a third orientation is added:

$$\phi_{GP} = K_1(135^\circ) - K_1(45^\circ) \quad (37)$$

$$\phi_{GI} = -K_1(135^\circ) - K_1(225^\circ) \quad (38)$$

## 7. CONCLUSIONS

Test and analysis procedures have been developed which permit the evaluation of the performance of a laser gyro during centrifuge testing. These procedures use counter-rotating tests on the centrifuge for evaluation of the gyro bias sensitivity to acceleration and fixed centrifuge tests for the determination of the gyro scale factor sensitivity to acceleration. Tests conducted on a Honeywell Model 1328AC laser gyro using these procedures revealed an apparent bias and scale factor sensitivity to the square of acceleration. It was shown that this apparent sensitivity could be caused by an acceleration sensitive gyro input axis misalignment relative to the centrifuge spin axis. From the tests conducted it was not possible to determine if this misalignment was internal to the gyro or if it was caused by a bending of the centrifuge. Additional test orientations have been suggested which should make it possible to more accurately locate the source of this misalignment.



REFERENCE

1. Inertial Navigation Equipment Evaluation Techniques, Department of Aeronautics and Astronautics, Massachusetts Institute of Technology, Cambridge, Massachusetts, 1963.

TITLE: ACCELEROMETER SCALE  
FACTOR AND LINEARITY  
CALIBRATION USING A  
LASER INTERFEROMETER

AUTHORS: PAUL KLINGENMEIER  
WILLIAM LANGE

BELL AEROSPACE TEXTRON  
Post Office Box One  
Buffalo, New York 14240

## ABSTRACT

TITLE: Accelerometer Scale Factor and Linearity Calibration  
Using a Laser Interferometer

Calibration of low-g full scale ranged, inertial grade accelerometers requires the accurate generation of g forces in the range of  $10^{-2}$  to  $10^{-6}$  (10 mg's to 1  $\mu$ g). One method of accomplishing this is to tilt the accelerometer sensitive axis from its null or true horizontal position by a known angle. The accuracy with which this angle can be generated, maintained, and measured determines the final accuracy of the calibration.

Conventional methods involve the use of either a dividing head or optical autocollimator which are manually adjusted and subject to reading errors by the operator. The resultant accuracy and resolution are in the order of 2 micro g's.

Accelerometers with full scale input limits of  $\pm 100$  micro g's and accuracies of 0.1% are now common requirements. To meet these requirements, improved versions of the autocollimator and several optical interferometers were studied and evaluated. The availability of laser interferometers with automatic fringe counting and outputs adaptable to recording proved to be the solution. The laser interferometer can readily resolve angles of .006 sec of arc. Converted to g's, this represents a basic measurement accuracy of .03 micro g. A test stand using the laser interferometer was completed in 1979, and is currently being used to calibrate electrostatic accelerometers with full scale input limits as low as 10 micro g's.

To measure angles, the laser is used as a distance measuring device. This is possible since for small angles the proportion of the earth's one g force coupled into the accelerometer sensitive axis is equal to the tilt angle in radians. For angles less than 0.05 radian the force is nearly a linear function of distance.

A change in distance  $D(\Delta D)$  is measured by the laser. With R (the tilt fixture hinge to measurement point) known, the change in input acceleration ( $\Delta G$ ) is equal to  $\Delta D/R$ .

Inherently the laser has zero linearity error. The accuracy is not dependent on dial calibrations or gear trains so there is no backlash or wind-up error to accumulate.

The laser measures only the tilt angle of the test stand with respect to the surface on which the fixture is mounted. It is insensitive to tilt of the stable base on which it rests.



The accuracy of the measurement is dependent on the accuracy to which  $R$  and  $\lambda$  are known and controlled.  $R$  can be physically measured to an accuracy of .005%. The wavelength  $\lambda$  is determined by the long term stability of helium-neon laser. It is expressed in terms of frequency deviation from the neon twenty emission line.

The complete accelerometer test station has been automated and is computer controlled.

Test programs can be readily modified to perform a large variety of measurements.

Typical tests cover linearity measurements of 10 to 50 points per scale.

The accelerometer operating temperature may be changed at discrete intervals to yield scale factor and linearity temperature coefficients.

Data output are printed for a permanent recording of input, output, time and temperature.

## INDEX

I INTRODUCTION

II DEVELOPMENT OF TILT ANGLE GENERATION

I  
III OPERATIONAL FEATURES

IV PERFORMANCE FEATURES

V SPECIFICATIONS

VI TEST RESULTS

1. Miniature Electrostatic Accelerometer (MESA)

2. Model XI, Pendulous, Force Balance Accelerometer

## I. INTRODUCTION

Performance testing and scale factor calibration of inertial grade low-g accelerometers has always presented a challenge to both the manufacturer and user of such devices.

The manufacturer needs to verify his design by testing and the user requires confidence in the design as well as accurate calibration data to meet his operational needs.

The generation of accurate inputs to a low-g accelerometer in the presence of the earth's 1 g field contributes considerably to this challenge.

Over the past years a number of approaches have been used to provide accurate acceleration inputs for this purpose. These techniques included the drop tower, aircraft, mass attraction, precision centrifuge, and tilt table.

The drop tower and aircraft techniques have the distinct disadvantage of high cost, low accuracy, and short test time duration.

Mass attraction techniques involve precise motion of large masses and are usually limited to the  $10^{-7}$  and  $10^{-10}$  range.

The precision centrifuge and tilt table are fairly compact and offer the advantage of large dynamic range, and a well defined null or zero input.

The tilt table offers the additional advantage of readily changing the input level in small increments for linearity measurement, and does not require slip rings to transport signals and power to the instrument under test.

The tilt table provides the means for coupling a known portion of the local 1 g acceleration force into the sensitive axis. The accelerometer axis is tilted from its true horizontal or zero g position by a known angle. The accuracy to which this angle can be generated, maintained, measured, and repeated determines the final accuracy of calibration. This latter method has been used extensively by Bell Aerospace, and an automated version of this technique is the subject of this paper.



## II. DEVELOPMENT OF TILT ANGLE GENERATION

In the earlier days of inertial grade accelerometer development, the basic tool used to generate and measure small angles was the dividing head. This device was designed primarily for use in the machine and tool industry. It was well suited for accelerometer calibration since it was readily available and represented a fairly massive stable test stand when properly isolated from local man-made disturbances.

The dividing head was used from about 1955 to 1965 for all accelerometer measurements. Its basic accuracy was two seconds of arc plus an additional one to two seconds for reading accuracy. This later error was dependent on the condition of the optics within a particular dividing head plus the operator's ability to read the dial calibration marks. Therefore, the worst case accuracy was four seconds with the average slightly greater than two seconds. Converted to g's, this represented a measurement accuracy in the range of 10 to 20 micro g's.

By 1965, requirements to produce instruments with full scale input limits of 1000 micro g's and accuracies of 0.1% of full scale (one micro g) became common. Since this was well beyond the capability of the dividing head, optical autocollimators were evaluated as a means to improve the angle measuring accuracy to the required one micro g. A number of automatic and manual models from several well known manufacturers were evaluated. Stability and reading error were noted under actual test conditions. The automatic or null seeking versions had excellent readout capability but suffered from repeatability and reliability problems. Since the servo loops were used at relatively high gain, the mechanical portions of the units suffered from wear due to continuous motion under noisy test base conditions.

The manual versions, although more difficult to read, were far superior in this respect since they had no active electronic circuits, motors or gear trains. In addition, the cost of manual models was only 20% of that of the automatics.

The accelerometers were still mounted to the dividing head together with a mirror which was viewed by the autocollimator. Accuracy thus obtained was an order of magnitude improvement over the dividing head. Each division on the readout dial represented 0.1 second of arc. The reading error added at least another 0.1 second to give an overall accuracy of 0.2 second of arc with worst case being in the order of 0.4 second. Converted to g's this represented a measurement accuracy in the range of 1 to 2 micro g's.

During the 1967-1970 period, requirements for even greater accuracy surpassed the capability of the optical autocollimator. Accelerometers with full scale input limits of 100 micro g's and accuracies of 0.1% now became common requirements. This meant angle generation and measurement had to improve another order of magnitude. To meet these new requirements improved versions of the autocollimator and several optical interferometers were studied and evaluated. The interferometer appeared to offer the most promise in both accuracy and readout ability. The availability of laser interferometers with automatic fringe counting and outputs adaptable to recording proved to be the solution. The laser interferometer can readily resolve angles down to .006 second of arc. Converted to g's, this represents a basic measurement accuracy of .03 micro g. The automated version of a test stand designed specifically for this application was completed in 1978 and is currently being used to calibrate accelerometers with full scale input limits as low as 10 micro g's. It represents the result of a 10 year company program to improve low g measurement accuracy.

### III. OPERATIONAL FEATURES OF THE LASER TEST STAND

To measure angles, the laser is used as a distance measuring device. For small angles the proportion of the earth's one g force coupled into the accelerometer sensitive axis is equal to the tilt angle in radians. For angles less than .05 radian the force is a linear function of distance. Figure 1 illustrates the basic principle involved.

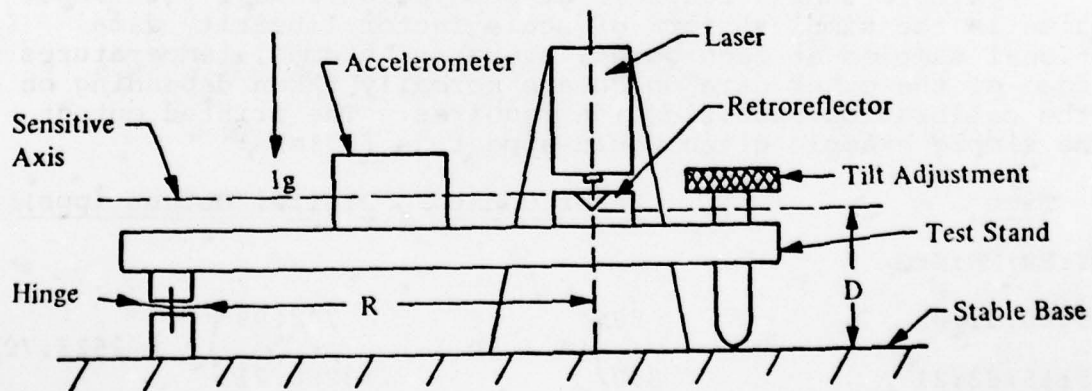


Figure 1. Distance to Angle Conversion

The change in distance  $D$ , ( $\Delta D$ ), is measured by the laser. With  $R$  known, the change in input acceleration ( $\Delta G$ ) is equal to  $\Delta D/R$ .

The smallest increment of  $\Delta D$  which can be resolved is dependent on the laser wavelength which in this case is 24.9 micro inches. The counter is mechanized to change a single digit for each  $1/40$  wavelength or 0.6225 micro inch.

With  $R$  equal to 18.675 inches and  $\lambda/40 = 0.6225$  micro inches,  $g = 0.6225/18.675 \times 10^{-6}$  or .033 micro  $g$  per digit change in the last place of the counter. Expressing the scale factor in terms of laser count pulses (LCP) per micro  $g$  is somewhat more convenient. In the example given, the scale factor is 30 LCP per micro  $g$ .

Assume the scale factor linearity of an accelerometer with input limits of  $\pm 100$  micro  $g$ 's is to be measured at 10 points on each side of null corresponding to 10 micro  $g$  steps. The coarse and fine tilt motors are manually controlled to adjust the accelerometer output to a null. The laser counter is reset to zero to coincide with the null. The tilt control motors are now adjusted until the laser counter reads +300 corresponding to an input of  $\pm 10$  micro  $g$ 's. The accelerometer output (voltage, current, or pulse rate) is now averaged and recorded over the desired sample period which is typically between 1 and 100 seconds. At the end of the sample period the tilt motors return the accelerometer to null and a new output sample is taken at null. Each measurement point thus has associated with it a null reading to make them independent of any slow base tilt over long periods of time.

A single sample recorded at each point, along with input and time is the simplest form of scale factor linearity data. Additional samples at each point, averages, sigmas, temperatures are some of the other data which are normally taken depending on what the calibration specification requires. The printed output in the simple example given would appear as follows:

<u>Time</u>	<u>Laser Count</u>	<u>Digital Output (pps)</u>
MO:DY:HR:MN:SEC		
02:15:15:31:05	89	742.99
02:15:15:33:21	390	3268.71
	} ( $\Delta = 301$ ) } $\Delta = 2525.72$	
02:15:15:35:44	90	449.40
02:15:15:37:55	692	5448.26
	} ( $\Delta = 602$ ) } $\Delta = 4998.86$	



Note that for two successive samples the input changed 1 count at null. The scale factor on this particular instrument was a nominal 250 pps/micro g.

The first input nominally 10  $\mu$ g, was actually  $(390-89)/30$  or 10.033  $\mu$ g. The output changed 3268.71 - 742.99 or 2525.72 pps. The resultant scale factor in pps/ $\mu$ g at 10  $\mu$ g input was  $2525.72/10.033$  or 251.74 pps/ $\mu$ g. The next input, nominally 20  $\mu$ g, was actually  $(692-90)/30$  or 20.067  $\mu$ g. The output changed 5448.26 - 449.40 or 4998.86 pps. The resultant scale factor in pps/ $\mu$ g at 20  $\mu$ g input was  $4998.86/20.067$  or 249.11 pps/ $\mu$ g.

A continuation of this process for both plus and minus inputs will yield the scale factor linearity over the entire  $\pm 100$   $\mu$ g range.

#### IV. PERFORMANCE FEATURES

Inherently the laser has zero linearity error. Unlike the autocollimator and dividing head, the accuracy is not dependent on dial calibrations or gear trains, so there is no backlash or wind-up error to accumulate. The accuracy is dependent on the stability of the wavelength and tilt arm radius R.

The laser measures only the tilt angle of the test stand with respect to the surface on which the fixture is mounted. It is insensitive to tilt of the stable base on which it rests. Normally a calibration point can be taken in a fairly short time (less than 3 min.). In this case, base tilt is negligible and may be ignored.

The accuracy of the measurement is dependent on the accuracy to which R and  $\lambda$  are known and controlled. R can be physically measured to an accuracy of +.001 inch or .005% of R. The wavelength  $\lambda$  is determined by the long term stability of helium-neon laser. It is expressed in terms of frequency deviation from the neon twenty emission line. After warm-up it is  $\pm 1$  MHz per day. This is one part in  $5 \times 10^8$  or  $\pm 0.00002\%$  of the laser frequency.

When measuring large distances (10 to 100 ft) the laser wavelength varies in the transmission medium and must be corrected for temperature and pressure. In this application the transmission path is 1/2 inch and is enclosed in a mylar sleeve which fits loosely over the end of the laser and retroreflector. This serves a dual purpose in that it gives the effect of a temperature controlled transmission medium (air) and also prevents convection currents from effecting the stability.

In addition to the precautions against wavelength variation, the test stand is temperature compensated by small equal length aluminum blocks which form a part of the fixture. This assures equal expansion on each end to prevent tilt due to temperature change of the fixture. The remainder of the fixture is steel.

Stability tests have given extremely good results. The output count was recorded continuously for a one-week period and remained within  $\pm 1$  count or  $\pm 3.3 \times 10^{-8}g$ . Periods of no count change were observed for as long as 36 hours.

An independent check on the scale factor of the laser expressed in laser count pulses (LCP) per micro g was made using a large number of readings (120) of an autocollimator viewing a mirror mounted on the side of the fixture. The autocollimator was adjusted to utilize only the 10% to 90% portion of its full range. Using 10 sets of 12 readings each gave a scale factor of 30.01 laser count pulses per micro g. Peak-to-peak variations in the 10 sets were 1 part in 6000 and 6 of the 10 were within 3 parts in 60,000 or .005%.

The tilt fixture and laser are controlled by an HP 9825A system controller. The calibration schedule or test program is recorded on the controller tape cassette. The accelerometer under test is placed within a thermally insulated container on the tilt table bed. Power is applied and the program is automatically executed in accordance with the taped instruction.

The first application of this device was to measure scale factor linearity and temperature coefficient of a 3 axis electrostatic accelerometer. Each axis in turn had 3 ranges or scales. The program called for a total of 1752 measurement points including several 24-hour power off periods to verify scale factor repeatability.

Before adding the 9825 controller the temperature, accelerometer range, tilt adjustment and output data recording were done manually. In the case of the three axis accelerometer this required approximately 240 man-hours, or 16 hours a day for 15 days with an elapsed time of 21 days. After automation the same test was performed with 12 man-hours and 6 days of elapsed time.

The number of computations that can be performed on the data by the 9825 is nearly unlimited. Typical examples of the extent to which this can be carried are presented in Section VI.

V. LASER TEST STAND SPECIFICATIONS

Range:	$\pm 12,000$ micro g's
Resolution:	$3.3 \times 10^{-8}$ g
Accuracy:	$\pm 3.3 \times 10^{-8}$ g
Laser:	Manufacturer: Hewlett-Packard
	Model: 5501A
	Type: Helium-Neon
	Wavelength: 24.91414 micro inches
Controller:	Manufacturer: Hewlett-Packard
	Model: 9825A
Test Fixture:	Manufacturer: Bell Aerospace
Temperature Control:	Manufacturer: Landa
	Model: K2R
	Range: 0°F to 160°F
	Accuracy: $\pm .05^\circ\text{F}$



## VI. TEST RESULTS

The laser test stand was developed to test a variety of inertial grade accelerometers. The most challenging application to date has been a three axis low g electrostatic accelerometer. Test results using this instrument as well as a higher g pendulous accelerometer will be described.

### 1. Electrostatic Accelerometer Test

The Miniature Electrostatic Accelerometer (MESA) was the first instrument to use the test stand. This particular version was a three axis, three scale per axis device as shown below.

<u>Axis</u>	<u>Range</u>	<u>+Full Scale</u> <u>(Micro g's)</u>
X and Y	A	6000
X and Y	B	600
X and Y	C	60
Z	A	15,000
Z	B	900
Z	C	60

The scale factor linearity on each range was measured at temperatures of 70, 80, 90, and 105°F. The input levels on each range were +20%, +40%, +60%, and +80% of full scale.

In addition to the required calibration schedule, several tests near null on the C (+60  $\mu$ g FS) range were made to determine linearity and reasonable sigma values that could be expected. These were run at input levels of +3, +6, +9, and +12 micro g's.

Typical data printout for one input level, temperature, axis, and range are shown in Figure 2.

Starting at the top of the page, the instrument serial number, year, and analog voltage correction factor are printed out. The correction factor is required to compensate for the input impedance of a voltmeter which monitors the temperature. The test temperature in this case is 90°F. The range is C or +60 micro g's in the Z axis.

AD-A076 567

ARMAMENT DEVELOPMENT AND TEST CENTER EGLIN AFB FL  
PROCEEDINGS OF THE BIENNIAL GUIDANCE TEST SYMPOSIUM (9TH) HELD --ETC(U)  
OCT 79

F/G 17/7

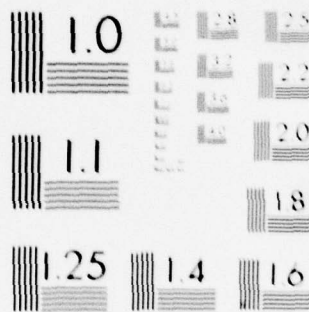
UNCLASSIFIED ADTC-TR-79-11-VOL-1

NL

3 OF 5

AD  
A076567





MICROCOPY RESOLUTION TEST CHART  
NATIONAL BUREAU OF STANDARDS-1963-A



INSTRUMENT : MESA S/N 4  
 YEAR=1979  
 ANALOG V CF = 1.003040

TESTING AT 90°F  
 TESTING C RANGE  
 Z AXIS

<u>TIME</u>	<u>LASER COUNT</u>	<u>DIGITAL OUTPUT</u>	<u>ANALOG OUTPUT</u>	<u>TEMPERATURE MONITOR</u>
MO:DY:HR:MN:SEC				
02:20:13:04:21	441506	-15581	-0.088431	2.76194
02:20:13:06:31	442948	-1112366	-6.362267	2.76092
02:20:13:08:57	441506	-12531	-0.070990	2.76021
02:20:13:11:10	442950	-1114005	-6.371698	2.75965
02:20:13:13:36	441504	-10131	-0.057312	2.75915
02:20:13:15:44	442950	-1114692	-6.375543	2.75880
02:20:13:18:05	441503	-14523	-0.082464	2.75845
02:20:13:20:13	442944	-1115256	-6.378814	2.75815
02:20:13:22:35	441498	-18221	-0.103610	2.75791
02:20:13:24:44	442936	-1112652	-6.363830	2.75765
02:20:13:27:07	441499	-16743	-0.095225	2.75745
02:20:13:29:18	442936	-1116167	-6.383975	2.75724

TEST AT THIS LEVEL IS SUCCESSFUL  
 INPUT = -48 MICRO G'S

DIGITAL DATA PULSES/SEC.	ANALOG DATA VOLTS	TEMPERATURE DATA VOLTS
-10965.54	-6.2916	2.7625
-10997.17	-6.3098	2.7610
-11012.74	-6.3186	2.7601
-11012.65	-6.3185	2.7594
-10972.44	-6.2954	2.7589
-11030.17	-6.3285	2.7584

AVERAGE = -10998.451    AVERAGE=-6.31039    AVERAGE = 2.7601

SIGMA    =    25.191    SIGMA    = 0.01442  
 SIG/AVE =    0.00229    SIG/AVE= 0.00229

FIGURE 2

The next five columns are time, input acceleration (laser count), digital and analog output, and temperature as monitored by a thermistor mounted on the accelerometer case.

The sample period was 100 seconds at each data point.

It is not necessary that the input be set to the exact value desired since this would result in excessive test time.

For each set of null and input data, the computer normalizes the analog and digital output to the values corresponding to the exact desired input change which was 48 micro g's in the sample shown.

The program called for six readings at each input level. The digital sigma limit was set at 50. In the event that this limit was exceeded in six readings, up to six additional readings were taken and the sigma recomputed. A limit of 12 readings was set at each point in the event that a particularly noisy base condition was encountered. The input in this case was a nominal 48 micro g's corresponding to an input count change of 1440.

After completing the six readings, the normalized average output pulse rate, analog voltage, and temperature for each of the six readings were computed and printed.

The average, sigma, and sigma/average, for the six readings were now computed and printed.

This data represents one of a total of 146 input levels measured.

## 2. Model XI Pendulous Accelerometer

Tests were conducted on the Model XI Pendulous Accelerometer using the laser test stand. The tests were performed in a manner similar to standard dividing head multipoint tests. The tests were run in the following sequence: 0 g to -full test range to +full test range to 0 g. The data was then fitted to a straight line using a least squares fit. The residual errors are shown in Figures 3 through 6 for runs from 100  $\mu$ g full test range to 10,000  $\mu$ g full test range. These residual errors are comprised of the following:

- 1) Readout equipment linearity errors
- 2) Readout equipment resolution of 0.1  $\mu$ g

3) Accelerometer linearity errors

4) Temperature sensitivity of accelerometer and laser test stand

5) Null stability of accelerometer and laser test stand.



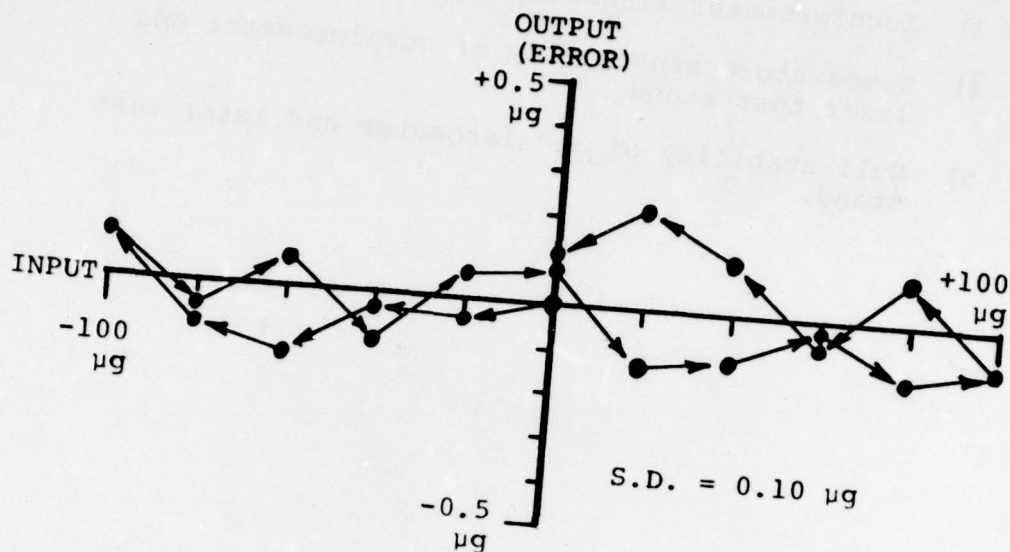


FIGURE 3. MODEL XI, S/N 023 DATA FROM -100μg TO +100 μg

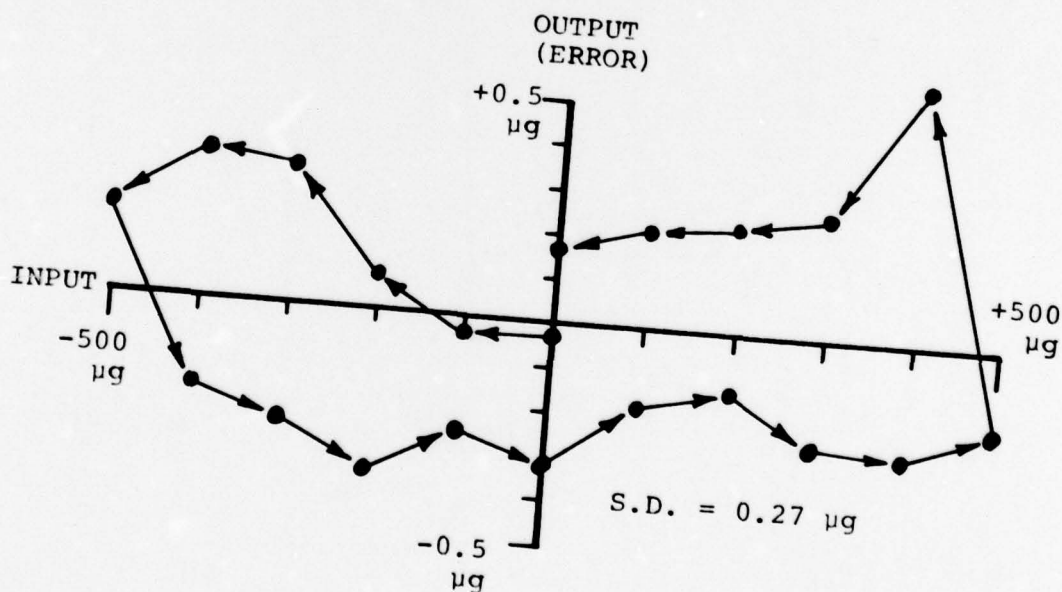


FIGURE 4. MODULE XI, S/N 023 DATA FROM -500 μg TO +500μg

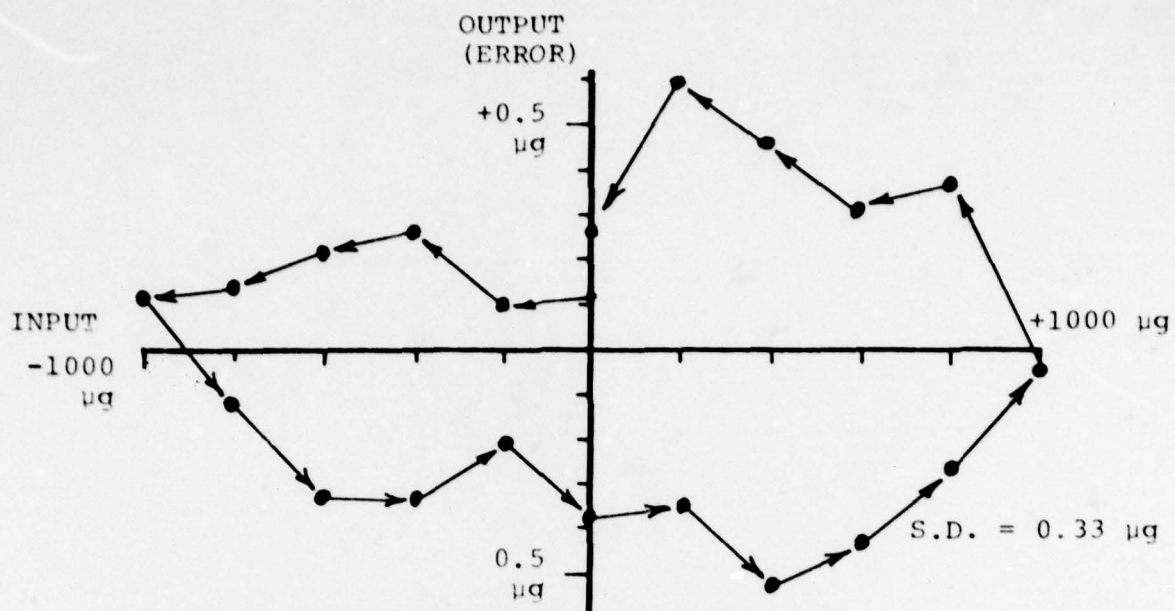


FIGURE 5. MODEL XI, S/N 023, DATA FROM -1000 µg TO +1000 µg

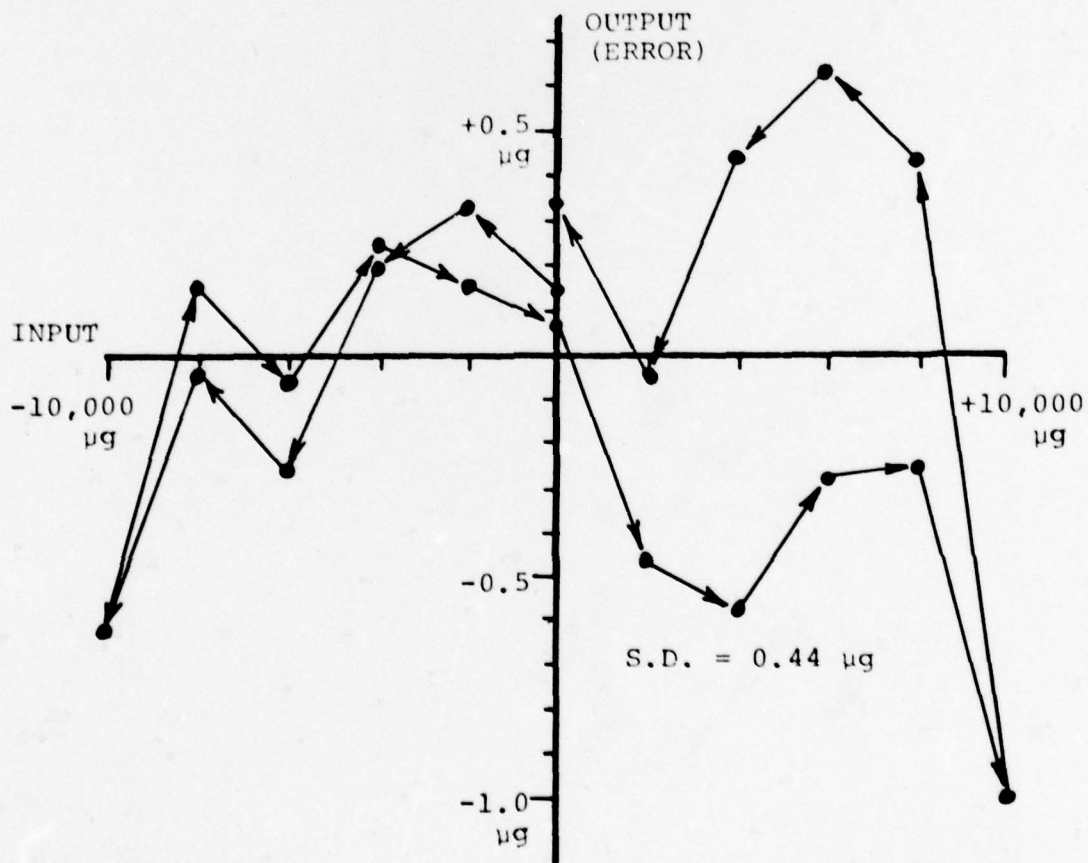


FIGURE 6. MODEL XI, S/N 023, DATA FROM -10,000 µg TO +10,000 µg

TITLE: EVALUATION OF AN FM/CW  
RANGE MEASUREMENT SYSTEM  
FOR VTOL LANDING

AUTHORS: DEAN G. KRENZ  
DAVID R. COLVIN

CUBIC CORPORATION  
Defense Systems Division  
San Diego, California

and

STANLEY K. MIYASHIRO  
FRANCIS E. MORRIS

NAVAL OCEAN SYSTEMS CENTER  
Tactical Sensors and EW Division  
San Diego, California



## ABSTRACT

A Precision Ku-Band FM/CW Range Measurement System was designed and built by Cubic for the Naval Ocean Systems Center to test and evaluate its effectiveness as a landing/guidance system for VTOL aircraft. Primary equipment consisted of an interrogator, transponder, control and display console, and government-furnished antennas and computer. The system operated on the principle that a continuous-wave signal modulated onto a radio-frequency carrier and propagated through free space undergoes a phase shift that can be measured to provide slant range. Test results conclusively indicate that the system provides more-than-adequate accuracy for the ranging requirements of a VTOL landing guidance system.

## INTRODUCTION

This paper describes: (1) the precision Ku-Band FM/CW Range Measurement System, with unique features, developed by Cubic for the Naval Ocean Systems Center (NOSC), and (2) the testing and evaluation of this system by NOSC as the ranging information source (sensor) of a landing aid for vertical takeoff and landing (VTOL) aircraft. A complete landing-aid system would also include a tracking antenna, which is not described in this paper.

An approach and landing guidance system is essential for landing helicopters and VTOL aircraft on ships. The system must provide coverage from approximately 5 miles to touchdown under clear and adverse weather. Weather conditions include heavy rain, zero ceilings, and horizontal visibility of less than 700 feet. Because of the small moving landing spot and the lack of maneuvering space on ships not designated as aircraft carriers, sensor accuracy must be better than  $\pm 1$  foot in position and  $\pm 1$  foot per second in velocity, at an update rate of 10 times per second during the last few hundred feet before touchdown. In addition, these stringent accuracy requirements must be achieved under conditions of extreme multipath reflections contaminating the direct radiation. Both the ocean surface and the superstructure of the ship contribute to these reflections.

The precision range measurement system developed by Cubic consists of a surface interrogator and airborne transponder. The system incorporates frequency modu-

lation of the Ku-Band transmitter to achieve precision range measurement. A variable modulation index feature was used to study the ranging accuracy at various modulation indexes, or spectrum widths, under extreme multipath conditions.

Testing was conducted at three locations to evaluate accuracy under the following general environmental conditions: (1) tests were made over a wire-screen ground plane located at NOSC on Point Loma to simulate conditions near and over the landing platform of small ships; (2) tests were conducted over water from Ballast Point to North Island — a distance of 986 meters — to simulate low-angle approach over water to the landing platform; and (3) flight tests were conducted with various approach patterns and aircraft altitudes, using the NASA Wallops Island Laser Tracking System as a ranging comparison standard.

Static tests under extreme multipath conditions indicated system accuracy to be within 2 to 3 inches. Analysis of this and other tests results leads to the conclusion that the Precision Range Measurement System more than adequately meets the requirements for the ranging information source of a VTOL guidance and landing system.

## SYSTEM DESCRIPTION

The Ku-Band FM/CW Precision Range Measurement System consists of an interrogator, a transponder, a control and display console, and the appropriate interconnecting cables. Antennas, RF waveguides and computer were government-furnished equipment. Figure 1 shows the items supplied by Cubic and the HP-9825A computer. A block diagram of the system is shown in Figure 2.

**INTERROGATOR** — The interrogator (Figure 1) functions as the master station in an interrogator/transponder arrangement. Accordingly, the interrogator contains the majority of frequency control, timing, and phase measurement circuits, and the data processing logic. It includes an internal power supply for operation from a standard 115 Vac power source. The interrogator is packaged in a standard ATR case.

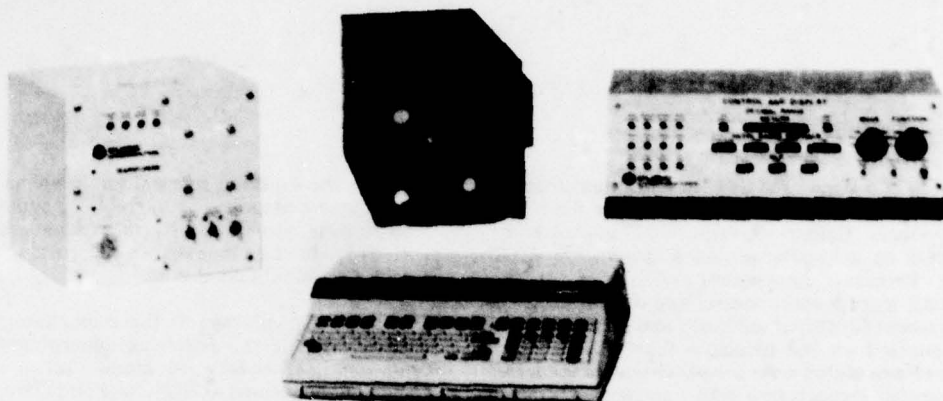


Figure 1. FM/CW Precision Range Measurement System with HP-9825A Computer

**CONTROL AND DISPLAY CONSOLE** — The control and display console (Figure 1) contains the operator mode and function controls and provides display of resolved decimal range, octal range partials, overlap corrections, relative signal strength, a data quality digit, and discrete data quality factors. The console also contains the system control logic, temporary data storage, binary-to-BCD conversion circuits, and the interface circuits for a computer. Packaged as a compact unit intended for desk-top operation, it may be mounted in a standard 19-inch rack if desired.

**TRANSPONDER** — The transponder (Figure 1) receives signals from the interrogator and processes and retransmits the signals automatically under control of the received signals. The only operator controls on the transponder are the power switch and the circuit breakers. The transponder will operate from either a standard 115 Vac power source; or any one of several possible +28 Vdc power sources. Housed in a portable case, it is suitable for mounting in a helicopter or other vehicle.

**SYSTEM OPERATION** — The Ku-Band FM/CW Precision Range Measurement System provides precise resolved range data to a computer at a data rate of 20 samples per second. In addition, the system displays the resolved range data and the unresolved range partials from four digital range-servo phasemeters. The range resolved data is displayed to a resolution of 25 millimeters. The system maximum unambiguous range is 104,857.6 meters.

The range measuring circuitry of the FM/CW DME operates on the principal that a CW electromagnetic wave propagated through space undergoes a phase change proportional to the distance travelled. The phase of the modulating frequencies transmitted by the interrogator, received and coherently retransmitted by the transponder, and received by the interrogator, are compared in the interrogator with the phase of the signals originally transmitted. The measured phase differences are converted to the analogous one-way distance between the interrogator and the transponder.

The system is capable of taking one range measurement every 50-milliseconds.

Four simultaneous modulating frequencies are used for range measurement — each frequency providing a progressively more precise measurement. The phase shift for each modulating frequency (or "range tone") is measured in digital servo phasemeters. Arithmetic logic in the interrogator resolves the corresponding ambiguities, provides automatic correction for interrogator calibration constants, and provides correction for fixed calibration constants. The output of the arithmetic processor is a binary resolved range word, 22 bits in length, with a maximum nonambiguous range of 104,857.6 meters, and a resolution of 25 millimeters.

The arithmetic processor also provides binary outputs of overlap corrections between the various adjacent range partial inputs from the digital servo phasemeters. The overlap corrections and the binary range data are transmitted to the control and display console where they are converted to numerical displays.

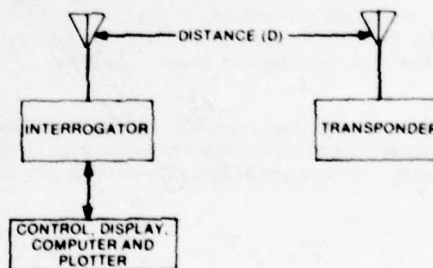


Figure 2. FM/CW Precision Range Measurement Block Diagram

The control and display console provides the operator with displays of data from the interrogator, contains the controls for selecting system modes and functions, and provides the interface for data and control signals between the system and the HP-9825A computer.

Provision is made in the system design to facilitate varying the range modulation index from 1.0 to 12.0 in order to investigate the effects of modulation index on range accuracy. Since the system accuracy and immunity to multipath effects improve as the modulation index and consequent bandwidth are increased, this capability was used to optimize the tradeoff between system accuracy and spectrum bandwidth requirements under realistic operating conditions.

#### SYSTEM INTERFACE WITH HP-9825A COMPUTER —

Although the interrogator is normally controlled from the control and display console, it is possible to interface the interrogator directly with a computer, and to provide interrogator control via the computer. The interrogator is compatible with IEEE-488-75 (or HP-IB) interface. It is, therefore, only necessary to provide a suitable interconnecting cable with proper connectors to interface the interrogator into such systems.

#### THEORY OF OPERATION

The FM/CW Precision Range Measuring System operates on the principle that a continuous-wave signal modulated onto a radio-frequency carrier and propagated through free space undergoes a phase shift directly proportional to distance traveled, in units of modulation wavelength. The phase shift is independent of carrier frequency, and can be measured in an electronic phasemeter and converted to a measurement of one-way distance (slant range).

A frequency synthesizer in the interrogator generates the range modulation that is transmitted to the trans-

ponder, retransmitted by the transponder, then received and demodulated by the interrogator receiver so that the round-trip phase delay can be measured and converted to range.

The basic system is designed to operate on a 50 millisecond time-shared cycle, wherein the interrogator may take range information from any of several transponders during sequential time periods. In testing however, only one transponder was required and all range data samples were taken from this transponder. In normal operation, most of the interrogations are ranging sequences where the interrogator measures the slant range to the transponder. Periodically, however, the system orders a calibration sequence where the interrogator interrogates an internal circuit in the RF front end in order to measure phase delays within the interrogator. The normal sequence provides for 2048 range data samples, then four calibration data samples — this cycle being continuously repeated.

For nonambiguous measurements, the modulating signal wavelength must be long enough so that the largest measurable phase delay (i.e., one-half wavelength) corresponds to the maximum range to be measured. For good resolution, however, a short wavelength is needed so that the smallest measurable phase delay corresponds to a small increment of range.

Four harmonically related frequencies ("range tones") are used. The highest frequency (or "fine" tone) establishes the system resolution; the lowest frequency (or "very coarse" tone) establishes the maximum range; and the two in-between tones, (designated "intermediate" and "coarse") permit the range ambiguities between fine and very coarse to be successively resolved. Stated another way, the very coarse tone puts you in the ball park, the coarse tone locates your section, the intermediate tone finds your row, and the fine tone puts you in your seat. The characteristics of the four range tones used by the FM/CW Precision Range Measurement System are listed in Table 1.

TABLE 1  
Range Tone Characteristics

Designation	Frequency (kHz)	Half Wavelength (Meters)	Resolution (Meters)
Fine (FN)	5,853.448	25.6	0.025
Intermediate (INT)	365.841	409.6	1.6
Coarse (CS)	22.865	6,553.6	25.6
Very Coarse (VC)	1.429	104,857.6	409.6

TABLE 2  
Range Modulation Frequencies

Symbol	Frequency (kHz)	Derivation	Modulation Index
D1'	5,853.448	FN	Variable to 12.0 max.
D2'	365.841	INT	2
D3'	388.706	INT + CS	2
D4'	341.547	INT - (CS + VC)	2



Because of the filtering problems that would be involved if frequencies of such wide variation as the basic range tones were to be transmitted and coherently tracked, the two lowest frequency tones are folded around the intermediate frequency using digital mixing techniques. The resultant range modulation frequencies are shown in Table 2.

The three lowest frequencies (D2', D3', and D4') are then added linearly to produce the composite range modulation baseband. The fine frequencies (D1') modulates the carrier separately. Because a large modulation index is used for D1' to minimize multipath error, the modulating signals are applied gradually to the carrier to prevent losing carrier loop lock at the transponder. The modulating signals are "ramped" onto the carrier during a 7-millisecond ramp period. The modulated carrier is transmitted to the transponder.

The transponder acquires and phase-locks to the interrogator carrier, demodulates and filters the modulation frequencies, recombines the three lowest frequencies, and applies the resulting baseband signals to its phase modulators. The transmitted signal is also used as the first local oscillator (LO) frequency for the transponder receiver. Therefore, a "modulation tracking" effect is achieved within the receiver. (During shop alignment, the phase of each modulating frequency is adjusted to provide negative feedback within the receiver circuits of the transponder.) The transponder then retransmits the signal on the transponder transmit frequency.

The interrogator receiver, in a manner similar to the transponder receiver, demodulates and separates the four ranging frequencies, recombines the three lowest frequencies, and uses the resultant signals to phase-modulate the VCO signal that generates the receiver first LO frequency, providing a negative feedback type modulation tracking loop. The individual tones derived from the demodulated transponder signal (which are now designated D1 through D4, corresponding to the D1' through D4' signals originally transmitted) are also translated to a common range servo frequency of 11.432 kHz through use of digital mixers and phase-locked loops. The D1' through D4' (originally transmitted) frequencies are used as references. The range servos themselves are phase-lock loops incorporating 8- and 10-bit counters in their feedback loops. The three lowest-frequency range servos each divide their respective measured phase delay into 256 parts. The fine servo, using a 10-bit counter, divides the phase delay into 1,024 parts. Further, after a suitable settling time, each servo is stopped as its reference reaches a zero crossing — automatically subtracting the reference so that the content of its feedback counter is a digital representation of the phase delay for the range tone. The zero crossing of the reference also ramps down the range modulation — terminating the interrogation and turning off the transmitter. Loss of carrier loop lock in the transponder receiver then causes the transponder to turn off its transmitter and revert to its standby (receive only) state.

Each of the four interrogator range servos presents the contents of its range data counter to an internal arithmetic processor. This processes the data from each servo using a subroutine that employs: (1) each range partial, (2) the current dynamic calibration data for the interrogator, and (3) the stored fixed calibration data for the transponder and antennas. The computation subroutine includes an ambiguity resolving algorithm which, with the corrections indicated above, finally produces a corrected composite range word representing the slant range to the transponder.

## SYSTEM TESTS AND EVALUATION

Extensive testing was conducted on the Cubic FM/CW Range Measurement System from June 1977 to December 1977. Since the ranging equipment is being considered as an integral part of an automatic VTOL landing system on small ships, the testing was directed toward simulation of these conditions.

Tests were run over a wire-screen ground plane located at NOSC on Point Loma. Specular multipath could be closely controlled over this surface and the conditions present over the landing pad of a small ship were closely simulated. It is during the final landing phase that the greatest accuracy is required and adverse multipath effects are at a maximum. Tests were also conducted on a 986-meter path over water at very low grazing angles to simulate the conditions during the early portions of the approach. Finally, flight tests were conducted at the NASA Flight Test Center at Wallops Island, Virginia. Various approaches and flight patterns were flown and the FM/CW system range data was compared to the range data from the NASA pulse laser ranging system.

Figure 3 illustrates the test set-up used for the ground plane tests. The ground plane used was approximately 50 meters square. This permitted test runs over a range of 10-50 meters. A rolling cart was attached to a

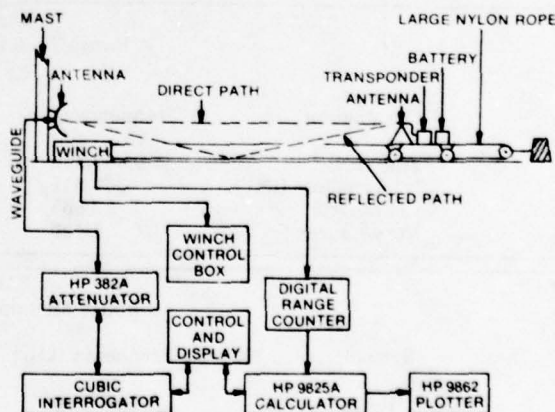


FIGURE 3. Test Setup for Ground Plane Tests



FIGURE 4. Test Range at NOSC

variable speed winch. As the cart was moved, the difference in the direct and the reflected path changed, and since the geometry could be closely controlled, the worst case multipath points were closely examined. The winch was instrumented to feed position information to an HP-9825 calculator. The calculator was used to control the system, to gather, record and reduce the data, and to furnish hardcopy data using the HP-9862 plotter. Raw information was recorded on magnetic tape and except for controlling the cart speed, the test runs were fully automatic.

Figure 4 is a photograph of the test range at NOSC.

Figure 5 is a plot of test data taken on the antenna range using broadband antennas and a modulation index of 1. The signal strength curve clearly shows the maximum multipath interference points. These occur where the difference between the direct and reflected path are a multiple of one RF wavelength. The standard deviation includes the mechanical error in the cart-measuring system, which was approximately 25 millimeters. There was a deliberate bias offset to facilitate clear discernment of the data.

In Figure 6, the modulation index was increased to 5.6 with a corresponding decrease in the standard deviation by a factor of two. The signal strength plot is essentially unchanged.

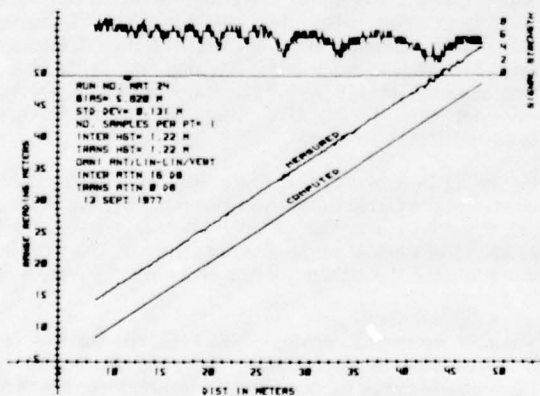


FIGURE 5. DME Range Plot: Modulation Index = 1

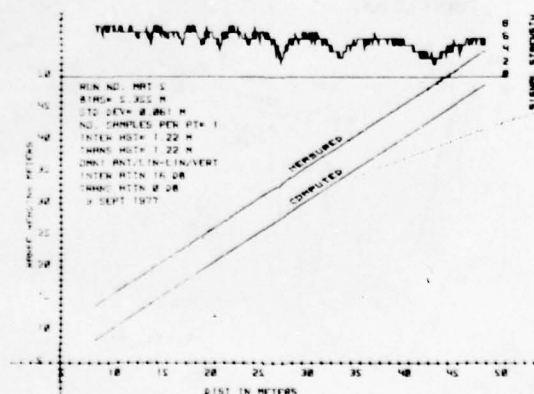


FIGURE 6. DME Range Plot: Modulation Index = 5.6

Figure 7 shows the omni antenna on the interrogator replaced with a three-degree-beamwidth parabolic antenna. The heights of the antennas were adjusted so that the minimum reflected path angle was 2 degrees. A range measurement standard deviation of 49 millimeters was obtained. Earlier anechoic chamber tests showed that the modulation index for minimum error was obtained at 5.6, although the equipment could produce a higher modulation index. This was felt to be due to bandpass limiting within the equipment. It is worth reemphasizing that the typical 49 millimeter error includes the mechanical error in the cart position.

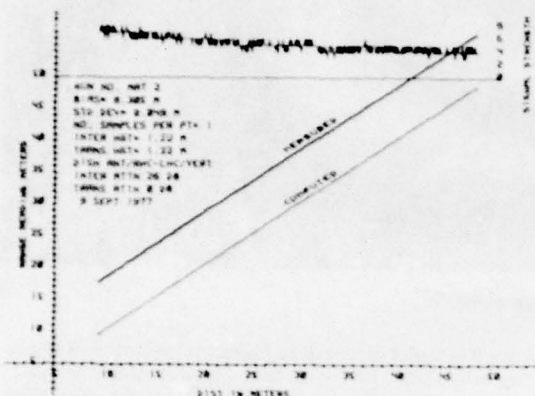


FIGURE 7. DME Range Plot: Three-Degree Antenna

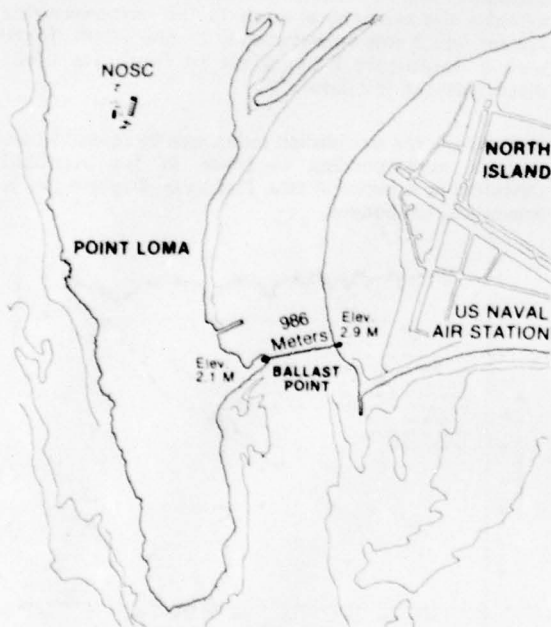


FIGURE 8. Over-Water Test Site

Long term stability runs were also made and these showed no shifts or drifts in excess of the resolution (25 millimeters) of the Cubic Range Measurement System.

The over-water path that was used to simulate the long-range low-angle approach of the VTOL's is shown in Figure 8. A path length of approximately 986 meters was used, and the interrogator and transponder were located at heights of 2.1 and 2.9 meters respectively. This yielded a grazing angle of 0.15 degrees.

Figure 9 shows the distributions for three stationary sets of 700 samples each. The bay surface was slightly disturbed by wind and ships passing. The antennas were linearly polarized and data was taken at a ten sample per second rate. As can be seen in the figure, a significant reduction in the standard deviation was obtained by increasing the modulation index from 1 to 2.4. Increasing the modulation index further to 5.6 also shows an improvement but not to the degree of the change from 1 to 2.4.

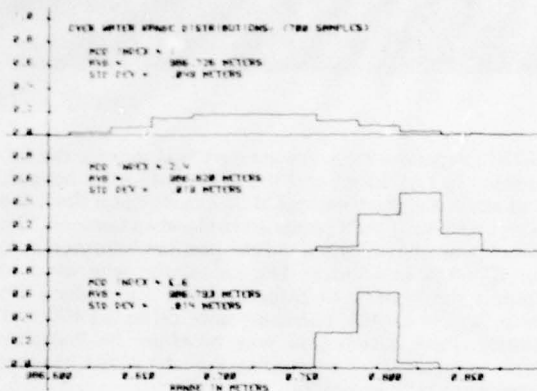


FIGURE 9. Over-Water Range Distributions

Figure 10 is a photograph of the controller, HP-9825A calculator, the plotter and floppy disc recorder at the NASA Flight Test Center. The range output of the laser was interfaced with the HP-9825. The 3-degree beamwidth antenna for the FM/CW Range Measurement System was mounted on a tripod and a rifle scope was mounted on it to permit manual tracking. The laser reflector and the FM/CW range transponder were mounted on a helicopter.

Figure 11 is a plot of 700 static samples, each, of the laser and the Cubic Range Measurement System before the dynamic runs. The offset in range is due to the geometry of the test set-up and not an error. The ratio of the standard deviations for the two ranging system is 17:1.

Various approach profiles were flown starting at approximately 8 kilometers. Figure 12 is a plot of time-versus-range for the FM/CW Range Measurement System for one of these runs. The section marked is enlarged in Figure 13.



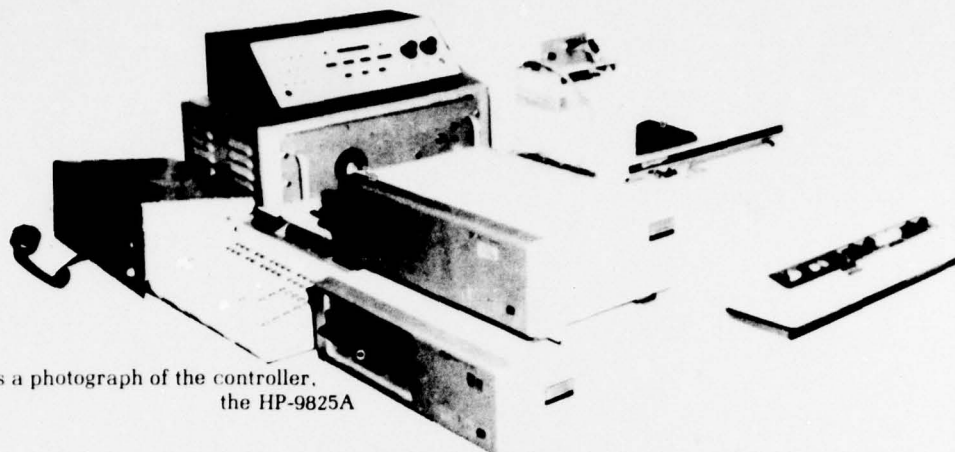


Figure 10 is a photograph of the controller,  
the HP-9825A

In Figure 13, the section marked in Figure 12 was approximately by a straight line, and the difference in range of the actual value and the straight line value is plotted for both the laser and the FM/CW Range Measurement System versus time. The significant difference in the standard deviation is obvious from the two traces. The offset between the two is again due to the test geometry. Data was taken at a rate of 10 samples per second.

#### CONCLUSIONS

Tests on the Cubic FM/CW Precision Range Measurement System show that this range measurement technique can meet the ranging accuracy requirements of a VTOL landing guidance system. During stability tests, the Cubic FM/CW range equipment showed no bias shifts greater than the 25 millimeter resolution of the equipment. The error standard deviation for static conditions was less than 25 millimeters for the higher values of modulation index. The accuracy under adverse multipath conditions depends on the modulation index and antenna directivity. For a nondirectional antenna, a modulation index of 5.6, and severe metal ground screen reflections, the total error

standard deviation is approximately 60 millimeters. With a directional interrogator antenna, the total error standard deviation is less than 50 millimeters.

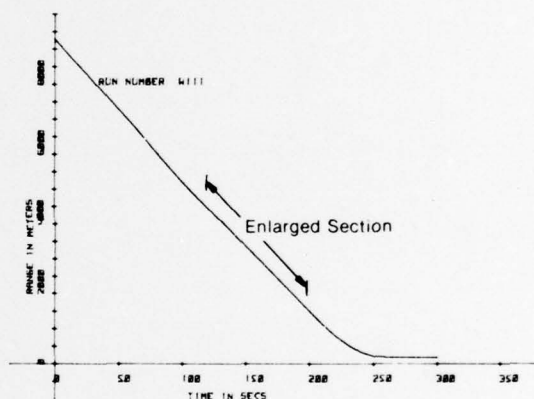


FIGURE 12. Typical Time-Versus-Range  
Plot for FM/CW System

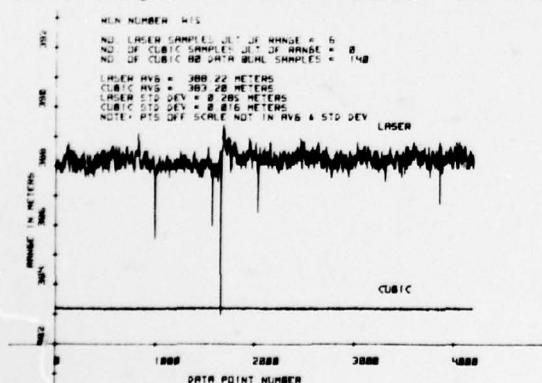


FIGURE 11. Comparative Plot of Laser  
and FM/CW system

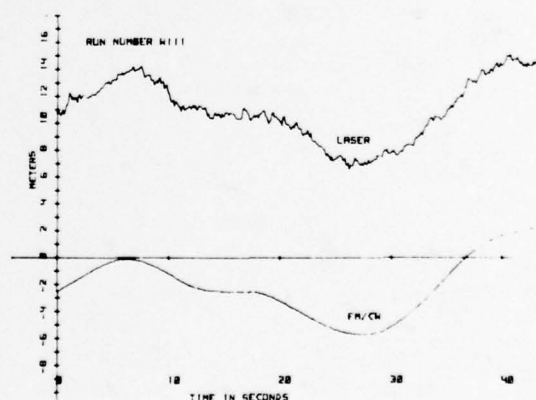


FIGURE 13. Enlarged Comparative  
plot of laser and FM/CW Data

TITLE: SPECTRAL NOISE PERFORMANCE  
OF A HIGH ACCURACY DRY TUNED  
GYROSCOPE AND THE NASA  
STANDARD REDUNDANT DRY  
ROTOR INERTIAL REFERENCE  
UNIT (DRIRU II)

AUTHORS: K. N. GREEN  
E. M. OSHIKA  
R. L. VAN ALSTINE

TELEDYNE SYSTEMS COMPANY  
19601 Nordhoff Street  
Northridge, California 91324

706

## TABLE OF CONTENTS

Paragraph		Page
1	INTRODUCTION .....	1
2	TEST HARDWARE DESCRIPTION .....	2
2.1	Teledyne SDG-5 Gyroscope .....	2
2.2	Standard DRIRU II Inertial Reference Unit .....	5
2.3	Modified DRIRU II Single Channel System .....	8
3	TEST METHODS AND TEST RESULTS .....	9
3.1	Background .....	9
3.2	Power Spectral Density .....	10
3.3	Noise Equivalent Angle .....	17
3.4	Random Walk .....	20
3.5	Low Frequency Drift Variations .....	23
4	SUMMARY .....	29
5	ACKNOWLEDGEMENT .....	29
6	REFERENCES .....	29



## ABSTRACT

An increasing number of space and military applications require low noise performance from gyroscopes and inertial reference systems due to increased precision required for spacecraft navigation and control systems and various pointing systems. Recent tests on the NASA Standard Redundant Dry Rotor Inertial Reference Unit (DRIRU II) and on the Teledyne SDG-5 dry tuned gyroscope have demonstrated noise levels well below any previously reported levels. These levels are sufficiently low to satisfy the most demanding of the known low noise applications.

This paper reports the results of noise tests conducted at Holloman Air Force Base Central Inertial Guidance Test Facility and Teledyne Systems Company on a standard DRIRU II system and on a modified version of DRIRU II with greater resolution and extended bandwidth gyro caging loops.

Two methods of measuring noise were used though not necessarily at each facility: power spectral density (PSD) of sensed output rate and overall noise equivalent angle (NEA). The latter method has been specified by several DRIRU II users as a means of expressing angle noise in the system output. It is particularly useful in fine pointing system applications where a total "jitter" specification is desired.

PSD measurements at CIGTF on the modified DRIRU II system demonstrated noise levels less than  $10^{-7} (^{\circ}/\text{hr})^2/\text{Hz}$  in the range of 0.0025 to 0.25 Hz. Above that range, and up to 250 Hz, noise levels were below  $10^{-4} (^{\circ}/\text{hr})^2/\text{Hz}$  except at isolated frequencies associated with the spin motor drive frequency. At these frequencies, 100 and 200 Hz, noise spikes of approximately  $10^{-3} (^{\circ}/\text{hr})^2/\text{Hz}$  were observed. The shape of the noise spectrum measured at CIGTF and at Teledyne verifies the absence of a random walk growth characteristic for the SDG-5 gyro drift.

Noise equivalent angle data are presented for tests conducted at Teledyne on standard DRIRU II hardware and on the modified version. Typical performance is a fraction of the basic DRIRU II specification of one arc second peak-to-peak total angular change for one hour.

The test methods and data reduction techniques are discussed and the analytic models that can be used to describe test behavior are considered. The basis for previously used random walk models and the modelling errors associated with their use are discussed in light of these test results.

## 1. INTRODUCTION

Several current applications generate a need for measurement and modelling of the noise properties of high precision gyroscopes. This paper presents recent measurements of the Teledyne SDG-5 dry tuned gyroscope and discusses the difficulties associated with measuring the low noise levels of this gyroscope. The SDG-5 is the basis of the NASA Standard High Performance Inertial Reference Unit, the DRIRU II<sup>1</sup>, which provides a precision attitude reference for a new family of spacecraft. Noise data generated for this application and related applications are shown in various forms. The use of the noise data is also discussed.

Accurate attitude measurement has been desired for many satellite borne payloads, particularly for earth and stellar observational packages, and future requirements will seek the best possible performance. Future projects such as space based observatories and monitoring stations, space based solar power relay stations and laser or directed energy systems presume the availability of accurate pointing and control. The development of the required control systems is in turn dependent on valid measurement and modelling of the noise characteristics of the sensors used for attitude measurement. The optimal filter<sup>2</sup> developed for use with DRIRU II is considered to be an example of the kind of processing required to obtain the desired performance.

In terrestrial applications, the development of inertial navigation systems has progressed to the point where it is reasonable to assume the availability of perfect attitude reference subsystems in the analysis of the inherent errors of the conventional inertial system. That is, the dynamic effects of the deflections of the vertical due to vehicle motion are now of concern since gyro errors can be made small in comparison to gravity uncertainties<sup>3</sup>. Operation from a moving base cannot approach the accuracy obtainable from a stationary base without compensation for the deflection of the vertical. Thus, improved inertial navigation systems seek to augment the conventional inertial navigator with gravity gradiometers or mappings of gravity correlated indirectly to other features<sup>4</sup>. However, these improved navigation systems are dependent on the practical realization of highly accurate attitude reference subsystems. The optimization of the attitude subsystems and the system as a whole also requires valid treatment of the noise of the sensors. The low noise levels and the simple models that were found for the SDG-5 gyro should thus also be of interest for improved inertial navigation.

The features of the SDG-5 gyro that cause it to be a low noise sensor are discussed below, together with a general description of its operation. The standard DRIRU II system is then briefly described as well as a modified version which was used for much of the SDG-5 testing. Finally, the test procedures and results from several test series are described, and the usage of the resulting measurements is discussed.

## 2. TEST HARDWARE DESCRIPTION

### 2.1 Teledyne SDG-5 Gyroscope

The SDG-5 gyroscope is a dry tuned gyroscope optimized for strapdown usage. It is one of the first gyroscopes that allowed strapdown inertial navigation accuracy in the one mile per hour category to be obtained. It is distinguished by its high accuracy design and high torquing rate capability when compared to other dry tuned gyroscopes. Long term drift in the 0.01 deg/hour category with torquing rates greater than 100 deg/sec are basic operational features.

In contrast to other dry tuned gyroscopes that are primarily used in gimballed inertial systems, the SDG-5 is a high angular momentum, low speed gyro ( $10^6$  gm-cm<sup>2</sup>/sec @ 100 revolution/sec). It is therefore more stable with respect to noise and error torques, but also larger than the less stable gyros. The 3 inch case diameter allows incorporation of a three gimbal suspension system without extreme minaturization. The three gimbal suspension further lowers the effect of error torques by eliminating several dynamic noise effects. The physical dimensions also allow the incorporation of a highly linear and symmetric magnetic design for torquing, and a proportional inductive pickoff that is well isolated from torquing inputs.

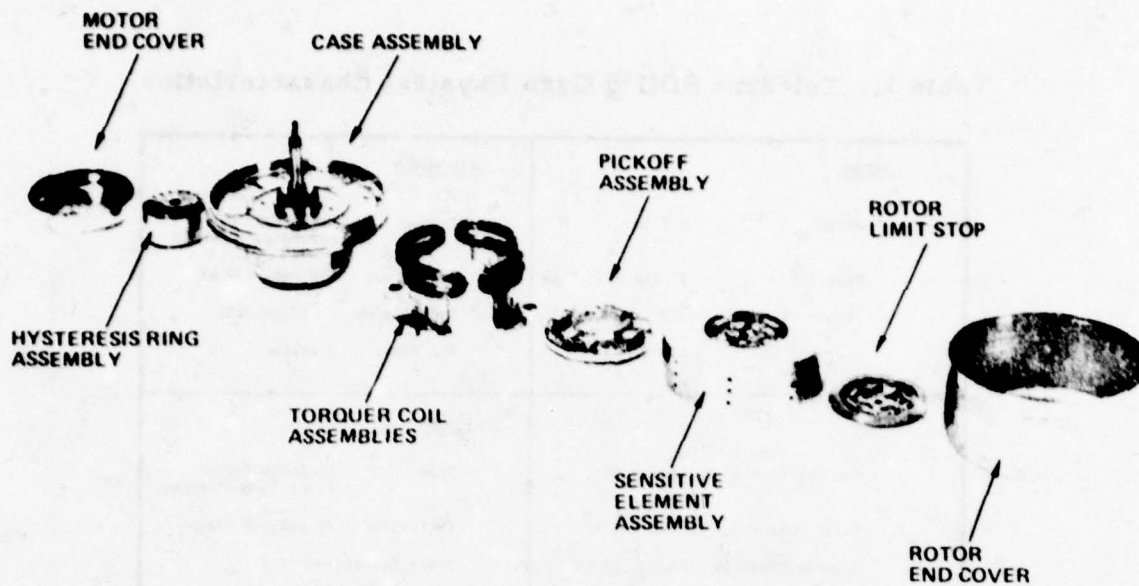
The gyro has been designed to be easily compensated for temperature effects, and thus does not require temperature control. Both analog electrical self compensation and digital computed compensation have been used to obtain high performance without temperature control.

The gyro has been designed to deliver high performance under severe environmental conditions, but the same design features provide low noise operation when operated in quiescent conditions. For the DRIRU II spacecraft attitude application, the gyro is effectively operated in a highly derated condition and delivers a very low noise level.

The SDG-5 consists of four major subassemblies: the case, torquer coils, pickoffs, and sensitive element containing the tuned three-gimbal suspension system and rotor. These subassemblies are shown in Figure 1 and a schematic cross section of the gyro is shown in Figure 2. The gyro case supports a set of ball bearings which in turn carry the shaft. Mounted on one end of the shaft is the motor hysteresis ring and on the other end is the rotor and suspension system. The torquer coils and pickoff subassembly are attached to the case. The end covers, when soldered in place, provide the hermetic seal for the gyro.

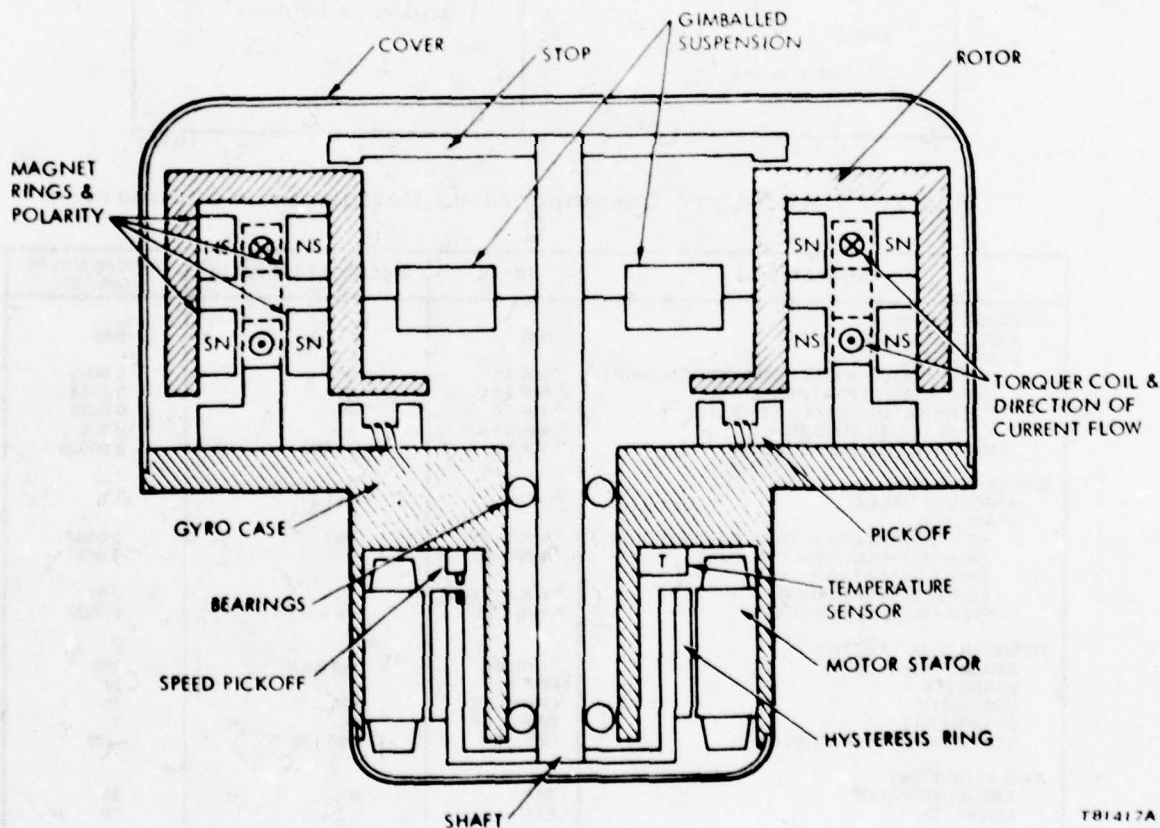
A summary of physical characteristics for the SDG-5 is presented in Table 1 and key performance characteristics are shown in Table 2.





P81419B

Figure 1. SDG-5 Strapdown Gyro Subassemblies



T81417A

Figure 2. Schematic Cross-Section of the SDG-5 Gyro

Table 1. Teledyne SDG-5 Gyro Physical Characteristics

<p><u>GENERAL</u></p> <p>Weight 2.3 lbs.</p> <p>Size 1" dia x 3" long</p> <p>Figure of Merit 320</p> <p>G-capability 150 g</p>	<p><u>SPIN MOTOR</u></p> <p>Type Hysteresis Synchronous, 2 or 3 <math>\phi</math></p> <p>Excitation 30V rms, 400 Hz</p> <p>Run-Up Time 30 seconds</p> <p>Run Power 2 watts</p>
<p><u>ROTOR</u></p> <p>Mass of Rotor 260 grams</p> <p>Polar Moment 1600 gm-cm<sup>2</sup></p> <p>Angular Momentum <math>1 \times 10^6</math> gm-cm<sup>2</sup>/S</p>	<p><u>PICKOFF</u></p> <p>Type Variable Reluctance Transformer</p> <p>Excitation 7V rms, 48 KHz</p> <p>Scale Factor 100v/rad</p>
<p><u>SUSPENSION</u></p> <p>Tuned 3 gimbal</p> <p><u>HEATER</u></p> <p>None required</p>	<p><u>TORQUER</u></p> <p>Type Permanent magnet</p> <p>Scale Factor 150°/hr/ma</p>

Y125976

Table 2. SDG-5 Gyro Uncompensated Performance Summary

PARAMETER	UNITS	SPECIFICATION VALUE	TYPICAL VALUE (MEAN)
<b>G-INSENSITIVE BIAS</b>			
ABSOLUTE VALUE	°/HR	0 ± 2.0	< 0.50
STABILITY			
CONTINUOUS OPERATION (RANDOM DRIFT)	°/HR 10'	.001	0.0005
SHUTDOWN REPEATABILITY	°/HR 10'	.01	0.0016
TEMPERATURE CYCLE STABILITY	°/HR 10'	—	0.0033
LONG TERM TRENDING	°/HR/YEAR	—	0.010
TEMPERATURE SENSITIVITY	°/HR/°F	0 ± .002	0.00050
<b>G-SENSITIVE BIAS</b>			
ABSOLUTE VALUE	°/HR/G	0 ± 1.0	< 1.0
STABILITY			
CONTINUOUS OPERATION (RANDOM DRIFT)	°/HR/G 10'	.002	0.0007
SHUTDOWN AND TEMPERATURE	°/HR/G 10'	—	0.008
CYCLE REPEATABILITY			
LONG TERM TRENDING	°/HR/G/YEAR	—	0.02
TEMPERATURE SENSITIVITY	°/HR/G/°F	0 ± .02	0.0032
<b>TORQUER SCALE FACTOR</b>			
ABSOLUTE VALUE	°/HR/MA	140 (MIN)	150
STABILITY	PPM 10'	—	27
LINEARITY	PPM PEAK	100	25
ASYMMETRY	PPM PEAK	—	3
TEMPERATURE SENSITIVITY	PPM/°F	-230 ± 20	-229
<b>AXIS ALIGNMENT</b>			
ABSOLUTE VALUE	SEC	60	30
STABILITY	SEC	—	10
<b>ANGULAR RATE CAPABILITY</b>			
STEADY STATE	°/SEC	100	> 100
TRANSIENT	°/SEC	400	> 500
ANISOTELASTICITY	°/HR/g <sup>2</sup>	0 ± .03	.01
GYRO TIME CONSTANT	SECONDS	100 (MIN)	200

Y10184

## 2.2

### Standard DRIRU II Inertial Reference Unit

DRIRU II is a strapdown redundant attitude reference unit for use in spacecraft. Its design emphasizes high accuracy, high reliability and low power consumption obtained through heaterless construction and CMOS electronics. The unit contains three independent channels, each of which provides two axes of output information, and is therefore redundant in a two channel of three basis. DRIRU II contains the following major elements:

- a. Three two-degree-of-freedom SDG-5 gyros
- b. Three independent sets of channel electronics, each containing five modules
- c. Three independent power supplies
- d. One isolated chassis and separate housing assembly

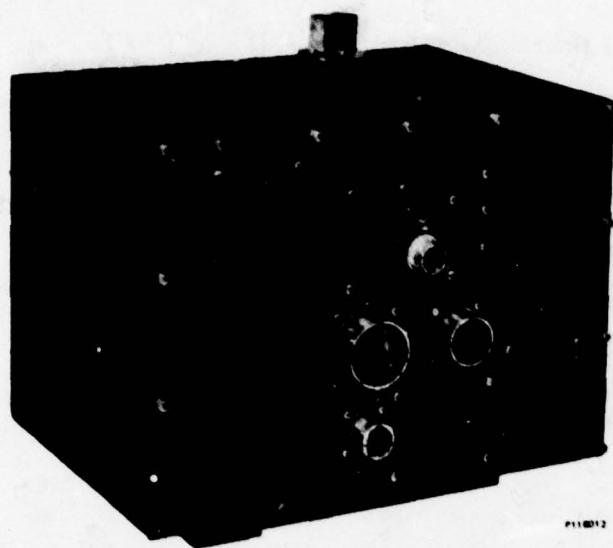
A photograph of the basic DRIRU II unit is shown in Figure 3. The exploded view in Figure 4 shows the mechanical relationship and modular construction of the major elements. The chassis containing the gyros, electronics and power supplies is supported by the housing through the use of four vibration isolators as shown. This isolation system provides protection from the high mechanical inputs during payload launch and deployment while maintaining the axis alignment stability required during use. A three point mounting referenced to the optical master reference cube is used for precision alignment.

DRIRU II operates on  $28 \pm 7$  VDC prime power and nominally consumes 22.5 watts. Dual range, analog rebalance loops are used with an externally supplied discrete range command for high rate tracking or low rate precision pointing. Gyro torquer self-test capability is also included. The system outputs are analog rates, digital incremental angles, and a clock reference. Telemetry outputs allow range status, gyro temperature, motor current and regulated voltage from each of the three channels to be monitored.

The functional block diagram for a single gyro channel shown in Figure 5 demonstrates the signal flow and indicates the relationship between the gyro and electronic modules. Low power, nuclear radiation resistant CMOS electronics are used throughout.

The gyros are caged in an analog torque to balance mode. The voltage developed by the restoring current passing through precision scaling resistors is digitized by reset integrating voltage to frequency converters. Two sets of scaling resistors are used per gyro axis to provide the externally commandable high and low rate ranging.





HEIGHT: 10.32 MAX.  
 DEPTH: 11.473 MAX.  
 WIDTH: 13.125 MAX.

Figure 3. DRIRU II System

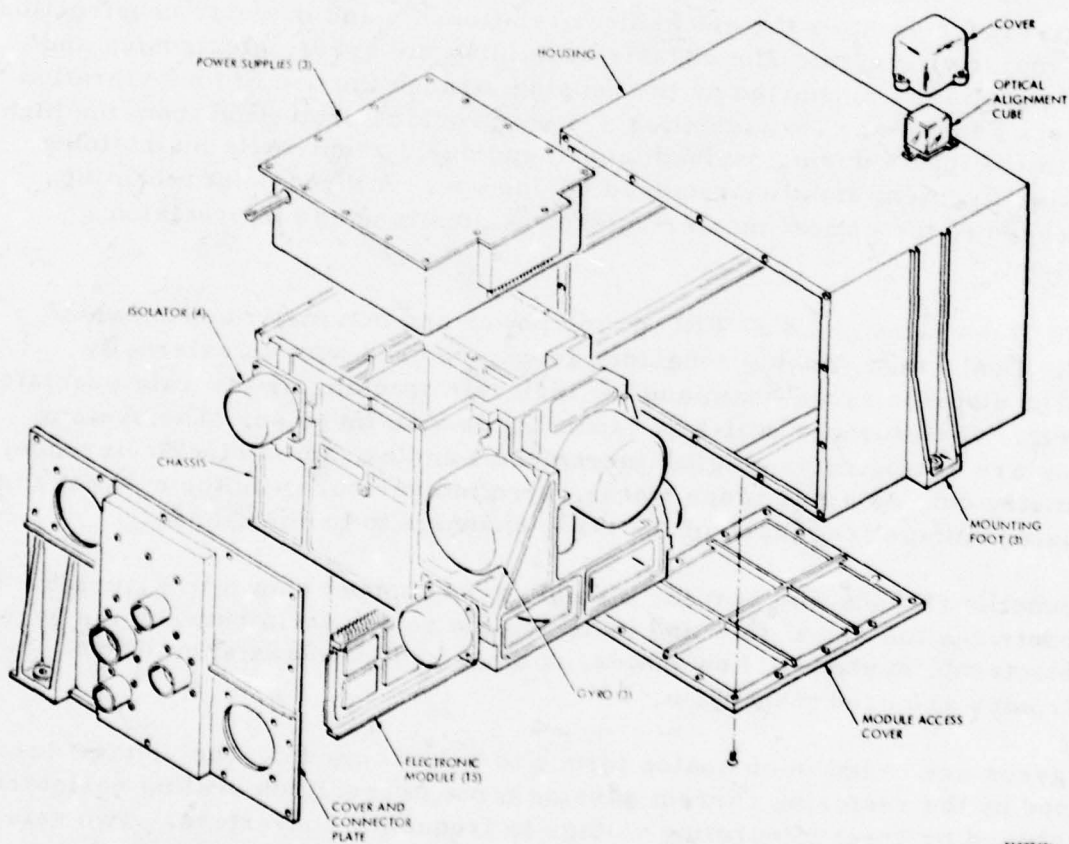


Figure 4. DRIRU II System Exploded View

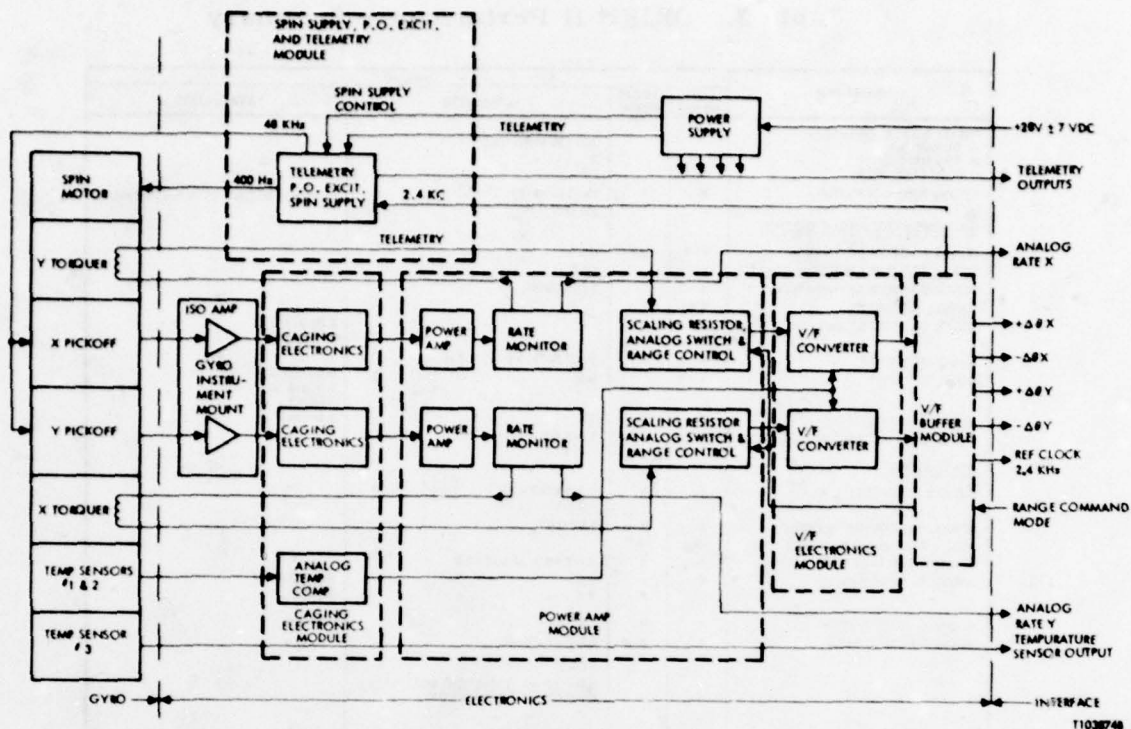


Figure 5. DRIRU II Single Channel Functional Block Diagram

Self-contained analog temperature compensation is employed for operation over a 40°C temperature range without the need for external software compensation. Each gyro contains three independent temperature sensors. One is used per axis for the self compensation and a third for telemetry output. The telemetry output may be employed to add software compensation if operation over a broader temperature range and/or increased performance over current specifications are desired. Wide range temperature performance is a consideration because no heaters or temperature control are used in DRIRU II. Significantly reduced power consumption and increased reliability through simplification are thereby obtained.

The performance of the DRIRU II is specified by NASA /Jet Propulsion Laboratory Specification ES511749, Revision C. A summary of key performance requirements is presented in Table 3.

Table 3. DRIRU II Performance Summary

PARAMETER			VALUE	
	LOW MODE	HIGH MODE	ABSOLUTE	STABILITY
INPUT RATES (DEG/SEC)			600 (20 MINUTES)	
A. SURVIVAL			2	
B. TRANSITION			1.6	
C. PERFORMANCE				
CROSS AXIS COUPLING	X	X	1% (TO 1 HZ) 2% (TO 7 HZ)	± 0.005% 30 DAY LOW RATE ONLY
INCREMENTAL ANGLE OUTPUT				
SCALE FACTOR (SEC/PULSE)	0.05	0.8	0.5%	
SCALE FACTOR LINEARITY (%)	X		0.01	
SCALE FACTOR ASYMMETRY	X		1±0.00005	
RANGE (DEG/SEC)	0.11	2.0		
SCALE FACTOR STABILITY	X			0.01%/MO. 0.1%/MO.
BANDWIDTH (HZ)	X	X	7 HZ MIN 0.5 < 1.0	
AIDR (SEC/SEC)	X		0.5	0.04/30DAY 0.003/6 HR 3.6/MO
ASDR (SEC/SEC/G)	X	X	3.0	0.04/MO
NOISE EQUIVALENT ANGLE (SEC)	X		1.0/1 HR P P	
ANALOG RATE				
RANGE (DEG/SEC)	X	X	± 1.0 LINEAR 2.0 SAT.	
SCALE FACTOR (V/DEG/SEC)	X	X	12 ± 0.6	
SCALE FACTOR LINEARITY	10%	SAT		
BANDWIDTH (HZ)	X	X	7 HZ MIN 0.5 < 1.0	
AIDR (BIAS) (SEC/SEC)	X		0.5	0.1/MO
		X	7.2	3.6/MO.
ASDR (G SENSITIVITY)	X	X	3.0	0.04/MO
NOISE (SEC/SEC RMS)	X	X	0.5 (0.1 7 HZ) 0.05 (0.01 1 HZ) 5.0 (100 HZ GREATER) MULTIPLES OF ROTOR FREQUENCY	
LIFE			2 YEAR (ORBIT) 2500 HOUR (GND) 600 1200 HOUR (PRE DELIVERY)	

112-3008

### 2.3 Modified DRIRU II Single Channel System

A single channel of DRIRU II electronics was modified for evaluation of the SDG-5 for use in fine pointing applications such as the Space Telescope mission. The major modifications consisted of the following:

- Increased gyro caging loop bandwidth from 7 Hz to 20 Hz
- Notch filtering of the gyro spin frequency (100 Hz)
- Improved low rate range resolution from 0.05 arc seconds/pulse to 0.0004 arc seconds/pulse by reducing the low rate range from  $\pm 400^\circ/\text{hr}$  to  $\pm 15^\circ/\text{hr}$  and increasing the V/F converter frequency deviation range from  $\pm 8$  kHz to  $\pm 40$  KHz.

These modifications were made to a breadboard version of the DRIRU II electronics which was packaged for transportability and ease of testing.



### 3. TEST METHODS AND TEST RESULTS

#### 3.1 Background

The tests used for noise measurements of gyros are intended to be conducted with zero or constant angular rate inputs. The variability about a constant bias rate is then considered to be noise. A number of methods for measuring and specifying noise have been developed to meet general or specific needs. Three of these methods, power spectral density, noise equivalent angle and random walk, are discussed here and test results are provided.

During any series of noise tests it is difficult to provide a truly constant (or zero) rate input to the gyro, especially at low frequencies that may be of interest. Both periodic (diurnal) inputs and random seismic or cultural inputs are observable in long duration tests. These low frequency effects are considered to be concealed in previous tests of the SDG-5,<sup>5,6</sup> and to have yielded noise models that are not appropriate, especially with respect to random walk.

It has also been found to be difficult to provide constant angular rates other than those due to earth rate. The sensitivity and angular quantization of the test data is such that harmonics of table motion have dominated measurements using rate tables. The positioning servos used for nearly all precision rate tables generate sinusoidal rate errors that are a function of the rate table position. The rate tables used in these tests generally employ a multi-speed inductosyn for position reference in the precision rate mode. The small differences between the inductosyn readout and the synthesized position reference cause a readily observable sinusoid corresponding to the inductosyn period. Post processing of data has been applied to correct for this effect, but no accurate method has yet been found to conduct tests at higher angular rates. (Higher in this instance refers to rates that approximate earth satellite orbital rates; 200 deg/hr is used in the DRIRU II tests).

The test data discussed in this paper are based on strapdown operation of the SDG-5 in which torques are applied to null the gyro. In this case the free rotor equations apply and, for constant rates, the torque is proportional to the rotor angular rate. The torque is integrated and digitized to obtain a measurement.

Tests of the SDG-5 with analog output electronics accomplished this measurement with the use of the Fluke 8500A integrating voltmeter. A sampling period of 1.1 seconds was used to obtain the extended records. In this case the voltage generated across a precision resistor by the torquing current

was provided directly to the meter. The integrated voltage was scaled by the integration time and converted to a digital value using an A/D converter within the meter. The value thus corresponds to the average angular rate over the sampling period. These values were then summed and averaged to obtain angular rate samples corresponding to more convenient periods for further processing.

Tests of the DRIRU II system and modified DRIRU used the system electronics instead of the meter. In this case a voltage-to-frequency converter is used to accomplish the integration and digitization. The resistor voltage is integrated and a pulse is output when the quantization level is reached. A pulse train with pulses of fixed angular weighting and with frequency proportional to the angular rate is thereby produced. The standard DRIRU II quantization is 0.05 arc second/pulse, and for the modified DRIRU electronics is 0.0004 arc second/pulse. The maximum deviation frequency is  $\pm 8$  kHz for DRIRU II and  $\pm 40$  kHz for the modified DRIRU which results in a maximum rate capability of  $\pm 400$  deg/hr and  $\pm 15$  deg/hr, respectively in the low range scaling.

The pulse train can be summed over any desired sampling period and scaled by the period to obtain periodic samples of the average angular rate. DRIRU II is intended for low angular rates so the shortest sampling period is normally 0.200 seconds, which is compatible with the 7Hz caging bandwidth.

The noise test data has been processed to yield both frequency spectrum information and time series behavior at various integration orders of the data. The frequency information is in the form of power spectral density of angular rate. The time behavior has primarily been examined as a noise equivalent angle, and the random walk has been considered with respect to both its frequency transform and time trend characteristics.

### 3.2 Power Spectral Density

The Power Spectral Density (PSD) is the most common and widely used form for presentation of noise data. The PSD can be interpreted in many ways. In this study the spectra have been used to establish the following SDG-5 characteristics:

- 1) Low power density, (less than  $10^{-6} (^\circ/\text{hr})^2/\text{Hz}$  from .0025 Hz to .5 Hz)
- 2) Low overall noise power ( $.01^\circ/\text{hr}$  rms from .0025 to 250 Hz)
- 3) Lack of significant low frequency harmonics

- 4) Flat (white) spectrum in the range of measurement
- 5) Undiscernible random walk content

The low noise power indicates that accurate pointing and attitude hold functions can be provided by the SDG-5.

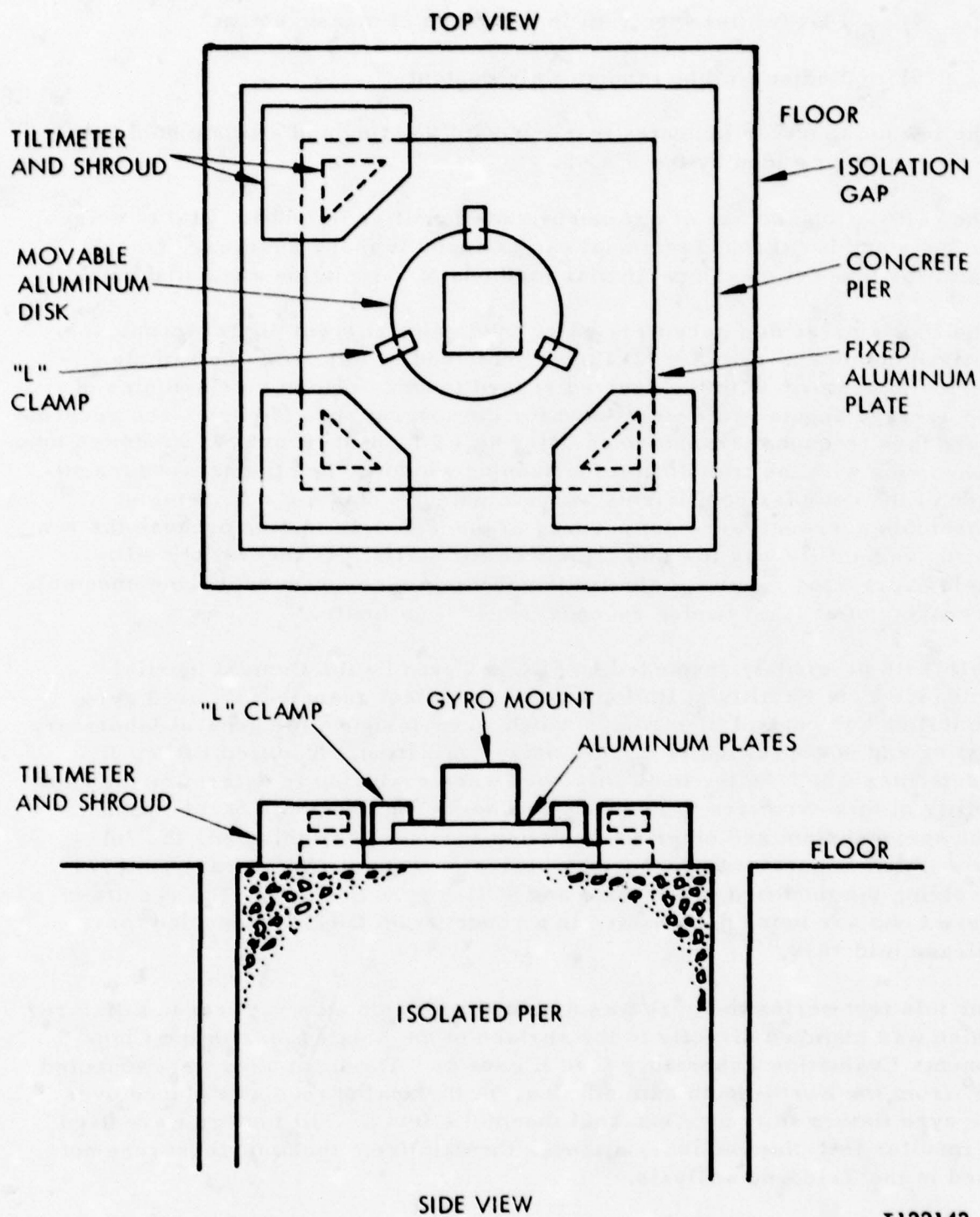
The calculation and use of power spectral densities is fundamental to noise analysis and background material can be found in many sources.<sup>7, 8</sup> Familiar properties and particular methods of calculation are noted below.

The PSD's presented here were calculated using current digital techniques. A fixed number of samples (2048) was obtained by adjusting the sample period to conform with the desired record length. One minute samples of the average angular rate were used for the longest runs (34 hr). The records were then frequency transformed using an FFT, post transform windowed by convolving with the transform of a Hanning window, then the squared magnitude of the complex coefficients was evaluated to obtain a PSD sample. Ensemble averages were not pursued in the Teledyne testing because the run to run variability was low and allowance for statistical uncertainty still yields very good results. The Holloman results do however include ensemble averaging of at least twelve records per PSD estimate.

PSD tests previously conducted on SDG-5 Gyros by the Central Inertial Guidance Test Facility at Holloman and other test agencies<sup>5, 6</sup> used gyro excitation and control electronics which were designed for general laboratory testing and not specifically for low noise evaluation. Modified DRIRU II electronics which better meet this need were evaluated to determine the capability of this hardware to meet the low noise requirements of the Space Telescope System and other fine pointing systems. To this end, the Jet Propulsion Laboratory sponsored a series of tests at CIGTF early in 1979 involving the modified electronics and SDG-5 gyro S/N 080. The results of these tests are being documented in a report from CIGTF scheduled for release mid 1979.

For this test series the gyro was mounted with spin axis vertical in a fixture which was clamped directly to the surface of an isolated pier in the Components Evaluation Laboratory (see Figure 6). The input axes were oriented 45° from the North-South azimuth line. A thermal shroud was placed over the gyro fixture to reduce external thermal effects. Tilt meters were used to monitor test pier motions, although the data from these meters were not used in the Teledyne analysis.





T122143

Figure 6. SDG-5 PSD Test Installation at Holloman CIGFF

PSD data were acquired from both the analog and digital output channels as shown in Figure 7. The analog outputs were fed into a Rockland Model 816 multichannel filter. The filter frequencies used were 0.3, 3.0, 30 and 300 Hz depending on the frequency of interest for each particular run. The outputs of the filters were analyzed as described previously using a Hewlett-Packard Model 5451 Fourier Analyzer. The data were taken in 12 frames of 2048 samples at sample rates of 0.5, 5, 50 and 500 Hz, corresponding to analysis frequencies of 0 to 0.25, 0 to 2.5, 0 to 25 and 0 to 250 Hz, respectively.

Figures 8 and 9 show composite plots of the PSD data acquired on the X and Y gyro axes. The overall noise power for each is less than  $0.01^{\circ}/\text{hr rms}$  to 250 Hz.

It is significant that the low frequency data is at least two orders of magnitude lower than previously reported data<sup>5,6</sup> and remains flat with decreasing frequency. This latter observation supports the conclusion that the drift output of the SDG-5 does not grow with time such as would be expected with a random walk drift model.

Three frequencies of interest are identified on the plots - the bearing retainer frequency (34 Hz), the rotor spin frequency (100 Hz), and the second harmonic of the spin frequency (200 Hz). Even these maximum noise frequencies show very low amplitudes and contribute very little to overall angular uncertainty. For example, the angular contribution of the worst case 100 Hz component would be only  $2.5 \times 10^{-8} (\text{arc sec})^2/\text{Hz}$ .

In order to verify the validity of the data, a calibration of the analog PSD channels was performed. A 1 volt peak, 100 Hz signal was injected in place of an analog gyro output signal and a PSD plot of the resultant noise was generated. Figure 10 shows that the calibration of the system was within 1 db, and that the noise measurement threshold itself, with the laboratory reference signal, was comparable to the low frequency noise levels exhibited during the gyro PSD tests plotted in Figures 8 and 9. This would indicate that the  $10^{-7} (^{\circ}/\text{hr})^2/\text{Hz}$  levels shown may be due to test instrumentation or other noise inputs and not indicative of ultimate gyro performance.

Subsequent testing at Teledyne supports this conclusion. Figures 11 and 12 show results of low frequency PSD tests run during the long term drift stability test series described in a later section in this paper. Note that generally flat noise levels of less than  $10^{-10} (^{\circ}/\text{hr})^2/\text{Hz}$  were measured. The frequency range was from  $8 \times 10^{-6}$  to 0.008 Hz, corresponding to periods of 34 hr to 120 sec. The data demonstrates exceptional performance capability for the SDG-5 gyro and for a system with modified DRIRU electronics.

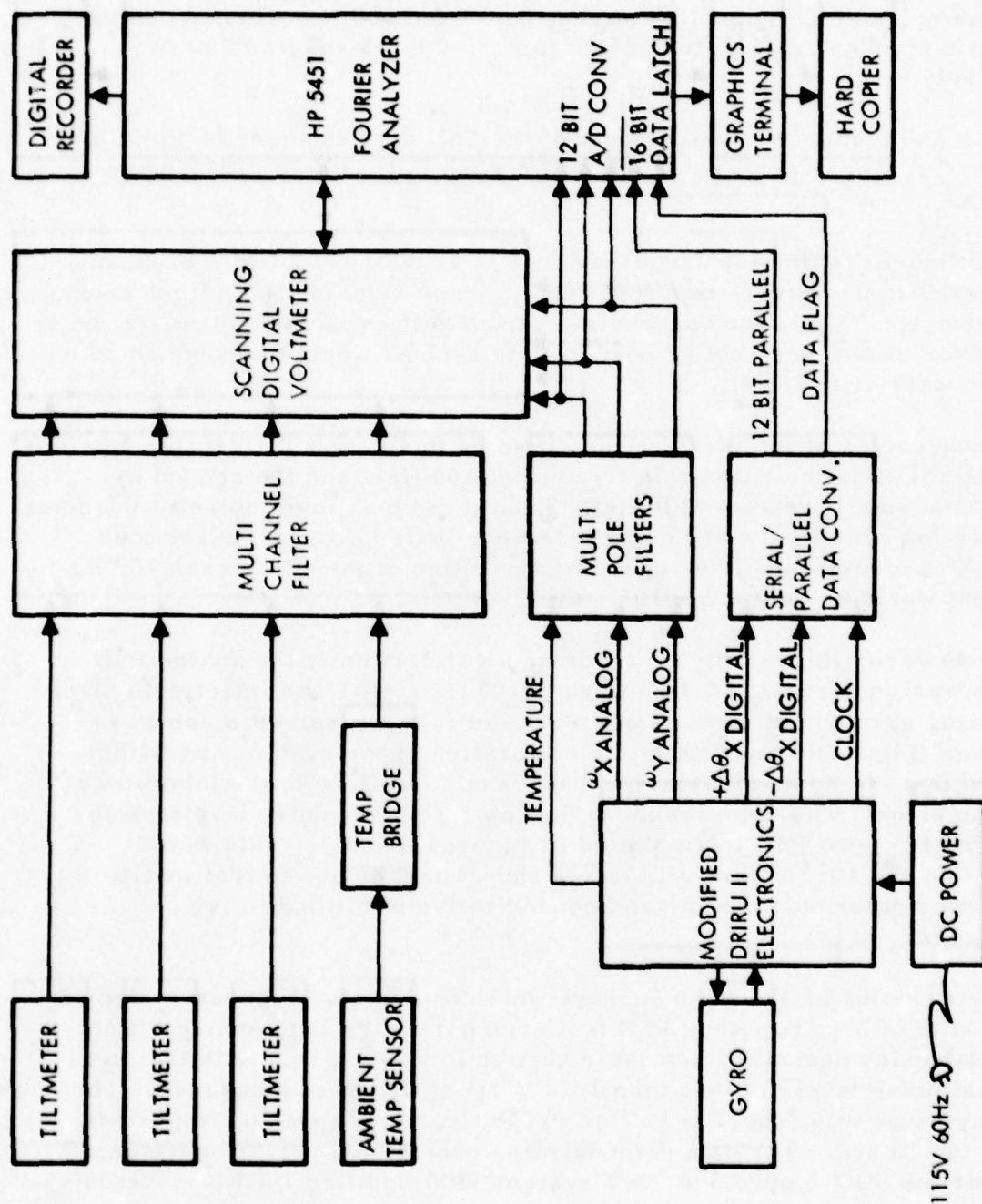


Figure 7. Data Acquisition System Block Diagram, Holloman PSD Tests

T122144A



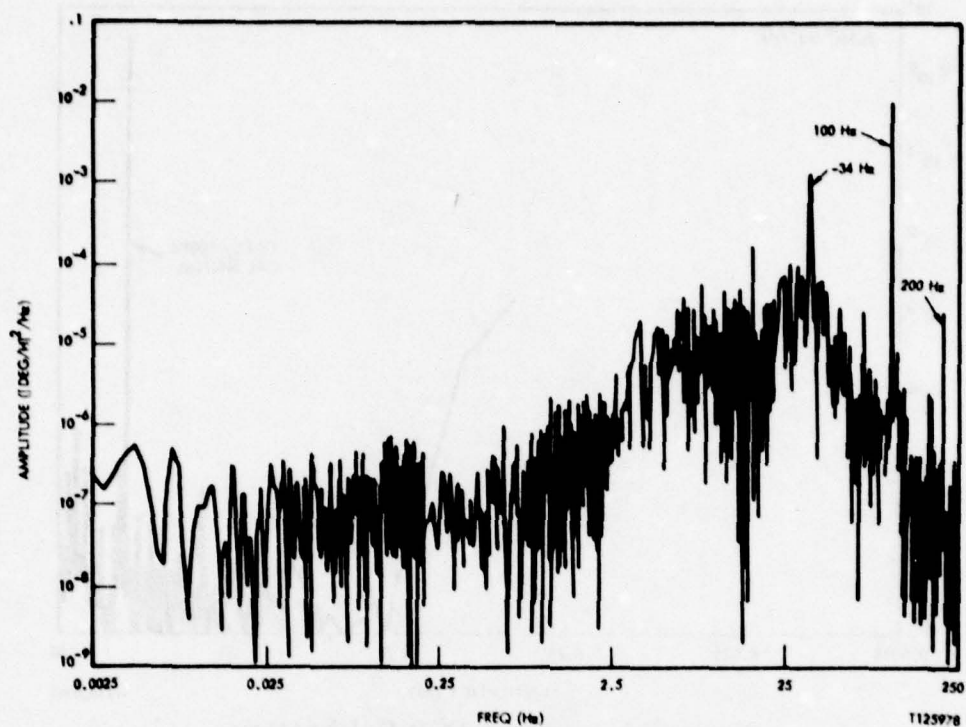


Figure 8. X Axis Analog Channel PSD, S/N 080

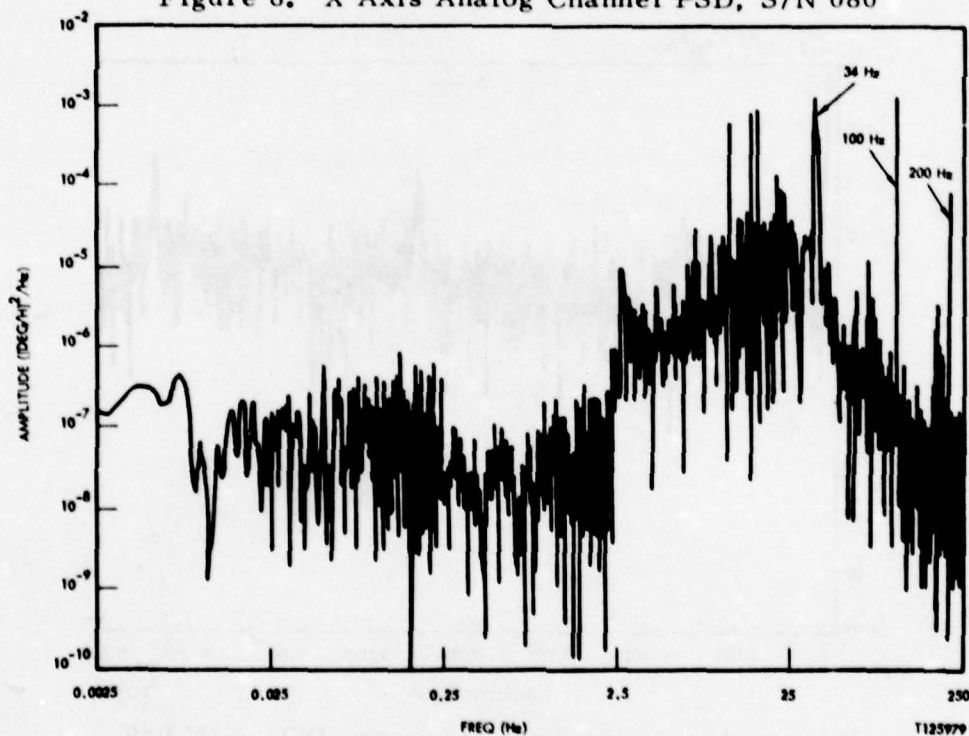


Figure 9. Y Axis Analog Channel PSD, S/N 080

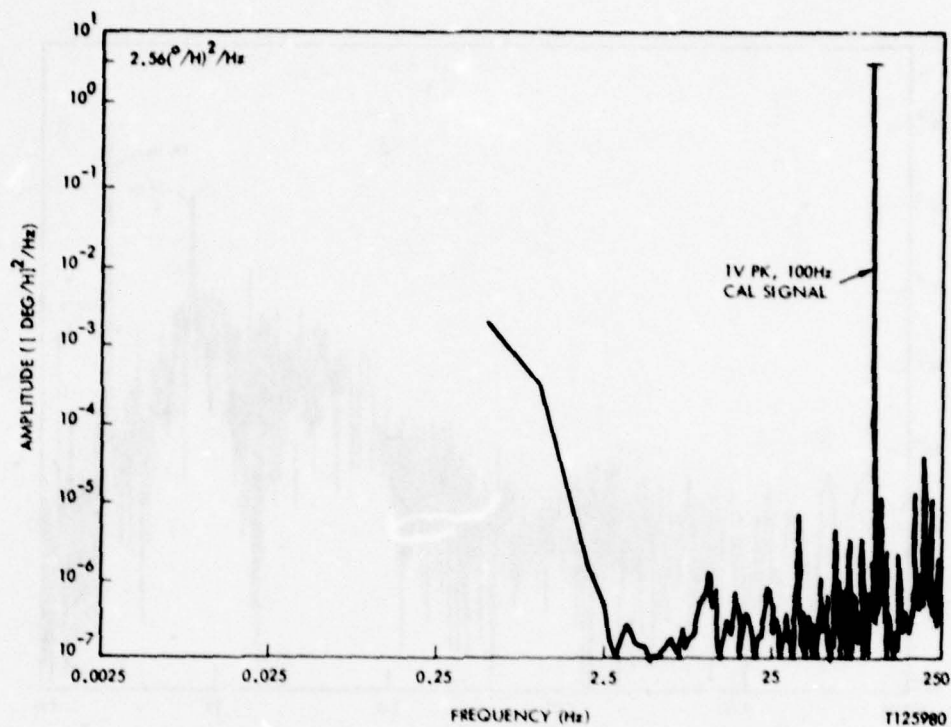


Figure 10. Analog PSD Calibration

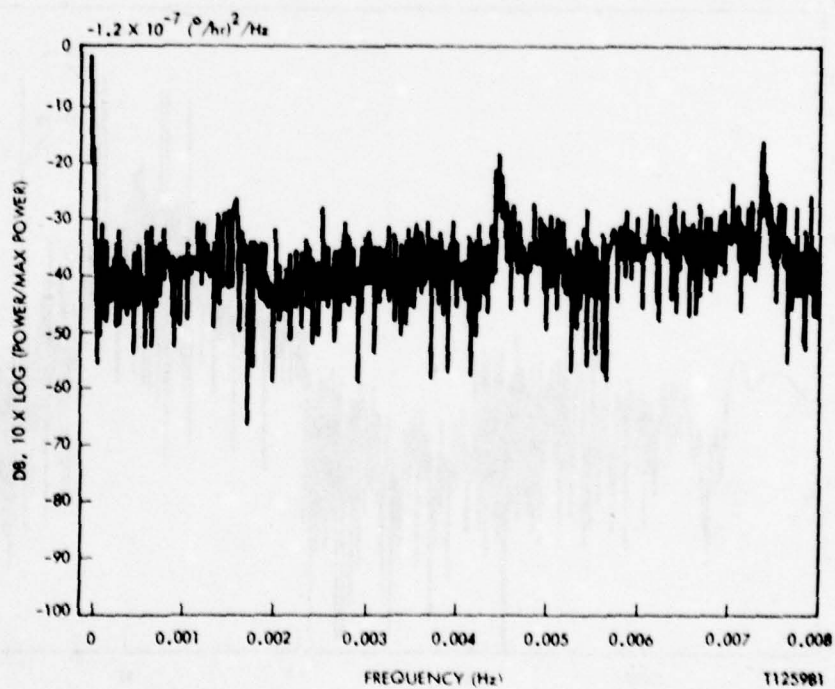


Figure 11. X Axis Low Frequency PSD, S/N 080

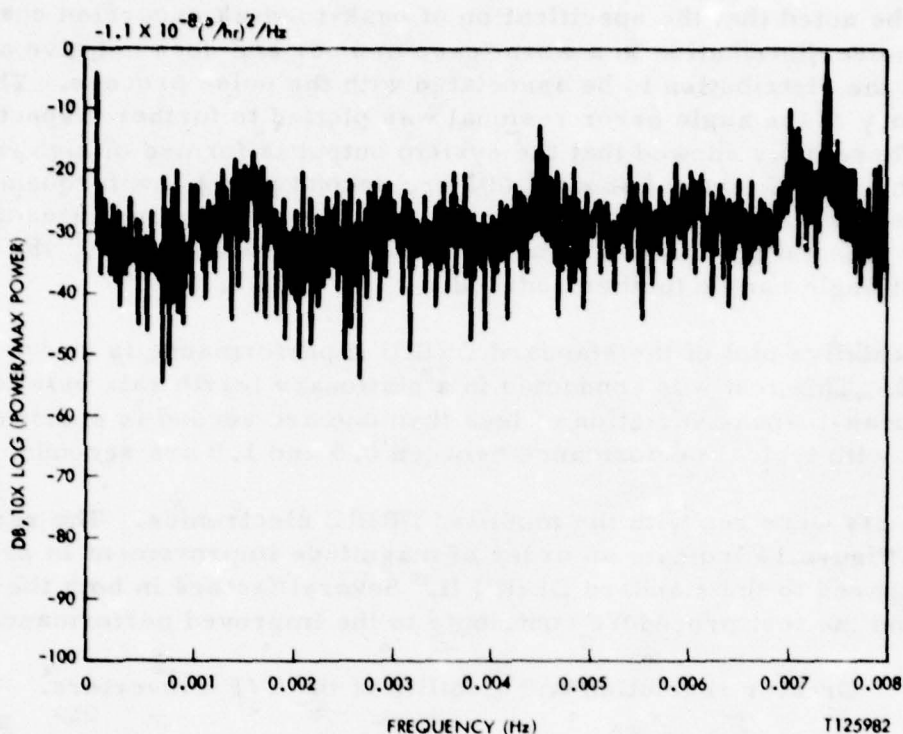


Figure 12. Y Axis Low Frequency PSD, S/N 080

### 3.3 Noise Equivalent Angle

A specialized test has been defined for evaluation of NASA attitude reference systems to assess pointing stability. The test, referred to as the Noise Equivalent Angle (NEA) test, directly estimates the pointing capability by measuring the peak-to-peak angle error during a specified observation time. For DRIRU II the test estimates the angle excursions expected during a one hour observation period based on angular rate sampled at a 200 millisecond (5 Hz) period. The system usage assumes the use of bias drift rate correction so the noise test processing consists of a two step procedure. First the angular rate samples are summed to obtain the total angle, then the linear trend corresponding to a fixed drift is removed using a least squares fit (linear regression). The peak-to-peak variation of the residual then characterizes the angle noise.

The DRIRU II system satisfies the specification limit of one arc second peak-to-peak for this test. Testing of individual gyros with the modified DRIRU electronics shows that the sensor contribution is well below the specification requirement, with levels of 0.04 arc seconds/hour being obtained in the current test series.



It should be noted that the specification of peak-to-peak excursion characterizes the noise distribution in a worst case manner and does not give an insight into the distribution to be associated with the noise process. Thus, the time history of the angle error residual was plotted to further inspect the noise. These plots showed that the system output is formed of high frequency noise with an RMS level of about 0.001 arc second plus a low frequency wander that determined the peak-to-peak excursion. This indicates that if real time bias estimation can be used to track the low frequency, the noise equivalent angle can be further reduced.

A representative plot of the standard DRIRU II performance is shown in Figure 13. This test was conducted in a stationary (earth rate only) condition. A peak-to-peak variation of less than one arc second is specified for this test, with typical performance between 0.5 and 1.0 arc seconds.

Similar tests were run with the modified DRIRU electronics. The results shown in Figure 14 indicate an order of magnitude improvement in performance compared to the standard DRIRU II. Several factors in both the electronics and the test procedure contribute to the improved performance:

- 1) Greater resolution and stability of the V/F converters.
- 2) Improved isolation from external thermal variations.
- 3) Improved mechanical stability by mounting directly to the test pier surface instead of a rate table.

The method of mounting was found to be very important. Throughout the test program it was evident that gyro noise performance, whether from PSD tests or NEA tests varied significantly from one test facility to another and depended to a large extent on the method of mounting the gyro to the test bed. The quietest NEA performance was obtained with the equipment bolted directly to the test pier surface (no intermediate table or granite block) and shrouded from external temperature changes, with data taken late at night to minimize local traffic in the test laboratory.

The application of the noise equivalent angle is to give a worst case evaluation of the blur diameter associated with direct use of the attitude reference system for a specified time. Although the time integral of the angle error, or the RMS level, might be more meaningful with respect to experiment or photographic exposures, the peak-to-peak definition and one hour time interval are used to allow comparison with previous systems that were also tested in the same way.

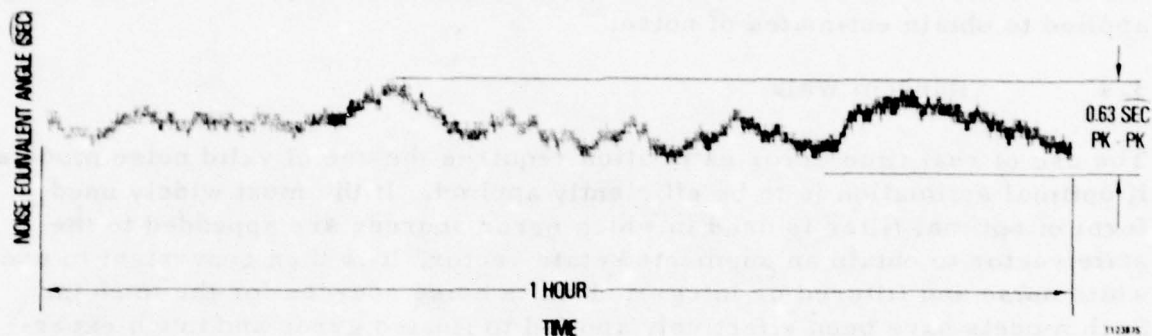


Figure 13. Standard DRIRU II NEA Test Results

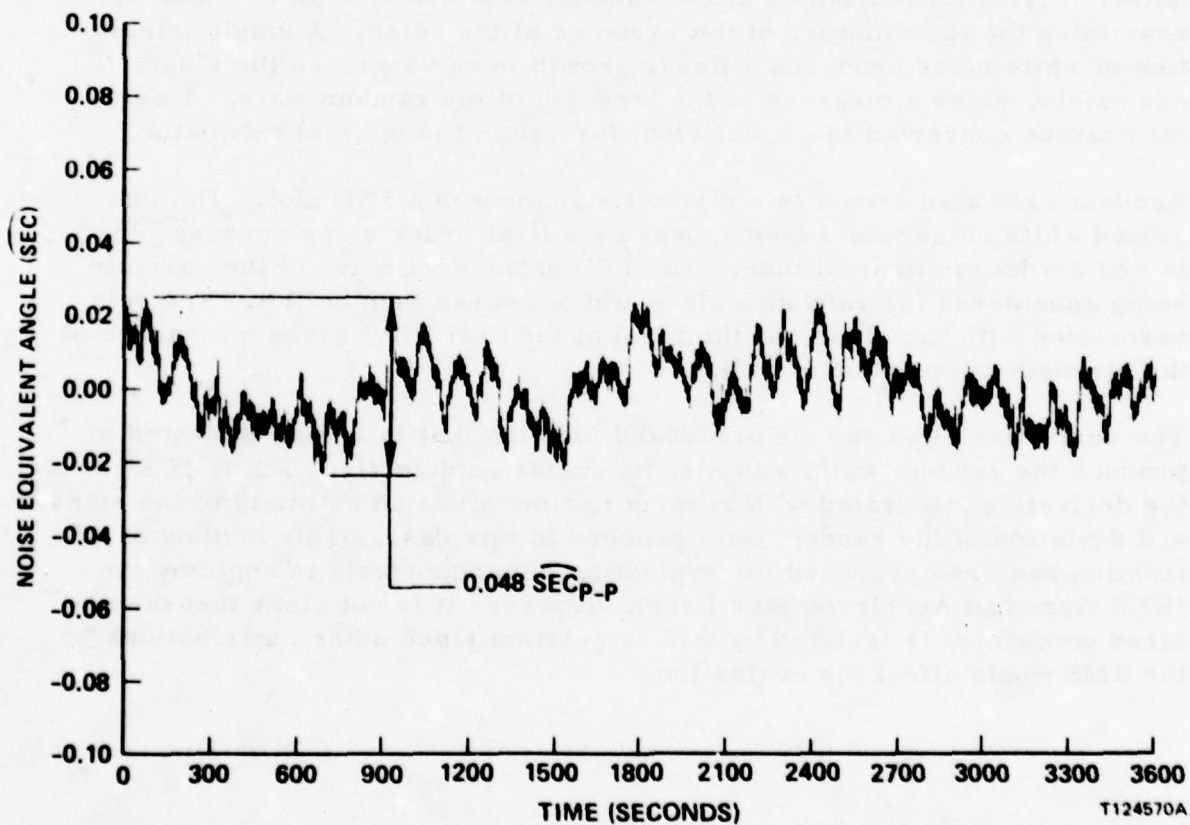


Figure 14. Modified DRIRU II Breadboard NEA Test Results

A particularly difficult test to perform is a variation of the basic NEA test in which observation from a spacecraft rotating at orbital rate is simulated. No particular operational difficulty or increase in noise is expected due to the increased base angular rate, however it has been found difficult to provide uniform angular rates of sufficient stability to verify the expected performance. Tests which are conducted at 200 deg/hr have been found to be strongly affected by rate table harmonic errors. Improved rate tables are currently being prepared for use, and digital filtering is currently being applied to obtain estimates of noise.

#### 3.4 Random Walk

The use of real time error estimation requires the use of valid noise models if optimal estimation is to be efficiently applied. If the most widely used form of optimal filter is used in which error sources are appended to the state vector to obtain an augmented state vector, it is then convenient to use white noise and filtered or integrated white noise sources for the models. Such models have been effectively applied to floated gyros and much experience has been obtained to validate the formulations.

Integrated white noise is commonly referred to as random walk. It effectively models a noise source that is equivalent to integrated broad band noise. Direct measurement of the random walk content can be made by examining the time history of the variance of the noise. A single integration of white noise produces a linear growth in variance, so the slope, if one exists, gives a measure of the strength of the random walk. This in turn can be converted to a coefficient for use in the optimal estimator.

Random walk also produces a distinct signature in a PSD plot. The integrated white noise would then appear as a first order slope corresponding to -20 db/decade in amplitude. The PSD of the derivative of the variable being considered for random walk would of course then be flat. The gain associated with the slope, or the level of the derivative gives a measure of the strength of the random walk.

The derivative, that is, the broadband function that is being integrated to produce the random walk, can also be evaluated directly. The RMS level of the derivative integrated with respect to time gives an estimate of the standard deviation of the random walk process in this case. This method of calculation has been proposed for evaluation of random walk in angle by the IEEE Gyro and Accelerometer Panel. However it is not clear that the desired component is isolated by this calculation since other contributions to the RMS would affect the evaluation.



Random walk is often included in optimal filters since it is convenient to include it and good modelling results have previously been obtained. It is convenient because the order of the system does not have to be increased if it is added to a state vector description that already allows for a white noise driven bias state.

The DRIRU II optimal filter due to Murrell<sup>2</sup> is shown below to show the filter form of a typical attitude estimator designed to be updated with the aid of star sensors.

For DRIRU II, with the assumed gyro error model, the total update filter state dynamics can be written as:

$$\begin{bmatrix} \dot{\phi} \\ \dot{\theta} \\ \dot{\psi} \\ \dot{\omega}_{XD} \\ \dot{\omega}_{YD} \\ \dot{\omega}_{ZD} \end{bmatrix} = \begin{bmatrix} 0 & \omega_Z & -\omega_Y & 0 & 0 & 0 \\ -\omega_Z & 0 & \omega_X & 0 & 0 & 0 \\ \omega_Y & -\omega_X & 0 & 0 & 0 & 0 \\ 0 & 0 & 0 & 0 & 0 & 0 \\ 0 & 0 & 0 & 0 & 0 & 0 \\ 0 & 0 & 0 & 0 & 0 & 0 \end{bmatrix} \begin{bmatrix} \phi \\ \theta \\ \psi \\ \omega_{XD} \\ \omega_{YD} \\ \omega_{ZD} \end{bmatrix} + \begin{bmatrix} \omega_{XN} \\ \omega_{YN} \\ \omega_{ZN} \\ \omega_{XR} \\ \omega_{YR} \\ \omega_{ZR} \end{bmatrix}$$

Where  $\phi, \theta, \psi$  denote the roll, pitch and yaw attitude determination errors.  $\omega_{XD}, \omega_{YD}, \omega_{ZD}$  are the roll, pitch and yaw gyro drift caused by random bias and random walk. It is this component of the gyro measurement error that is estimated by the update filter.  $\omega_{ZN}, \omega_{YN}, \omega_{XN}$  are the gyro white noise drift processes;  $\omega_{XR}, \omega_{YR}, \omega_{ZR}$  are white noise processes that generate the gyro random walk drift.

An Euler parameter formulation is used to maintain total attitude, so the linear errors are used to update the total attitude described by  $a_{1-4}$  below.

The Euler parameters correspond to an unnormalized quaternion formulation that define the Euler axis and angle.

$$\begin{bmatrix} a_1 \\ a_2 \\ a_3 \\ a_4 \end{bmatrix} = \begin{bmatrix} a_1 \\ a_2 \\ a_3 \\ a_4 \end{bmatrix} + \frac{1}{2} \begin{bmatrix} 0 & \hat{\phi} & -\hat{\theta} & \hat{\psi} \\ -\hat{\phi} & 0 & \hat{\theta} & \hat{\psi} \\ \hat{\theta} & -\hat{\theta} & 0 & \hat{\phi} \\ -\hat{\psi} & -\hat{\psi} & -\hat{\phi} & 0 \end{bmatrix} \begin{bmatrix} a_1 \\ a_2 \\ a_3 \\ a_4 \end{bmatrix}$$

This expression is the same as the Euler parameter integration algorithm. In both cases the Euler parameters are being updated for the effects of small angle rotations about the reference axis.

The gyro drift compensation parameters are updated as follows:

$$\begin{bmatrix} \omega_{DX} \\ \omega_{DY} \\ \omega_{DZ} \end{bmatrix} = \begin{bmatrix} \omega_{DX} \\ \omega_{DY} \\ \omega_{DZ} \end{bmatrix} + \begin{bmatrix} \hat{\omega}_{DX} \\ \hat{\omega}_{DY} \\ \hat{\omega}_{DZ} \end{bmatrix}$$

At the time this filter was developed the SDG-5 noise measurements were not available so random walk was included.

Intuitively such models might be seen to be applicable to floated integrating gyros since a physical correspondence can be noted to a wideband noise source (the rotor and float assembly) and a free integration (the flotation and suspension system). In fact, a good fit has been obtained in most cases although exceptions can be noted.

However, the application of a random walk model to the dry tuned gyro is not clear. Previous measurements have indicated that the SDG-5 power density spectrum has a shape similar to that of floated integrating gyros, although of lower magnitude. Thus, the use of a random walk model was justified based on the increasing amplitude at decreasing frequency. However, it now appears that this characteristic was more due to the measurement than the sensor itself. The more recent PSD tests discussed above show that such a slope does not appear even at very low frequencies, and that the spectrum is essentially flat or white.

Variance plots also verify the absence of random walk. These plots were obtained for a series of 34 hour tests (described in the next section) using the modified DRIRU electronics. Differences in drift rate measured at

various fixed intervals during each test run were used to obtain variance estimates for each interval. These variances, when plotted versus interval, did not show a linear growth characteristic and therefore verified the absence of random walk.

This conclusion is heuristically satisfying when the physical construction of the DTG is considered. The dry tuned gyro contains a broadband error source, the tuned suspension and rotor, but acts like a free rotor. There is negligible damping corresponding to the fluid within a floated sensor, and a white noise model is intuitively more appropriate.

Although the removal of random walk removes terms from the system matrix, the removal does not decrease the number of states required for bias estimation, so software simplification may be minor. However, the use of more appropriate models in analysis and design is desirable. The random walk can be used to account for unmodelled errors, but in this case it probably is better to use techniques more directly designed for the desired effect.

Markov models may be similarly considered, except that filter signatures instead of pure integrations are sought in the PSD. The break frequency which corresponds to correlation times then is of concern. However, the lack of notable features in drift rate PSD shows that Markov models are also unnecessary.

### 3.5 Low Frequency Drift Variations

A series of four 34 hour drift tests were conducted using the modified DRIRU II electronics in conjunction with SDG-5 gyro S/N 080. The same test set up was used as previously described for NEA testing with the gyro spin axis vertical. Three Fluke 8500A integrating voltmeters were used to measure the analog voltages corresponding to the X and Y gyro axes and internal gyro temperature. A Hewlett-Packard 9845 desktop computer was used to accept the voltmeter readings and process the data. Since the goal of this test series was to measure low frequency drift variations, fifteen minute averaging of raw data was used for data handling convenience.

Neither the gyro nor the electronics were actively temperature controlled so it was necessary to provide a means of compensating the measured drift data for the small temperature variations that were present even though the test hardware was essentially isolated from laboratory ambient changes. This was accomplished by monitoring the internal gyro thermal sensor and determining a best fit straight line of the output data with respect to the temperature information by the method of least squares (linear regression).



Figure 14 shows the uncompensated drift data obtained from the gyro axes during one of the 34 hour tests (Run 4) and also the recorded gyro temperatures. Note the correlation between the drift variations and temperature changes, particularly for the X axis which was sensing the horizontal component of earth's rate. The larger temperature effect for this axis is due to the temperature sensitivity of the torquer circuit. This effect results in a scale factor sensitivity which is highly linear with respect to temperature that is normally self compensated within a system.

Figure 15 shows the same data after being compensated for temperature as described above. Note the extremely low residual drift variations, 0.00005 and 0.00004<sup>o</sup>/hr, one sigma about the mean, for the two gyro axes. This demonstrates the accuracy with which it is possible to compensate for temperature effects using the internal gyro sensor.

Table 4 shows the one sigma drift variations for each of the four tests with and without temperature compensation. Note that in each case the gyro axis which was sensing a component of earth's rate had a larger uncompensated drift variation due to the torquer scale factor temperature sensitivity. Note also that after compensation the differences between the two axes were negligible and the one sigma variations were extremely small. The one exception is Run 2 which included a one time drift change of 0.0004<sup>o</sup>/hr on both axes occurring 7 hours into the test. The effect of this step change can be seen by observing the improvement in the compensated data that results from the deletion of the first ten hours of data (Run 2a) from the data record. The cause of this step change is unknown. Since it affected both gyro axes and did not recur during the test program, it is thought to be due to a momentary loss of power causing the gyro wheel to lose synchronism for a short period.

The compensated data for each of the test runs were further analyzed to determine the nature of the growth characteristic of the drift rate variance with time as described above. Figure 16 shows the results of this analysis for the two gyro axes for Run 4. The variance does not increase linearly with time, thus indicating that the drift rate does not exhibit a random walk characteristic.

The variance plot for the compensated X-axis data from Run 2 is shown in Figure 17 along with a similar plot for the last 24 hours of that run (Run 2a). The only significant difference in the two data records is the 0.0004<sup>o</sup>/hr step change which occurred after approximately the first 7 hours. The effect of this event on the calculated variance growth characteristic is dramatic and the need for well controlled and monitored testing is obvious. Other factors which could adversely affect this type of performance analysis include drift ramps or cyclic variations caused by measurement equipment instability or uncompensated external inputs (e.g., periodic tilts due to local traffic patterns or other daily variations).

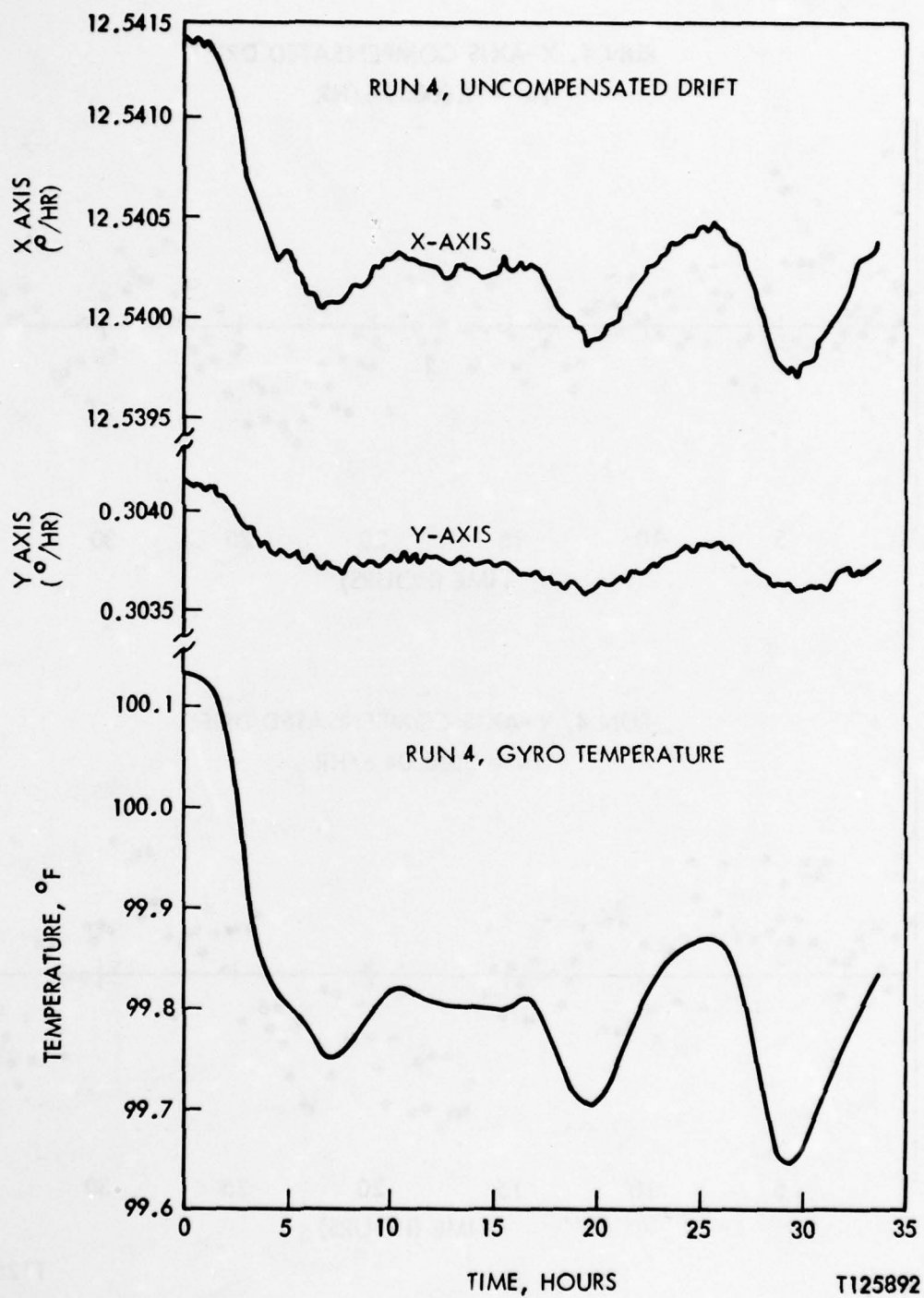
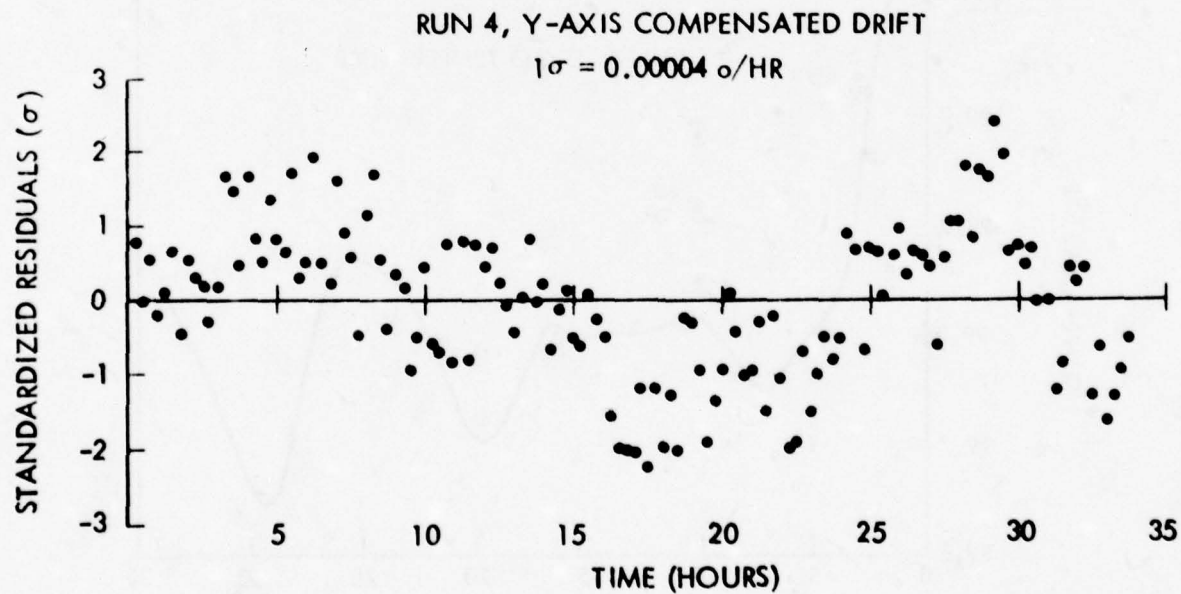
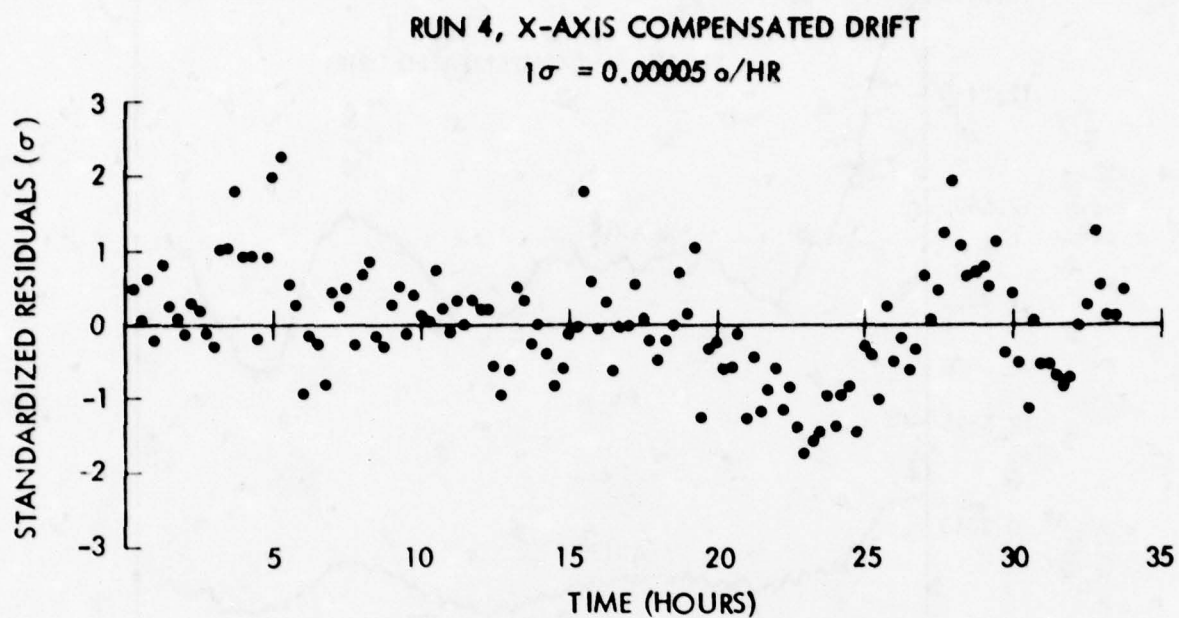


Figure 14. Uncompensated Drift and Temperature, Run 4



T125983

Figure 15, Standardized Residuals Versus Time for Run 4, Compensated

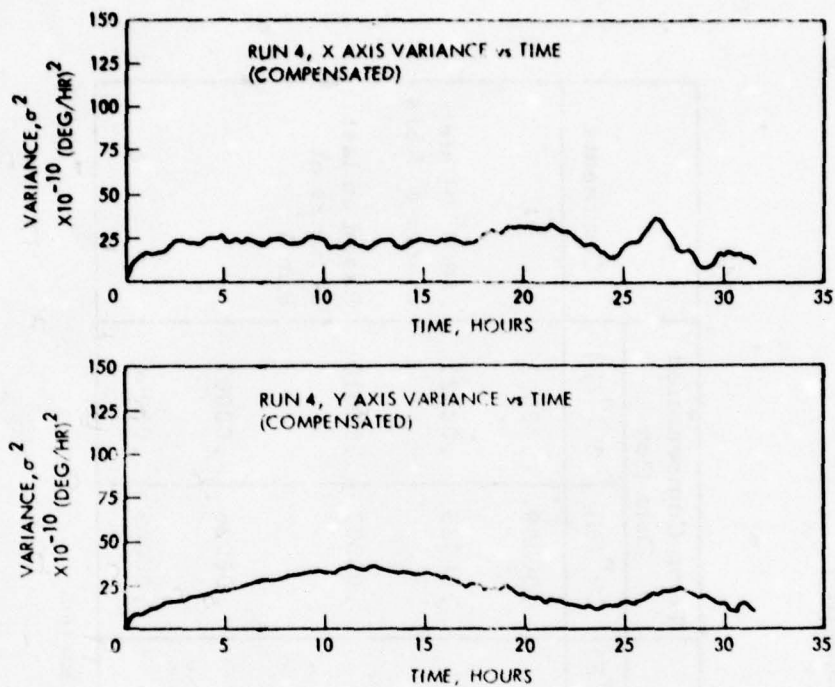


Table 4. SDG-5 S/N 080 Drift Stability

Run No.	Orientation	Duration Hours	Uncompensated Data (1σ)				Temp Compensated Data (1σ)		Comments
			X (°/H)	Y (°/H)	Temp (°F)	X (°/H)	Y (°/H)	Y (°/H)	
1	SA <sub>v</sub> , X <sub>n</sub> , Y <sub>e</sub>	34	.00039	.00008	.12	.00009	.00003	.00003	.0004°/H step change @ 7 hrs Based on last 24 hours of Run 4
2	SA <sub>v</sub> , X <sub>w</sub> , Y <sub>n</sub>	34	.00025	.00045	.09	.00023	.00021	.00021	
2a*	SA <sub>v</sub> , X <sub>w</sub> , Y <sub>n</sub>	24	.00013	.00044	.11	.00007	.00010	.00010	
3	SA <sub>v</sub> , X <sub>n</sub> , Y <sub>e</sub>	34	.00031	.00010	.09	.00006	.00007	.00007	
4	SA <sub>v</sub> , X <sub>n</sub> , Y <sub>e</sub>	34	.00035	.00012	.10	.00005	.00004	.00004	

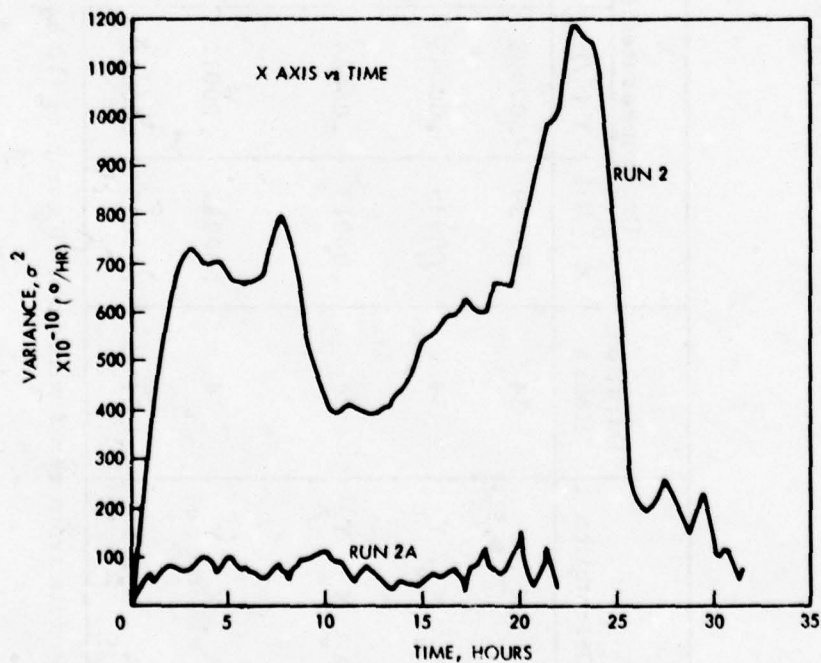
\*Based on data from run 2 with first 40 samples (10 hours) eliminated.

T125999



T125984

Figure 16. Variance Versus Time, Run 4



T125985

Figure 17. X Axis Variance Versus Time, Run 2

#### 4. SUMMARY

The SDG-5 dry tuned gyro is capable of extremely low noise performance and is well suited for use in a wide variety of space and terrestrial applications where this characteristic is important. The nature of the noise signature of the SDG-5 is such that its drift rate can be modelled by a flat spectrum with no discernible random walk content. The DRIRU II strapdown redundant attitude reference unit, which employs the SDG-5 gyro for rate sensing, has also shown extremely low noise performance in the standard configuration and in a modified version optimized for resolution in a low rate sensing mode.

#### 5. ACKNOWLEDGEMENT

This work was supported in part by the Jet Propulsion Laboratory, California Institute of Technology, under NASA contract NAS-7100.

#### 6. REFERENCES

- <sup>1</sup> Irvine, R. B and Ritter, J. W., "DRIRU II - The NASA Standard High Performance Inertial Reference Unit." Paper presented at the Rocky Mountain Guidance and Control Conference of the American Astronautical Society, February 1979.
- <sup>2</sup> Murrell, J. W. "Precision Attitude Determination for Multimission Spacecraft", AIAA paper 78-1248, presented at the 34th Annual Meeting of the AIAA, Palo Alto, California, August 1978.
- <sup>3</sup> Heller, W. G. and Jordan, S. K., "Error Analysis of Two New Gradiometer-Aided Inertial Navigation Systems," Journal of Spacecraft and Rockets, Vol. 13, No. 6, June, 1976, pp. 340-347.
- <sup>4</sup> Bernstein, U. and Hess, R. I., "The Effects of Vertical Deflections on Aircraft Inertial Navigation Systems," AIAA Journal, Vol. 14, No. 10, October 1976, pp. 1377-1381.
- <sup>5</sup> Irvine, R. B. and Ritter, J. W., "An Examination of Low Power Spectral Density (PSD) Noise Performance of a Dry Tuned Gimbal Two-Degree-of-Freedom Gyroscope, and Methods for Further Noise Reduction." Paper presented at the Eighth Biennial Guidance Test Symposium, Holloman AFB, New Mexico, May 1977.
- <sup>6</sup> Final Report ADTC-TR-77-17 "Teledyne SDG-5 Gyro Test," Central Inertial Guidance Test Facility, 6585th Test Group, Holloman AFB, New Mexico, February 1977.
- <sup>7</sup> Blackman, R. B and Tukey, J. W., "The Measurement of Power Spectra." New York: Dover, 1959.



\*Bingham, C., Godfrey, M.D. and Tukey, J.W., "Modern Techniques of Power Spectrum Estimation," IEEE Transactions on Audio and Electroacoustics, Vol. AU-15, No. 2, June, 1967, pp 56-66.

TITLE: COMBINED ENVIRONMENTAL  
TESTING OF THE AGM-86  
INERTIAL NAVIGATION ELEMENT  
FOR CRUISE MISSILE

AUTHOR: BARRY HARDISON

LITTON GUIDANCE AND CONTROL SYSTEMS  
5500 Canoga Avenue  
Woodland Hills, California 91364

## INTRODUCTION

Litton first became aware of Air Force requirements for combined environmental testing of the AGM-86 in the fall of 1976. At this time we were concurrently participating in the AGM-86 TCP-121 trade studies program through the Boeing Aerospace Company and responding to the USAF AGM-86 FSD phase RFP. After an extensive and fruitless search for existing facilities other than the Air Force Flight Dynamics Laboratory (which was not available), and capitalizing upon our progressive attitude toward reliability requirements, Litton initiated action directed toward building its own Combined Environmental Test (CET) facilities to support the pending AGM-86 FSD contract.

A full-scale CET design and procurement program was initiated in the fall of 1976, which culminated in "on line" facilities early in 1978. Since that time the operation has been refined and expanded.

In recent months the CET requirements for the AGM-86 have undergone several modifications and changes. These changes now appear to be firm and include modification of the original CET requirements to include some of the environmental qualification test requirements. CET testing of the AGM-86 is scheduled for the period September 1979 through November 1979 in the GCS test facility. One system will be subjected to the combined environments of high temperature, low temperature, humidity, altitude, and random vibration.

The test plan calls for a minimum of eight environmental cycles of 28 hours duration each. Test results that are available before the October 10 symposium will be presented at the symposium along with the published paper.

## CET FACILITY

### BACKGROUND

Many of the people involved in environmental testing of airborne avionics have long been disturbed by the existing test techniques, that is to say the sequential nature of environmental qualification exposure such as temperature, altitude, humidity, vibration, shock, etc. Even with the combination of temperature and altitude, it is still essentially a series of environmental exposures. Air borne vehicles simply do not experience environments one at a time. A reasonable argument can be formulated for exposing equipment to such environments as shock, sand and dust, explosion, and salt fog,



one at a time. However, some environments, and in particular vibration, temperature, altitude, and humidity exist simultaneously in airborne vehicles and can produce failure mechanisms that would not be isolated or even detected with conventional test methods.

The paper, "Combined Environment Reliability Test (CERT) for Avionics Subsystems," by David Prather and David Earls of the Air Force Flight Dynamics Laboratory, published in March 1976, created considerable interest at Litton GCS. It was felt that the environmental technique described in the paper was an extremely useful and meaningful test method. Therefore, when the requirement for the AGM-86 combined environment testing became known, Litton initiated a design and procurement program.

### PHYSICAL CHARACTERISTICS

The Litton CET facility has been installed in the Environmental Laboratory. The chamber-shaker combination along with the control console is located in an enclosed test area. See Figure 1. All auxiliary and support equipment is located in an equipment area immediately adjacent to the test area. See Figure 2. The chamber-shaker combination is a piggy-back (chamber on top of a shaker) arrangement with a usable chamber volume of approximately 75 cubic feet.

Although the Litton CET is intended for the testing of comparatively lightweight airborne equipment, the facility's requirements are considerable. The approximate weight, power requirements, and space allocations of the facilities are:

Shaker and amplifier	10,500 pounds
Chamber (including ECA)	10,500 pounds
Chamber control	700 pounds
Chamber ancillary (vacuum pump, refrigeration, (2) compressor, dryer, boiler)	14,225 pounds
Power substation	5,000 pounds
Water tower	<u>3,000</u> pounds
Total weight	43,925 pounds
Average power requirements	235 kva
Test area	450 square feet
Ancillary equipment space	1125 square feet

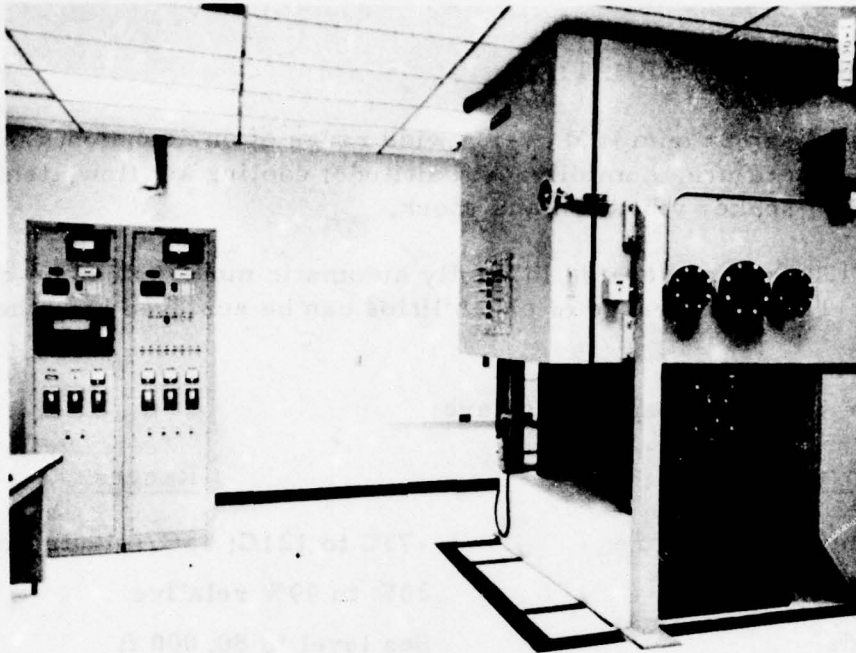


Figure 1. Facility for Combined Environmental Testing

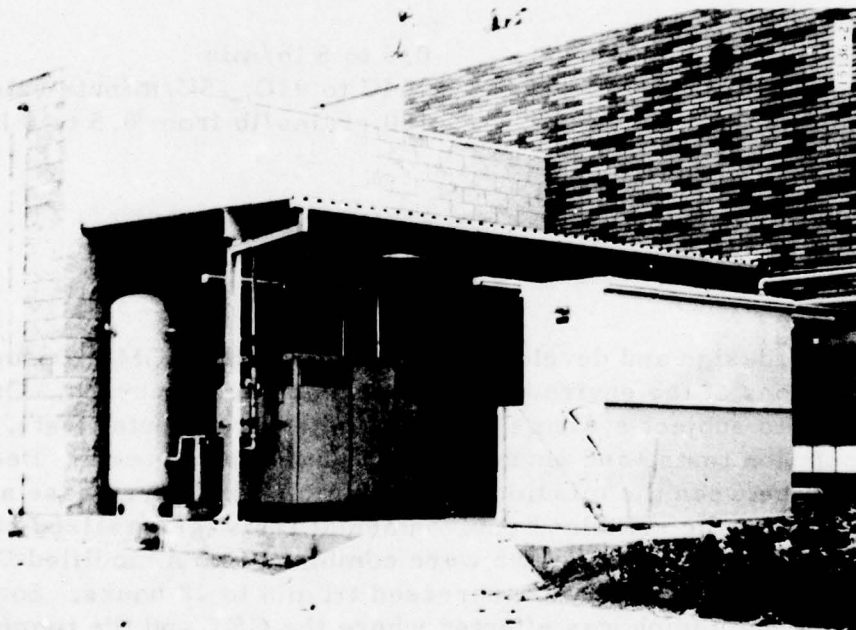


Figure 2. Auxiliary and Support-Equipment Area

## PERFORMANCE CAPABILITIES

The CET can be operated over a wide range of environments that include chamber temperature, humidity, and altitude; cooling air flow, temperature, and humidity; shaker vibration and shock.

The CET can be operated in a fully automatic mode or can be controlled manually. The entire range of capabilities can be achieved by either mode of control.

The performance capabilities are:

<u>Environmental</u>	<u>Ranges</u>
Chamber temperature	-73C to 121C; 15C/minute (avg) rate
Humidity	20% to 99% relative
Altitude	Sea level to 80,000 ft
Vibration	10,000 lb force, sinusoidal 8,000 rms lb force, random
Shock	15g, 8 millisec, half-sine
Cooling air	
Flow	0.5 to 8 lb/min
Temperature	-54C to 93C; 15C/minute rate
Humidity	150 grains/lb from 0.5 to 8 lb/min

## AGM-86 COMBINED ENVIRONMENT TEST

### BACKGROUND

During the design and developmental stages of the AGM-86 program, several iterations of the environmental test plan have occurred. Originally it was planned to subject systems to combined environmental tests, mission profile simulation tests, and environmental qualification tests. Because of the similarity between the mission profile simulation (worst-case actual environments) and the combined environmental tests (generalized combined environmental step stress) the two were combined into a modified CET. The length of the new CET cycle was increased from 8 to 18 hours. Somewhat later a further combining was effected where the CET and the temperature-humidity-altitude portion of the environmental qualification test were appropriately merged into one test. The length of the new CET cycle was further increased from 18 hours to 28 hours.



## SCHEDULE

Combined environmental testing of the AGM-86 is scheduled for the period September 1979 through November 1979 in the Litton GCS test facilities. One system will be subjected to the combined environments of high temperature, low temperature, humidity, altitude, and random vibration. The test plan calls for eight cycles of combined environments of 28 hours duration each. After successful completion of the eight cycles, the system will be exposed to two cycles of 28-hour duration at 110% CET level followed by two cycles at 120% CET level.

During the first eight cycles, all failures will be subjected to repair/corrective action and the corrective action will be exposed to eight full cycles of failure free operation. During the last four cycles (two at 110% and two at 120%) failures will be repaired and only the remaining portion of the test performed.

## ENVIRONMENTS

The 28-hour basic combined environmental cycle is shown in Figure 3. The details of the cycle is as follows.\*

<u>Step</u>	<u>Time</u>	<u>Conditions</u>
1	T+0	Reduce chamber temperature to -65F within a 2-hour period.
2	T+2 hr	Reduce chamber pressure at a rate of 100 to 1500 feet/min to 50,000 feet altitude while maintaining the specified (-65F) temperature. The time duration of this step shall be 4 hours.
3	T+6 hr	Turn on warmup power to the INE and begin warmup. Apply vibration. Begin coolant air flow. Continue this mode until the INE is to operating temperature (40 minutes maximum).
4	T+6 hr 40 min	Discontinue vibration. Turn INE on at a minimum voltage, and begin alignment. Align for 30 minutes. Switch to navigate, apply vibration and maintain for 2 hours. The time duration of this step is 2 hours and 30 minutes.
5	T+9 hr 10 min	Discontinue vibration, switch from navigation to align and perform a 30 minute alignment. Maintain coolant flow.
6	T+9 hr 40 min	Switch to navigate and change coolant temperature and flow rate. Apply vibration. Continue to navigate for 2 hours.

\*These details have not yet been finalized and may be subject to change.

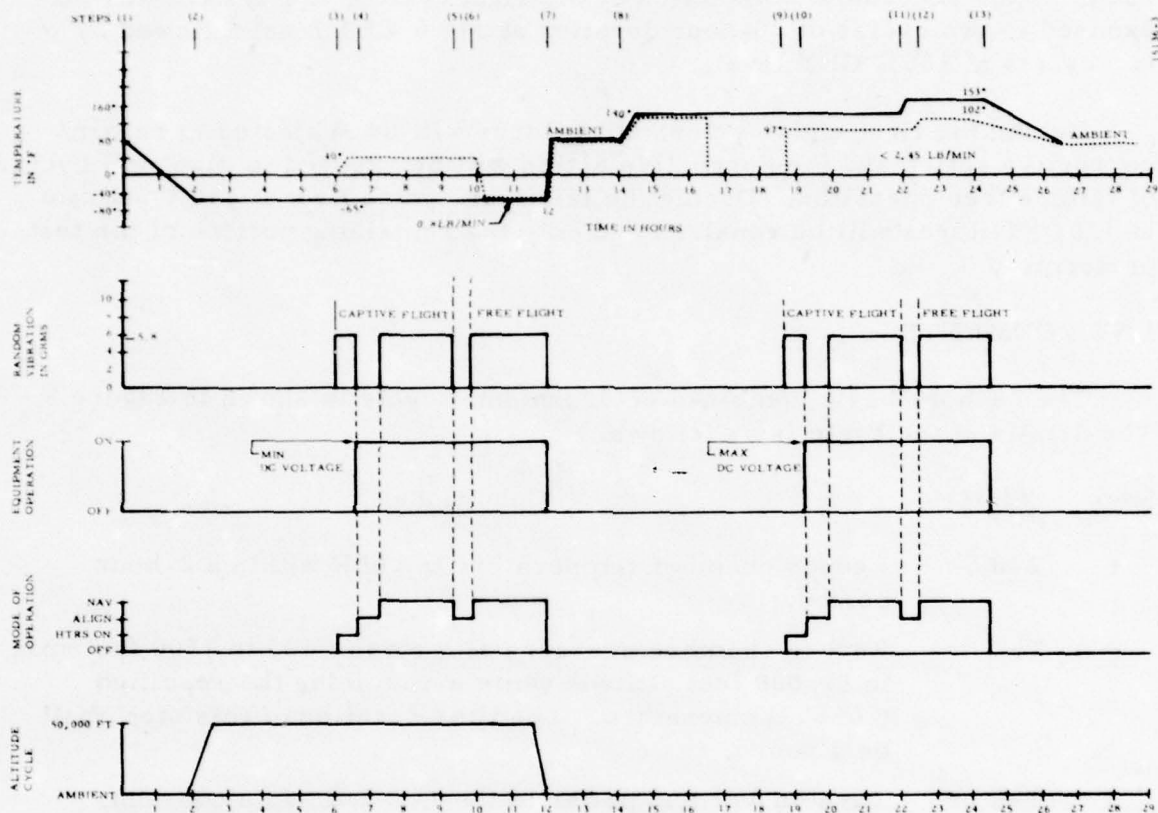


Figure 3. AGM-86 CET Profile (100% Level)

<u>Step</u>	<u>Time</u>	<u>Conditions</u>
7	T+11 hr 40 min	Discontinue vibration and turn off all power to INE, within the next 30 minutes raise chamber pressure and temperature to ambient conditions and increase coolant temperature to ambient temperature. After attaining ambient pressure and temperature raise chamber RH to 95% and maintain for 2 hours.
8	T+14 hr 10 min	During the next 30 minutes, increase the chamber and coolant temperature to 140F while maintaining a constant absolute humidity. The relative humidity shall be allowed to adjust naturally. Maintain temperature and humidity conditions for 4 hours. Maintain coolant flow at 140F for only the first 2 hours of this step.
9	T+18 hr 40 min	Turn on warmup power and begin warmup. Apply vibration. Begin coolant flow at the specified temperature with the corresponding flow rate. Continue this mode until operating temperatures are attained (40 minutes maximum).
10	T+19 hr 20 min	Discontinue random vibration. Turn INE on at maximum voltage and begin alignment. Align for 30 minutes. Switch to navigate, apply vibration and navigate for 2 hours.
11	T+21 hr 50 min	Discontinue vibration, switch from navigation to align and perform a 30-minute alignment. Maintain coolant flow.
12	T+22 hr 20 min	Switch to navigate and change coolant to hottest specified temperature and the corresponding flow rate. Apply vibration. Continue to navigate for 2 hours.
13	T+24 hr 20 min	Discontinue vibration and turn off power to the INE. During the next 2 hours reduce the chamber and coolant temperature at a uniform rate to standard ambient temperature. At the end of the 2-hour period the relative humidity shall be 95%. Maintain these conditions for 2 hours.

Once the eight basic cycles have been successfully completed, two cycles at 110% CET level and two cycles at 120% CET level will be performed. See Tables I and II.



TABLE I  
CET DEFINITION

CET Level	Vibration (g rms)	Altitude (ft)	High Temp °F		Low Temp (°F)	Humidity (% R. H.)	Cooling Air (INE) (lb/min/(°F))	
			High	Low			High	Low
100%	5.8	50,000	153	140	-65	95%	2.45/102	1.0/140
	5.8						1.0/40	0.8/-65
110%	6.4	55,000	168	154	-72	95%	2.45/112	1.0/154
	6.4						1.0/44	0.8/-72
120%	7.0	60,000	184	168	-78	95%	2.45/122	1.0/168
	7.0						1.0/48	0.8/-78

TABLE II  
COMBINED ENVIRONMENTAL TEST SEQUENCE

Test Sequence	Test Description	Test Environment
1	Eight cycles	100% env level
2	Two cycles	110% env level
3	Two cycles	120% env level

## REFERENCES

1. Prather, D.K. and Earls, D.L. "Combined Environment Reliability Test (CERT) for Avionics Subsystems," the Journal of Environmental Sciences, March/April 1976, pages 11-22.
2. Hardison, Barry, "Design, Procurement and Installation of a Combined Environmental Test Facility," The Institute of Environmental Sciences, 1978 Proceedings.

## BIBLIOGRAPHY

HARDISON, BARRY - Reliability Project Engineer; Litton Systems, Inc., Guidance and Control Systems Division, Woodland Hills, California.

Mr. Hardison received his degree of BSEE from the University of California, Berkely. From 1974 through 1978 he was the manager of the Environmental Laboratory at the Litton Guidance and Control Systems Division. His 24 years of experience include environmental testing, system integration, inertial navigation equipment, and automatic control.

He has presented papers and articles at various technical and professional society meetings.

TITLE: CALIBRATION AND ALIGNMENT  
PERFORMANCE EVALUATION OF  
THE ROCKWELL ASP-IMU TEST  
BED, TECHNIQUES AND  
RESULTS

AUTHOR: V. D. HENDERSON

ROCKWELL INTERNATIONAL  
Autonetics Strategic Systems Division  
3129 Glenn Holly  
Anaheim, California 92804



## ABSTRACT

The Rockwell Advanced Stable Platform (ASP) was designed and built to provide an appropriate test-bed environment for the CSDL-designed Third Generation Inertial Instruments (TGII). These instruments are used in the floated-platform AIRS-IMU currently in the advanced stages of development. This latter IMU is required to provide advanced state-of-the-art accuracy for new and upcoming ballistic systems applications. The ASP IMU is especially useful as a test bed due to its four-gimballed unlimited angular freedom and platform-mounted mirrors for optical readout.

The ASP system has been mechanized with a version of the Rockwell/Autonetics developed "Advanced Inertial Mechanization" (AIM) which was described in somewhat detail in the Proceedings of the Eighth Guidance Test Symposium, Volume 1, ADTC TR 77-3. The co-authored paper presented therein is entitled, "An Advanced Software Mechanization For Calibration and Alignment of The Advanced Inertial Reference Sphers (AIRS)". And, since the paper presently described herein reports performance assessment and evaluation of the AIM-mechanized ASP, along with test results and further delineation of techniques, it can be considered in many respects as a sequel to the above cited works.

In addition to a brief presentation of AIM/ASP background information, the present paper gives a summary description of the pertinent details of the ASP mechanization, with particular attention given to the Auxiliary Reference Monitor (ARM) portion of it. The ARM mechanization utilizes external auto-collimators and other reference devices to provide an optical system for precision instrumentation of ASP alignment and other performance features. Significantly new and novel mechanization techniques are used to provide remarkably rapid measurement response-time with very low-bandpass characteristics with regards to noise. A summary of performance results is also given for both IMU calibration and alignment, presented in terms of unclassified non-dimensional ratios of statistical measures of achieved ASP performance to a like measure of specification performance established for the "MPMS-version" of the AIRS IMU.

The paper reports mechanization developments and test findings which had essential bearing upon achieving the excellent performance obtained using Kalman filtering techniques for accomplishing completely self-contained calibration and alignment, without external references. These topics include "Dynamic Error Modeling", "Computational Algorithms", and "Special Pre-correlation Techniques" which contributed directly to repeatable unbiased calibration results. Other topics include "Composite Drift Rate Trend States", "Torque-word and SFIR Data Delay Compensation", "Gyro Float-Motion Compensation", and "Reference Torquing Techniques" which especially contribute to achieving repeatable unbiased platform azimuth alignments.

Other discussion presents the Auxiliary Reference Monitor Techniques which gave way to an Automatic Absolute Azimuth Verification (AAV) mechanization in which platform mounted mirrors are referred to an external precision azimuth monument which is maintained in an isolated controlled environment. An error analysis of the AAV instrumentation is included.

The ARM system also provides an Automatic Platform Mirror Calibration mechanization which utilizes precision measurements of gravity (via platform-mounted SFIR(s)) to tie the mirror-normals to the platform reference-coordinate frame. Damped Mercury Pools are used to provide optical level-reference for the mirror-normals, the precision of which ultimately reflects into the ability to achieve precise azimuth measurements with the platform-mounted mirrors. An error analysis of the Mirror Calibration instrumentation is also included.

Finally, a technique for calibrating the external autocollimators immediately prior to obtaining measurements from them is described. The technique consists of utilizing a computer-controlled servo table which removes a pentaprism from the autocollimator/monument-mirror line-of-sight just prior to making an autocollimator/platform-mirror measurement. During Automatic Mirror Calibration, pentaprisms/mercury-pools are used in like manner to calibrate the autocollimators in level. This technique removes the low-frequency components of instability from the autocollimator optical references. The higher-frequency components are removed via filtering in the data collection process. An error analysis, as well as empirically obtained results, are also included for these operations.

In summary, it is believed that many of the techniques developed for the ASP system are new innovations having useful application elsewhere; and several aspects of the test results and findings can contribute to improvements in performance of other related IMU systems. In particular, experience and test results obtained with the ASP system have direct application to the Advanced Inertial Reference Sphere (AIRS) IMU.

## TABLE OF CONTENTS

	<u>Page</u>
Background Information About the ASP IMU. . . . .	1
Summary Description of the AIM/ASP Mechanization . . . . .	2
Mechanization Developments From Past Testing of AIRS. . . . .	4
New Developments From ASP Test Results and Findings . . . . .	7
Summary of Calibration Performance Results. . . . .	12
Summary of Platform Alignment Results . . . . .	16
Discussion and Error Analysis Results of AAV. . . . .	20
Plans for Further Investigative and Developmental Testing . . . . .	25



## LIST OF FIGURES

	<u>Page</u>
1. Optimum Continuous Cal/Align. . . . .	3
2. Illustration of Cal/Align Portion of AIM . . . . .	5
3. Optimum Continuous Cal/Align Trajectory . . . . .	8
4. ASP Absolute Azimuth Verification Lab Setup . . . . .	17

## LIST OF TABLES

I. ASP CALIBRATION RESULTS (30-DEG/HR). . . . .	14
II. ASP CALIBRATION RESULTS (60-DEG/HR). . . . .	15
III. ASP ALIGNMENT REPEATABILITY. . . . .	19

Calibration And Alignment Performance Evaluation  
of the Rockwell ASP-IMU Test Bed,  
Techniques And Results

BACKGROUND INFORMATION ABOUT THE ASP IMU

The Rockwell Advanced Stable Platform (ASP) was designed and built to provide an inertial systems test-bed environment for the Third Generation Inertial Instruments (TGII), developed by the Charles Stark Draper Laboratory of Cambridge, Massachusetts. The ASP IMU is especially useful as a test bed due to its four-gimballed design. This provides unlimited angular freedom with platform-mounted mirrors available for optical read-out.

ASP hardware design provides instrument mounting cavities which enclose the TGII inside a spherical beryllium platform. The cavities are thermally insulated to eliminate convection heat paths. And the internally generated heat is directed to the instrument mounting flanges, which are controlled to provide a constant temperature heat-sink. The bulk temperature of the spherical platform is controlled by a closed-system gas flow, along fixed paths, beneath an insulating shroud attached to and enclosing the ball. With this arrangement, the TGII performance is relatively independent of platform motion and orientation with respect to the housing or an earth-fixed frame.

The ASP software mechanization provides self-contained calibration and alignment of the IMU, without the need for external references. However, the ASP platform is equipped with auxiliary external references, which include the mirror/autocollimator optical readout, gimbal resolver-null locking, as well as two-axes level-detectors, etc., which are utilized by a software mechanized module called the "Auxiliary Reference Monitor" (ARM). The ARM subsystem operates independently of the calibration/alignment process and provides monitoring of alignment error, as well as an efficient diagnostic capability for rapidly identifying and isolating various types of hardware failures or performance problems.

Calibration of the ASP inertial instrument requires level-axis platform rotation, in turn, about three non-colinear (preferably orthogonal) platform-fixed axes. In addition, platform rotation about the local vertical is also required in order to effect observability for both calibration and platform alignment. The level rotations, or tumbling, causes the local gravity-vector to probe along instrument axes in such a way as to excite acceleration sensitive parameters, producing distinct error-propagations into the accelerometer-derived calibration observables. Rotation about the local gravity-vector effects separation of platform drift rate fixed in the platform and that fixed in the earth due to alignment error.

The self-contained software mechanization for the ASP has been developed from test results experience, over the past years, on various floated platform and/or TGII hardware applications. The present configuration has evolved from its conception on the SABRE IMU test program (a predecessor of the AIRS IMU), through its application in the MPMS/AIRS program to its current implementation on the Rockwell ASP. Thus, the self-contained calibration and alignment mechanization, developed by the Autonetics Division of Rockwell, is also a "Third Generation" mechanization concept, denoted by the name "Advance Inertial Mechanization," or simply AIM.

The remainder of this paper is devoted to a further description of the mechanization, a delineation of pertinent test results and findings, and a summary of performance results for evaluation of the current ASP hardware/software combination.

#### SUMMARY DESCRIPTION OF THE AIM/ASP MECHANIZATION

The AIM mechanization provides for determination of all of the inertial instrument calibration parameters which are observable in a one-g gravitational field. This includes instrument axes misalignment and platform axes orientation relative to a locally-level (or launch-point) earth-referenced geographic frame. The multitude of calibration parameters also includes instrument scale factors, bias errors, g-sensitive and  $g^2$ -sensitive parameters, and certain parameter trends. Other error parameters (including those unobservable in a one-g field) are determined at the instrument level of testing, and used in the mechanization to provide compensation. The observable error parameters are modeled in a real-time on-line Kalman filter which processes the SFIR (accelerometer) derived data to generate error estimates, while the platform is commanded along its tumbling/carrouseling calibration trajectory. Thus, the calibration is accomplished in a completely automatic, self-contained way. The azimuth orientation of the platform axes, relative to earth axes, is also determined without the use of direct external aids. Only the indirect influence of earth's gravity and spin-rate vectors is utilized in the calibration and alignment process.

Among several noteworthy features of the AIM mechanization is its modular design concept based upon functional building blocks. Many of the functional modules are common to each of the various system modes of operation. Thus, an integrated modular mechanization approach eliminates duplication of computer program coding and checkout along with the related initialization and mode transition problems. The modular design is illustrated in Figure 1. Another important feature of the modular design is the ease and efficiency it affords for making program changes and improvements. Impact of coding changes and checkout are localized to the particular modules being modified.

There are four basic system-performance operating modes provided by appropriate linkage and initialization of the basic functional building blocks comprising the mechanization. A rapid align mode is provided



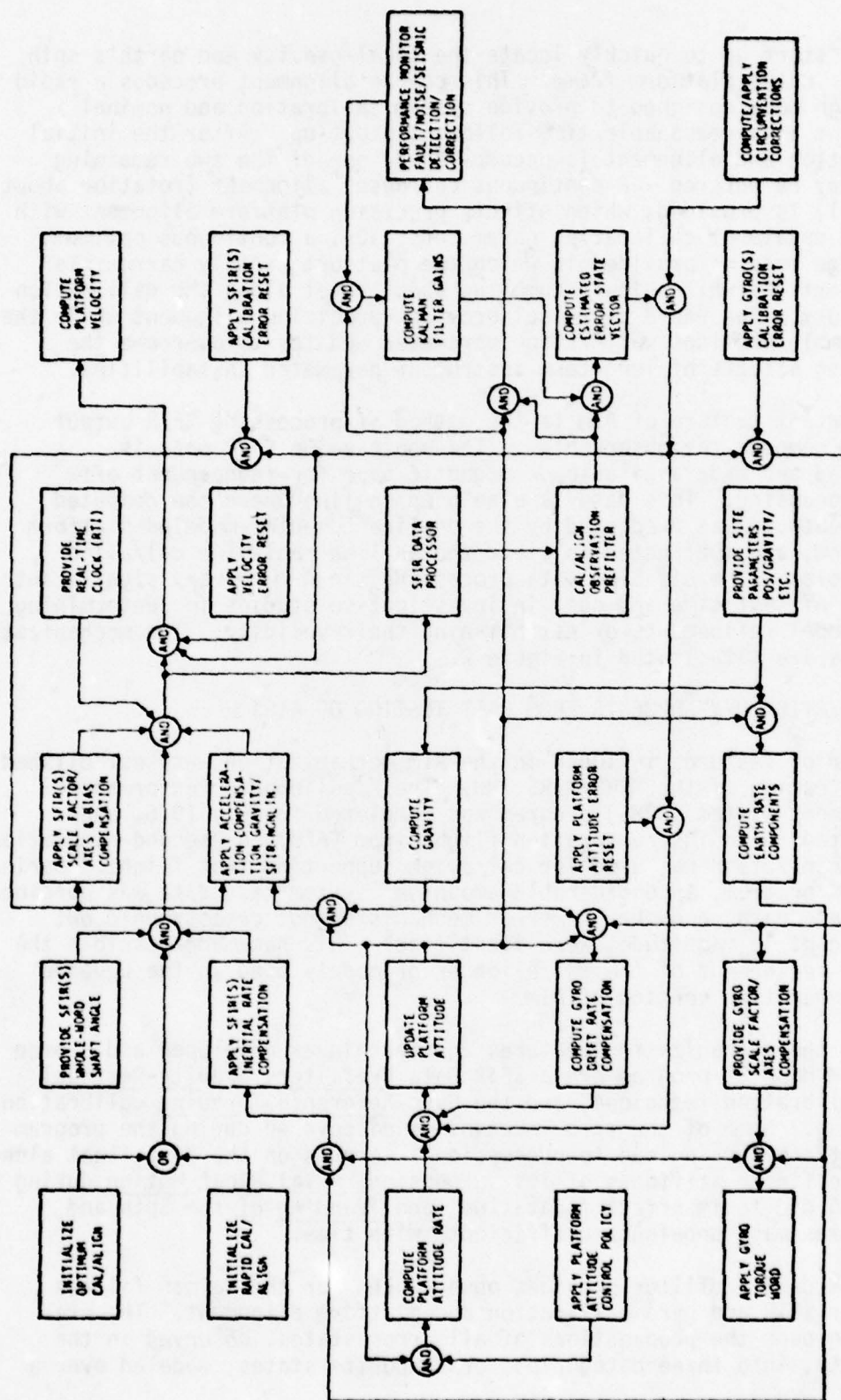


Figure 1. Optimum Continuous Cal/Align

for IMU start-up to quickly locate the local-gravity and earth's spin vectors in the platform frame. This coarse alignment precedes a rapid cal/align mode designed to provide system calibration and nominal alignment in a reasonable time following start-up. After the initial calibration and alignment is accomplished, one of the two remaining modes may be entered. A continuous carousel alignment (rotation about vertical) is provided, which effects precision platform alignment with limited update of calibration parameters. Or, a continuous optimum cal/align mode is provided in which the platform rapidly carrouseles about vertical while slowly tumbling about level along the calibration trajectory. The rapid carousel provides precision alignment while the slow tumble provides calibration parameter updates to overcome the degrading effects of long-term instrument parameter instabilities.

An important feature of AIM is the method of processing SFIR output data to compute the observables. The whole-value SFIR data is processed and made available on magnetic tape for independent off-line processing. This data is also used on-line where the computed "SFIR" outputs, as predicted by the on-line computer-modeled platform algorithm, are subtracted to yield the on-line real-time cal/align observables. The off-line data processing can achieve very significant savings of test time and cost in investigative studies for determining error-model refinements or establishing their validity. The mechanization features are illustrated in Figure 2.

#### MECHANIZATION DEVELOPMENTS FROM PAST TESTING OF AIRS

A number of features included in the AIM mechanization were established during testing of the MPMS/AIRS IMU. The Missileborne Performance Measurement System (MPMS) program was completed in July 1976, and culminated in an instrumentation flight from VAFB. A "second-generation" AIM mechanization was used for cal/align supporting that flight. During the MPMS program, a considerable amount of system test data was obtained. From these data, a number of error mechanisms, not catastrophic but significant in magnitude, were identified. This has made possible the further refinement of the cal/align error-models used in the updated third-generation version of AIM.

Some of the mechanization features and techniques developed and proven on the MPMS/AIRS program are a SFIR Data Prefilter, Gravity-Residual SFIR calibration technique, and the Gyro Reference Torquing calibration technique. Some of the error-mechanisms discovered during the program are Platform-Cocking due to precessional torques on the gyro float along with the finite-stiffness of its suspension, Axial Float-Motion during tumbling due to imperfect floatation, and Trending of the Spin and Input axes mass unbalance coefficients with time.

The SFIR data prefilter provides observables for the Kalman filters used for SFIR and gyro calibration and platform alignment. The pre-filter groups the propagations of all error states, observed in the SFIR data, into three categories, or composite states, modeled over a

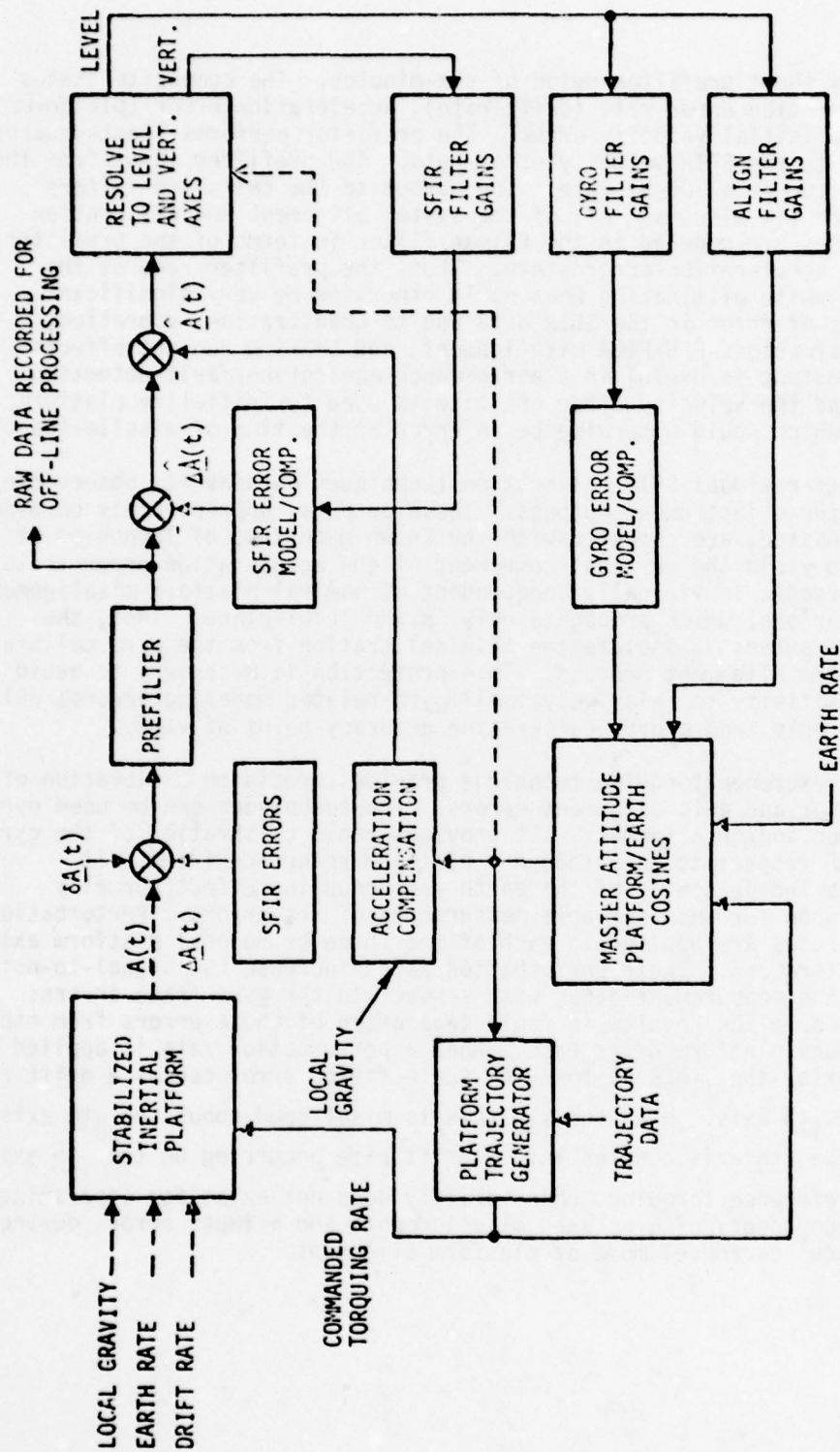


Figure 2 An Illustration of the Cal/Align Portion of the Advanced Inertial Mechanization (AIM)



relatively short prefilter period of six-minutes. The composite states are acceleration error-rate (drift-rate), acceleration error (platform tilt), and initial velocity error. The prefilter performs least-squares data fits to the SFIR velocity-error data. The prefilter input from the SFIR(s) occur at a 100-Hz rate. The output to the cal/align filters occurs each six-minutes. All of the system alignment and calibration error states are modeled in the Kalman filter in terms of the prefilter composite acceleration-error state. Thus, the prefilter reduces the data rate while eliminating what would otherwise be very significant components of error in the SFIR data due to quantization, vibration, encoder harmonics, PIG-PIGA misalignment, and bearing run-out effects. The rate output is useful in a performance-monitoring/fault-detection scheme; and the velocity error estimate is used to initialize platform velocity which would otherwise be in error at the time of missile-launch.

The gravity-residual SFIR calibration techniques obtains its observable from the three instrument outputs. These outputs, appropriately combined and compensated, are compared with the known magnitude of launch-point gravity to yield the vertical component of the acceleration-error vector. This observable is virtually independent of nominal platform misalignment and gyro errors, which propagate only in the level-plane. Thus, the technique serves to isolate the SFIR calibration from the gyro calibration and platform alignment process. This protection is necessary to avoid undue sensitivity to relatively small gyro-related modeling errors; which are small only from a gyro calibration accuracy point of view.

The gyro reference torquing technique provides precision calibration of scale factor and axis alignment errors. The techniques can be used during calibration and/or alignment. It provides rapid calibration of the gyro frame with respect to an orthogonal platform reference frame. It calibrates independently of the earth-rate coupling effect normally depended upon for an observable measurement of the errors. Perturbation torquing rates are applied to each of the three orthogonal platform axes, via gyro torquers. These perturbation rates increase the signal-to-noise ratio of the measurement data, with respect to the gyro-frame errors; and the modulation results in rapid separation of these errors from others that produce platform drift rate. When a perturbation rate is applied to the  $i$ th axis, the  $i$ th axis torquing scale-factor error causes a drift rate about the  $i$ th axis. When the  $i$ th axis is misaligned about the  $j$ th axis, a rate on the  $k$ th axis couples into a drift rate occurring on the  $i$ th axis.

Without reference torquing, observability does not exist for separating certain components of gyro axes misalignments and azimuth error, during the vertical carousel mode of platform alignment.

## NEW DEVELOPMENTS FROM ASP TEST RESULTS AND FINDINGS

During the ASP hardware/software development and checkout portion of the program, a number of new developments and findings were made.

### Gyro Axial Float Motion

As previously mentioned, MPMS/AIRS testing revealed certain unmodeled error mechanizations affecting IMU performance. One of the error mechanisms is a gyro axial float-motion, which produces a drift rate corrupting the calibration of gyro scale factor and axes misalignments, during tumbling in the one-g field. Gyro mass unbalance calibration is similarly affected, but to a somewhat negligible degree. In order to eliminate the deleterious effect upon scale factor and axes calibration, an additional carrousel rotation was added to the calibration trajectory.

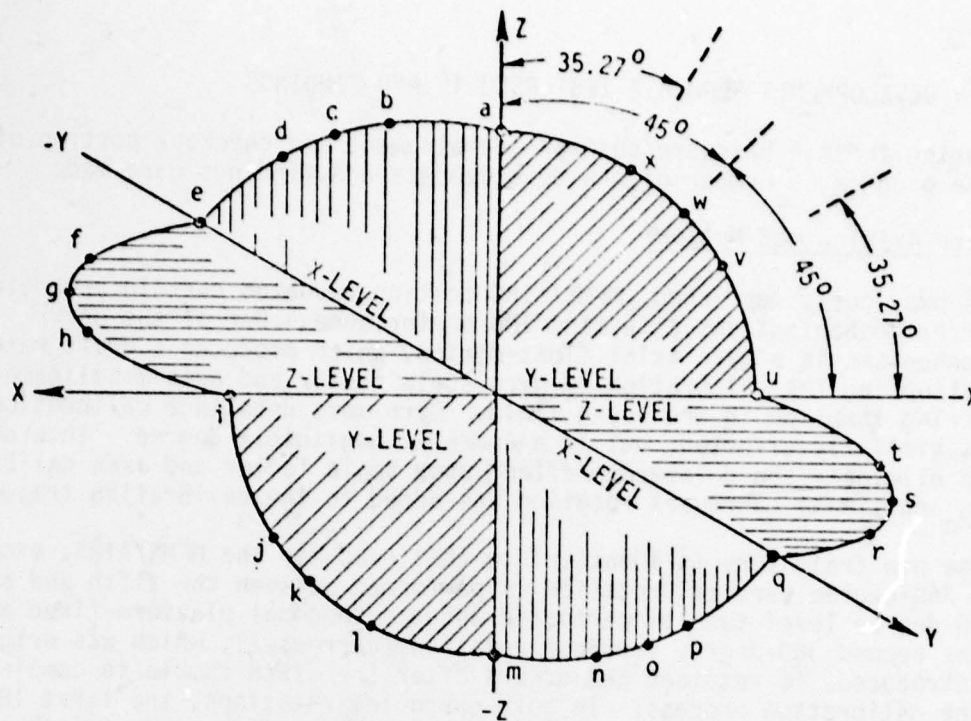
The new trajectory is identical to that used for the MPMS/AIRS, except a 360-degree vertical rotation is performed between the fifth and sixth 90-degree level tumbles performed about orthogonal platform-fixed axes. The second 360-degree vertical rotation (carrousel), which was originally introduced, is retained and occurs after the sixth tumble to complete the calibration process. In both carrousel rotations, the first 180-degrees of rotation is made during a six-hour period, while gyro axial float position reaches steady-state. During the second 180-degrees of rotation, the reference torquing technique is used to re-calibrate the gyro scale-factor and axes misalignments. At the end of the carrousel rotation, reference torquing is turned off and the Kalman filter-gains for scale-factor and axes, alone, are kept zeroed until after the sixth tumble and first 180-degrees of the last carrousel have been completed. The two periods of three-axes reference torquing are performed at platform orientations separated by 90-degrees relative to the gravity vector. Thus, they provide complete observability for re-calibrating all nine gyro scalefactor and axes errors. This occurs during periods of absence of any axial float motion. The cal/align trajectory is illustrated in Figure 3.

### Platform-Cocking

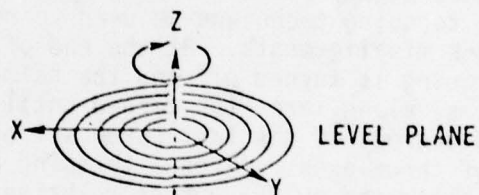
Another unmodeled error mechanism is that of platform-cocking about the input axes of each gyro to which a torquing rate is being applied. Since the net rotation angle is proportional to the gyro float suspension stiffness (spring coefficient) and the applied torquing rate, a real-time computation of the motion (or its effect) is now used to compensate the error while operating on-line.

### Torque-Word Delay

An error source also requiring compensation similar to that for platform-cocking is torque word transmission delay. A time-delay in applying the gyro torque words produces an azimuth bias error proportional to the carrousel rate and the time delay. An even more serious problem arises



TGG, SFIR CALIBRATION ORIENTATIONS FOR OPTIMUM EXCITATION OF ERROR-STATES



ROTATION ABOUT VERTICAL PROVIDES CAL/ALIGN

Figure 3 An Optimum Continuous Cal/Align Trajectory of the Gravity Vector in the Platform Frame



when the delay is present during reference torquing. The drift-angle response is confused with and interpreted as being a scale-factor or axes alignment error of about 5-ppm or 1-sec per millisecond of delay. This error can result in subsequent azimuth alignment bias error of like magnitude. One cannot overemphasize the importance of accounting for all input/output data transmission delays, as well as any internal delays produced by data filtering, sampling, etc.

#### SFIR Data Delay

On the ASP IMU, a 3.1-msec delay in SFIR data sampling has been purposely introduced to avoid overlapping certain communications read/write cycles. It was found necessary to also account for this delay, at the SFIR data level, because of the resulting data-lag occurring when platform rates normal to the gravity vector were applied.

#### Gyro Mass Unbalance Trends

A very detrimental error source which degraded alignment on the MPMS/AIRS IMU was a trending of the gyro spin-axis and input-axis mass unbalance coefficients with time. Some unanswered questions still remain concerning the exact error-model behavior of these drift rate trends. Data from the MPMS/AIRS testing shows a somewhat random, at least unpredictable, nature of the trends over periods of several days. This is indicated by back-to-back calibrations completed at about 48-hour intervals. The stop-gap solution on the MPMS program was to fit a "best" straight line slope to a plot of the gyro bias compensation data obtained during a carousel alignment. The estimated slope numbers were used for compensation on a following alignment. The lack of stability of the trends was evidenced by an inability to predict their future values with sufficient accuracy.

The solution used for the ASP program consists of modeling composite drift-rate bias trends on each of the three platform axes. These are enabled during carousel alignment to track the net drift-rate trend and provide compensation for it. An uncompensated trend prevailing along a vertical-axis causes a bias azimuth error. An uncompensated trend along a level-axis causes sinuous propagations of azimuth error, as the platform is carouselled. Individual trends for each mass unbalance parameter cannot be modeled during alignment, for lack of observability. Only the net composite trends are observable. At present, additional testing and error-model investigations are planned before attempting to model the trends during the platform calibration process.

### Dynamic Error Modeling

On prior test programs, such as MPMS/AIRS, the mobility torquing rates used to move the platform along its tumbling/carrouseling cal/align trajectory were limited to about 30-deg/hr. The error models used to relate all of the error-states to each other, and to the observables, were expressed by a simplified closed-form approximate solution. For example, it was found to be quite adequate to treat direction-cosine variables as being constants (mid-interval values) over the 6-minute Kalman cycle when integrating them with respect to time. Also, the gyro drift rate error-model, in which dynamically changing values of gravity excitation occur, was also treated as having constant parameters over the Kalman cycle. These simplifications were found to be grossly inadequate with the higher mobility rates used on ASP.

The ASP platform uses cal/align mobility rates up to 90-deg/hr. This results in larger changes in the platform/earth direction-cosines and the gyro drift-rates during each six-minute filter cycle. While the simplified filter models continued to be adequate at 30-deg/hr. rates, the Kalman estimates of system errors deteriorated and converged to erroneous values when the mobility rate was progressively increased to the 90-deg/hr. level. Using IBM-computer simulations with numerical integration techniques, the problem was traced to the simplified error-model forms used in implementing the Kalman filter. In particular, estimation of the  $g$ -sensitive and  $g^2$ -sensitive gyro parameters was seriously affected. The simplified, mid-point constant products-of-variables approximation turns out to be the constant-term of a series representation of the products of time-varying direction-cosines. Some of the  $g^2$ -parameters have cubic products of variables. The problem was corrected by adding additional matrix terms to the filter transition matrix and the output or measurement matrix. These additional matrix terms add considerable complexity to the Kalman filter computations, but they provide the dynamic error-modeling necessary to achieve required estimation accuracy at the higher mobility rates. The added terms include all components through second-degree.

### Computational Algorithms

A computational problem very similar to the error-modeling problem also arose in computing platform direction-cosines and gravity compensation for the cal/align observables. Since errors in these computations affect accuracy in a direct first-order sense, the effect of the higher mobility rate upon accuracy was even more devastating. The solution was an addition of higher-order terms to the direction-cosine solution algorithm. Terms through fourth-degree were required. A similar solution corrected the gravity compensation algorithm problem.

### Special Pre-correlation Techniques

A very important finding from the ASP test-bed program resulted in a pre-correlation technique which has greatly improved the overall accuracy of the calibration. In the past, considerable difficulty was encountered in calibrating the gyro  $g^2$ -sensitivities. Typically, under the best of conditions, the accuracy of system estimates of these parameters was somewhat poor. With the pre-correlation technique, not only is overall parameter estimation accuracy improved, but in particular, the  $g^2$ -sensitivities are accurately estimated with relative ease.

The estimation problem has apparently been present to some degree in all of the known cal/align mechanizations for the AIRS/TGII type cal/align applications. The subtlety arises from ignoring the fact that some type of coarse pre-alignment is required in order to bring the alignment error-states into the range of a linear Kalman filter. Typically, a form of gyrocompass alignment is used to obtain the rudimentary knowledge of the north unit-vector, as required. This pre-alignment may in some cases be effected by a few iterations of the Kalman filter, with the platform stationary, before re-initializing and beginning the calibration trajectory tumble. In any event, the gyrocompass prealignment biases out the east-west axis drift rate with an equivalent equal and opposite-sign azimuth error. The uncalibrated system normally has relatively large drift rates, and the north-south axis component causes a correspondingly large north-south axis platform tilt. The tilt cannot be corrected by leveling error resets alone, because the tilt immediately reappears after the reset, due to the uncompensated drift rate. Thus, attempts to model large initial conditions for level tilts in the Kalman filter covariance matrix fails to alleviate the problem.

The detrimental effect upon the estimation process begins when the platform tumbling rate is applied. At this point in time, the Kalman filter responds as though the initial "uncorrelated" tilts had been significantly reduced; and expecting an error response due to gyro scale factor error, proportional to the newly applied rate, the filter gains apply a large amount of the "unidentified" tilt observable into an erroneous scale factor error correction. This begins a chain of events that compound the estimation accuracy degradation, at each subsequent filter error-reset, with the unaccounted scale factor error being particularly confused with the  $g^2$ -sensitive error propagations.

A very effective solution was found to be a pre-biasing/pre-correlation technique in which gyro biasing loops were added to the stationary gyrocompass pre-alignment mode used for coarse alignment prior to Kalman calibration. After the biasing loops reach steady-state, the platform tilt is near zero, and azimuth error is strongly correlated with all components of gyro drift rate acting along an east-west axis (this includes biases,  $g$ -sensitive,  $g^2$ -sensitive, etc.) Also, the sum of all drift rate components acting along a north-south axis add up to zero.



This is precisely the information needed by the Kalman filter covariance matrix in order to perform the subsequent calibration in an accurate manner. The information is passed on to the Kalman filter by performing a pre-correlation reset upon the initial, diagonal covariance matrix, using a specially computed correlation gain matrix. The correlation gains are the steady-state leveling, biasing, and gyro-compassing gains of the pre-alignment. A word of caution at this point is advice that the "generalized" Kalman reset equation is mandatory for this application. With the reset applied, the Kalman filter proceeds in excellent manner with the calibration process; proving once again the value of telling the Kalman filter the truth.

#### SUMMARY OF CALIBRATION PERFORMANCE RESULTS

The ASP IMU has been operating with SFIR(s) and gyro(s) from the MPMS/AIRS program. For the most part, the same set of TGII have been used throughout the ASP development and testing program. Thus, the performance results presented herein are representative of one given set of instruments. In order to make a meaningful assessment of the quality of performance obtained from the ASP, the first objective of performance testing was to duplicate the cal/align baseline testing procedures used in the MPMS/AIRS test program. The ASP results could then be compared statistically to AIRS results and to the MPMS/AIRS IMU error budget specifications.

In Table I, the results of six ASP calibrations are shown, which correspond to the MPMS/AIRS baseline test conditions (includes filter statistics, calibration trajectory, etc.). The first three calibrations, #78-90 through #78-92, were performed without using the reference torquing technique. The results are normalized by dividing each quantity by its corresponding MPMS/AIRS budgeted specification value. The second group of three calibrations, #78-93 through #78-95, were obtained immediately following the first three, and under the same test conditions, except the reference torquing system was enabled.

In Table II, the results of seven calibrations are shown. Again the first three, #78-96 through #78-98, were performed without reference torquing; while the remainder, #78-99 through #78-102, used the reference torquing technique. These calibrations were made immediately after the first group, in Table I, and under the same test conditions, except the mobility rate was increased to 60-deg/hr. Thus, the latter group of calibrations were each completed in half of the time, and with half of the number of six-minute data points, than that of the former group. The results are once again normalized with respect to specification values.

### Discussion of Calibration Results

The test conditions for calibrations in Table I satisfy the objective of obtaining a data set comparable with the MPMS/AIRS data base and budgeted specifications. Although not shown here, the results do compare favorably with the AIRS data base. The indications are that the TGII are a typical sample from the MPMS/AIRS instrument family, and that the ASP IMU is essentially performing as expected from design. These calibration results are also compared to the MPMS/AIRS budgeted specification values, as presented herein. For the most part, the parameter errors are either near spec or better than spec value.

The calibrations reported in Table II were performed at the increased, 60-deg/hr, rate to satisfy a test objective to determine the effects of using higher torquing rates for the calibrations. The MPMS/AIRS did not have the higher torquing rate capability.

Upon examination and comparison of the calibration results, the following discussion and observations are made.

1. For the 30-deg/hr cals, Table I, the reference torquing technique appears to:
  - (a) improve gyro bias, scale-factor, and axes-alignment accuracy by a factor of approximately two,
  - (b) make little difference in estimating gyro mass unbalance (g-sens.) parameters,
  - (c) improve accuracy significantly for some of the gyro compliance ( $g^2$ -sens.) parameters.
2. Comparing the 30-deg/hr cals, Table I, with 60-deg/hr cals, Table II, both without the reference torquing (upper halves of Tables), the following observations are made:
  - (a) Except for perhaps the gyro bias, the two data sets, when compared as one group versus the other, show no significant difference in indicated estimation accuracy.
  - (b) Since the 60-deg/hr group contains half the number of data-points as the 30-deg/hr group, it appears that perhaps more data than is necessary is obtained at the lower rate, or increasing the rate brings about improvements which offset the disadvantage of a smaller data set. In any event, with the higher calibration rate, a factor of two savings in calibration time is accomplished with no significant degradation of performance.

TABLE I. ASP CALIBRATION RESULTS (30-DEG/HR)  
ENSEMBLE STATISTICS CALS 78-90 THRU 78-95

PARAMETER GROUP MPMS/AIRS TGII		$\sigma$ /SPEC
Gyro Cal (30-deg/hr)  Without Reference Torquing (3 Cals)	Scale Factor	0.404
	Misalign.	0.562
	Bias	1.708
	G Sen. {	0.369
		0.431
		1.718
	G <sup>2</sup> Sen. {	1.385
		1.231
		0.981
		3.462
		0.942
Gyro Cal (30-deg/hr)  With Reference Torquing (3 Cals)  ± 8-deg/hr	Scale Factor	0.195
	Misalign.	0.205
	Bias	0.985
	G Sen. {	0.554
		0.303
		0.462
	G <sup>2</sup> Sen. {	0.615
		1.231
		0.192
		0.769
		0.154
SFIR Cal (30-deg/hr)	Scale Factor	0.123
	Bias	0.123
	Misalignment	0.308

SPEC = BUDGET VALUE PER TRW DOCUMENT #27870-6233-TE-00

"MPMS ERROR MODEL, BASELINE ERROR BUDGET AND CAPABILITY  
ESTIMATE - REVISION 1", APRIL 1976



TABLE II. ASP CALIBRATION RESULTS (60-DEG/HR)

ENSEMBLE STATISTICS CALS 78-96 THRU 78-102

Parameter Group MPMS/AIRS TGII			$\sigma$ /Spec
Gyro Cal (60-deg/hr)	Scale Factor Misalignment Bias		0.405
			0.719
			0.615
	Without Reference Torquing (3 Cals)	G Sensitivity { DI	0.569
		DS	0.892
		DO	0.513
	G <sup>2</sup> Sensitivity	DII	2.154
		DSS	2.923
		DIS	0.500
		DIO	0.462
		DOS	0.269
Gyro Cal (60-deg/hr)	Scale Factor Misalignment Bias		0.373
			0.432
			0.200
	With Reference Torquing (4 Cals)	G Sensitivity { DI	0.354
		DS	0.262
		DO	0.333
	± 8-deg/hr G <sup>2</sup> Sensitivity	DII	0.692
		DSS	0.538
		DIS	0.115
		DIO	0.385
		DOS	0.115
SFIR Cal (60-deg/hr)	Scale Factor Bias Misalignment		0.108
			0.123
			0.308

SPEC = BUDGET VALUE PER TRW DOCUMENT #27870-6233-TE-00

"MPMS ERROR MODEL, BASELINE ERROR BUDGET AND CAPABILITY

ESTIMATE - REVISION 1", APRIL 1976

3. Referring to the 60-deg/hr calcs, and comparing the upper and lower portions of Table II, the reference torquing technique, used at the higher mobility rate, appears to:
  - (a) improve gyro bias accuracy by a significantly greater amount than the improvement obtained at the lower rate, improve gyro scale-factors and axes-alignment accuracy by a significantly smaller amount than that obtained at the lower rate,
  - (b) produce a slight improvement in mass unbalance accuracy, and
  - (c) effect improvement in the estimation accuracy of the compliance parameters of about a factor of three, rather than a factor of two obtained at the lower rate of 30-deg/hr.
4. Upon comparing the SFIR data results in both Table I and Table II, the accuracy performance does not appear to be significantly affected by the increase in mobility rate.

In summary, the data results show that the ASP TGII test bed exhibits essentially the same performance excellence as the MPMS/AIRS. Also, that using higher mobility rates with reference torquing and other techniques implemented in the Rockwell AIM mechanization, the ASP performance exceeds the budgeted specifications established for the MPMS/AIRS TGII by significant margins.

#### SUMMARY OF PLATFORM ALIGNMENT RESULTS

In order to test the azimuth alignment performance of the ASP IMU, an optical system was setup in which autocollimators can be calibrated to a geodetic azimuth monument mirror, referred to Polaris, and then used to measure the location of mirrors mounted on the ASP stable element. The laboratory setup is shown in Figure 4.

The Advanced Stabilized Platform (ASP) Test Bed Absolute Azimuth Verification (AAV) mechanization utilizes two mirrors located 90 degrees apart on the equator of the platform stable member sphere. These mirrors are precisely calibrated with respect to the SFIR coordinate frame so that the mirror normals can be accurately related to the computer coordinate frame used for gyrocompassing.

The gyrocompassing process (Precision Align) is the same as was mechanized by Autonetics for MPMS, i.e., a 15 state Kalman filter which actively estimates platform attitude (3 states), gyro biases (3 states), gyro scale factors (3 states), and gyro misalignment angles (6 states). This process is performed with the stable member rotating about the vertical (carrousselling), typically at 60 deg/hr, but with capability of up to 90 deg/hr. Reference torquing is used during Precision Align.

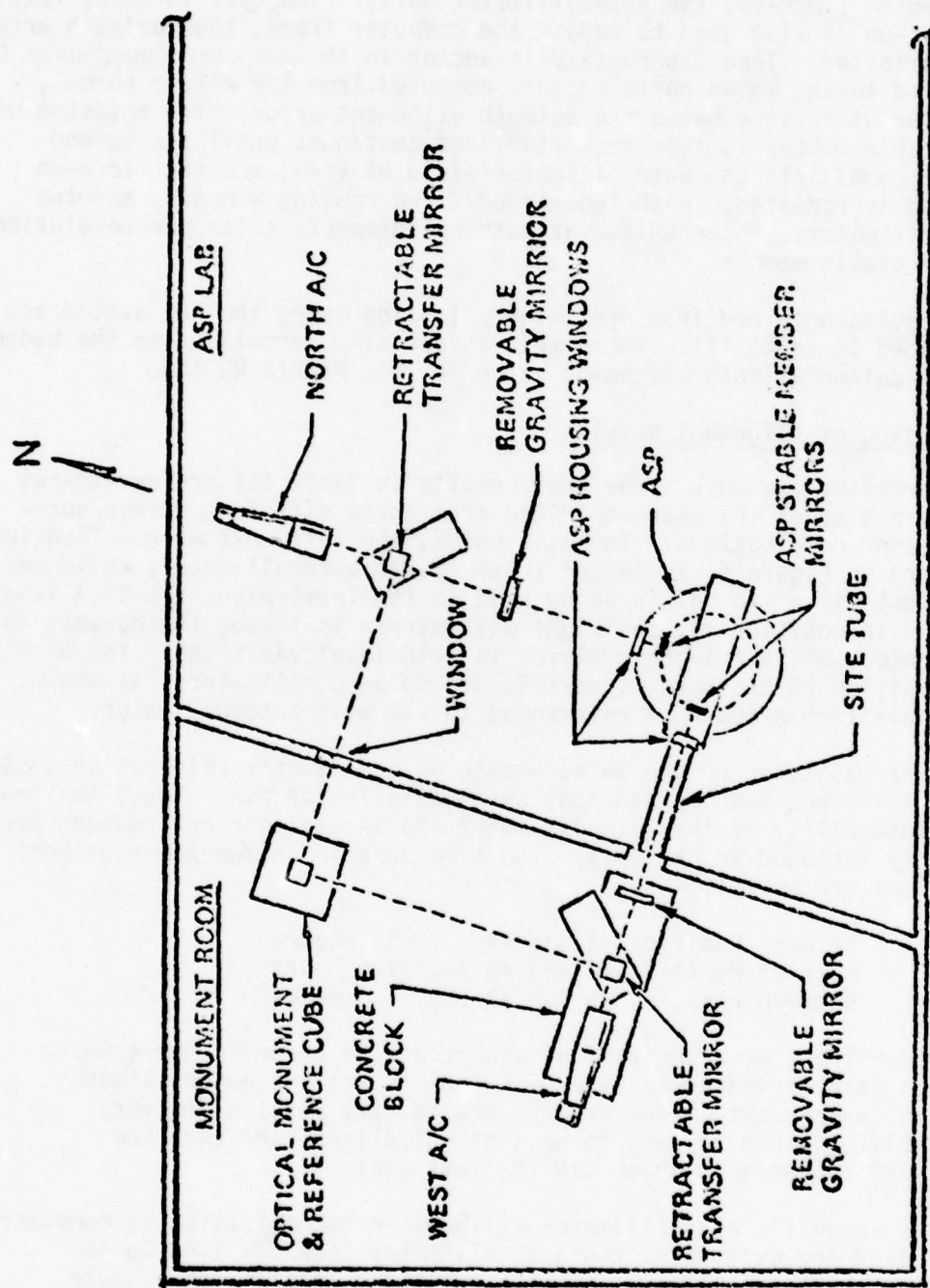


FIG. 4. ASP ABSOLUTE AZIMUTH VERIFICATION (AAV) LABORATORY SETUP



When one of the mirrors approaches the field of view of the two-axis autocollimator, which has been aligned to the precision optical reference, the stable member rotation is stopped, and then moved via gyro torquing to hold to (lock-on) the autocollimator nulls. The gyro torquing required to lock-on is also used to update the computer frame, thus azimuth error is unaffected. Then the north unit-vector in the computer coordinate frame is compared to the known north vector, computed from the mirror normal, with the difference being the azimuth alignment error. The rotation of the stable member is then restarted, and continues until the second mirror comes into the autocollimator field of view, and the "lock-on" process is repeated. With two mirrors, two housing windows, and two autocollimators, three unique azimuth measurements exist per revolution of the stable member.

The results obtained from preliminary testing using the AAV system are presented in Table III. These results are also normalized to the budget specification azimuth alignment value for the MPMS/AIRS IMU.

#### Discussion of Alignment Results

The normalized azimuth error test results in Table III are rev-to-rev deviations about the mean, obtained from three different mirror/autocollimator combinations. In position #2, the left-most mirror (looking downward in Figure 4) is locked to the north autocollimator, while the right-most mirror normal is being held in the level-plane via SFIR leveling loops. In position #4, the right-most mirror is locked to the west autocollimator, while the other mirror is held level via SFIRS. The orientation for position #5 has both mirrors locked to autocollimators, as shown, where platform azimuth is referenced to the west autocollimator.

The data was taken before an automatic autocollimator calibration system, which has since been mechanized, was available for use. Thus, the long-term instability of the autocollimator and its seismic environment are directly included in the data. The time duration between measurement positions are as follows:

Between Position #2 and #4 ...	3. hours
Between Position #4 and #5 ...	1.5 hours
Between Position #5 and #2 ...	1.5 hours

Tests confirm that a substantial amount of the error in the azimuth readout data is indeed long-term instability of the autocollimator and its environment. However, the preliminary results are very favorable, and can be seen to be substantially better than the MPMS/AIRS budget spec which was the test goal.

The new automatic autocollimator calibration mechanization is computer controlled and calibrates the autocollimator line-of-sight to the fiduciary reference line-of-sight six-minutes before each azimuth measurement. Thus, most of the long-term instability of the instrumentation system will be virtually eliminated. The same system

TABLE III. ASP AZIMUTH ALIGNMENT REPEATABILITY  
NORMALIZED TEST RESULTS

CARROUSEL REV-TO-REV VARIATIONS ABOUT MEAN			
READOUT POSITION NO.	2	4	5
$\Delta \psi_V / \text{Spec}$	- 0.24	0.18	- 0.37
	0.10	0.83	- 0.39
	0.03	0.54	0.17
60- Deg/Hr Carrousel Rate	0.13	0.11	- 0.22
	- 0.11	0.30	0.14
	- 0.35	- 0.66	- 0.04
3 - Lock Cycles Each Stop Pos.	0.95	0.04	0.29
	- 0.28	- 0.81	- 0.16
	- 0.19	- 1.26	- 0.30
MPMS/AIRS TGII	- 0.01	- 0.37	0.90
		1.08	
$\sigma / \text{Spec}$	0.35	0.68	0.37
ENSEMBLE $\sigma / \text{Spec}$ 0.48			

SPEC = BUDGET VALUE PER TRW DOCUMENT #27870-6233-TE-00,  
"MPMS ERROR MODEL, BASELINE ERROR BUDGET AND CAPABILITY  
ESTIMATE - REVISION 1", APRIL 1976

automatically calibrates the autocollimators to level-references six-minutes before measurements, during the platform-mirror calibration. The augmented system is currently being checked out, at the time of this writing, and will soon be available for advanced state-of-the-art determination of azimuth alignment on the ASP IMU.

A further discussion of the AAV and the ARM portion of the AIM mechanization is presented in the following section.

#### DISCUSSION AND ERROR ANALYSIS RESULTS OF AAV

The following discussion presents background information about the AAV, some of the design rational from requirements for the optical system, and a description of a novel filtering scheme for the ARM. Following the discussion, a summary of the AAV error analysis results are given.

##### Background Information About the AAV

The ASP Auxiliary Reference Monitor (ARM) is a subsystem mechanized to process data from various auxiliary reference devices such as autocollimators, level detectors, attitude resolvers, etc., for IMU performance verification and/or diagnostics.

The present discussion pertains to two of the important functions of ARM involving external autocollimators. An automatic mirror calibration mode calibrates external autocollimators to true-level, while using them to precisely locate the platform-mounted mirror-normal vectors in the calibrated platform reference frame.

This operation is in preparation for the second important function, that of performing absolute azimuth verification (AAV) while the platform operates in an about-vertical carrousel alignment mode. During the latter mode, the calibrated mirrors are referenced to the autocollimators, in azimuth, to provide the optical link to a Polaris-reference azimuth monument cube. Calibration of the autocollimators to the reference monument cube is accomplished automatically by the ARM, during the periods of time when platform mirrors are not in the field-of-view. A servo-driven table carrying a precision pentaprism provides calibration of the autocollimator to the monument line-of-sight. This calibration is accomplished by processing the A/C null data, in the system computer, up to a time of 6-minutes before each lock.

In the mirror calibration process, the true mirror-normal is servoed to level, via an autocollimator, while the platform mounted SFIR(s) precisely locate the true vertical-vector for calibrating one of the two mirror coordinates. The other coordinate is measured by repeating the process, after rotating the platform through 90-degrees. Actually, a minimum of four-measurements for each mirror are obtained at 90-degree spacings. This provides for any earth-fixed bias error in the autocollimator calibration to be cancelled out, since the same autocollimator is always used.



In the absolute azimuth verification (AAV) process, the calibrated platform is aligned while rotating about the local-vertical. Azimuth destination vectors for the pre-calibrated mirror normals have been previously computed to correspond to the azimuth orientations of the autocollimator(s) line-of-sight. Thus, when the platform/mirror is rotated to an azimuth destination, as indicated by computer-reckoned direction-cosines, the mirror-normal, in an error-free situation, will be exactly along the autocollimator known line-of-sight. In an actual situation, the alignment error between true platform and computationally determined platform frames will result in the mirror arriving within the autocollimator field-of-view. Upon closing the locking loop, the angular distance moved by the platform in nulling the autocollimator gives a measure of the prevailing alignment error. Each angular increment applied through gyro torquing to achieve autocollimator lock-on is also applied to the computer mechanized direction-cosine solution, so that the true azimuth error remains unchanged.

#### Data Processing Requirements

The required data processing techniques are dictated by the method chosen for obtaining alignment-error and mirror-calibration measurements. The characteristics of an ideal optical readout device would include the capability for strobing the platform-mirror position while the platform continues to rotate along its carousel alignment path. Suitable measurements would require high-resolution, low-noise, plus linearity and stability of the readout with respect to both time and position. Such a device was not found to be commercially available; and thus, a conventional autocollimator with electromechanically driven internal mirror and readout potentiometer prevails. This device typically exhibits a very low-bandpass, due to servo compensation required to attenuate the otherwise relatively large amplitude of servo noise and jitter. Past test results established the non-feasibility of using this device for measurements "on-the-fly."

The principal accuracy problems arising from the dynamic readout application are scale-factor nonlinearity, two-axis cross-coupling, inability to precisely predict servo-delay, and adverse effects of noise on determination of the beam cross-over position and time. It appears that the inherent accuracy of the device can be achieved only by using the autocollimator as a "steady-state" position-error nulling device with the platform mirror being held stationary during the measurement.

An important data-processing requirement to consider is that of providing an autocollimator/platform-mirror locking-loop for precisely positioning the platform mirror along the autocollimator line-of-sight. A rapid response-time is required in nulling initial-position errors of up to the  $\pm 60\text{-sec}$  field-of-view. At the same time, steady-state angular follow-up control to the platform mirror (via gyro torquing) requires between one and two orders of magnitude attenuation of read-out noise, for the autocollimator used. A data-processing mechanization for

satisfying these requirements was developed. It consists of a novel and innovative scheme for discrete-time estimation and control, in which statistically controlled gains achieve a rapid initial-condition response, with a very low-bandpass response in the steady-state. The next topic of discussion is devoted to describing this novel filter.

#### Description of the Platform Locking Filter for the ARM

When the platform arrives at its commanded destination, the autocollimator internal servo-system locks its beam to the platform mirror-normal vector. The null-error output signal from the readout potentiometer is supplied to the computer. It represents the acquisition error of the platform from the reference position. This error signal must be filtered and used to supply a feedback torquing signal to the platform gyros for driving the platform to the required null-position. The platform must be precisely held in the known reference position (locked to the A/C-null reference-line) while the computed direction-cosines are providing the computer reckoned direction of North for comparison. The difference between the known platform and computed vectors is the azimuth error. The platform locking filter must provide the rapid response and precision positioning required.

The locking filter consists of a modified average-of-average (AOA) prefilter that processes the sampled A/C null data at 10-msec intervals. The filter weighting function is adjustable from an optimum filter for broadband noise to a near-optimum filter for narrowband noise. It can be empirically adjusted, using real data, to provide the best attenuation for any combination of the two types of noise. The raw autocollimator data primarily exhibits a narrowband noise with center frequency near the one-Hertz region. The prefilter has a zero-frequency gain of unity, with a roll-off roughly approximated as -12 db/octave. It has a zero at one-Hertz, and negligible noise above one-Hertz passes through the filter. The output of the filter occurs at 1-second intervals, and is scaled by a time-varying statistically controlled gain to provide the feedback torquing to the platform gyros.

A digital compensation is derived from the prefilter output. It is applied at the input to account for the prefilter time-delay, and to stabilize the locking loop response. A portion of the digital compensation consists of a back-bias, corresponding in magnitude to the output-measurement of the filter. It is applied to the input at precisely the filter output sampling-time; and it provides a mask of the newly measured error sample, while the gyro torquing loop is removing that portion of the null-error in a linear manner. The second part of the compensation is computed and applied to the input of the prefilter at the input sampling rate. Its function is to incrementally "count-down" the mask in accordance with the actual incremental removal of the null-error via the feedback torquing. This scheme effectively decouples the error estimation and control processes, and reduces the residual component of error-signal to zero-frequency over each measurement interval.

The final feature of the locking loop that provides the rapid initial-condition response, plus a very low bandpass steady-state, is the statistically controlled time-varying follow-up loop gain. The gain is computed at each 1-second loop-processing interval, using formula for a "best linear estimator" for gaussian noise. The initial variance of null-error is set to correspond to the 60-sec acquisition range of the autocollimator. The variance of the prefilter output noise, which is also the measurement noise for the follow-up loop, has been determined empirically from test data. And finally, long-term instability statistics for the autocollimator, its interface, and its thermal and seismic environment have been established from appropriate long-term data. These statistics are used to compute the optimum gain at each filter cycle, which is in turn used to supply the feedback control and update the null-error filter variance accordingly. The locking filter works very well, and exhibits rather amazing speed and accuracy performance.

#### Summary Error Analysis Results for the AAV

The following error sources for the AAV instrumentation system were investigated, and error estimates established. The summary result from the error analyses is given in a normalized form. This makes it possible to make a meaningful comparison with the AAV system data previously presented in Table III. The normalization is the same as was used for the AAV system data reported therein.

#### Optical Alignment Test Equipment Errors:

1. Azimuth uncertainty from astronomic north, using Polaris
2. Azimuth uncertainty of monument calibration
  - (a) primary cube surface
  - (b) trunion axis estimate
  - (c) transfer measurement error from primary to secondary cube faces
  - (d) cube face stabilities
  - (e) off-center position effect on light beam
3. Transfer mirror off-set plus variability
4. Davidson 707 Autocollimator
  - (a) optical path air instability
  - (b) image degradation



- (c) temperature bias and instability\*
- (d) time instability\*
- (e) cross-coupling and other readout errors

5. Platform Window

6. Platform Mirror

\* These errors will be eliminated, for all practical purposes, when the automatic A/C calibration, previously described, is used.

Data Acquisition and Data Processing Errors

1. Autocollimator/platform locking error
  - (a) loop noise
  - (b) inertial system cal related errors
2. Platform mirror calibration error
3. Data processing error
  - (a) algorithms
  - (b) numerical resolution
  - (c) timing resolution

Error Analysis Summary Results:

1. Without Automatic A/C Calibration

<u>Total rss Error for:</u>	<u><math>\sigma</math>/Spec</u>
Optical test equipment	0.72
Data acquisition and processing	<u>0.17</u>
Grand Total rss	0.80

2. With Automatic A/C calibration

<u>Total rss Error for:</u>	<u><math>\sigma</math>/Spec</u>
Optical test equipment*	0.47
Data acquisition and processing	<u>0.17</u>
Grand Total rss	0.54

Note: This error analysis estimates the expected total absolute error-estimation accuracy of the AAV instrumentation. It includes both random and bias errors.

The data reported in Table III is measured repeatability-data which includes only the random portions of the above error analysis. The bias portions would appear in the test data mean.

#### PLANS FOR FURTHER INVESTIGATIVE AND DEVELOPMENTAL TESTING

The following list includes several of the test objectives planned for the ASP IMU test-bed future testing program.

1. Further AAV testing with automatic A/C cal.
2. Verification of gyro axial float-motion error model, and performance assessment of its on-line estimation and compensation.
3. Further investigate, develop and validate error model for g-sensitive trends, and feasibility assessment of its on-line estimation and/or compensation.
4. Develop and test more efficient cal/align trajectories to improve system timeline.
5. Investigate improved reference torquing techniques and evaluate performance.
6. Characterization and performance testing of latest design of AIRS gyros, should they become available to the ASP test-bed program.

TITLE: 3D SCENE MODELING:  
A FLEXIBLE APPROACH  
TO REFERENCE MAP  
GENERATION

AUTHORS: E. M. ROUNDS  
A. T. ZAVODNY

TECHNOLOGY SERVICE CORPORATION  
2811 Wilshire Boulevard  
Santa Monica, California 90403

(Paper not published due to lack of  
clearance. May be published later  
as an addendum)



TITLE: PROPOSED USE OF RETRO  
ROCKETS FOR OPTIMIZING  
ANALYSIS OF INERTIAL  
GUIDANCE SYSTEM ERRORS  
IN 100-G SLED TESTS

AUTHOR: NORMAN L. INGOLD

CENTRAL INERTIAL GUIDANCE TEST FACILITY  
6585th Test Group/GD  
Holloman Air Force Base, New Mexico 88330

## ABSTRACT

A useful procedure in the evaluation of an inertial guidance system consists of three steps: forcing the propagation of system errors by subjecting the system to an appropriate test; generating an accurate error function by comparing the system performance to an appropriate reference; and finally analyzing the error, i.e., identifying, separating and quantifying the component elements of the error function.

For the case of sled tests this analysis is aided by the effects of a passive water brake. The brake provides sufficient negative acceleration to separate the effects of odd and even powers of acceleration sensitivities of the system tested. For low acceleration sled tests the analysis is successful for two reasons: high powers of acceleration sensitivities are not sufficiently driven to be an observable problem; and the water brake is of sufficient magnitude, compared to the rocket boost acceleration, to in fact accomplish the desired separation.

In order to establish the limits of such success, computer simulations were made, using various sled acceleration profiles. Correlations of the expected component error functions were computed to determine separability. Through this procedure it was possible to obtain a sled acceleration function which was optimized for analysis of guidance system errors. However, when applied to the case of high accelerations (above 100 G's) problems occurred. Higher order errors could indeed now be observable, the required water brake magnitude could exceed sled structure limits and be extremely short in duration, and the error separability could be degraded.

Relaxing the constraints on the simulation resulted in the fact that a longer brake at the required magnitude could dramatically decrease error function correlations. However, such a duration would necessitate a negative sled velocity: a function unattainable from water brake, but certainly possible through the technologically feasible use of retro rockets.

This paper presents the techniques and results used to justify the use of retro rockets, for high acceleration sled tests, from the viewpoint of enhancing guidance system error analysis. The paper also specifies classes of acceleration profiles which are optimized for this purpose, both for high and low acceleration regimes.

## 1. INTRODUCTION

For many years, the Central Inertial Guidance Test Facility (CIGTF) has been involved in the rocket sled test and evaluation of inertial guidance systems. Such evaluation, or analysis, primarily involves two procedures: establishing an appropriate model to describe the errors observed, and quantifying the component elements of those errors. The first is accomplished through use of a priori knowledge of the sensor characteristics and from observation of anomalies observed in the error functions. The second is accomplished by some established computational regression analysis. Both procedures, however, depend on sufficient dissimilarity of the individual error effects to allow error separability: errors which cannot be distinguished from one another cannot be quantified, visually or computationally. The desired separability, in turn, is a function of the sled test inputs.

Unfortunately, the acceleration profile,  $A(t)$ , of sled tests is heavily dictated by environmental requirements (e.g., G-level) imposed by the customer agency; by propulsion characteristics (in turn dependent on availability and costs); and by sled weight and structure limitations. All too often the test acceleration profile eventually becomes one during which several guidance system errors propagate in a near-similar manner. This can result in the unproductive situation where the customer sees, possibly for the first time, plots indicating the combined error of his guidance system in a simulated missile environment, but cannot gain quantitative access to the sources of the error. The situation can be further compounded by uncertainties in initial orientation of the system. These uncertainties can produce erroneous effects which themselves resemble guidance system errors and which can add to, or even subtract from, the actual system error function.

For some sled tests the problem of error separation has been solved by modifying the test. Acceptable shaping of the boost portion of sled runs (by changing G-level) and the deceleration region (by vigorous scooping of water in a water brake) have significantly improved error separation for low acceleration ( $<10$  G) tests. The water brake enhances separation of the effects of odd and even powers of acceleration sensitivities of the system tested. The low G-level inhibits propagation of high powers of such errors.

In the last few years, however, requests for higher, and even constant accelerations have been made. This, on the one hand, denies the opportunity to shape the sled thrust profile and, on the other hand, limits the water brake deceleration by taxing the sled structure. The result inevitably has been increased difficulty in analyzing guidance system errors. In fact, some recent experimental profiles have involved boost accelerations of 120G with NO water brake: analysis of the performance of accelerometers on the sled was actually unsuccessful, largely because of the error inseparabilities.

## 2. PROBLEM DEFINITION

The following thoughts were consolidated to clarify the problem and to identify questions to be answered in obtaining a solution:



a. During positive acceleration (boost), guidance system velocity errors propagating in powers of acceleration, i.e.,  $\int (A^n) dt$ , become more positive for all  $n$ . (They all are rather similar, especially for near-constant-acceleration boost profiles.)

b. During the relatively low-magnitude aerodynamic drag after engine burnout (coast), velocity errors, for  $n \geq 2$ , essentially remain unchanged, i.e., they are still similar.

c. During large negative acceleration (e.g., water brake), velocity errors, for even  $n$ , become more positive; but, for odd  $n$ , become more negative. (Only here do they become noticeably dissimilar.)

d. Thus, it is evident that strong sled braking is the key to error separation.

For the case of high  $G$  ( $>100G$ ) sled tests of guidance systems, further insights are available:

a. The track reference data will tend toward lesser accuracy because of expected higher velocities, and because of greater system-to-sled relative motion at higher  $G$ -levels.

b. The higher accelerations are likely to force higher-order test item nonlinearity errors.

c. The necessary short boost at high  $G$  (because of sled velocity limitations) cannot be shaped, i.e., system errors propagated during boost and coast will be even more similar than low- $G$  runs.

d. Hence, water brake becomes even more important to the success of analyzing high- $G$  sled test data; but, there is a limit, because of sled structure, to the magnitude of water brake deceleration.

The above paradox, i.e., that sled braking is both the key to successful sled test error analysis and also vulnerable to mechanical limitations, leads to the conclusion that, if the performance of guidance systems during high- $G$  sled tests is to be evaluated, the following questions need to be answered:

a. How much relative deceleration is in fact required?

b. Is it possible to obtain that deceleration with present technology?

c. If it is not possible with present technology, but is possible with updated technology, then what are those updates?

### 3. COMPUTER SIMULATION

The problem was addressed in two phases: establishing a level of merit for sled acceleration profiles, particularly for the high- $G$  case, based on the likelihood of the test system performance being successfully analyzed;

and searching for the general parameters of high-merit profiles; as criteria for answering the questions posed above.

A common method of investigating a new area of concern of this type is to simulate the problem using one or more forms of noise as a "real life" contaminant. The least realistic contaminant is idealized: computer-generated white noise, for example. More realistic is actual noise recorded from some assumed similar environment. Yet another method was used for this investigation, however (and later corroborated through use of available data from existing sled test data files). This other method involved a study of the correlations of the various individual component functions comprising the complete guidance system error propagated during a sled test.

The reason for following this approach is that nearly 15 years experience exists in the realm of evaluating the success of guidance system error analysis as a function of system type, sled test profile, error model length, and correlations of the functions in the terms making up the error models. Since this information inherently incorporates other, subtle effects such as analyst experience, guidance system and test instrumentation evolution, equipment degradation and repair cycles, seasonal variations, etc, then correlation investigation seemed a realistic and promising approach.

The mathematical correlation between two functions,  $F_1(u)$  and  $F_2(u)$  is

$$\text{COR12} \triangleq \text{Correlation } (F_1, F_2) = \sqrt{\frac{[\int (F_1 \cdot F_2) du]^2}{\int (F_1)^2 du \cdot \int (F_2)^2 du}}$$

If  $F_1$  and  $F_2$  are perfectly correlated (look identical), the correlation becomes 1.0; if they are uncorrelated, it becomes 0.0. For example, if the functions are two straight line slopes, their sum will just be a new straight line and it will be impossible to separate that sum into the original components. Mathematically,  $F_1 = K_1 t$ ;  $F_2 = K_2 t$ ;  $du = dt$ . Then

$$\text{COR12} = \sqrt{\frac{[\int (K_1 t \cdot K_2 t) dt]^2}{\int (K_1 t)^2 dt \cdot \int (K_2 t)^2 dt}}$$

$$= \sqrt{\frac{\frac{1}{9} K_1^2 K_2^2 t^6}{\frac{1}{9} K_1^2 K_2^2 t^6}}$$

$$= 1.0; \text{ perfectly correlated, i.e., inseparable}$$

as stated.

As another example, it is possible with the human eye to distinguish between a straight line slope,  $F_1 = K_1 t$ , and a quadratic,  $F_2 = K_2 t^2$ . Here

$$\begin{aligned} \text{COR12} &= \sqrt{\frac{[\int (K_1 t \cdot K_2 t^2) dt]^2}{\int (K_1 t)^2 dt \cdot \int (K_2 t^2)^2 dt}} \\ &= \sqrt{\frac{\frac{1}{16} K_1^2 K_2^2 t^8}{\frac{1}{15} K_1^2 K_2^2 t^8}} \\ &= \sqrt{\frac{15}{16}} \\ &= .9682 \end{aligned}$$

However, the human eye cannot easily distinguish between a quadratic and a cubic, especially in the presence of a degrading element such as noise (a fact of life when analyzing real test data); the correlation between a quadratic and a cubic is .9860.

The experience mentioned above can be synopsized as follows:

a. Error functions whose correlations are higher than .995 have been separated from the dynamic portion of some sled test data. This is for the case of classic low-G (7-G maximum) sled runs with long thrust durations ( $\approx 10$  seconds), low velocity (1350 fps maximum), testing precision gimballed guidance systems.

b. Error functions whose correlations are no higher than  $\approx .97$  have been separated for the case of low-G (7 G max) sled runs with somewhat shorter boost durations (3.5 - 6.5 sec) and intermediate velocities (1600 - 1850 fps max), testing medium accuracy gimballed and strapdown systems.

c. Error functions whose correlations are around .95 have been separated for the case of various strapdown systems tested at 15 - 30 G for 1.5 to 3.2 sec at maximum velocities ranging from 1700 to 1950 fps.

d. Error functions whose correlations are around .93 have been separated for the case of a low-accuracy strapdown system tested at an acceleration which grew from 40-G to 80-G during a 1.8 sec boost; the maximum velocity was 3300 fps.

The apparent trend is toward lower analysis success for the case of lower accuracy, strapdown, systems tested at increasingly short boost durations at higher accelerations and velocities. Such a trend can be due to two possibilities: decreased knowledge of the model describing the error



and/or increased noise contamination of the error. Both possibilities require some qualification.

On the first possibility, simply not knowing the error model is not the intended meaning. Eventually the model describing gyro drifts and accelerometer anomalies is known, even if, as is common, the errors are observed for the first time during sled tests. In the velocity domain, these are low frequency errors, whose characteristics can be easily generated from accelerometer or reference data for use in the regression analysis. Performance characteristics which are more difficult to synthesize, however, are high frequency often sinusoidal products such as the effect of tangential and centripetal accelerations, due to angular vibration, on accelerometers not located on the axis of such rotational motion. Still other difficult, high and low frequency, errors are those caused by limited algorithm precision, especially in the presence of vigorous test inputs, in flight computers. These model uncertainties, it is noted, are more common for the case of strap-down, rather than gimbaled, systems.

On the second possibility, considerable research by CIGTF has shown that reference system noise content grows with velocity and velocity squared. Also there is the fact that, higher, shorter accelerations produce more relative motion between the guidance system and the sled. More subtle, however, is the decreased amount of reference data obtained from higher-G sled tests. The number of reference data points,  $N$ , is a function of distance traveled. The greater water brake deceleration demanded to separate guidance system errors when high boost acceleration is used results in rapid velocity loss and early sled stoppage. Since the confidence in the error coefficients obtained grows approximately as  $\sqrt{N}$ , the short sled runs associated with high-G tests effectively results in contamination of the reference itself. Finally, data quantity is decreased by a test item fault: accelerometer bias often changes at sled launch and sled stop. Regression analysis cannot use the data recorded before launch or after stop in such cases. Enhanced modeling methods could account for such changes, of course, but systems with such problems usually have several other unanticipated difficulties as well.

The point, however, is that trends are indicated: it would appear reasonable to demand correlations  $<.90$  for successful analysis of systems tested at accelerations  $>100$  G.

The next question is, what error model functions are to be decoupled? Recent sled tests have identified an increasing tendency toward accelerometer scale factor asymmetry, possibly caused by pre-amp, servo loop, or A/D converter mismatch. A study of such errors revealed that, although serious, such errors, in addition to a number of other, classical, accelerometer and gyro errors, were not correlated as badly as accelerometer scale factor and nonlinearity errors:  $\int A = V$ ,  $\int A^2$ ,  $\int A^3$ ,  $\int A^4$ , ... . ( $A$  is acceleration,  $V$  is velocity, and  $\int A^n$  is notational shorthand signifying  $\int (A^n) dt$ .) The function,  $\int A^4$ , is especially included because, for the case of high-G sled tests, it may be significant, and if so should be identifiable (separable). Also, for the case of the 80-G sled run mentioned earlier,  $\int A^4$  and  $\int A^2$

were so highly correlated as to be inseparable (water brake level was only -35 G), but, after truncating the error model at  $\int A^3$ , the coefficient obtained for  $\int A^2$  considerably exceeded expected values: thus possibly in fact demonstrating the presence of an  $\int A^4$  term in the system error.

The initial investigation consisted of a computer simulation of a high-G sled test acceleration profile and computation of the correlations of the error model functions  $V$ ,  $\int A^2$ ,  $\int A^3$ , and  $\int A^4$ . That is, the following correlations were studied:

COR12	$\triangleq$	Correlation ( $V$ , $\int A^2$ )
COR23	$\triangleq$	Correlation ( $\int A^2$ , $\int A^3$ )
COR34	$\triangleq$	Correlation ( $\int A^3$ , $\int A^4$ )
COR13	$\triangleq$	Correlation ( $V$ , $\int A^3$ )
COR14	$\triangleq$	Correlation ( $V$ , $\int A^4$ )
COR24	$\triangleq$	Correlation ( $\int A^2$ , $\int A^4$ )

The acceleration profile was divided into four segments.

- a. Boost - Constant G-level because of short time duration; a program input parameter.
- b. Coast - Changing G-level because of aerodynamic drag; calculated automatically by the program nominally using drag characteristics from the 80-G sled test mentioned earlier, but changeable by input parameter.
- c. Brake - Constant G-level because of short available time duration; a program input parameter.
- d. Post brake - Low, changing G-level because of residual velocity and track and aerodynamic drag; calculated by the program.

The input parameters were:

- AB = boost acceleration (G)
- AW = brake acceleration (G)
- VM = maximum sled velocity (fps)
- VW = brake entrance velocity (fps)
- CD = coast drag parameter (1.0 = the nominal 80-G sled drag profile.)

The output of the program was 90 values of acceleration at equal time intervals and the above-identified correlations. Program turnaround was about 10 seconds, mostly involving entering input parameters and displaying results on the screen.

#### 4. RESULTS

The requirement of 120 G maximum acceleration, somewhere during the sled run, and a maximum velocity of 3500 fps, were levied. The simulation provided the following rather explicit results:

a. A boost of 120 G with a 60 G, or smaller, water brake, with a water brake entrance velocity less than 1500 fps, produces correlations which are too high for error separation.

b. The worst correlation problem is between the function,  $\int A^2$ , and the new function expected (and even sought) from high-G sled tests, namely,  $\int A^4$ .

c. Better sled streamlining reduces some of the correlations, but marginally.

d. Velocity at entrance to water brake should be about one-half the maximum sled velocity.

e. The water brake acceleration should have a magnitude about TWICE that of the boost acceleration, and will thus have a duration,  $\tau$ , such that

$$\tau_{\text{WATER BRAKE}} \approx \frac{1}{5} \tau_{\text{BOOST}}$$

Examples of the results are given in Table I. The column headings (AB, AW, ..., COR24) are as defined in previous paragraphs.

The above results vividly reinforce the usefulness of braking as the physical mechanism required for error separation. They also underline two problems already mentioned: a water brake of such magnitude is probably unrealizable because of sled structural limitations; and, if such a brake were realizable, it would probably be too short in duration for proper operation and evaluation of the servos, flight computer manipulations, etc, of the guidance system tested.

With little regard for the mechanism necessary to accomplish the required brake, and if only to address the statements in the previous paragraph, specifications can be established for the required braking device. It must supply:

- a. Very large decelerations
- b. For a long time
- c. Without harming the sled



AD-A076 567

ARMAMENT DEVELOPMENT AND TEST CENTER EGLIN AFB FL  
PROCEEDINGS OF THE BIENNIAL GUIDANCE TEST SYMPOSIUM (9TH) HELD --ETC(U)  
OCT 79

F/G 17/7

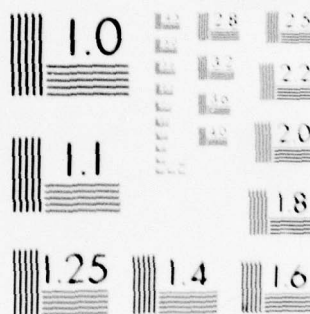
UNCLASSIFIED ADTC-TR-79-11-VOL-1

NL

4 OF 5

AD  
A076567





MICROCOPY RESOLUTION TEST CHART  
NATIONAL BUREAU OF STANDARDS-1963-A

TABLE I

COMPUTER SIMULATION INPUT PARAMETERS AND RESULTING CORRELATIONS

AB	AW	VM	VW	CD	COR12	COR23	COR34	COR13	COR14	COR24
120	-30	3500	1500	1.	.8574	.9986	.9999	.8827	.8775	.9992
120	-30	3500	2000	1.	.7389	.9967	.9998	.7904	.7781	.9982
120	-60	3500	1500	1.	.8151	.9932	.9984	.8729	.8477	.9982
120	-60	3500	2000	1.	.6537	.9836	.9954	.7769	.7154	.9964
120	-120	3500	2000	1.	.5634	.8675	.8693	.8906	.5680	.9999
90	-120	3500	2000	1.	.4373	.4736	.3874	.9825	.3534	.9954
60	-120	3500	1500	1.	.4856	.5275	.3523	.9643	.3209	.9806
60	-120	3500	1750	1.	.4117	.2957	.4969	.7198	.2135	.9758
60	-120	3500	1750	0.8	.4635	.1321	.3760	.7866	.2378	.9681
60	-120	3500	2000	1.	.3706	.4649	.6206	.6320	.1988	.9827
30	-120	3500	2000	1.	.2819	.9380	.9910	.0577	.0750	.9758



d. Within the constraints of existing technology.

#### 5. RETRO ENGINE BRAKING

The acceleration and time requirements imply the probability of negative velocity, i.e., going backwards. Negative velocity is not possible with water brake, but it is certainly possible through the technologically feasible use of retro rockets. The computer simulation program was consequently modified to allow the existence of negative velocity. A new parameter was introduced: VN, maximum (in magnitude) allowed negative velocity.

Constrained again to the requirements of 120 G acceleration at some time and 3500 fps positive velocity, the program readily demonstrated that dramatic reductions in correlation were now possible. In fact, not only was error separation now a possibility, but, again, explicit guidelines for a "best class" of acceleration profile were provided:

a. The brake acceleration magnitude should still exceed the boost acceleration, by a factor of between two and four. (In fact, error separation remained impossible when this criterion was not met.)

b. The brake initiation velocity, VW, should now be low (400 - 800 fps). This has the highly desirable added advantage that considerable test track distance is used (up to 30,000 feet positive, plus 10,000 feet negative); thus even further enhancing error separation by increasing the number of reference data points, N, mentioned earlier.

c. The magnitude of the negative velocity should be one-fourth to three-fourths that of the maximum positive velocity, i.e., significant but hardly critical.

d. The effect of streamlining the sled becomes insignificant, as far as error separation is concerned.

Illustrative examples of these results are given in Table II, where the parameter VN (maximum magnitude of negative velocity) has been added to those used in Table I. The bottom two examples in Table II are the best profile characterizations yet attained: all correlations are easily sufficiently low for separation of the guidance system errors simulated.

It was reasonable to apply the simulation to past, water brake, low-G sled test acceleration profiles in order to corroborate past analysis success trends. Of particular interest was the classic profile used for tests of precision gimballed guidance systems. When the acceleration and velocity requirements were dropped to 7 G and 1350 fps, and  $fA^4$  was assumed not to be observable, the correlations were found to be sufficiently low for error separation; in accordance with the past successful analysis of data from such sled runs using water braking. However, even these runs benefitted when modified, in the simulation, to allow negative velocity: correlations dropped by as much as 25%. It is thus indicated that retro braking to produce negative velocity enhances analysis of sled test data in general.

TABLE II

## COMPUTER SIMULATION INPUT PARAMETERS AND RESULTING CORRELATIONS

AB	AW	VM	VW	VN	CD	COR12	COR23	COR34	COR13	COR14	COR24
120	-30	3500	1750	-1000	1.	.7012	.9960	.9997	.7611	.7469	.9978
120	-60	3500	1750	-1000	1.	.5366	.9716	.9916	.7158	.6242	.9940
120	-120	3500	1750	-2000	1.	.1287	.5660	.5677	.8713	.1325	.9999
60	-90	3500	750	-2000	1.	.4909	.6726	.4623	.8861	.3005	.9665
60	-120	3500	750	-2000	1.	.4349	.3746	.0663	.8879	.0664	.8996
60	-120	3500	750	-2500	1.	.4109	.2800	.1993	.8792	.0071	.8843
30	-120	3500	750	-1000	1.	.6814	.0959	.7180	.5829	.0520	.6202
30	-120	3500	555	-2400	1.	.5730	.0597	.7840	.5644	.0874	.5707

The classic, low-G acceleration profile is shown in Fig 1, along with the associated velocity and distance. Figure 2 shows the radically different retro brake profile proposed for high-G application, along with its velocity and distance functions.

Further modification of the simulation to include other guidance system errors did not change the results: acceleration profiles with negative velocities described by the above guidelines produced results which permitted error separation for the case of high-G sled test.

Finally, reference noise from several available sled test files was superimposed over the error functions expected from various high-G water brake and retro brake acceleration profiles: again, success of error coefficient recovery adhered to the simulation results. For this test, it was recognized that faults were no doubt introduced through use of lower-than-100 G sled test noise. However, an added problem in regression analysis is that linear combinations of error functions can be highly correlated, and this test was considered necessary for confidence in the simulation results.

A question can be raised concerning alternative methods of obtaining negative velocity. Why could negative velocity not be obtained by having two separate sled runs; i.e., either by fitting the sled, after a normal one-direction run, with engines thrusting in the opposite direction; or by towing the sled back to the start point, slewing the guidance system around and then repeating the sled run? (This has in fact been suggested, in Reference 1.)

The strongest reservation to these alternatives is the effect of time on the validity of the test. Because of track safety regulations as well as practical limitations, neither engine refit nor tow-back can be accomplished (or even initiated, for the case of small, power-limited high-G sleds) before guidance power runs out. Hence the guidance system would have to be shut off before the next sled firing. Turn off/turn on variations in guidance system performance are even greater than the variations (already noted) at sled launch and stop. Until such time as guidance systems designed for high-G operation become insensitive to turn off/turn on effects, such a dual sled test would amount to tests of different systems, thus negating the beneficial effect of negative velocity on error separation.

Another reservation is associated with positioning. If a guidance system were to be towed back and slewed around, there would be a new set of alignment uncertainties which would have to be separated from the true system errors. Such additional separation may not be possible, if any other system errors changed value between turn off and turn on. This problem would also exist for the case of refitting with reverse thrusters, i.e., not slewing the guidance system: the sled could not be allowed to move or settle in any way during the time it was (necessarily) turned off.

Finally, the correlations associated with two identical-but-opposite (as viewed by the guidance system) sled runs would be too high for separation; unless, as indicated by the simulation, the second run boosted at a level two to four times that of the first run. It therefore seems that providing the reverse thrust is most validly accomplished through use of retro engines in the manner proposed in this paper.



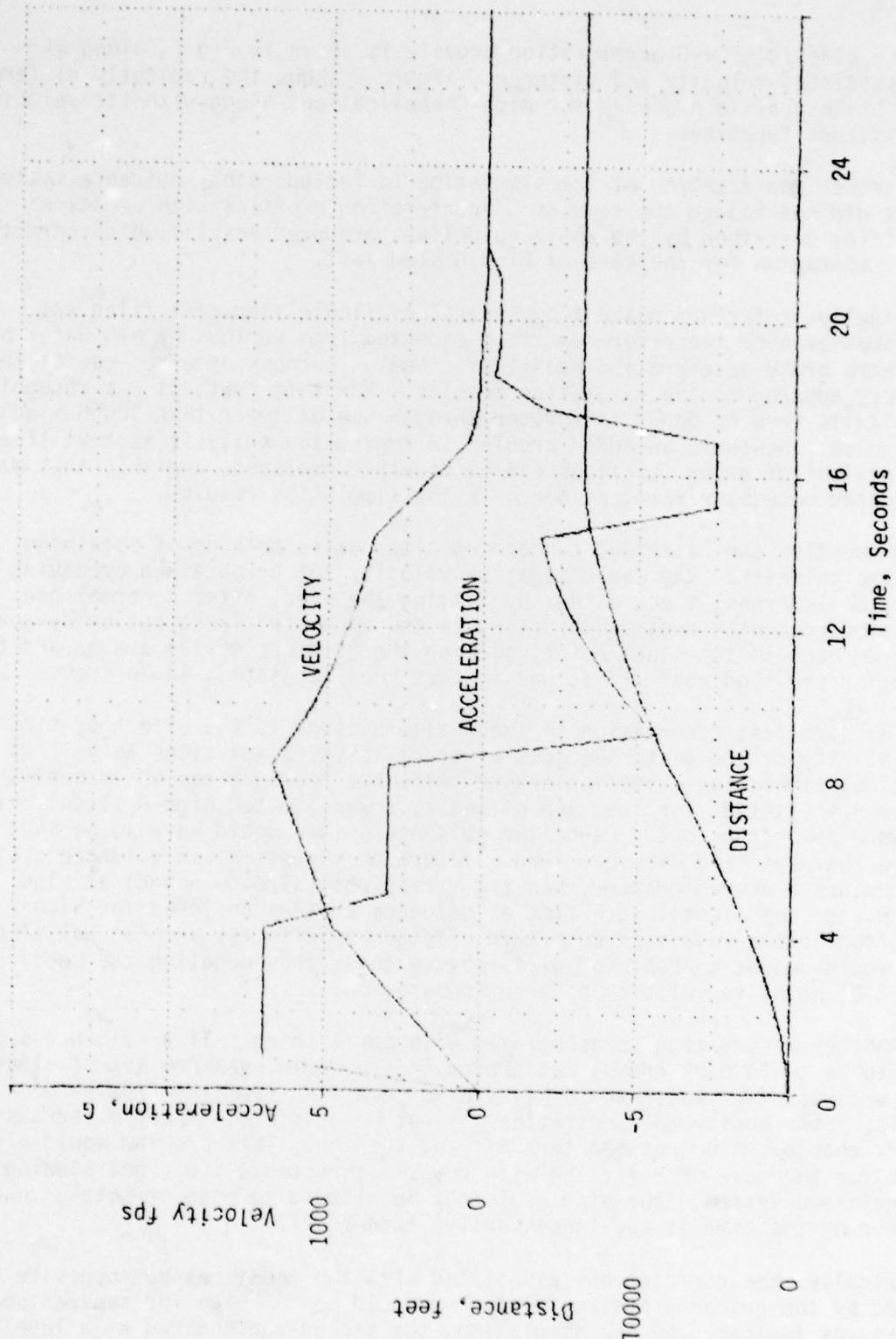


FIGURE 1. CLASSIC WATER BRAKE PROFILE

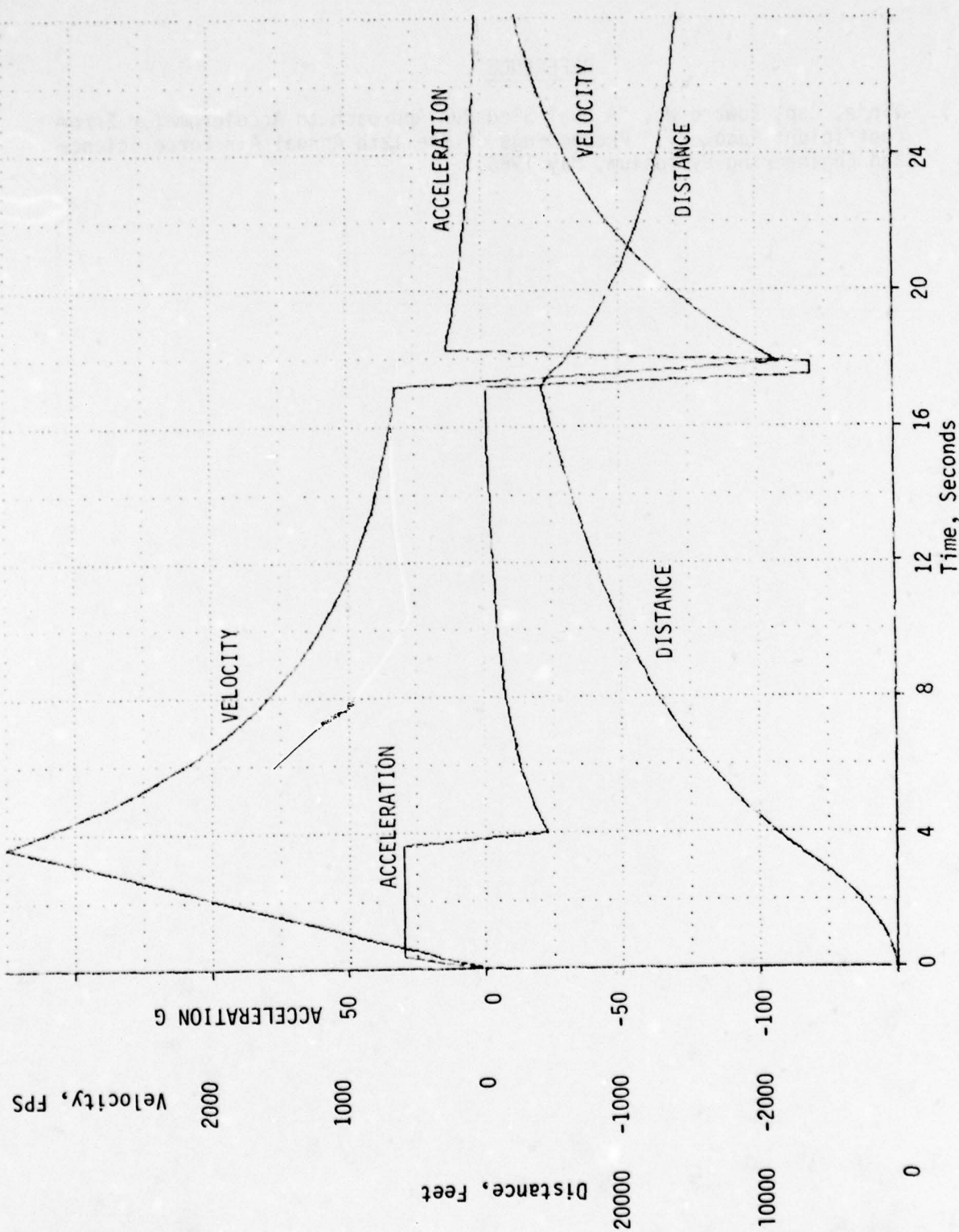


FIGURE 2. PROPOSED BRAKE PROFILE

#### REFERENCE

1. Vinje, Capt Edward W., "A Dual Sled Run Approach to Accelerometer Error Coefficient Recovery," Proceedings of the 12th Annual Air Force Science and Engineering Symposium, May 1966.



TITLE:        PROGRESS AND PLANS FOR THE  
              DEVELOPMENT OF A PRECISION  
              GUIDANCE TEST FACILITY

AUTHORS:    MR W. J. WHITESELL  
              MAJOR T. R. HOOTEN, USAF

CENTRAL INERTIAL GUIDANCE TEST FACILITY  
6585TH TEST GROUP (AFSC)  
HOLLOMAN AIR FORCE BASE, NEW MEXICO 88330

## ABSTRACT

Guidance Laboratory test data, historically, has been corrupted by unwanted random noise due to seismic, cultural, facility and other sources. In the past, these effects (relative to test article performance) could be tolerated. However, from 1980 through the year 2000, it is anticipated that test item performance and sensitivity will be obscured by these effects. This paper reviews the conceptual design work accomplished on a facility relatively immune to such noise sources and covers future plans for construction of the facility.

For example, if one assumes that test facilities should be an order of magnitude better than the test item, then an inertial instrument with sensitivities of  $10^{-8}g$  over a frequency band of DC to 100 Hz should have a facility quiescent to  $10^{-9}g$  over that band. This is the facility goal since instruments which meet the above criteria and are test candidates have been identified. The goal is particularly ambitious since it approaches the theoretical minimum quietness attainable on earth.

A feasibility study concluded that such a facility was possible, given proper site selection and a combination of special facility construction techniques and active isolation. Of course, site selection was critical. Accordingly, site selection criteria have been developed for the Continental United States and promising sites identified.

Proposed plans include the design and fabrication of a prototype active isolation system and, if approved, construction of the facility will begin in FY 1984.

## TABLE OF CONTENTS

	<u>Page Number</u>
I. INTRODUCTION	1
II. BACKGROUND	1
III. APPROACH	2
IV. SUMMARY	4
FIGURES	
1. Inertial Grade Gyroscope Accuracy Trends	
2. Inertial Grade Accelerometer Accuracy Trends	
3. Precision Guidance Test Facility (PGTF) - Milestones	
4. Precision Guidance Test Facility (Artist's Concept)	
5. Input Excitations	
6. Input and Response vs Facility Goals	
7. Transfer Functions	
8. Regional Criteria Decision Flow	
9. Subregional Criteria Decision Flow	
10. Site Criteria Decision Flow	
11. Desk Top Survey	
12. Proposed Seismically Stable Platform	



## I. INTRODUCTION

The Advanced Inertial Test Laboratory (AITL) at the Central Inertial Guidance Test Facility (CIGTF) and the Frank J. Seiler Research Laboratory (FJSRL) at the Air Force Academy are the two most seismically controlled locations known which can test future inertial grade instruments without long-term filtering and averaging the data. Translational motion at both facilities is assumed to be not more than  $10^{-7}g$  since instruments approaching these levels have been tested successfully at both locations. However, estimated future instrument accuracy trends (Figures 1 and 2) argue for a more stable test environment. Considering estimated long-term instrument accuracy trends, and user need dates, the CIGTF has forecast a Precision Guidance Test Facility (PGTF) in the Military Construction Program (MCP) for FY84. Figure 3 shows the scheduled events leading to that capability.

## II. BACKGROUND

Some of the milestones have been completed. In 1975, the facility feasibility study was accomplished by Burns and Roe of Los Angeles. This study produced engineering and design data for the "brick and mortar" portion of the facility as well as criteria for a vibration attenuation system. Figure 4 is an artist's concept of the Burns and Roe design. Burns and Roe also concluded that a combination of active/passive isolation techniques plus judicious choice of site location could feasibly provide a test station relatively immune to translational motions greater than  $10^{-9}g$  in the DC to 100 Hz frequency band. Figure 5 is extracted from the Burns and Roe study and depicts the range of input excitations versus peak accelerations. Also shown is the facility goal. Tilts, in the low frequency regime (.1 to 0 Hz), are assumed to be controlled to .02 arc seconds by the active control system. The remaining input accelerations must be controlled through facility design/construction and proper site selection. Using the range of input excitations in Figure 5 and the Burns and Roe conceptual design for the facility and active/passive isolation system, one obtains the dynamic inputs at the base of the pier and response at the test station shown in Figure 6. Figure 7 graphically depicts the transfer functions for the various subsystems. The question could be posed here of why we cannot measure these inputs and extract them from the data? This would be a less expensive and easier way to test future instruments. However, to the best of our knowledge, there is no current or forecasted technique to do this with the degree of certainty required to characterize future inertial instruments. Accordingly, our approach is to isolate the test item to the maximum extent through facility design/construction and site selection.

### III. APPROACH

The feasibility study by Burns and Roe, in 1975, was the first step in an attempt to determine if isolation of the test article from all translational inputs greater than  $10^{-9}$  was practical.

The second step was to define the criteria by which a site could be selected. This was accomplished in 1978-79 with a study by Civil Nuclear Systems Corporation of Albuquerque, New Mexico. The developed criteria provides a methodology for determining promising regions within the CONUS and converging on the best seismic sites which will be tested to verify the methodology prior to site selection. Such things as surface winds, temperatures, seismic motions, agricultural activity, and storm cycles are criteria. Also, the proximity to lakes, rivers, highways, railroads, aircraft flight paths, and mineral exploration areas are serious areas of concern. The main conclusion of the study was that potential sites meeting all the criteria do exist. However, occupation of the potential sites with adequate instrumentation should be conducted for a one-year period. This one-year, on-site measurement should prevent any surprises (i.e., if a site were only measured for a small portion of a year and some one-time normal occurrence were missed).

The site selection rationale and methodology allows area screening of the Continental United States in three phases. This screening consisted of: (1) a regional area elimination and preference ranking (Figure 8), (2) a further elimination and preference ranking of area on a finer sub-regional scale (Figure 9), and (3) identification of a number of local sites where earth noise spectral amplitudes were expected to be at a minimum (Figure 10). Advancing to that point involves no detailed field work. The only field work recommended is to include noise source and tectonic mapping. Figure 11 is an example of a preliminary desk top survey using the criteria. It provides a "feel" for all the variables that must be considered. The sites shown are some of the more promising based on the criteria. They include Oregon (OR), Colorado (CO), Arizona (AZ), New Mexico (NM), and Utah (UT).

The fourth and final phase of the site selection is Site Evaluation Techniques. This phase of the investigation consists of field instrumentation and is broken into two stages. The first stage consists of surface instrumentation placement and monitoring at all previously selected sites. The quietest of these sites (recommended to be less than five) would then be advanced to Stage Two. The Stage Two investigations are designed to thoroughly investigate each of these sites to provide high-confidence earth noise data at various depths down to

the maximum possible facility depth and to also provide required long term (one-year) data. Using this approach, the long term and depth data would be acquired at only the best of sites and thus greatly reduce the cost of PGTF site selection. Having the data on several sites will allow the various non-technical factors, ever-present in the final site selection decisions, to be weighed in balance with the technical (earth noise) factors.

The Burns and Roe study strongly recommended that an actively controlled pad be investigated prior to the building of a PGTF.

Plans were made and a contract negotiated, in June of 1979. The contract was for the design and construction of an actively controlled test pad in Room 13 of the CIL at Holloman. The design goals for this effort are to be able to control tilts to 0.02 arc seconds over a frequency band of DC-50 Hz. Suspension and isolation of the design should allow for a seismic quietness at the control sensor location of  $10^{-8}g$  in the stated frequency band. Figure 12 shows the proposed installation.

A transfer function will be taken from the earth, directly below the control sensor location and related to the control sensor location itself. In-house instrumentation will be used.

This equipment's (Portable Seismic Monitor) outputs have been calibrated at the Air Force Metrology Laboratory in Newark, Ohio. Simultaneous measurements at two different locations and directions can be made. Data will be fed into a Fast Fourier Analyzer and the horizontal and vertical transfer functions derived.

Using the aforementioned functions, with data taken from potential PGTF sites, it is possible to dynamically simulate the PGTF testing capability. This coordinated, planned approach will allow for in-depth knowledge of how the potential site will react and allow for a solid engineering decision on the best technical site. We are not so naive as to believe that this will be the site; however, technically, we will have arrived at the correct selection.

The Department of Energy has shown interest in providing the site electrical power which does not induce 60 Hz seismic motion to the site. They have studied several options and are pursuing underground power cables and vibrationless transformer development.

The ANSER Corporation is conducting a survey of potential users of a PGTF. This effort started in January of 1978 and continued for nine months. The final report on this effort is not available.



#### IV. SUMMARY

The schedule, as shown previously, is designed to obtain engineering feasibility information at the least cost. If data does not support the next step of the plan, then the project will be terminated.

We have studies completed which state that it is technically feasible to build. Criteria has been developed to logically pick the best site for the facility. Engineering data will be available in 1980 to determine the transfer function of a seismically stable, actively controlled test pad.

We have been extremely pleased with the cooperation of inertial industry representatives, the scientific community, and our Air Force Systems Command counterparts. Excellent support has been received from the Frank J. Seiler Research Laboratory and the Air Force Metrology Laboratory.

# INERTIAL GRADE GYROSCOPE ACCURACY TRENDS

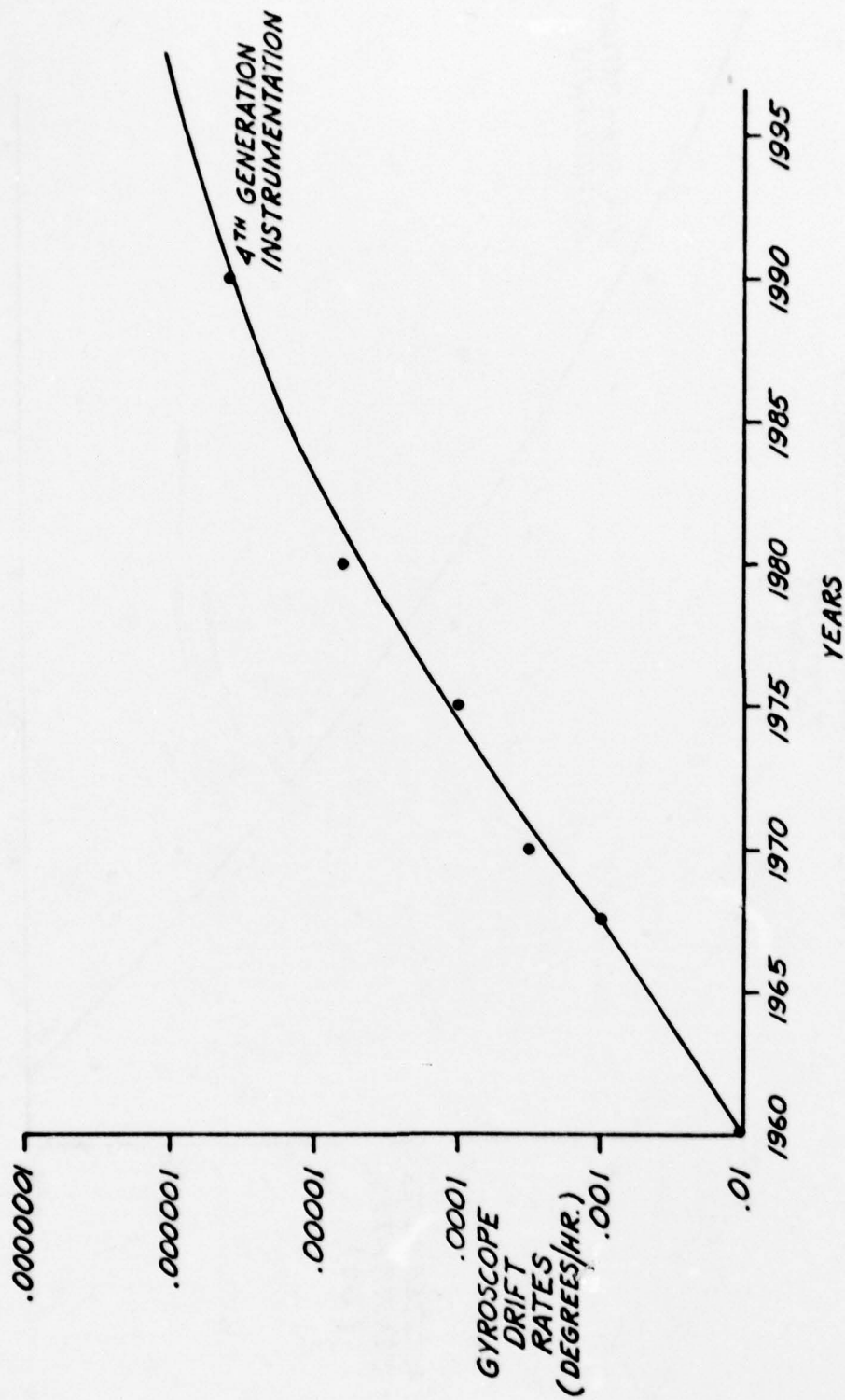


FIGURE 1 - Inertial Grade Gyroscope Accuracy Trends

# INERTIAL GRADE ACCELEROMETER ACCURACY TRENDS

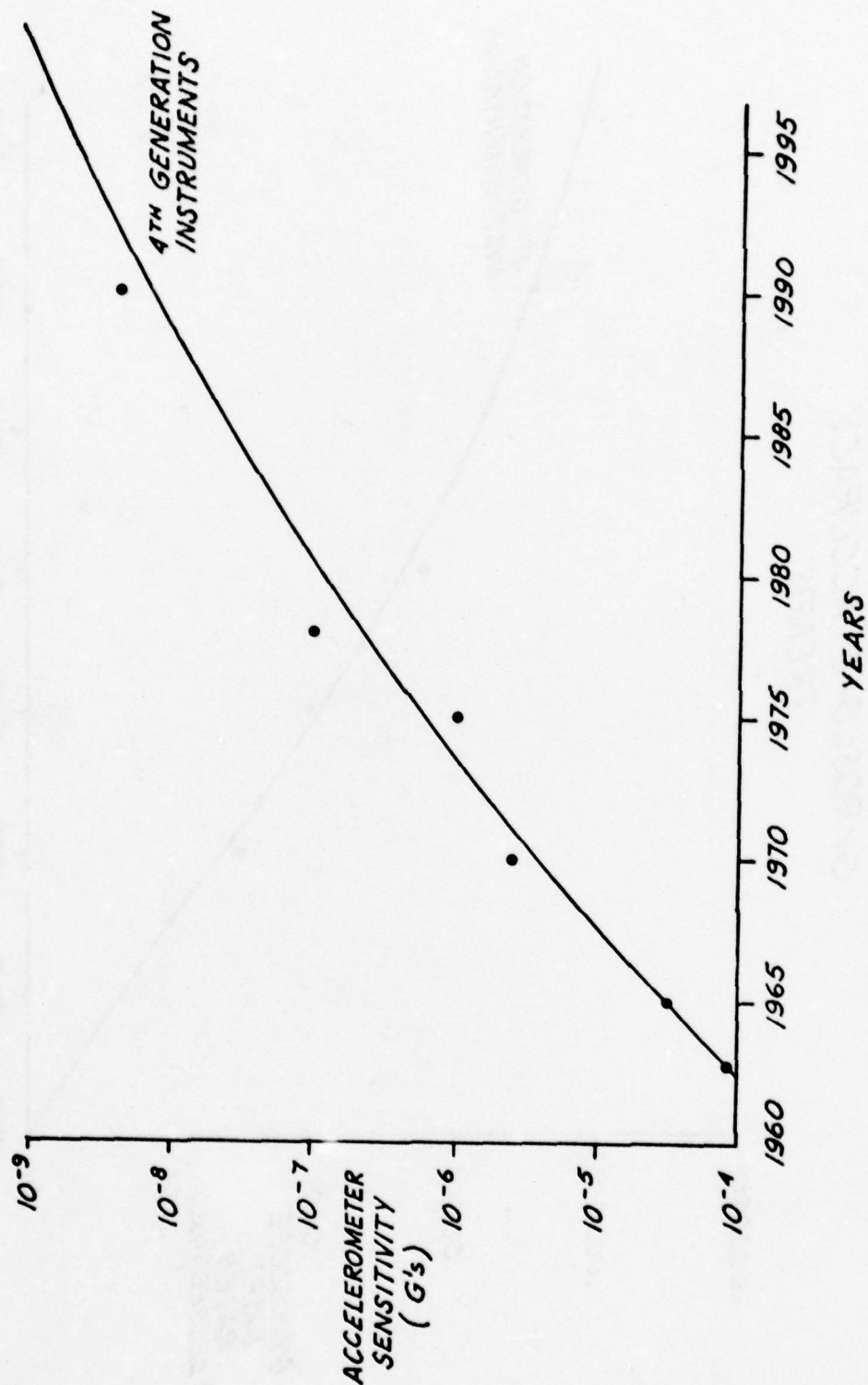


FIGURE 2 Inertial Grade Accelerometer Accuracy Trends



# PRECISION GUIDANCE TEST FACILITY MILESTONES

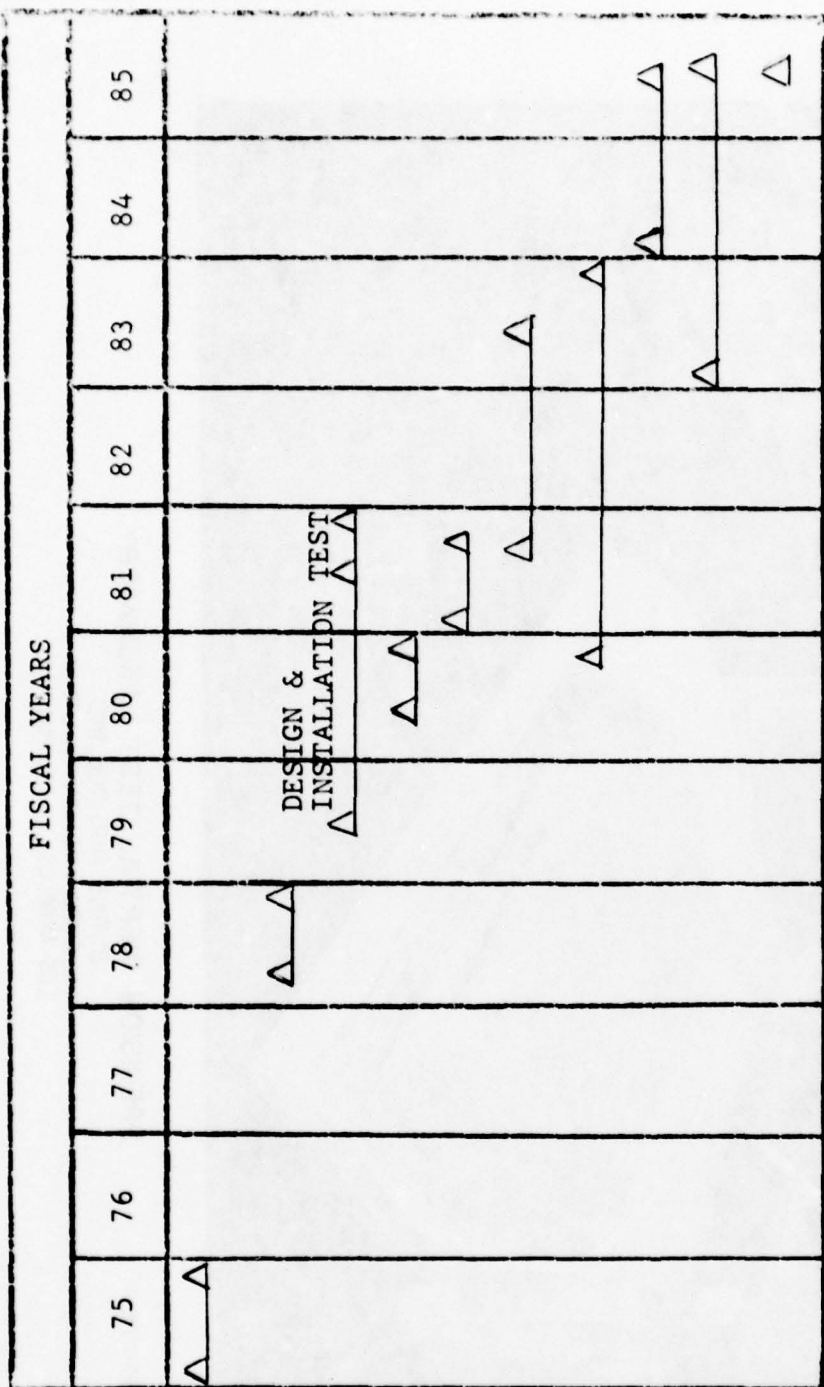


FIGURE 3 - PGTF MILESTONES

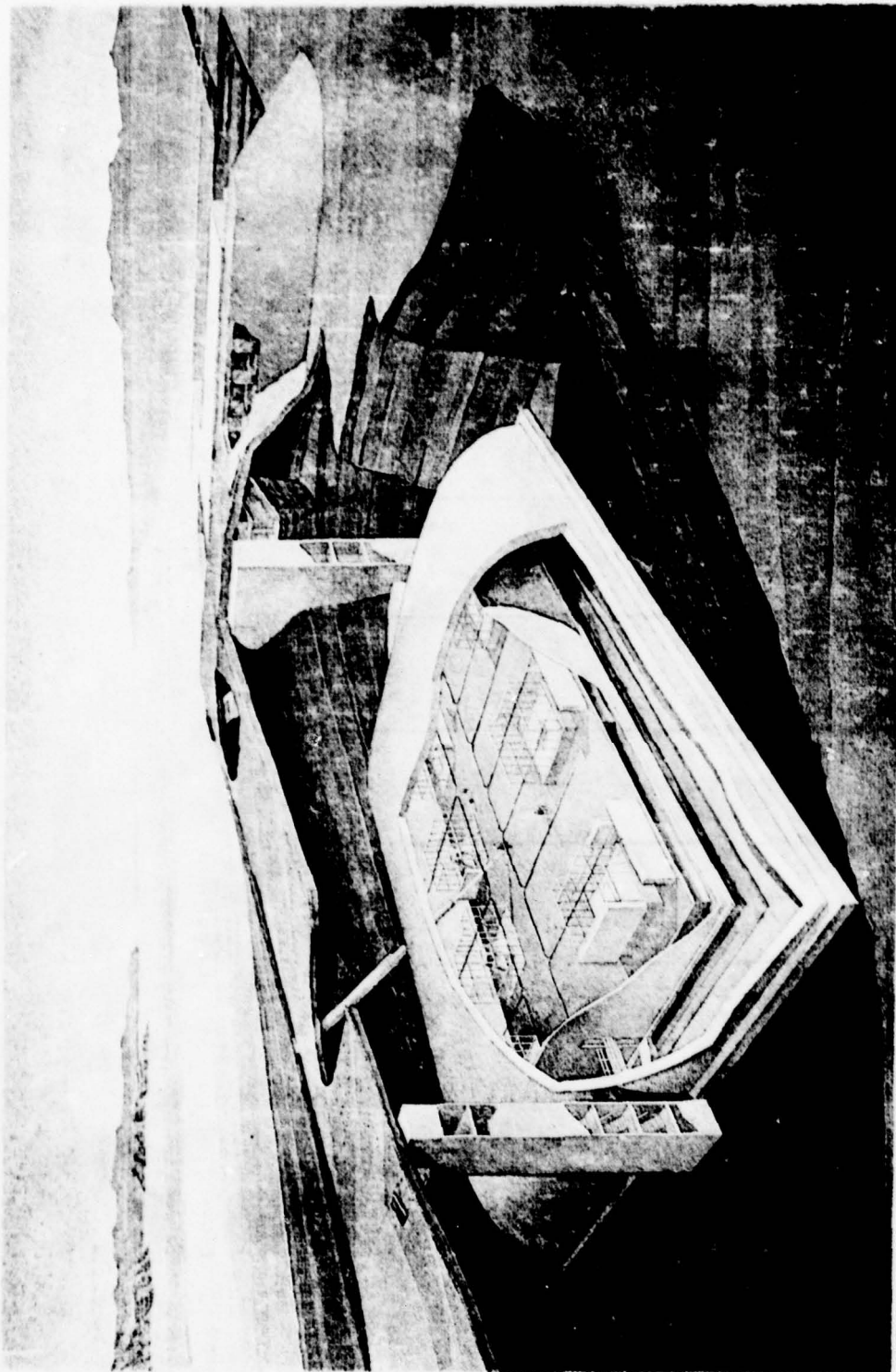


FIGURE 4 - PRECISION INERTIAL TEST LABORATORY  
BURNS AND ROE, INC.  
ENGINEERS AND CONSTRUCTORS  
LOS ANGELES, CALIFORNIA

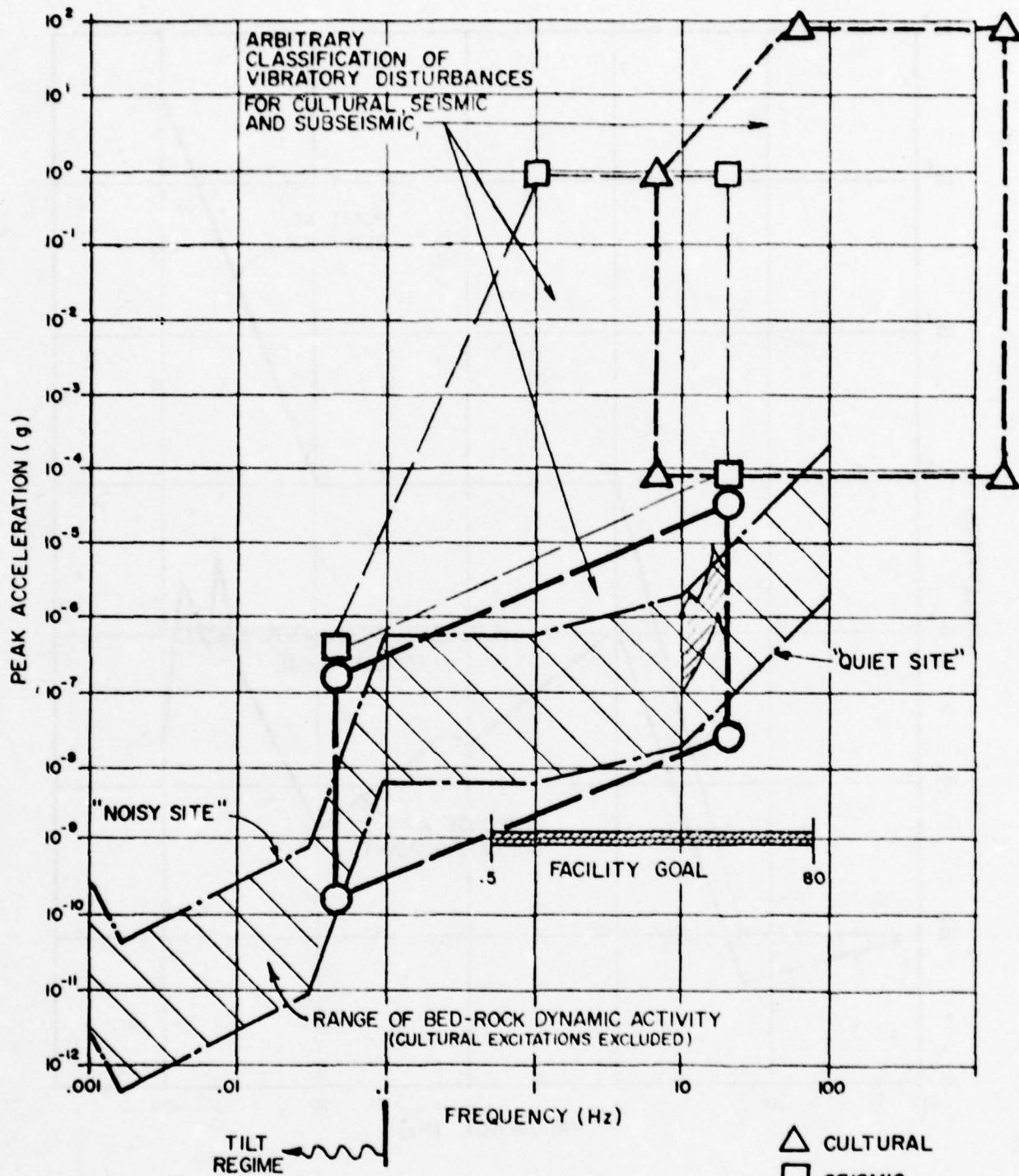


FIGURE 5 - INPUT EXCITATIONS



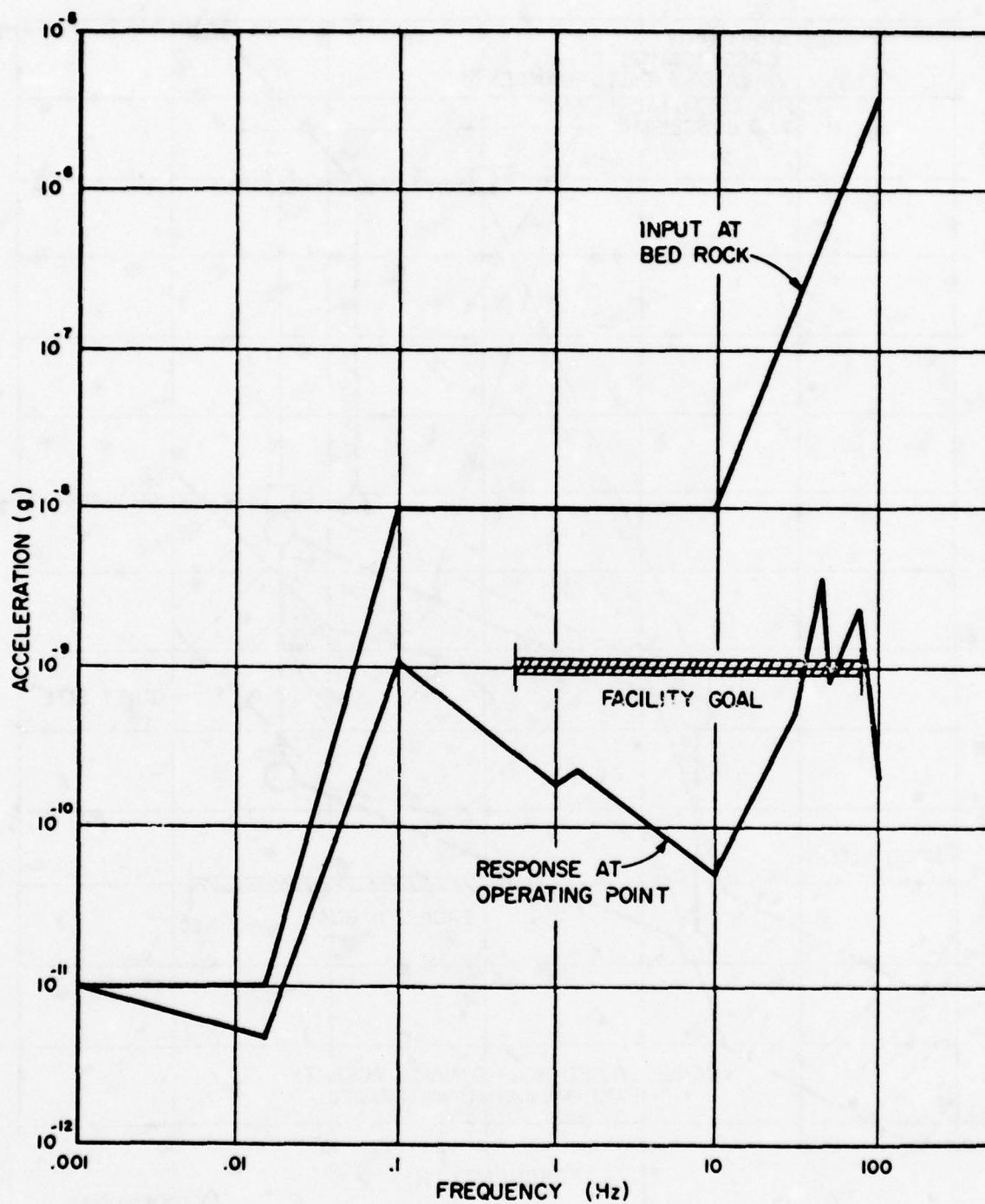


FIGURE 6 - INPUT AND RESPONSE vs FACILITY GOALS

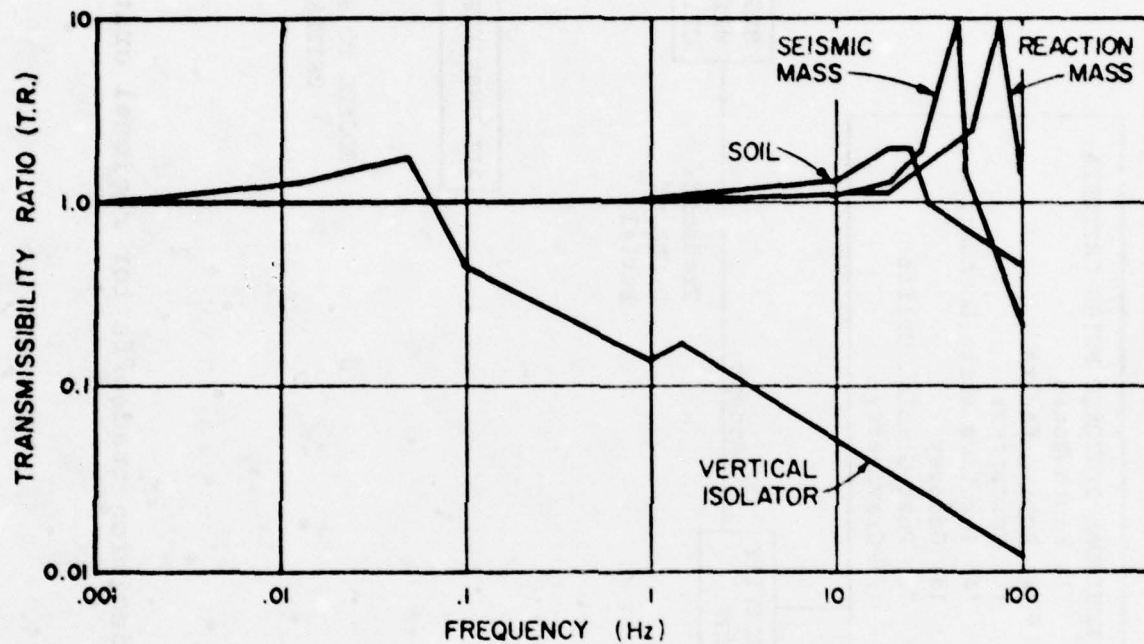


FIGURE 7 - TRANSFER FUNCTIONS

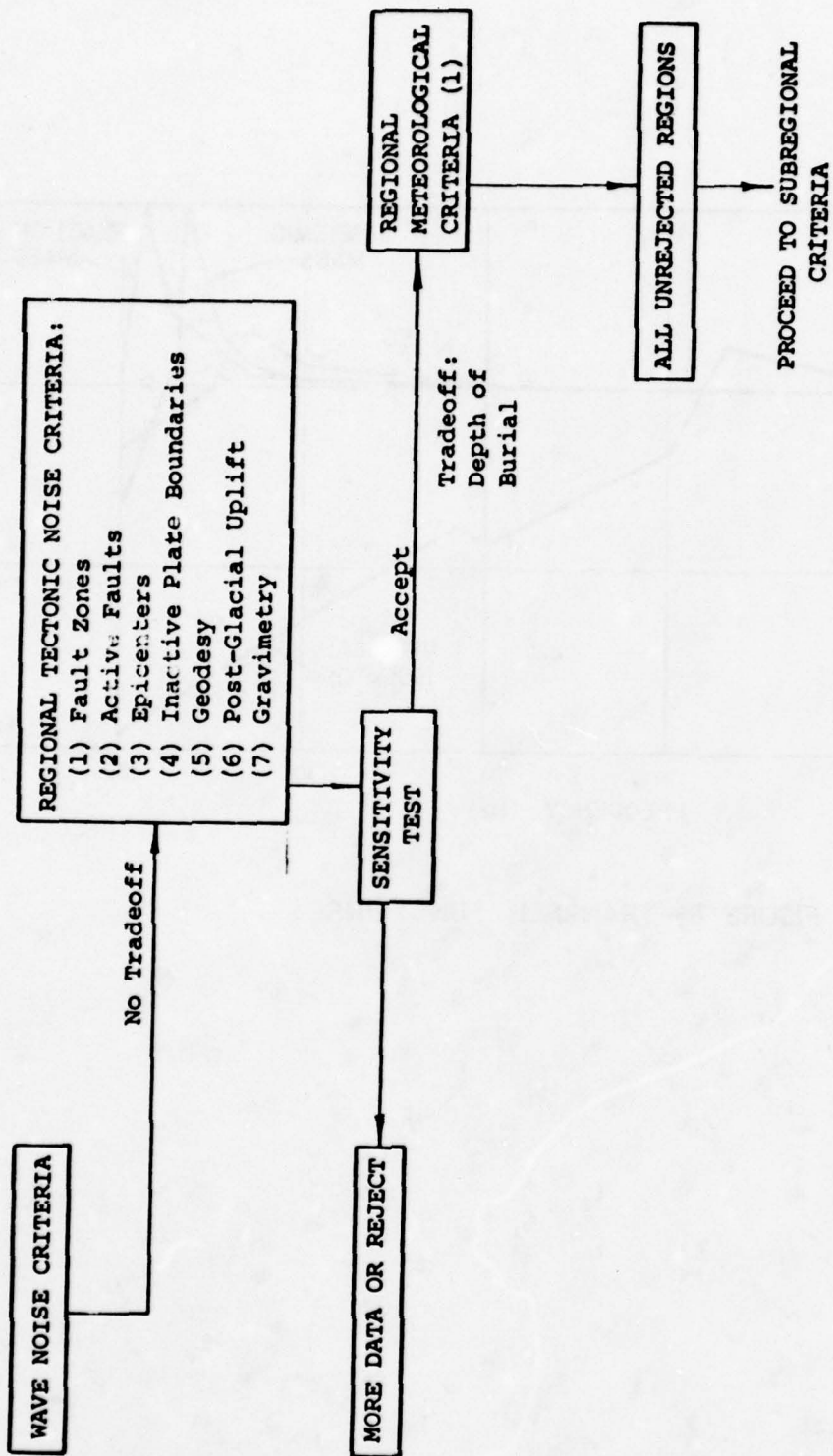


FIGURE 8 -Flow chart and decision tradeoffs for regional criteria.



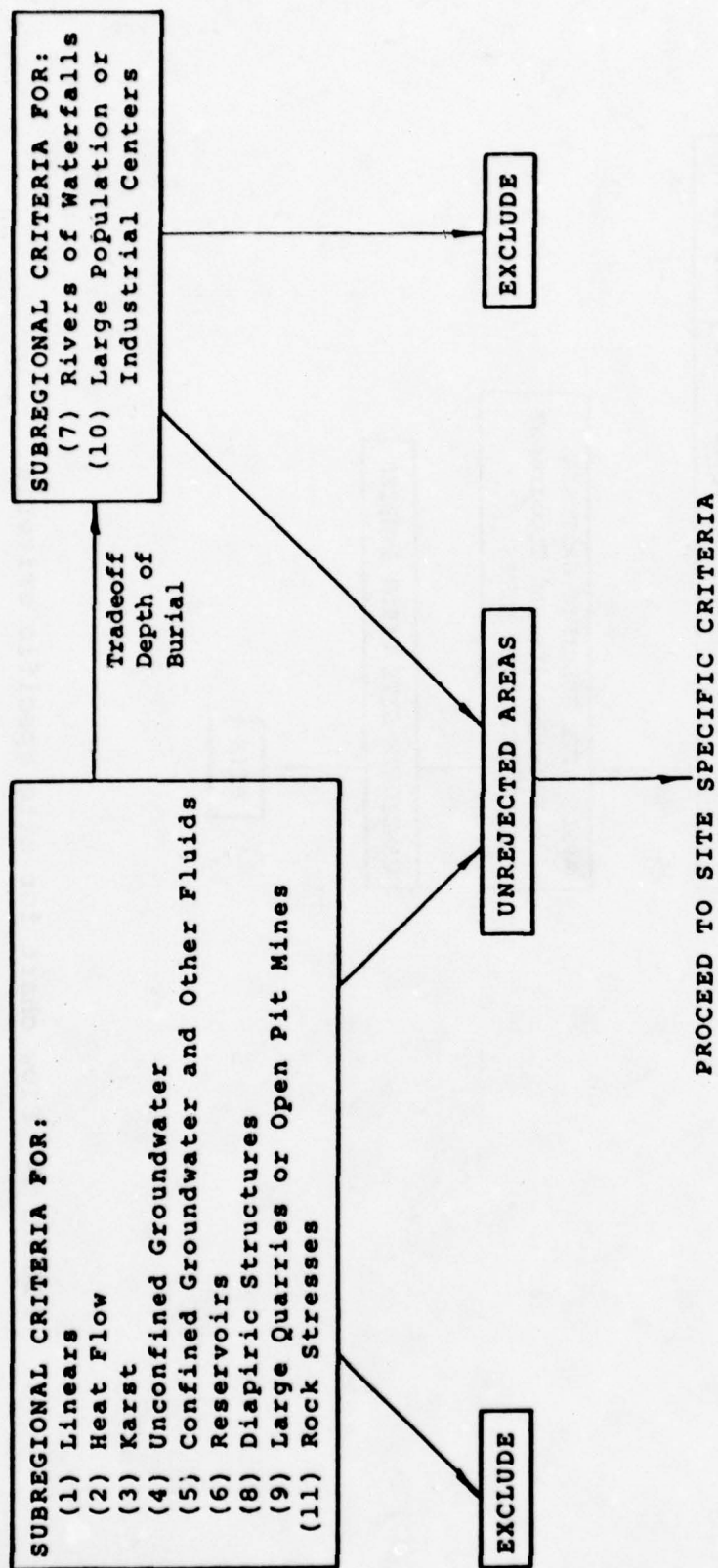


FIGURE 9 - Flow chart and decision tradeoffs for subregional criteria.

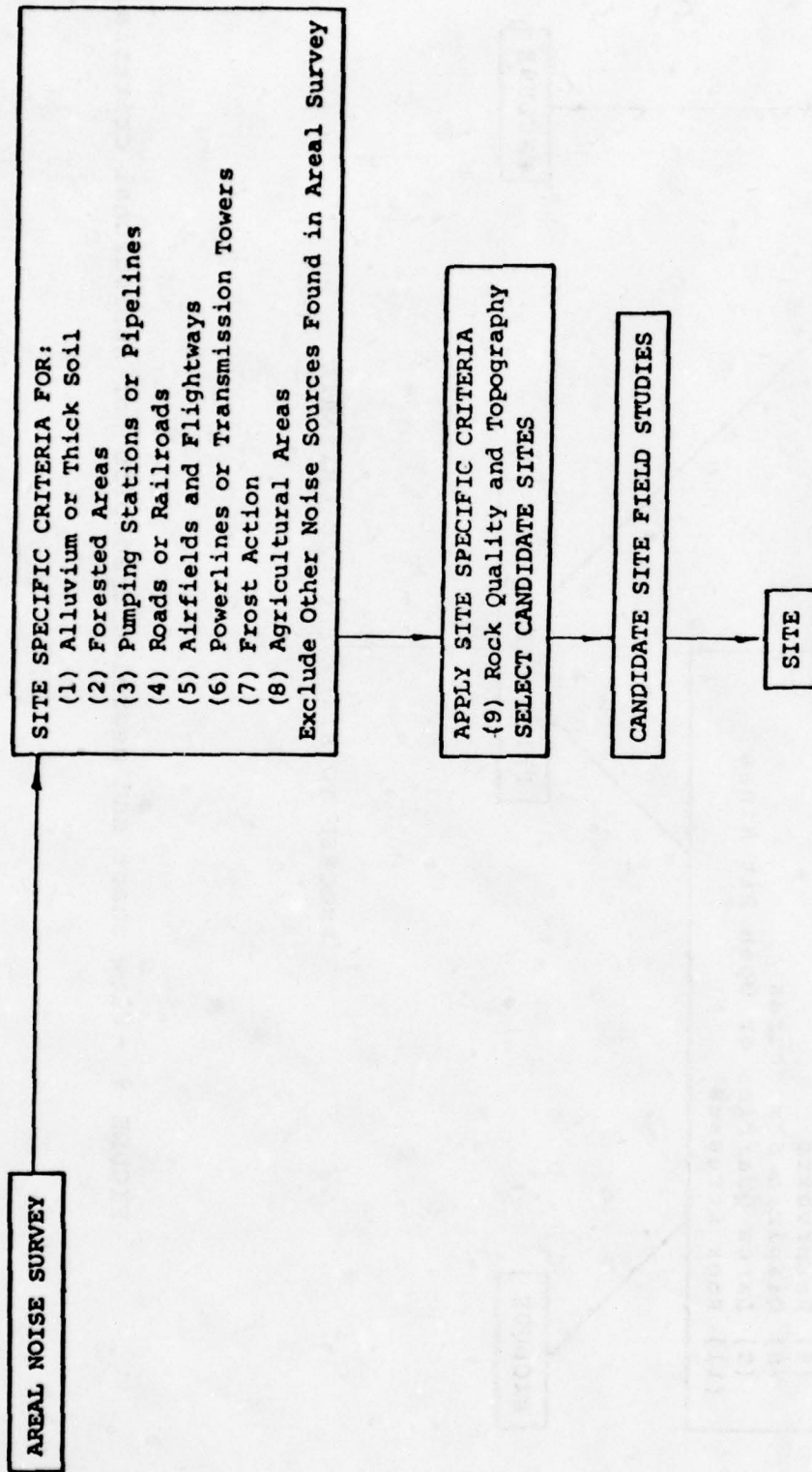


FIGURE 10 - Flow chart for site specific criteria.

SITE	AVERAGE ANNUAL WIND VELOCITY (MPH)	DAYS WITH ONE OR MORE THUNDERSTORMS	FREQUENCY OF TORNADOES	AVERAGE ANNUAL DAYS THUNDERSTORMS	SUMMERTIME RATE OF ALTERNATION - HIGHS AND LOWS	WINTERTIME RATE OF ALTERNATION - HIGHS AND LOWS	FREQUENCY OF LOWS DURING 20 OCTOBERS	FREQUENCY OF LOWS WITH FRONTS DURING 20 OCTOBERS	STRAIN RELEASE EQUIVALENT NUMBER OF MAGNITUDE FOUR EARTHQUAKES	MAXIMUM MODIFIED MERCALLI INTENSITIES	AIRCRAFT NOISE PROBABILITY	DISTANCE FROM OCEAN	PROXIMITY TO SEISMICITY
1-OR	8	10	1	10	50	50	4	16	<.25	<IV	NONE	ACC.	OK
2-OR	8	10	1	10	50	50	4	16	<.25	<IV	NONE	ACC.	OK
3-OR	8	10	1	10	50	50	4	16	<.25	<IV	NONE	ACC.	OK
4-OR	8	10	1	10	50	50	4	16	<.25	<IV	NONE	ACC.	NEAR
5-OR	8	5	1	10	50	50	4	16	<.25	<IV	SLIGHT	ACC.	NEAR
6-OR	8	5	1	10	50	50	4	16	<.25	<IV	SLIGHT	ACC.	OK
7-CO	8	30	1	40	50	75	23	16	<.25	<IV	NONE	ACC.	NEAR
8-CO	8	30	1	40	50	65	23	16	<.25	<IV	NONE	ACC.	NEAR
9-CO	10	40	3	60	75	75	23	16	<.25	<IV	SLIGHT	ACC.	OK
10-CO	10	30	3	60	75	75	23	16	<.25	<IV	SLIGHT	ACC.	OK
11-CO	10	30	3	40	75	75	23	16	<.25	<IV	SLIGHT	ACC.	OK
12-AZ	8	20	1	20	25	50	23	16	<.25	<IV	NONE	SUSPECT	NEAR
13-AZ	10	20	1	20	25	50	23	16	<.25	<IV	SLIGHT	SUSPECT	NEAR
14-AZ	10	20	1	20	25	50	23	16	<.25	<IV	SLIGHT	SUSPECT	NEAR
15-AZ	10	20	1	20	25	50	4	16	<.25	<IV	SLIGHT	SUSPECT	OK
16-AZ	10	20	1	20	25	50	4	16	<.25	<IV	SLIGHT	SUSPECT	OK
17-NM	10	30	2	40	25	75	4	16	<.25	<IV	NONE	ACC.	OK
18-UT	8	20	1	40	50	50	23	16	<.25	<IV	NONE	ACC.	OK
19-UT	8	20	1	40	50	50	23	16	<.25	<IV	NONE	ACC.	OK

FIGURE 11 - Preliminary Desk Top Survey



NEAR RESERVATION	TYPE OF LAND	AVERAGE ANNUAL PRECIPITATION	FLOOD PROBABILITY	PROXIMITY TO MAJOR PLATE TECTONIC ELEMENTS	VEHICULAR TRAFFIC	RAILROADS	POWER LINES	MINING OPERATIONS	OIL OR GAS WELLS
OK	PUBLIC	20 in	NO	OK	SECONDARY	NONE	NONE	NONE	NONE
OK	PUBLIC	20 in	NO	OK	SECONDARY	NONE	NONE	NONE	NONE
OK	PUBLIC	20 in	SLIGHT	OK	SECONDARY	NONE	NONE	NONE	NONE
OK	PUBLIC	20 in	NO	OK	SECONDARY	NONE	NONE	NONE	NONE
OK	PUBLIC	20 in	NO	OK	SECONDARY	NONE	NONE	NONE	NONE
OK	PUBLIC	20 in	NO	OK	SECONDARY	NONE	NONE	NONE	NONE
NEAR	NATIONAL FOREST	25 in	NO DATA	NEAR	SECONDARY	NONE	NONE	YES	NONE
NEAR	NATIONAL FOREST	25 in	NO DATA	NEAR	SECONDARY	NONE	NONE	YES	NONE
OK	PRIVATE	16 in	NO DATA	NEAR	PRIMARY	NONE	NONE	NONE	SPL
OK	PRIVATE	16 in	NO DATA	NEAR	PRIMARY	NONE	NONE	NONE	SPL
OK	PRIVATE	16 in	NO DATA	NEAR	PRIMARY	NONE	NONE	NONE	SPL
NEAR	INDIAN RESERVATION	15 in	SLIGHT	NEAR	SECONDARY	NONE	NONE	YES	NONE
NEAR	NATIONAL FOREST	15 in	SLIGHT	NEAR	SECONDARY	NONE	NONE	YES	NONE
OK	NATIONAL FOREST	15 in	SLIGHT	NEAR	SECONDARY	NONE	NONE	YES	NONE
OK	PUBLIC	15 in	NO	NEAR	NONE	NONE	NONE	NONE	NONE
OK	PUBLIC	15 in	NO	NEAR	NONE	NONE	NONE	NONE	NONE
OK	PUBLIC	12 in	NO	NEAR	SECONDARY	NONE	NONE	NONE	NONE
OK	PUBLIC	20 in	SLIGHT	OK	SECONDARY	NONE	YES	YES	YES
OK	PUBLIC	20 in	NO	OK	SECONDARY	NONE	YES	YES	YES

FIGURE 11 (Continued)  
Preliminary Desk Top Survey

MILITARY CONSTRUCTION PROJECT DATA (Continued)		3. DEPARTMENT	4. INSTALLATION
5. CAL YEAR	6. PROJECT TITLE		

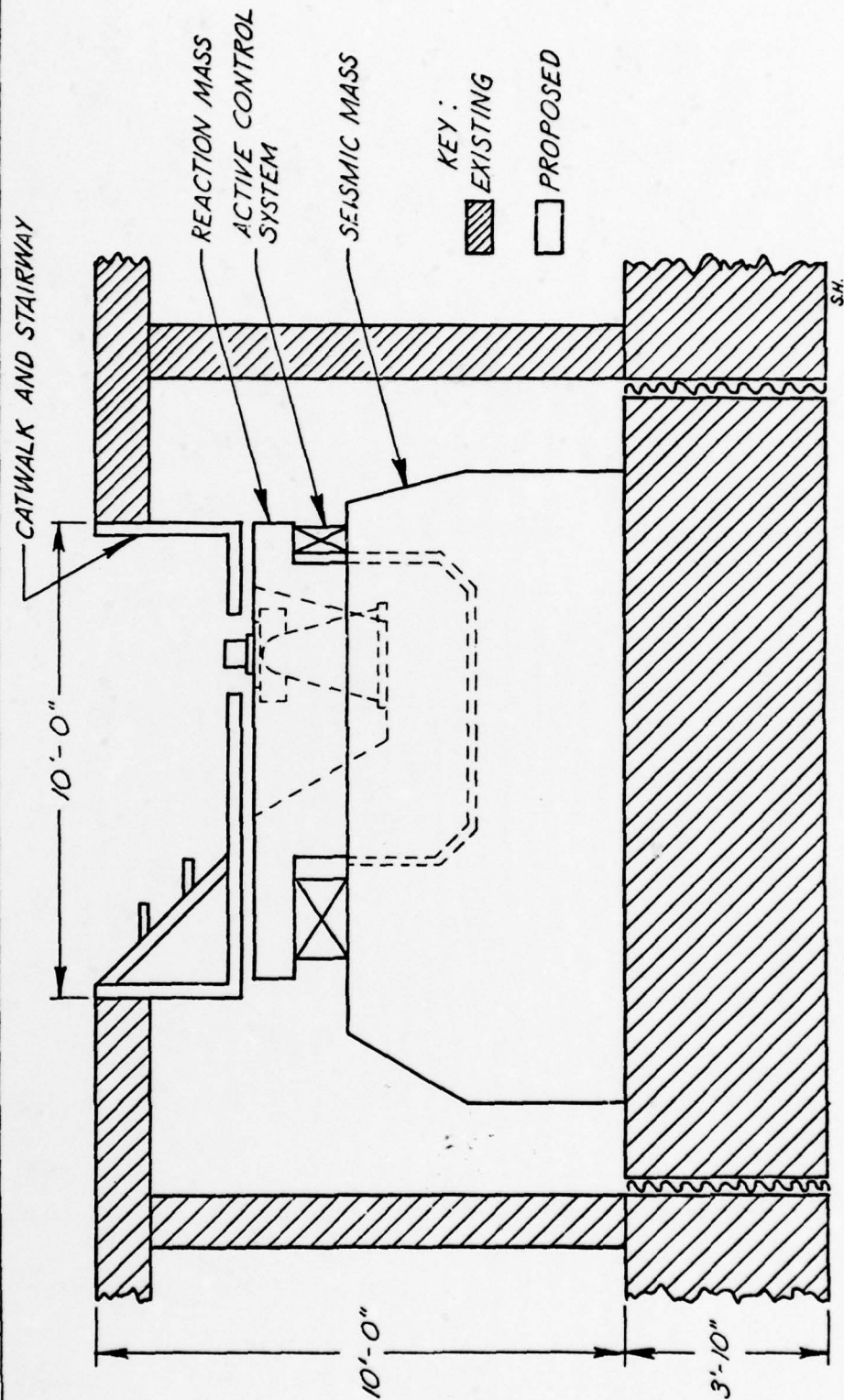


FIGURE 12 - Proposed Seismically Stable Platform

TITLE: STRAPDOWN SYSTEM  
PERFORMANCE IMPROVEMENT  
BY ROTATING THE INERTIAL  
INSTRUMENTS

AUTHOR: J. C. PINSON

ROCKWELL INTERNATIONAL  
Autonetics Strategic Systems Division  
Electronic Systems Group  
3370 Miraloma Avenue  
P. O. Box 4192  
Anaheim, California 92803



# ABSTRACT

Rockwell's low-cost, strapdown inertial navigation system is the N73. It meets the need for the standard medium-accuracy (0.8 nautical-mile-per-hour radial position error CEP rate) navigation system for future aircraft/missiles. It employs instrument rotation to reduce error propagations. The gyro errors caused by some important classes of electronic imperfections are analyzed, as is the improvement in these errors attained on account of instrument rotation. Data are presented substantiating the benefits of rotation.

## 1. INTRODUCTION

The objective of inertial navigator design is to meet a performance specification at the lowest possible cost. A part of the performance specification is navigation accuracy - CEP rate, velocity error, and attitude error. These navigation errors are caused mostly by gyro and accelerometer errors. The inertial navigator designer must make use of accurate instruments and must create a system operating environment that minimizes the propagation of the instrument errors into navigation errors.

All inertial navigation systems have implemented some sort of instrument error model in the computer that is used to compensate most of the instrument errors. The coefficients in this error model are determined by instrument or system level calibration. The instrument errors of concern, then, are those that remain after compensation. These residual errors exist for the following reasons:

- (a) Errors that have not been properly mechanized in the model. These can be systematic effects that have not been modeled correctly, or short-term noise effects.
- (b) Error model coefficients that have not been determined accurately during calibration. The error sources listed in (a) above are the chief cause of this.
- (c) The instrument error coefficient values can have shifted in the time since calibration.

Whatever the instrument errors may be, the choice of system mechanization influences their propagation into navigation errors. Some of the possible system mechanizations are:

- (a) Stable Platform - The angular rates imposed on the instruments are small. The computation load is light. The advantage is attained that instrument errors and gyrocompassing errors remain well correlated during the flight (ref 1). Heading sensitivity is sometimes a problem because the housing moves relative to the platform when the aircraft changes heading. This mechanization is the most complex mechanically.
- (b) Strapdown - Here mechanical simplicity is attained at the expense of increased computational load. The instruments must operate at high angular rates. Heading sensitivity is a problem because of the loss of correlation between instrument errors and gyrocompass alignment errors at headings different than the alignment heading (ref 1).
- (c) Strapdown with Instrument Rotation - This system is obtained by taking the strapdown system of (b) above and adding something to it. Added is a motor driven axis of rotation about the housing yaw direction, permitting the gyros and accelerometers to rotate relative to the housing. This instrument package is rotated through

360°, first in one direction and then the other (to avoid using slip rings), at a rate of about 1 rpm. The rotation pattern is carried out continuously, both during alignment and in navigation. Because the heading of this strapdown system is forced to vary continuously through a full 360° during all phases of system operation, the heading sensitivities present in the strapdown system of (b) above are averaged out. Because the rotation pattern relative to the system housing never varies, the heading sensitivities of the platform system of (a) above are not present. A resolver on the rotation axis measures the rotation angle and is used in determining aircraft attitude only (the other navigation outputs are independent of the resolver).

Rockwell's low-cost strapdown inertial navigation system is the N73. It meets the need for the standard medium-accuracy (0.8 nautical-mile-per-hour radial position error CEP rate) navigation system for future aircraft/missiles. It is mechanized as a rotated strapdown system.

The N73 strapdown inertial navigator uses three accelerometers, one oriented with its sensitive axis along aircraft yaw, and the other two mounted in such manner to complete the orthogonal triad. It uses two electrostatic gyros with spherical rotors that spin approximately perpendicular to each other. The rotors are suspended electrostatically by eight (spherical triangle-shaped) capacitor plates that have been applied to the inside of a spherical cavity.

The system configuration, rapid-reaction alignment mechanization, and calibration software have been described in ref 2, 3, and 4. It is the purpose here to derive the propagation of a set of critical gyro electronics errors into gyro performance errors, and to study the effect of rotation in averaging out these errors.

## 2. GYRO PICKOFF DESCRIPTION

Each N73 gyro makes use of a wide angle pickoff; that is, the orientation of the gyro case relative to the rotor spin axis can be determined for all case attitudes. The wide angle pickoff mechanization is made possible by a small radial mass unbalance that is incorporated in the gyro rotor during its fabrication. The rotor mass center is displaced from the rotor geometric center in a direction perpendicular to the rotor spin axis. The rotor spins with its mass center held at the center of the spherical cavity in the gyro case by the gyro support electronics.

Figure 1 shows a two-dimensional representation of this rotor surrounded by the pairs of plus and minus numbered capacitor plates used to support it. The rotor has its mass center at the cavity center, and its geometric center displaced from the cavity center by the amount of the radial mass unbalance. This displacement is represented by the vector,  $\underline{a}$ , the Mass Unbalance Modulation (MUM) vector. The relative dimensions are grossly distorted in this representation to make the features visible. In fact, the rotor diameter is 0.4 in, the average gap between the rotor and plates is 200  $\mu$ in, and the MUM vector is 15  $\mu$ in long.



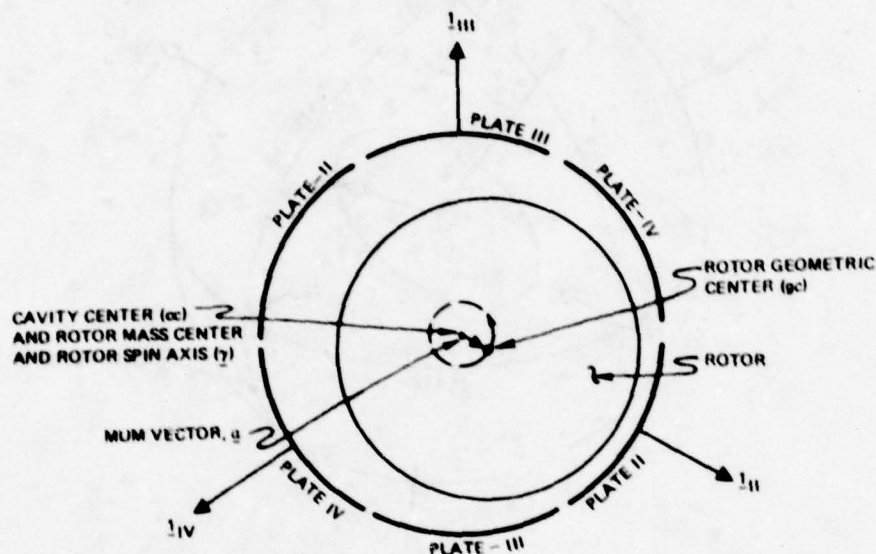


Figure 1. Two Dimensional Gyro Representation

The rotor spins at 2500 Hz about an axis perpendicular to the paper in Figure 1. Thus, the MUM vector,  $\underline{\alpha}$ , spins around in the plane of the paper at 2500 Hz as the rotor geometric center traverses the track indicated.

A different representation of the same physical situation is shown in Figure 2. Here, the plate geometry is more accurately shown. The view shown is looking down on the center of the +I plate, with all of the other plates shown except -I, which is out of sight on the underside. Unit vectors can be associated with each of the plate-pair axes. They are vectors perpendicular to the plate surface at the centers of the plus numbered plates.  $\underline{l}_I$  is a vector straight up out of the paper, so cannot be shown. The centers of the II, III, and IV plates lie over the horizon of the diagram so  $-\underline{l}_{II}$ ,  $-\underline{l}_{III}$ , and  $-\underline{l}_{IV}$  have been shown drawn from the centers of plates -II, -III, and -IV. The cavity center, rotor geometric center, and MUM vector,  $\underline{\alpha}$ , have been shown, but no representation of the rotor surface is shown. The rotor spin axis is represented by the unit vector,  $\underline{\gamma}$ , perpendicular to the plane in which  $\underline{\alpha}$  rotates.  $\underline{\gamma}$  is drawn beginning at the cavity center and terminating at a point on the case (plate) (cavity). Also shown are a set of orthogonal unit vectors,  $\underline{l}_x$ ,  $\underline{l}_y$ ,  $\underline{l}_z$ , drawn perpendicularly out at the corners of the +I plate. (The plate axes are not orthogonal, of course.)

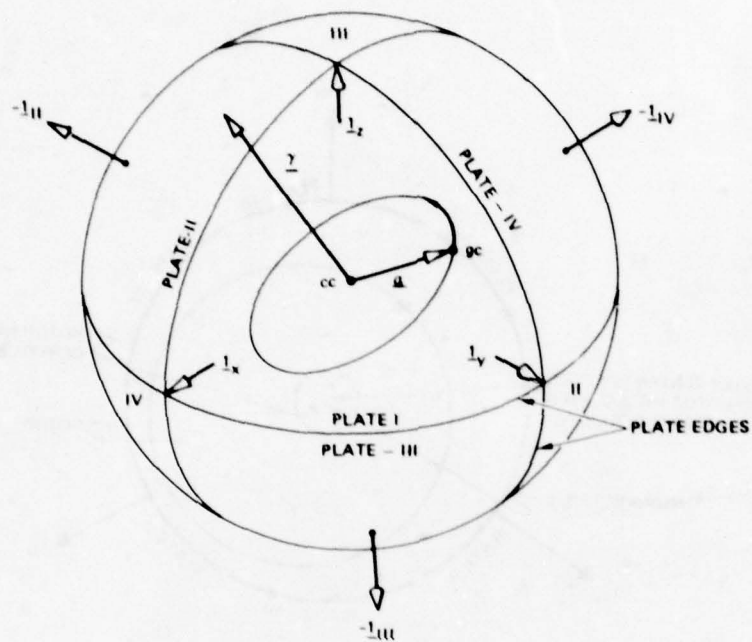


Figure 2. Projected View of Gyro

Recall that this introduction relates to using the rotor radial mass unbalance to mechanize a wide-angle gyro pickoff. The electronics associated with each plate pair is configured so that it generates a voltage proportional to the component of rotor displacement toward the center of the respective plus numbered plates. Thus

$$\alpha_I = l_I \cdot \underline{a} , \alpha_{II} = l_{II} \cdot \underline{a} , \alpha_{III} = l_{III} \cdot \underline{a} , \alpha_{IV} = l_{IV} \cdot \underline{a} \quad (1)$$

are all available as voltages. These voltages, representing  $\underline{a}$  components on the nonorthogonal plate axes, are combined in such a way as to produce voltages that represent the  $\underline{a}$  components on the orthogonal x, y, z axis set. Let us derive the formula implemented to do this. The plate axis unit vectors expressed in x, y, z components are

$$l_I = \frac{1}{\sqrt{3}} \begin{bmatrix} 1 \\ 1 \\ 1 \end{bmatrix} , l_{II} = \frac{1}{\sqrt{3}} \begin{bmatrix} -1 \\ 1 \\ -1 \end{bmatrix} , l_{III} = \frac{1}{\sqrt{3}} \begin{bmatrix} -1 \\ -1 \\ 1 \end{bmatrix} , l_{IV} = \frac{1}{\sqrt{3}} \begin{bmatrix} 1 \\ -1 \\ -1 \end{bmatrix} \quad (2)$$

using Eq (2), Eq (1) can be written in matrix form as

$$\begin{bmatrix} \alpha_I \\ \alpha_{II} \\ \alpha_{III} \\ \alpha_{IV} \end{bmatrix} = \frac{1}{\sqrt{3}} \underbrace{\begin{bmatrix} 1 & 1 & 1 \\ -1 & 1 & -1 \\ -1 & -1 & 1 \\ 1 & -1 & -1 \end{bmatrix}}_{\underline{\underline{A}}} \begin{bmatrix} \alpha_x \\ \alpha_y \\ \alpha_z \end{bmatrix} \quad (3)$$

Given the vector on the left-hand side of Eq. (3), how do we find  $\alpha_x$ ,  $\alpha_y$ ,  $\alpha_z$ ? The familiar least squares solution is

$$\begin{bmatrix} \alpha_x \\ \alpha_y \\ \alpha_z \end{bmatrix} = \left( \underline{\underline{A}}^T \underline{\underline{A}} \right)^{-1} \underline{\underline{A}}^T \begin{bmatrix} \alpha_I \\ \alpha_{II} \\ \alpha_{III} \\ \alpha_{IV} \end{bmatrix} \\ = \frac{\sqrt{3}}{4} \begin{bmatrix} 1 & -1 & -1 & 1 \\ 1 & 1 & -1 & -1 \\ 1 & -1 & 1 & -1 \end{bmatrix} \begin{bmatrix} \alpha_I \\ \alpha_{II} \\ \alpha_{III} \\ \alpha_{IV} \end{bmatrix} \quad (4)$$

Equation (4) has been implemented in the electronics. Another form of this equation, convenient for error analysis purposes, is

$$\underline{\underline{\alpha}} = \frac{3}{4} \left( \frac{1}{4} \alpha_I + \frac{1}{4} \alpha_{II} + \frac{1}{4} \alpha_{III} + \frac{1}{4} \alpha_{IV} \right) \quad (5)$$

Now that we have  $\underline{\underline{\alpha}}$  in terms of  $x$ ,  $y$ ,  $z$ , we can find  $\underline{\underline{y}}$ , the unit vector along the rotor spin axis.  $\underline{\underline{y}}$  is simply the vector normal to the plane in which  $\underline{\underline{\alpha}}$  is rotating. That is, it is the unique unit vector for which

$$\underline{\underline{y}} \cdot \underline{\underline{\alpha}} = 0 \quad (6)$$



for the various values of  $\underline{\alpha}$  generated as it rotates.  $\underline{\gamma}$  is computed in the N73 digital computer by taking the vector cross product of two values of  $\underline{\alpha}$  separated by  $90^\circ$  of rotation.

$$\underline{\gamma} = \underline{\alpha}_{0^\circ} \times \underline{\alpha}_{90^\circ} = \begin{bmatrix} \gamma_x \\ \gamma_y \\ \gamma_z \end{bmatrix} \quad (7)$$

The  $\underline{\gamma}$  vector is normalized in the computer to have unit length. Only its direction, the direction of the rotor spin axis, has meaning anyway.

Now we have in the computer  $\gamma_x, \gamma_y, \gamma_z$ , the direction cosines between the gyro rotor spin axis and the gyro case fixed x, y, z axes. These quantities are just what is needed for the strapdown navigation equations. Velocity increments are available 64 times per second in these same coordinates from the accelerometers. This  $\Delta \underline{v}$  vector is dot multiplied with the following three vectors (1)  $\underline{\gamma}$  of the first gyro, (2)  $\underline{\gamma}$  of the second gyro and, (3) the vector cross product of the  $\underline{\gamma}$ 's of the two gyros. These three dot products are the  $\Delta v$  components on a set of inertially fixed axes. From this point in the mechanization on, the equations are just like those for an inertially fixed stable platform system.

## 2.1 PROPAGATION OF ELECTRONIC GAIN ERRORS

We have presented the essentials of the gyro wide-angle pickoff mechanization.  $\underline{\alpha}$  spins at rotor spin rate, and voltages that are its components on the four plate-pair axes are generated. These voltages are combined to give voltages that are  $\underline{\alpha}$  components on the three case-fixed x, y, z orthogonal axes. The rotor spin axis,  $\underline{\gamma}$ , is generated in the digital computer by noting that it is the unique unit vector always perpendicular to  $\underline{\alpha}$ .

A block diagram of the  $\underline{\alpha}$  manipulations is shown in Figure 3. There are electronic operations (sampling, demodulation, etc) that occur, operating on both the 4-space (I, II, III, IV) and the 3-space (x, y, z)  $\underline{\alpha}$  component voltages. These operations are shown in Figure 3 simply as unity gain elements in the various lines. It is the purpose here to derive the propagation of electronics gain errors into errors in determining  $\underline{\gamma}$ .

Suppose that the unity gain shown in the x-channel of Figure 3 is not unity but is, in fact,  $1 + k_x$ . Its output is not  $\alpha_x$ , but  $(1+k_x)\alpha_x$ . The MUM vector is not  $\underline{\alpha}$ , but

$$\begin{aligned} \underline{\alpha} + \delta \underline{\alpha} &= \underline{1}_x (1 + k_x) \alpha_x + \underline{1}_y \alpha_y + \underline{1}_z \alpha_z \\ &= \underline{\alpha} + k_x (\underline{1}_x \underline{1}_x^T) \underline{\alpha} \end{aligned} \quad (8)$$

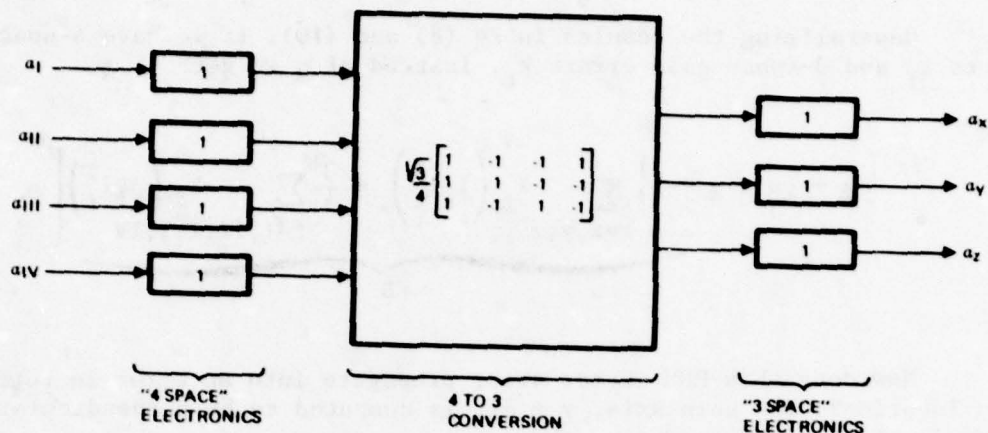


Figure 3. Obtaining  $\underline{\alpha}$  Components on Orthogonal Axes

$(\underline{1}_x \underline{1}_x^T)$  is the  $3 \times 3$  matrix

$$\underline{1}_x \underline{1}_x^T = \begin{bmatrix} 1 & 0 & 0 \\ 0 & 0 & 0 \\ 0 & 0 & 0 \end{bmatrix} \quad (9)$$

Suppose that the unit gain shown in the I-channel of Figure 3 is not unity but is, in fact,  $1 + k_I$ . Propagating this error through to the end, making use of Eq (5), it is seen that  $\underline{\alpha} + \underline{\delta\alpha}$  is obtained.

$$\begin{aligned} \underline{\alpha} + \underline{\delta\alpha} &= \frac{3}{4} \left[ (1 + k_I) \underline{1}_I \alpha_I + \underline{1}_{II} \alpha_{II} + \underline{1}_{III} \alpha_{III} + \underline{1}_{IV} \alpha_{IV} \right] \\ &= \underline{\alpha} + \frac{3}{4} k_I (\underline{1}_I \underline{1}_I^T) \underline{\alpha} \end{aligned} \quad (10)$$

with

$$\frac{3}{4} (\underline{1}_I \underline{1}_I^T) = \frac{1}{4} \begin{bmatrix} 1 & 1 & 1 \\ 1 & 1 & 1 \\ 1 & 1 & 1 \end{bmatrix} = \frac{1}{4} \begin{bmatrix} 0 & 1 & 1 \\ 1 & 0 & 1 \\ 1 & 1 & 0 \end{bmatrix} \quad (11)$$

In the second step in Eq (11) the 1's on the diagonal are eliminated to simplify the matrix; this does not change the direction of  $\underline{\alpha} + \underline{\delta\alpha}$  in Eq (10), only its length (which doesn't matter).

Generalizing the results in Eq (8) and (10), if we have 4-space gain errors  $k_f$  and 3-space gain errors  $k_t$ , instead of  $\underline{\alpha}$  we get

$$\underline{\alpha} + \underline{\delta\alpha} = \underline{\alpha} + \underbrace{\left\{ \sum_{t=x,y,z} k_t \left( \underline{1}_t \underline{1}_t^T \right) + \frac{3}{4} \sum_{f=I,II,III,IV} k_f \left( \underline{1}_f \underline{1}_f^T \right) \right\}}_{\underline{\Delta_B}} \underline{\alpha} \quad (12)$$

How does this MUM vector error propagate into an error in rotor spin axis location? The spin axis,  $\underline{\gamma} + \underline{\delta\gamma}$ , is computed to be perpendicular to the plane in which  $\underline{\alpha} + \underline{\delta\alpha}$  rotates, thus

$$\begin{aligned} \left( \underline{\gamma} + \underline{\delta\gamma} \right)^T \left( \underline{\alpha} + \underline{\delta\alpha} \right) &= 0 \\ \underline{\delta\gamma}^T \underline{\alpha} + \underline{\gamma}^T \underline{\delta\alpha} &= 0 \quad \left( \begin{array}{l} \text{neglecting second} \\ \text{order terms} \\ \text{and using Eq (6)} \end{array} \right) \end{aligned} \quad (13)$$

Using Eq (12) in Eq (13)

$$\left( \underline{\delta\gamma}^T + \underline{\gamma}^T \underline{\Delta_B} \right) \underline{\alpha} = 0 \quad \text{for any } \underline{\alpha} \quad (14)$$

$$\begin{aligned} \underline{\delta\gamma} &= -\underline{\Delta_B}^T \underline{\gamma} + \underbrace{(\text{any scalar}) \underline{\gamma}}_{\text{irrelevant}} \\ &= -\underline{\Delta_B}^T \underline{\gamma} \end{aligned} \quad (15)$$



Working out the B matrix defined in Eq (12) explicitly

$$\underline{\delta \underline{y}} = \begin{bmatrix} k_x & \frac{1}{4} \begin{pmatrix} +k_I - k_{II} \\ +k_{III} - k_{IV} \end{pmatrix} & \frac{1}{4} \begin{pmatrix} +k_I + k_{II} \\ -k_{III} - k_{IV} \end{pmatrix} \\ \frac{1}{4} \begin{pmatrix} +k_I - k_{II} \\ +k_{III} - k_{IV} \end{pmatrix} & k_y & \frac{1}{4} \begin{pmatrix} +k_I - k_{II} \\ -k_{III} + k_{IV} \end{pmatrix} \\ \frac{1}{4} \begin{pmatrix} +k_I + k_{II} \\ -k_{III} - k_{IV} \end{pmatrix} & \frac{1}{4} \begin{pmatrix} +k_I - k_{II} \\ -k_{III} + k_{IV} \end{pmatrix} & k_z \end{bmatrix} \begin{bmatrix} \underline{y}_x \\ \underline{y}_y \\ \underline{y}_z \end{bmatrix} \quad (16)$$

The matrix is symmetric. The 3-space gain errors appear along the diagonal at the appropriate places. All the 4-space gain errors appear in each off-diagonal element. They appear in the xy and yx elements with the sign pattern of the z row of the matrix in Eq (4), etc. Notice that if all the  $k_f$ 's are equal, and all the  $k_t$ 's are equal,  $\underline{\delta \underline{y}} = k_t \underline{y} =$  (no error in  $\underline{y}$  direction). Thus, only gain balance matters.

The 3-space and 4-space electronic operations shown in Figure 3 are subject to phase errors as well as gain errors, of course. The analytical development leading to the  $\underline{\delta \underline{y}}$  resulting from phase errors follows the line of the development just presented. Define a rotor-fixed-vector,  $\underline{\beta}$ , rotating in the plane perpendicular to  $\underline{y}$  and leading  $\underline{\alpha}$  by  $90^\circ$ .

$$\underline{\beta} = \underline{y} \times \underline{\alpha} \quad (17)$$

Now with a phase error  $\phi_I$ , instead of  $\alpha_I$ , we get  $\alpha_I + \phi_I \beta_I$ . Following through, as before, we obtain

$$\underline{\delta \underline{\alpha}} = B' \underline{\beta} \quad (18)$$

where  $B'$  is the matrix of Eq (12), but with phase errors,  $\phi_t$  and  $\phi_f$  instead of gain errors  $k_t$  and  $k_f$ . Analogous to Eq (14) is

$$\begin{aligned} 0 &= \underline{\delta \underline{y}}^T \underline{\alpha} + \underline{y}^T \underline{\delta \underline{y}} \\ &= \underline{\delta \underline{y}}^T \underline{\alpha} + \underline{y}^T B' \underline{\beta} \\ &= \underline{\delta \underline{y}}^T \underline{\alpha} + \underline{y}^T B' (\underline{y} \times \underline{\alpha}) \quad \text{for all } \underline{\alpha} \end{aligned} \quad (19)$$

From which

$$\underline{\delta \underline{y}} = - \left[ \underline{\underline{y}}^T B'(\underline{\underline{y}} \underline{x}) \right]^T = \underline{\underline{y}} \underline{x} \left( B'^T \underline{\underline{y}} \right) \quad (20)$$

This expression is like that of Eq (15) for scale factor error propagation, but premultiplied by  $-\underline{\underline{y}} \underline{x}$ , which merely rotates the  $\underline{\delta \underline{y}}$  error by  $-90^\circ$  about  $\underline{\underline{y}}$ .

The above discussion has dealt with gyro angle readout error. Another important class of gyro error is rotor spin axis precession in inertial space, that is, gyro drift rate. It is asserted without derivation that drift rate expressions of the form

$$G = B'' \underline{\underline{y}} + \underline{\underline{y}} \times B''' \underline{\underline{y}} \quad (21)$$

characterize a substantial part of the gyro drift rate errors.  $B''$  is a symmetric matrix having to do with rotor oblateness and cavity shape errors.  $B'''$  is a symmetric matrix having to do with suspension servo phase errors. Notice that the drift rate of Eq (21) has the same form in  $\underline{\underline{y}}$  as the pickoff error expressions of Eq (15) and (20).

We see then that errors of the form  $B \underline{\underline{y}}$  arise from many sources and that it is important to know the effect of gyro case rotation on these errors.

## 2.2 THE AVERAGING EFFECTS OF ROTATION

Three accelerometers and two electrostatic gyros are part of Rotating Assembly Unit (RAU) in the N73 navigator. The RAU rotates  $360^\circ$  within the N73 housing about the yaw axis in 1 minute (15 seconds during alinement). The RAU then reverses its direction of rotation and goes  $360^\circ$  the other way. The N73 operates continuously as a strapdown navigator, just as a nonrotated strapdown navigator would in an aircraft that was changing heading back and forth through  $360^\circ$ .

The time of RAU rotation is short compared to an 84-minute Schuler oscillation period so instrument errors are effectively averaged over an RAU rotation cycle before influencing system navigation errors. To see the averaging effects of RAU rotation upon the gyro errors described in the previous section, consider Figure 4. The gyro is mounted in the RAU so that the rotation axis,  $\underline{\underline{l}}_r$ , falls at the center of plate I. As the gyro case rotates with the RAU, and the rotor spin axis does not, the spin axis,  $\underline{\underline{y}}$ , (shown in Figure 4 drawn from the gyro cavity center to the cavity surface), moves in a closed circular track on the cavity surface, such as the one shown in Figure 4. This is nominally the case when the aircraft roll and pitch angles are essentially constant for the length of the RAU rotation cycle, a condition prevalent the vast majority of the time.





Figure 4,  $\underline{l}_t$  (for "track") and  $\underline{l}_c$  (for "cross-track") is suitable for averaging error components. It is approximately inertially fixed most of the time.

$$\underline{l}_t = (\sin \theta)^{-1} (\underline{\gamma} \times \underline{l}_r) \quad (23)$$

$$\underline{l}_c = \underline{\gamma} \times \underline{l}_t \quad (24)$$

We can resolve the  $\delta \underline{\gamma}$  given in x, y, z components onto the t, c axes by means of a transformation involving  $\phi$  and  $\theta$ , and then average the result over  $360^\circ$  of  $\phi$ .

Fortunately, the arduous procedure just described can be avoided by making use of a potential function formulation of Eq (15). If  $b_{ij}$  is the element of the  $i^{\text{th}}$  row and  $j^{\text{th}}$  column of the symmetric matrix B of Eq (15), we can rewrite Eq (15) as

$$\delta \underline{\gamma} = \underline{\nabla} G \quad (25)$$

where  $\underline{\nabla}$  is the gradient operator

$$\underline{\nabla} = \frac{\partial}{\partial \underline{\gamma}} = \underline{l}_x \frac{\partial}{\partial \gamma_x} + \underline{l}_y \frac{\partial}{\partial \gamma_y} + \underline{l}_z \frac{\partial}{\partial \gamma_z} \quad (26)$$

and G is the scalar function

$$\begin{aligned} G &= -\frac{1}{2} \underline{\gamma}^T B \underline{\gamma} \\ &= -\frac{1}{2} b_{11} \gamma_x^2 - \frac{1}{2} b_{22} \gamma_y^2 - \frac{1}{2} b_{33} \gamma_z^2 - b_{12} \gamma_x \gamma_y - b_{23} \gamma_y \gamma_z - b_{31} \gamma_z \gamma_x \end{aligned} \quad (27)$$

Our plan is to substitute the  $\phi$ ,  $\theta$  forms of  $\gamma_x$ ,  $\gamma_y$ ,  $\gamma_z$  from Eq (22) into Eq (27), average this scalar function over  $360^\circ$  of  $\phi$ , having left a scalar function of  $\theta$  only, and now take its gradient to obtain  $\delta \underline{\gamma}$ . We have

$$\begin{aligned} \text{Av. over } \phi \left\{ \gamma_x^2 \right\} &= \frac{1}{3} \cos^2 \theta + \left( \frac{2}{3} \sin^2 \theta \right) \left( \frac{1}{2} \right) = \frac{1}{3} \\ &= \text{Av over } \phi \left\{ \gamma_y^2 \right\} \\ &= \text{Av over } \phi \left\{ \gamma_z^2 \right\} \end{aligned} \quad (28)$$

$$\begin{aligned}
\text{Av over } \phi \left\{ \gamma_x \gamma_y \right\} &= \frac{1}{3} \cos^2 \theta + \frac{2}{3} \sin^2 \theta \underbrace{\cos \phi \cos (\phi + 120^\circ)}_{\text{Av over } \phi = -\frac{1}{4}} \\
&= \frac{1}{3} \cos^2 \theta - \frac{1}{6} \sin^2 \theta = \frac{1}{2} \cos^2 \theta - \frac{1}{6} \\
&= \text{Av over } \phi \left\{ \gamma_y \gamma_z \right\} \\
&= \text{Av over } \phi \left\{ \gamma_z \gamma_x \right\} \quad (29)
\end{aligned}$$

Averaged over  $\phi$ , the potential function of Eq (27) becomes

$$\begin{aligned}
\text{Av over } \phi \left\{ G \right\} &= -\frac{1}{6} (b_{11} + b_{22} + b_{33}) \\
&\quad - \left( \frac{1}{2} \cos^2 \theta - \frac{1}{6} \right) (b_{12} + b_{23} + b_{31}) \quad (30)
\end{aligned}$$

We take the gradient of this function to obtain  $\delta \underline{Y}$ . The gradient operator of Eq (26) can be written

$$\begin{aligned}
\underline{\nabla} &= \frac{\partial}{\partial \underline{Y}} = \frac{\partial \theta}{\partial \underline{Y}} \frac{\partial}{\partial \theta} + \frac{\partial \phi}{\partial \underline{Y}} \frac{\partial}{\partial \phi} + \frac{\partial |\underline{Y}|}{\partial \underline{Y}} \frac{\partial}{\partial |\underline{Y}|} \\
&= \frac{1}{c} \frac{\partial}{\partial \theta} + \frac{1}{t} (\sin \theta)^{-1} \frac{\partial}{\partial \phi} + \underline{Y} \frac{\partial}{\partial |\underline{Y}|} \quad (31)
\end{aligned}$$

The second and third terms of the gradient operator given in Eq (31) produce zero when operating on the potential function given by Eq (30). We have then, from Eq (25)

$$\begin{aligned}
\text{Av over } \phi \left\{ \frac{\delta \underline{Y}}{|\underline{Y}|} \right\} &= \frac{1}{c} \frac{\partial}{\partial \theta} \left[ \text{Av over } \phi \left\{ G \right\} \right] \\
&= (b_{12} + b_{23} + b_{31}) \frac{1}{c} \cos \theta \sin \theta \\
&= \frac{1}{2} (b_{12} + b_{23} + b_{31}) \frac{1}{c} \sin 2 \theta \quad (32)
\end{aligned}$$

In terms of the electronic gain errors (see Eq (16))

$$\text{Av over } \phi \left\{ \frac{\delta Y}{\underline{1}} \right\} = \frac{1}{c} \sin 2 \theta \left( \frac{3}{8} k_I - \frac{1}{8} k_{II} - \frac{1}{8} k_{III} - \frac{1}{8} k_{IV} \right) \quad (33)$$

Equation (33) is the average-with-rotation error expression we have been seeking. Notice that the 3-space gain errors,  $k_x$ ,  $k_y$ ,  $k_z$ , do not appear there. Three-space gain (and phase) errors are completely averaged to zero by the rotation. The 4-space gain errors are not averaged to zero, with the propagation of  $k_I$  being larger than the others.  $\underline{\delta Y}$  due to  $k_I$  (nonrotated) is

$$\underline{\delta Y} = \frac{3}{4} k_I \underline{1}_I \begin{pmatrix} 1^T \\ \underline{1}_I \end{pmatrix} \underline{Y} \quad (34)$$

With the rotation axis along  $\underline{1}_I$ , the  $\underline{\delta Y}$  due to  $k_I$  is independent of  $\phi$ . Thus rotation does nothing to reduce the propagation of  $k_I$ . Before rotation the propagations of  $k_{II}$ ,  $k_{III}$ ,  $k_{IV}$  are similar to that of  $k_I$ ; their directions are different but the rms value taken all over the case is the same. From Eq (33) it is clear that rotation reduces the rms propagation of the 4-space gain errors  $k_{II}$ ,  $k_{III}$ ,  $k_{IV}$  by a factor of 3. If gain errors are equally likely on each of the 4-space axes, then rotation reduces the overall rms gain error propagation by a factor of  $\sqrt{3}$ .

In summary, rotation does nothing for the 4-space gain (and phase) error along the rotation axis, reduces the other 4-space gain (and phase) error propagations by a factor of 3, and averages to zero the propagation of 3-space gain (and phase) errors.

The drift rates given by Eq (21) benefit similarly from rotation. The propagation of the on-diagonal elements of the matrices  $B''$  and  $B'''$  is reduced to zero. The propagation of the off-diagonal elements of the matrices is reduced by a factor of  $\sqrt{3}$  when the rms value is taken all over the case.

It is significant to notice that at  $\theta = 0^\circ$  and  $\theta = 90^\circ$ , all these errors average to zero with rotation. By spinning the two N73 gyros up, one with its spin axis along the rotation axis (i.e., vertical), and the other with its spin axis perpendicular to the rotation axis (i.e., horizontal) all of these errors are averaged out. The advantage of this spinup orientation is particularly important during fast reaction gyrocompass alignment because it reduces the thermal settling requirements on the electronics. The spin axes move away from this special orientation in time, as the earth turns, but by then the critical gyrocompassing operation is complete.



### 3. N73 PERFORMANCE RESULTS

Two feasibility demonstrator systems, designated N57, were built in 1973-1974. The N57 is an ESG strapdown navigator that does not incorporate instrument rotation. The two N57 systems were tested in a variety of environments in 1973-1975. They consistently demonstrated performance better than 1 nmi/hr.

A series of tests made with an N57 in 1976 provides an excellent basis for comparing rotated and nonrotated ESG navigator performance (see ref 1). First, 20 laboratory navigation runs were made, including heading changes to simulate the flight attitude environment. Then 10 laboratory runs were made in which the N57 was rotated using the inner axis of a Goerz automatic 3-axis table to achieve instrument rotation by rotating the whole N57 system. Additional motions to simulate the flight attitude environment were imposed via the Goerz table axes. The CEP rate exhibited in the rotated runs was one-half that of the nonrotated runs. The velocity errors of the rotated runs were one-third those of the nonrotated runs. The improvement with rotation was, as expected, very substantial.

Two N73 Engineering Prototype Model (EPM) navigators were built in 1976-1977. They make use of the instrument rotation feature we have been describing. The test programs on the two EPM systems began in 1977 and are still continuing.

The radial position error rates from the tests on N73 EPM No 1 for a period of more than a year are shown in Figure 5. The results of both laboratory runs and flight tests are shown there. A series of 7 flights was made by Northrop in their Gulfstream II aircraft in July, 1978; a series of 8 flights was made in October 1978 in the same aircraft.

Several things should be noted about the data presented in Figure 5. First, performance is excellent. The median radial error rate (roughly, CEP rate) over the test series is one-third that required by the Standard Navigator specification. Second, radial error rate values arising from the flight tests look like those from the laboratory tests. The flight environment causes no degradation in performance for this strapdown system. Last, all of these results, obtained over a time span of more than a year, are from a single system calibration at the beginning. The slope of the best fit line to the points is negative. While not suggesting that the calibration improves with age, it is at least true that no performance degradation with time is evident.

Units of the N73 preproduction model (PPM) design, also using instrument rotation, are now in test at CIGTF, and doing well.

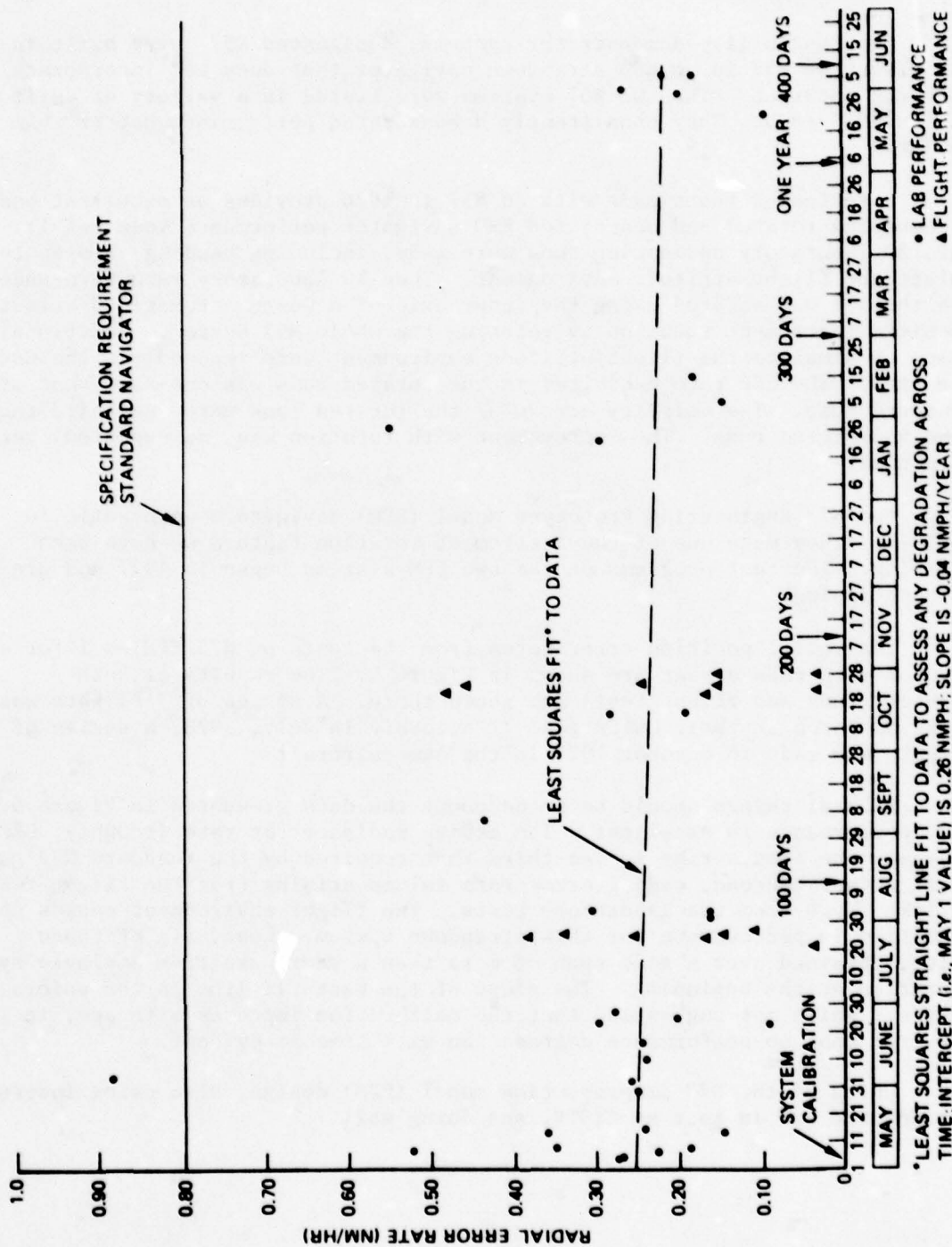


Figure 5. N73 EPM No. 1 Navigation Performance/Calibration Stability

#### REFERENCES

1. J. C. Pinson "MICRON Configured to Meet Standard Medium Accuracy Navigator Specification," Presented to Eighth Biennial Guidance Test Symposium, HAFB, New Mexico, 11-13 May, 1977, dated January 13, 1977
2. A. P. Truban "Application of Instrument Rotation in the N73 Standard Inertial Navigation System", Presented at NAECON, Dayton, Ohio May 15-17, 1979, dated March 23, 1979
3. B. E. Bona and R. M. duPlessis "Rapid Reaction Time Techniques for a Strapdown Navigator Employing Electrostatic Gyro Technology" Presented at NAECON, Dayton, Ohio 15-17 May 1979, dated March 23, 1979
4. L. P. Stave "Automatic Test Software for Calibrating Strapdown Systems" Presented at NAECON, Dayton, Ohio 15-17 May, 1979, dated March 23, 1979



TITLE: MEASUREMENT OF AN  
ACCELEROMETER SECOND  
ORDER ERROR COEFFICIENT  
THROUGH A LINEAR VIBRATOR  
MECHANIZATION

AUTHOR: LEO A. KELLER, JR.

HONEYWELL INERTIAL COMPONENT DESIGN  
13350 U.S. Highway 19  
St Petersburg, Florida 33733

## I. INTRODUCTION

A linear vibrator facility that Honeywell has under development has opened up a new and unique method for evaluating a significant 2nd order cross axis accelerometer error ( $F_{X1}$ ) in the MX missile application. The needed precision for this measurement has so far eluded other test methods. The technique described in this paper is eventually expected to meet the accuracy requirements with a relatively simple setup. The test simply stated is vibrating perpendicular to the input axis and determining the squared response in the SFIR output.

At the time that the abstract for this paper was submitted, it was anticipated that enough data would exist to substantiate the validity of the linear vibration technique. Due to the test base (slab) stability problems, this is now considered inappropriate. Some of the data appears to have good repeatability and quality but now, having knowledge of the resonant responses of the slab, the aggregate of the data is considered questionable. This is true even though the test values for  $F_{X1}$  approached calculated values. The emphasis of this paper is now on test methodology which includes test mechanizations and technical approach. It is anticipated that with the vibration facility modifications, valid data can be produced in August 1979. Operating on the data with post processing techniques now being developed will assume that meaningful test results will be presented at the symposium. The report will have to be given in a classified session.

The basic test problem is to derive high resolution data from a dynamic vibratory environment that is a composite of urban seismic background "noise" and a larger spectrum of disturbances being excited by the linear vibrator itself. The accuracy need for the  $F_{X1}$  is far below typical urban seismic disturbances. Exact numbers are being avoided to keep this paper unclassified. Specific numbers will be presented at the symposium. An interesting aspect of this program is the planned use of a SFIR instrument of the same type being evaluated, for characterization of the forcing function vibration being applied to the SFIR specimen accelerometer during the test.

The need for a  $F_{X1}$  installation is a relatively recent test requirement that has been identified on the MX missile development program. This is modelled as an error term which is excited by accelerations perpendicular to the designed input axis of each system accelerometer. The missile impact range error contributed by this term is large; therefore, there is considerable concern over the current calibration.

The linear vibrator technique under development has the potential of being a uncomplicated set-up and simple to run to meet the application accuracy requirements. The basic set-up consists of a low frequency, long stroke precision linear vibrator. Several procedures and fixtures were developed to accomplish this task. These

are one time methodology activities and once established will make repetitive production tests routine. The salient features of the system is the 10 inch usable stroke of the vibrator which has a precision linear motion from 1 to 20 Hz. Figure 1 shows the acceleration and frequency specifications of the vibrator and Figure 2 is a photograph of the control console.

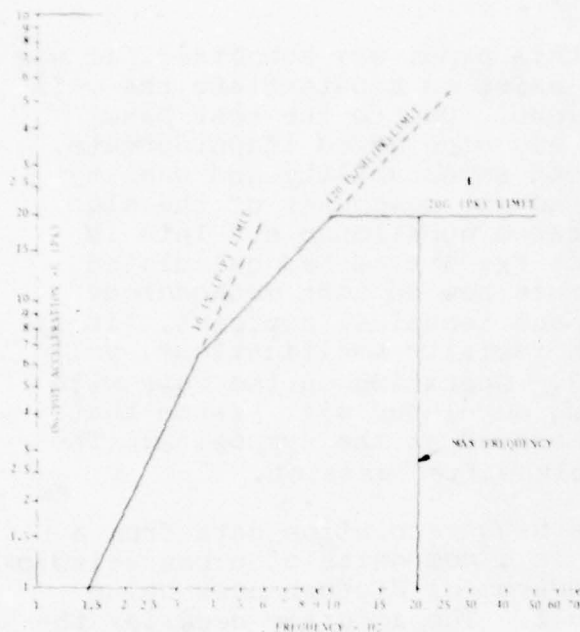


FIGURE 1

CHARACTERISTICS OF LINEAR  
VIBRATOR

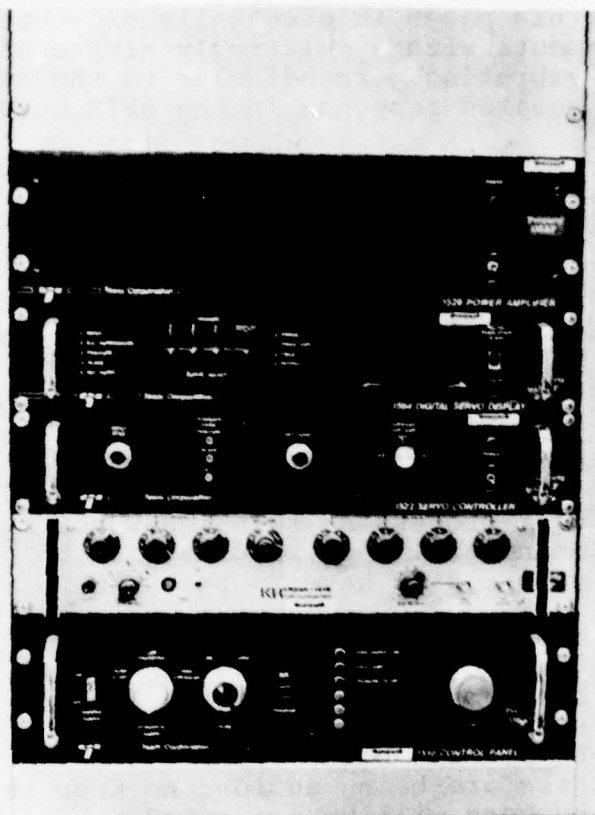


FIGURE 2

LINEAR VIBRATOR CONTROL  
CONSOLE

The stroke is carefully channeled into near perfect zero cross talk. This is accomplished by close tolerance and high balancing forces on a hydraulic bearing. A very high centering force (15,000 lbs.) is produced to keep the thrust centered in the bearing. Low frequency capability is the key for approaching and extrapolating into a zero (steady state) frequency response.

The overall facility is pictured in Figure 3. This is an experimental set-up as evidenced by the 50 gallon drum for cooling the vibrator oil and other features characteristic of an engineering set-up. The impending move to a permanent location will benefit much from work in this area. A more sophisticated set-up is in the plan.



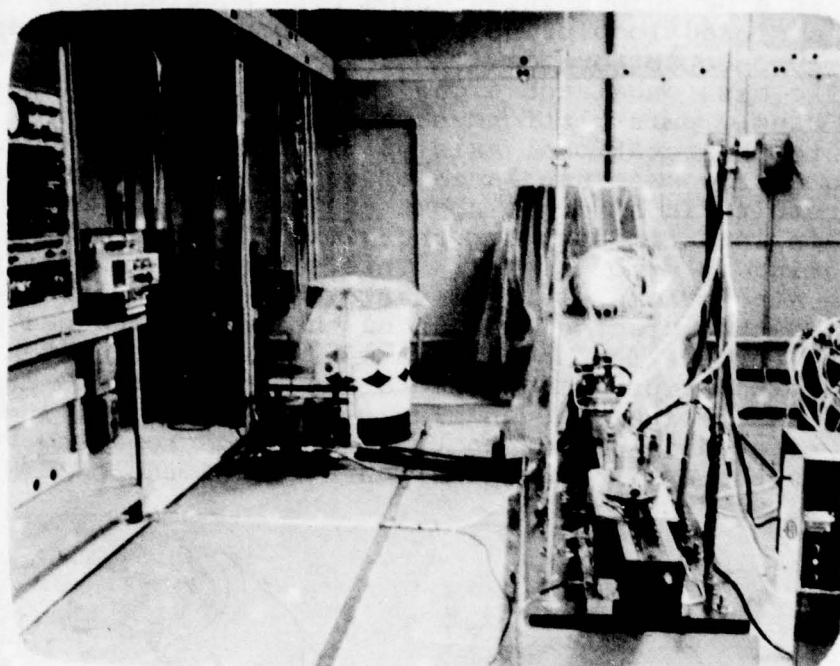


FIGURE 3. OVERALL LINEAR VIBRATION SET-UP

The key to making the measurement practical is to reduce the disturbances in the test environment to the point that the mathematics of the method can account for them. Computers and special instrumentation loops are used to sort out the coherent functions between the test sample outputs and the cross axis stimulus for harmonics of concern.

## II. TEST OBJECTIVES

The basic objectives of this program are:

1. Utilize the dynamics of vibration to determine the  $F_{x1}$  coefficient family characteristics of the MX/SFIR accelerometer.
2. Develop a test applicable for production units. The alternative would involve the resources of a large complex facility, i.e., centrifuge.

The MX/SFIR is a pendulous integrating gyro accelerometer which operates on a closed loop principle where pendulous torques are balanced by gyroscopic torques. The unit consists of a gyro having a specific mass unbalance along the spin reference axis slaved to a single axis platform such that the gyro output axis is parallel to the rotational axis of the platform. A specific force acting on the mass unbalance of the Pendulous Integrating Gyro (PIG) results in a torque about the gyro output axis. This torque results in a tendency for the gimbal to move off null, thus, generating an error signal. This signal is conditioned to drive the single axis platform servo motor and a gyroscope torque induced that precisely balances the torque induced by the pendulous force. The angular rate of the servo driven member (SDM) is proportional to acceleration along the PIG input axis and the integral of the angular rate or the total angle the SDM has rotated at any given time is proportional to velocity. Figure 4 shows the cylindrical configuration of the MX/SFIR and Figure 5 is a cut-a-way.

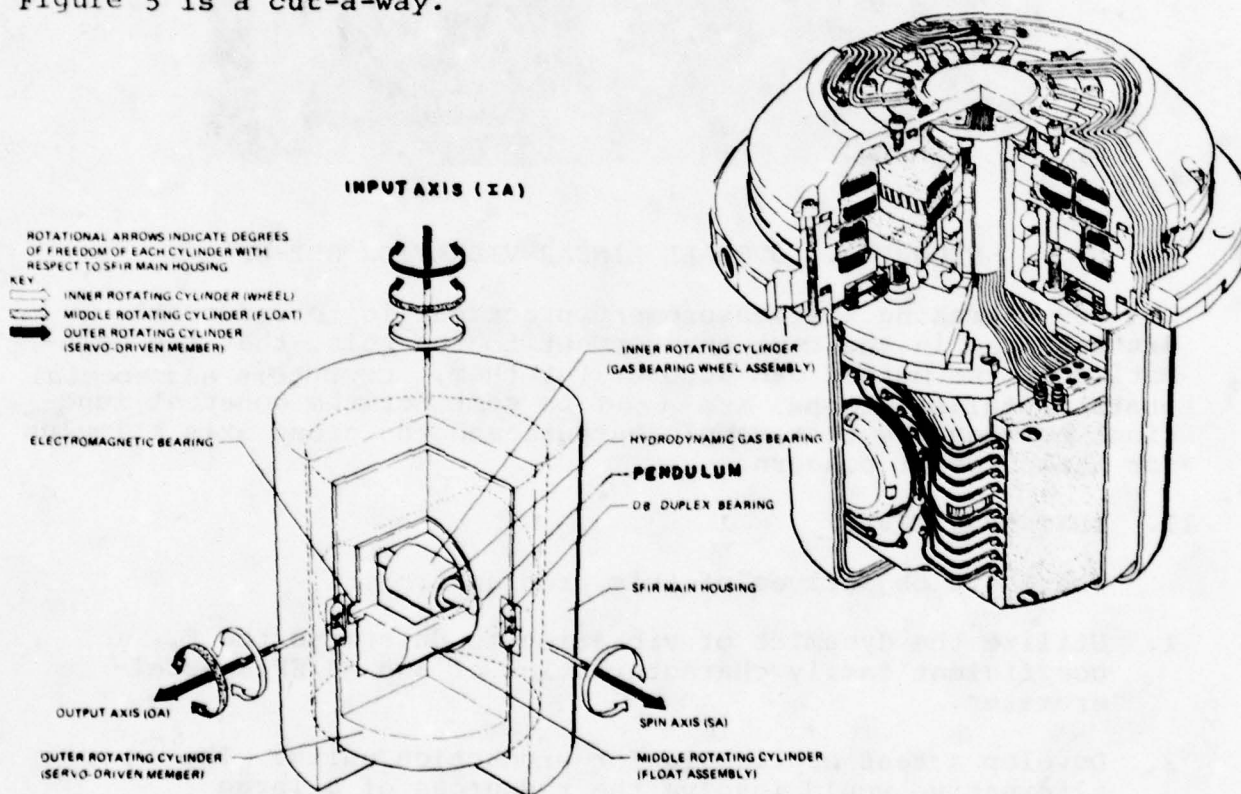


FIGURE 4. CYLINDRICAL CONFIGURATION OF SPECIFIC FORCE INTEGRATING RECEIVER

FIGURE 5. MX/SFIR CUT-A-WAY

$F_{X1}$  in the SFIR model equation is the term that responds to an acceleration perpendicular to the input axis. This response is a squared function to the exciting acceleration. Given this relationship, it is theoretically possible to amplify 2nd order responses with precise low frequency (1-20 Hz) vibrating inputs at higher than local "g" (1-20g) into the OA/SA plane. The  $F_{X1}$  information is then in the output of the SFIR and the uniqueness of the methodology is in the reduction of the information to obtain  $F_{X1}$  from output highly contaminated with other dynamic responses of the environment.

The reason  $F_{X1}$  is so important is rooted in a system requirement to know either  $F_{I1}$  or  $F_{X1}$  very accurately (classified numbers).  $F_{I1}$  is a 2nd order error term that is a function of acceleration into the SFIR input axis. If one is known, the other can be derived in System CAL & Align, which is a slow tumbling mechanization which exposes all axis, i.e., Input (IA), Output (OA) and Spin (SA), to local gravity (refer FIGURE 1). The system problem is one of separation due to an interdependence of a  $\cos \theta$  term where  $F(\theta)$  is involved in the application of local "g" into the IA and SA/OA plane. This relationship is developed in the next section.  $F_{I1}$  measurement has always been an Acceptance Test Procedure (ATP) as a relatively simple and a very repeatable test. Technical questions have been raised this past year as to whether the ATP test is really determining all the  $F_{I1}$  mission response through the SFIR servo driven member simulation of high "g". The development of an accurate  $F_{X1}$  vibration test will, as a minimum, help evaluate the real  $F_{I1}$  coefficient as a qualification endeavor and, as a possible maximum, replace the  $F_{I1}$  test in the ATP.

Two other methods have been tried to precisely determine  $F_{X1}$  but at present, neither meet accuracy objectives of this test program. The first method is a one "g" tumbling technique where a 2nd order curve is fitted to the data. This has so far been lacking by at best an order of magnitude for system requirements. The 2nd method is a major undertaking involving a complex centrifuge setup, i.e., CIGTF. Theoretically, this has the precision, but requires more engineering to meet system requirements. The latter method could never in a practical sense be applied to a production run. The vibration technique proposed in this test plan has the capability of being both accurate and not a complex operation for ATP testing.

### III. TEST MECHANIZATION

Long Stroke Linear Vibrator -- This facility makes the measurement possible as it permits the application of a low distortion sinusoidal waveform of acceleration at a high "g" and low frequency. The latter two points are salient and are the difference between this test and previous attempts to derive SFIR responses through linear vibration. The long stroke allows high "g" acceleration near the effective 0 Hz of the mission environment and puts the test frequencies far from resonant responses of the device when on stiff mounted fixturing.



The physical property of  $F_{x1}$  which keeps the same polarity sense whether the SFIR IA is up ( $\uparrow$ ) or down ( $\downarrow$ ) allows for separating the true  $F_{x1}$  from other 2nd order terms, i.e., IA rocking from fixturing or slab motions caused by the driven accelerations. The latter motion changes sign with  $180^\circ$  rotation from IA  $\uparrow$  to IA  $\downarrow$ . Algebraically adding (effectively subtracting absolute values) leaves a result that is a dynamic bias change due to  $F_{x1}$ . The holding fixture is capable of precisely inverting the device without changing the effective c.g. It is imperative that all the dynamic responses stay the same in both positions. If the accelerometer output responses are small enough, a subtraction between up and down leave a detectable residual which is the cross axis component. The present holding fixture is shown in Figure 6 and Figure 7 which shows the swival inversion process which is a clever way to keep connectors aligned and heat applied to the flange. This can be carefully rotated while the SFIR is in a closed servo loop. FIGURE 8 shows a development of a wind shield to relieve air turbulence around the SFIR and cable.

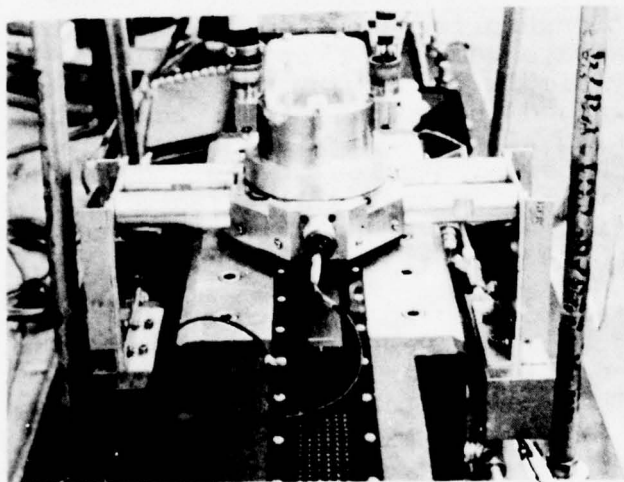


FIGURE 6  
FIXTURE ARRANGEMENT WITH IA  $\uparrow$   
(NOTE: "WINGS" TO BRING DOWN C.G.)

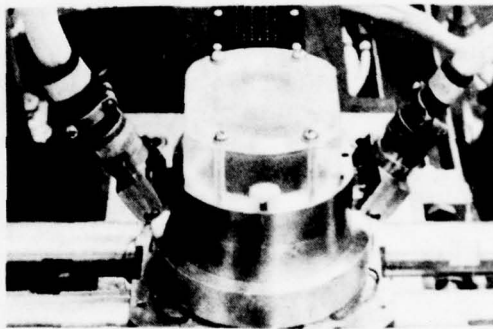


FIGURE 7. FIXTURE CONFIGURATION SHOWING CONNECTOR SWIVALS

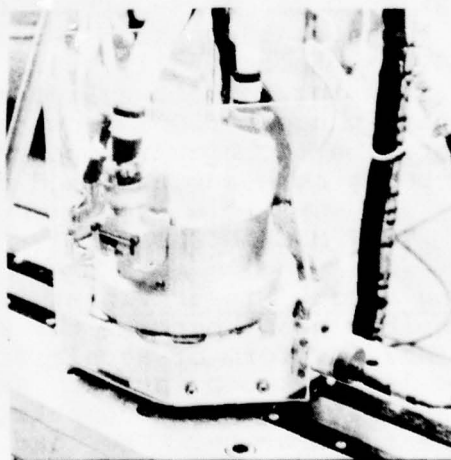


FIGURE 8. FIXTURE WITH WINDSHIELD CONFIGURATION

Two methods are currently used to extract  $F_{X1}$  from test data:

- 1) Solve the relationship

$$\bar{\Delta}A_o = F_{X1} a^2 \text{ (RMS)}$$

where:

$\bar{\Delta}A_o$  = Average change from 0 "g" input

$a_n \text{ (RMS)}$  = RMS Acceleration at n frequency

derivation:

$$\begin{aligned} \bar{\Delta}a_{\text{cross}} &= F_{X1} a_{\text{cross}}^2 \\ &= F_{X1} (a_o \sin wt)^2 \\ &= F_{X1} \left( \frac{2}{\sqrt{2}} a_{\text{rms}} \sin wt \right)^2 \\ &= F_{X1} (2 a_{\text{rms}}^2 \sin^2 wt) \\ \bar{\Delta}a_{\text{cross}} &= \frac{1}{2\pi} \int_0^{2\pi} 2 F_{X1} a_{\text{rms}}^2 \sin^2 wt \, d(wt) \\ &= \frac{1}{2\pi} (2 F_{X1} a_{\text{rms}}^2) \left[ \frac{1}{2} (wt) - \frac{1}{4} \sin 2wt \right]_0^{2\pi} \\ &= F_{X1} a_{\text{rms}}^2 \end{aligned}$$

Acknowledgement: Paul Steranka, CSDL Derivation.

- 2) Fit a 2nd order curve to the data (details in Section IV). This can be done by getting the best fit for  $IA \uparrow$  rate vs g and repeat  $IA \downarrow$  rate vs g and then use simultaneous equations to isolate that part of the 2nd order coefficient which is  $F_{X1}$ . The same technique can be applied with  $\Delta$ rate between up and down.
- 3) A 3rd method is being experimented with and this is to determine the  $\cos 2\theta$  coefficient in a Fourier expansion of the rate data. The 2nd harmonic is proportional to  $F_{X1}$ . This trigonometric relationship is expanded in Section IV.

Various techniques will be applied to determine the true acceleration harmonic content of the input waveform and also the true RMS of the waveform. A planned use of a SFIR to record very precise acceleration waveform measurements for computer processing

is a unique instrumentation application of a SFIR.

At the low planned test frequencies, frequency sensitivity is not expected. However, a series of tests are planned to see if there is such a response. The steady state acceleration will be determined by extrapolating back to 0 Hz from the responses obtained from constant "g" and variable frequency testing.

The readout from the SFIR will be obtained both from integral time increments over revolutions of the servo driven member (SDM) and from incremented angle changes (whole angle) of the SDM. The calculation and computer processing for rate data is as follows:

1) Time interval data:  $\frac{10 \text{ Rev}}{\text{time}} = \frac{62.83185307}{t} \frac{\text{rad}}{\text{sec}} c\omega$

and  $\Delta\omega$  rate in  $\mu\text{rad} = \mu g$

The 10 rev. data will be the average of at least 15 intervals or in reality 150 rev. data. The data collection is in 10 rev. to study the data for trend or unusual behavior within 10 rev. intervals.

2) Whole angle data:  $\frac{\Delta\theta}{t \text{ (fixed)}} \frac{\text{rad}}{\text{sec}}$

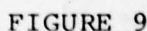
t will be fixed by set strobe rates controlled by the station clock. The rates will be 12.5, 25, 50 or 100 Hz, depending on the development of the test techniques for recording 2 SFIR's simultaneously.

The first method involves a counter and has been for years the easiest and standard method for obtaining well filtered readout data to detect small changes over a long period. The counter is triggered by zero crossings from the SFIR resolver processor in the test station. The 2nd method is the same as the system readout which is a digital angular output indicating SDM position. It differs from the system in that the station can strobe at higher and different frequencies which is varied for wave analysis. The advantages of the whole angle data are its high resolution characteristics, which allows following the SDM over vibrating partial revolutions at low "g" (using a SFIR for an indication instrument), utilizing computer filtering techniques and the elimination of counter triggering as a source of error.

A new evaluation technique for determining the validity of the test results utilizes a recently configured HP noise measurement test system. With software development, it can determine the



with explanation is shown in Figure 9 and the CRT display of the spectrum analyzer in Figure 11. The CRT shows a high vertical response to the 2nd harmonic at a horizontal driven acceleration of 18 Hz. Figure 10 shows the front of this key item in the measurement loop.



### BLOCK DIAGRAM OF NOISE MEASUREMENT TEST SYSTEM

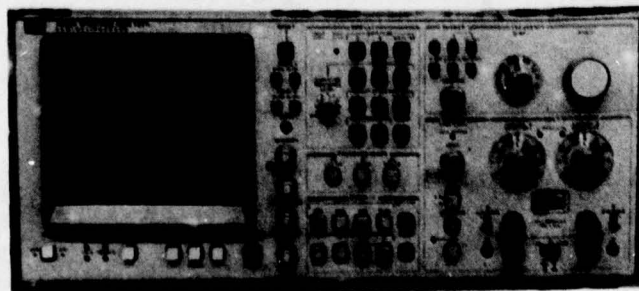


FIGURE 10  
FRONT CONTROLS AND CRT  
OF SPECTRUM ANALYZER

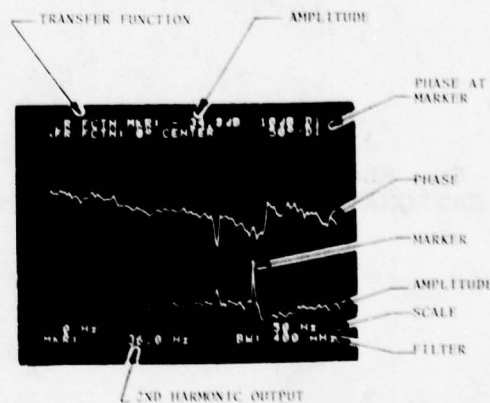


FIGURE 11

CRT DISPLAY OF  
SPECTRUM ANALYZER

#### IV. TECHNICAL APPROACH

##### 1. Model

Figure 12 shows why the cross axis effect produces a 2nd order error term.

The general model out to a 3rd order is developed from the vector diagram in Figure 13 below for a earth base system.

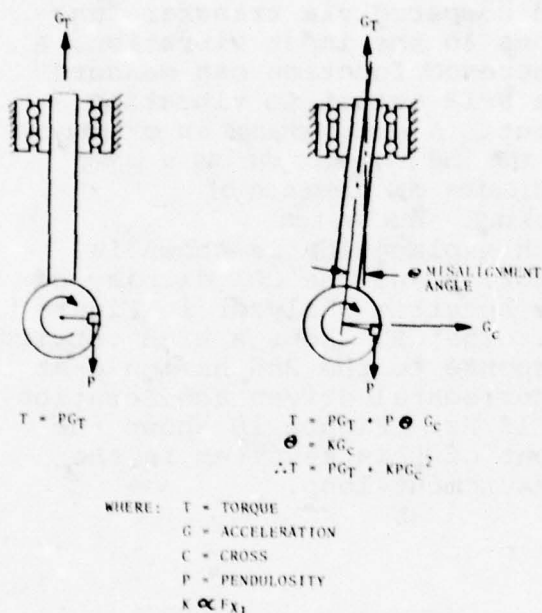


FIGURE 12

$FX_1$  MECHANIZATION SHOWING  
RATIONALE FOR SQUARED EFFECTS

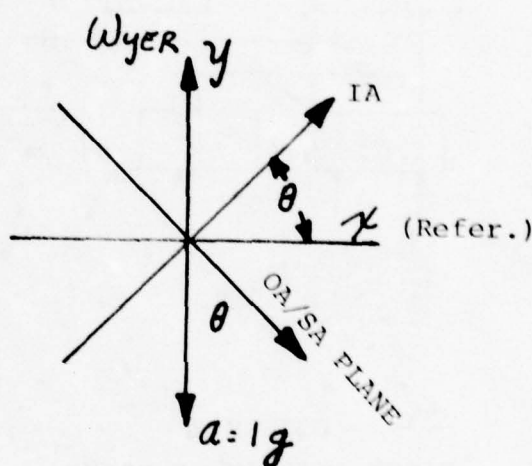


FIGURE 13

CONVENTIONS FOR  
GENERAL EQUATIONS

$$\omega_{SDM} = SF \left[ B + \left[ a - \frac{\omega_{YER}}{SF} \right] \sin \theta + FI_1 a^2 \sin^2 \theta + \right. \\ \left. FX_1 a^2 \cos^2 \theta + FI_2 a^3 \sin^3 \theta + FX_2 a^3 \cos^3 \theta \right]$$

where:

- $\omega_{SDM}$  = Rate of Servo Driven Member in rad/sec
- $\beta$  = Bias term ug
- SF = Scale Factor rad/sec/g
- $FI_1$  = 2nd Order response of acceleration in IA ( $\mu g/g^2$ )
- $\omega_{YER}$  = Vertical component of earth rate ( $\mu$ rad/sec)

$F_{X1}$  = 2nd Order response of acceleration into  
OA/SA plane (cross axis effect) ( $\mu g/g^2$ )

$F_{X2}$  &  $F_{I2}$  = Higher order responses ( $\mu g/g^3$ )

The interdependence of  $F_{X1}$  and  $F_{I1}$  is shown in the following identities:

$$F_{I1} a_x^2 \sin^2 \theta = F_{I1} a_x^2 \frac{1 - \cos 2\theta}{2}$$

$$F_{X1} a_x^2 \cos^2 \theta = F_{X1} a_x^2 \frac{1 + \cos 2\theta}{2}$$

This opens up another possibility of deriving  $F_{X1}$  since in the vibration position  $F_{I1} a_x^2$  is negligible. Through wave analysis, the 2nd Harmonic can be determined using a technique of synchronizing the fundamental whole angle strobe to the vibration frequency and developing a sliding window technique to generate enough whole angle data to determine the harmonics in the SFIR output. This technique is under consideration at present.

## 2. Current Analysis Technique

The most frequently used data analysis technique using the model equation involves fitting a quadratic to the rate vs g data and evaluating for a good correlation coefficient. A response that will show up in 2nd order effects along with  $F_{X1}$  is rocking of the SFIR around a horizontal axis. Fortunately, this changes sign with 180° change in orientation, i.e.,  $IA \uparrow$  to  $IA \downarrow$ . Simplifying the general equation out to the 2nd order shows this relationship ( $F_{I1}$  is negligible in the vibration cross axis orientation). Figure 14 shows the vibration orientation and case rocking motion of concern.

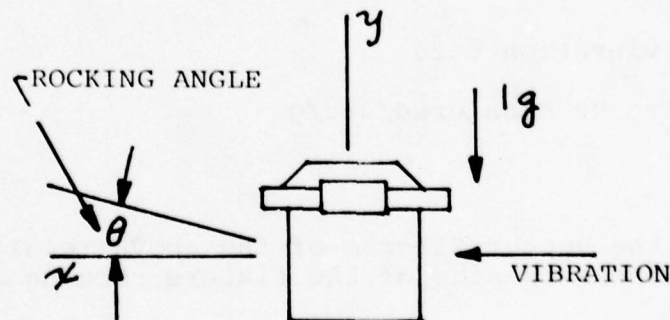


FIGURE 14

BASIC VIBRATION ORIENTATION WITH FIXTURE/SLAB ROCKING MOTION



$$W_n = SF \left[ B + a_y - a_x^2 (FX_1 - FR_1) \right]$$

$$-W_n = SF \left[ B - a_y + a_x^2 (FX_1 + FR_1) \right]$$

where:  $W_n$  = SDM rate urad/sec @ n vibration frequency

$a_y$  = Normal 1st order acceleration (lg) into IA

SF = Scale factor of SFIR  $\mu$ rad/sec/g

$\beta$  = Bias ( $\mu$ g)

$a_x$  = Cross axis acceleration (g)

$FX_1$  = Cross axis coefficient  $\mu$ rad/sec/g<sup>2</sup>

$FR_1$  = Rocking coefficient  $\mu$ rad/sec/g<sup>2</sup> (instrumentation effect)

$$\Delta W \uparrow = W_{O \uparrow} - [\beta_o + a_y] SF + a_x^2 [FX_1 - FR_1] SF$$

$$\Delta W \downarrow = W_{O \downarrow} - [\beta_o - a_y] SF + a_x^2 [FX_1 + FR_1] SF$$

$$FX_1 = \frac{\Delta W \uparrow + \Delta W \downarrow}{2 a_x^2}$$

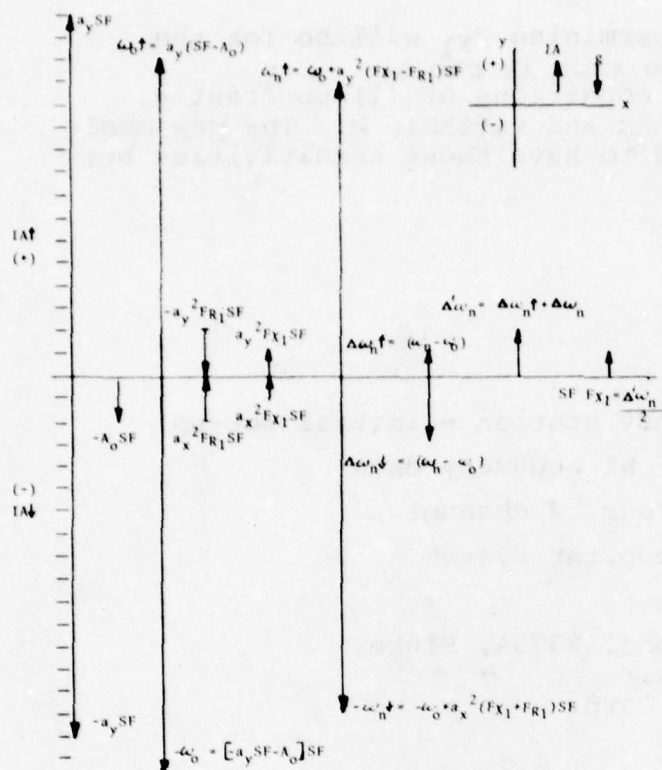
$$FR_1 = \frac{\Delta W \downarrow - \Delta W \uparrow}{2 a_x^2}$$

where:

$W_o$  = 0 vibration rate

$\beta_o$  = zero Hz bias  $\mu$ rad/sec/g

Figure 15 shows the vector diagram of the above relationships.  
Figure 16 shows the mechanics of the fixture rocking and  $FX_1$ .



Note: Values for terms through  $\omega_n^2$  treat as (+) and assign (-) for  $IA \downarrow$

FIGURE 15

VECTOR REPRESENTATION OF  
SFIR MODEL  $-F_{X1}$  DETERMINATION

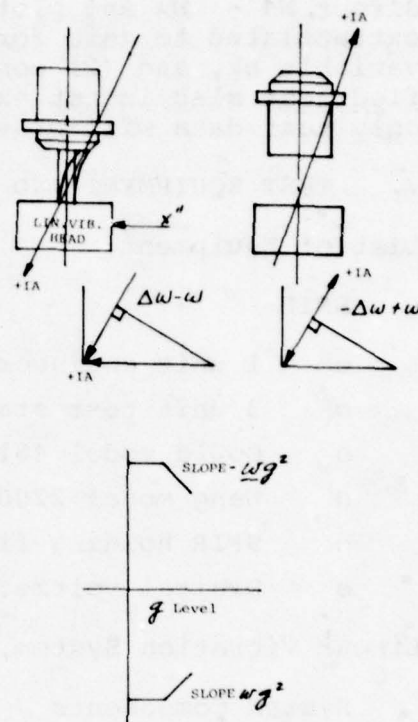


FIGURE 16

MECHANICS OF ROCKING MOTION

Curve fitting is done for the rate up where the power series coefficients are determined out to the 2nd order, i.e.:

$$W \uparrow = \beta + K_1 a_y + K_2 a_x^2$$

$$W \downarrow = \beta - K_1 a_y + K_2' a_x^2$$

where:

$$K_2 = F_{X1} - F_{R1}$$

$$K_2' = F_{X1} + F_{R1}$$

The above is solved simultaneously for  $F_{X1}$ . Another way of processing the rate data which should produce the same  $F_{X1}$  is to fit a curve to the  $\Delta$ rate from  $IA \uparrow$  to  $IA \downarrow$ . This automatically drops out the steady state and rocking terms and leaves just the 2nd order component plus residuals.

The other direct method of determining  $F_{X1}$  will be for the direct  $W\uparrow - W\downarrow$  and plot  $F_{X1}$  so that it can be extrapolated to zero for both conditions of (1) constant  $g$ , variable  $Hz$ , and (2) constant  $Hz$  and variable  $g$ . The new modified test slab is not expected to have these sensitivities but only test data will prove it.

#### V. TEST EQUIPMENT AND SET-UP

##### List of Equipment:

###### SFIR

- o 1 unit engineering test station - initial set-up
- o 3 unit test station - hi accuracy data
- o Gould model 481 recorder, 8 channel
- o Wang model 2200 VP computer system
- o SFIR holding fixtures
- o Digital voltmeter, model 8375A, Fluke

##### Linear Vibration System, Team Corp.

###### System Components

- o Hydrostatic bearing table, Team Corp. Model 1528
- o Hydraulic power supply, Team Corp. Model HPS 140LP

###### Control Console Components

- o Power amplifier panel, Team Corp. Model 1528
- o Digital servo display panel, Team Corp. Model 1564
- o Servo controller panel, Team Corp. Model 1522
- o Control panel, Team Corp. 1510
- o Oscillator panel, Kron-Hite Model 4025 AR
- o Oscilloscope panel, H-P Model 122AR

##### Accelerometer Pick-Off

- o Servo accelerometer, Kistler, Control Model 305B - horizontal
- o Thermal converter, HP 11049A
- o MX/SFIR used as instrumentation accelerometer
- o Sytron Donner - Vertical

##### Noise Measurement Test System

- o Components listed on Figure 7.



## VI. TEST PROCEDURES

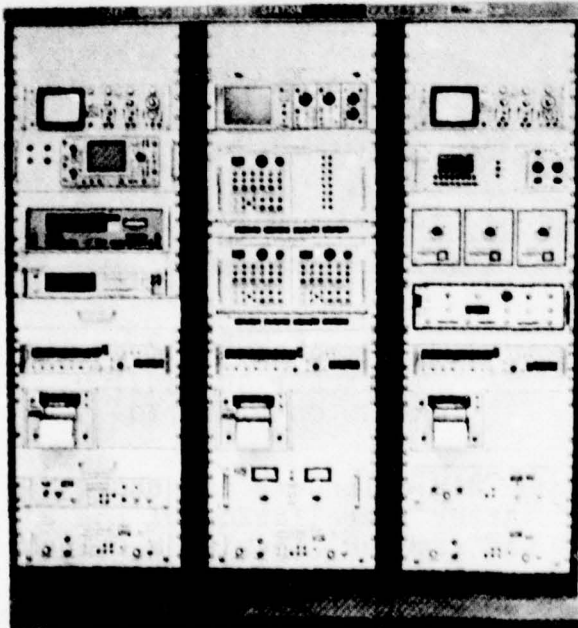
The basic test sequence is summarized in this section. The primary data is SFIR rate output in either the IA up (') or IA down (.) positions. Initially data will be taken without vibration as a reference, after which a vibration sequence will be applied. Initially the rate output will be recorded in time interval units but eventually whole angle readout will be used for harmonic analysis.

It is important that the data generation is with a well stabilized unit both thermally and dynamically. A minimum of 15 minutes of data should be taken at each g level. For time interval data the device itself integrates out the noise and produces an average rate over about 50 revolutions of the SDM. For whole angle data there will be 11,250 to 90,000 data points, depending on a strobe rate of 12.5 to 100/sec. This high resolution will allow computer smoothing and wave analysis.

The procedure beyond collecting data is not further defined at this point for the operation is in a highly developmental status. The data processing, frequency, g levels, test configuration will be adjusted as the experiment continues.

The SFIR test station initially used in the vibration facility was a MPMS one modified to MX design. This was considered adequate for set-up and scoping the problems. The precision data will be taken with the new 3 Unit SFIR Test Station (3USTS), which is capable of multiple unit testing. It has whole angle readout

capability along with other features which are the same as the system, i.e., straw-man servo, and resolver processor. This station is shown in Figure 17.



It is planned to use this station to run 2 SFIRs simultaneously recording the high resolution whole angle outputs. One SFIR will be the specimen and the other will record the input acceleration.

FIGURE 17

3USTS TEST STATION

## VII. PROBLEMS

The measured rocking resonant modes were the major problems in the first series of tests. Due to the large amplitudes, they produced the classical problem in analysis of trying to take a difference between two large numbers to produce a small reliable remainder. There were also vertical displacements along the IA but these did not influence the data except for exciting  $F_{I1}$  a negligible amount. The rocking modes peaked up all through the 5-20 Hz range and this was traced to the uneven interface of the slab to the sub-floor. Calculations were made to design a different suspension system. A massive steel bracket support system was designed which calculated to put the resonance beyond 50 Hz. Figure 18 shows an outline drawing of the test slab configuration with the bracket modification and Figure 19 is a photograph of the actual installation of the brackets.

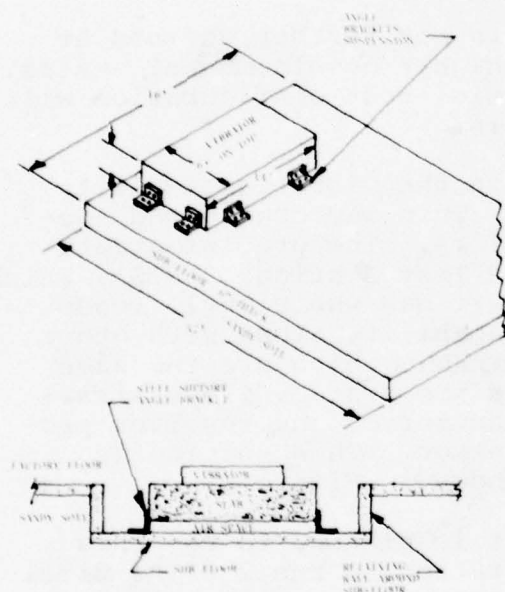


FIGURE 18  
MODIFIED SLAB  
CONFIGURATION

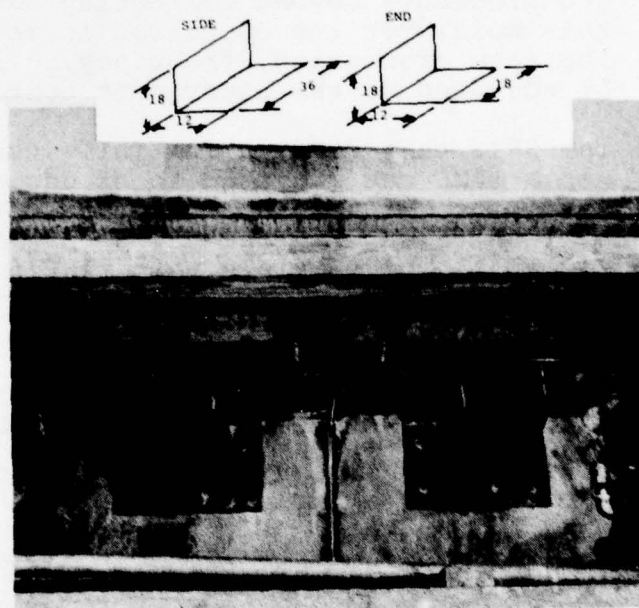


FIGURE 19  
BRACKET SUSPENSION  
DESIGN ON VIBRATION SLAB

The slab was originally supported on air cylinders and these were activated to raise the slab. After installation of the 8 large iron brackets, the pressure was removed, leaving a 6-inch air gap to the floor. The brackets will act as very stiff members putting the response of the slab beyond the 1-20 Hz frequency of concern in this test. The technique is acceptable since only short term slab stability is important.

There was concern for rocking within the vibrator bearing gap and the holding fixture itself so a modification was made to the fixture to add wings to put weight below the vibrator bearing center line, which was calculated to put the fixture C.G. along the center line (reference Figure 6). Experience shows that this did not significantly improve the rocking phenomenon which was mostly due to slab mounting. The rationale, however, for getting the fixture C.G. along the center line is a good idea.

Determining the test slab and fixturing responses was a problem until the rental of the HP spectrum analyzer #3582A which is a powerful tool for evaluating dynamic phenomenon. This instrument allowed the determination of coherent functions between the Kilser driving accelerometer and the Systron Donner used for a pick-up sensor in the vertical axis. Other crystal accelerometers that were calibrated against vibration pick-off standards were used to sort the difference between the rocking and translational motions. The analyzer is now being used in the development of the noise measurement system, which will make the next slab evaluation very automatic and easier to evaluate.

The cables whipping around under high "g" were a concern because of the SFIR connector bracket putting torques on the SFIR housing. Changes were made for transferring this loading to the mounting plate. The real solution will lie with plans to go to slip contacts and avoid all the problems with fixed cabling. Since the machine produces such large forces, putting a heavy pre-load for continuous continuity will be no problem.

#### VIII. CURRENT PLANS

1. Finish the modification to the present test base slab and run a slab dynamic evaluation test. The basic objective is to get the resonant rocking modes beyond the 1-20 Hz test program frequency operation range.
2. Test several SFIRs during August 1979 and evaluate the results in all the ways previously mentioned. Run correlation tests between input harmonics and SFIR output responses and remove from the output the  $\cos 2\theta$  contribution from the input.
3. Compare  $Fx_1$  vibration derived coefficient from those obtained from precision step tumbling tests now in progress in Honeywell's automatic computer controlled dividing head. The quality of the tumbling data looks good. Although the potential accuracy of the linear vibration technique is greater than tumbling, at this point in the development cycle, it would be significant for a favorable comparison. The coefficients will also be compared to an analytical calculation based on measured SDM bearing compliances.



4. All of the above items will be reported on during the presentation at the 9th Biennial Symposium in a classified session.

#### IX. FUTURE PLANS

1. The vibration facility will be moved to another building in two months so that the experiments and modification to the present slab will be reflected in a new design that is expected to be stable enough to get more precise  $F_{x1}$  data. The basic objective will be the same, to get the dynamic responses significantly above 20 Hz. This could involve I beams incased in the concrete tying the suspension angle brackets to the slab, jacks tying the slab top to the factory floor, thick retaining walls, and perhaps, a hollow stiff slab construction.
2. Design a saddle fixture to put the C.G. of a 2 SFIR (IA up and IA horizontal) fixture right along the center line of the vibrator bearing. The vertical mount will be designed to be rotatable without opening the SFIR servo loop and still keeping the same C.G. The horizontal SFIR will be used to very accurately determine the input acceleration and the whole angle will be processed to determine the harmonics in the waveform. Using the SFIR as a facility accelerometer is many times more accurate than any other vibration detector. A simplified drawing of this fixture is in Figure 20.

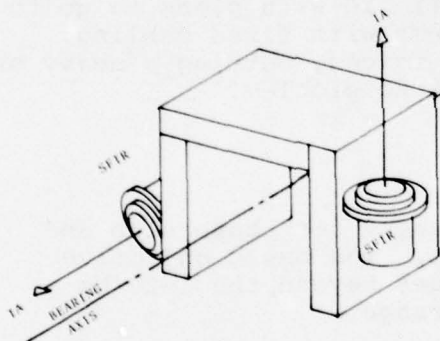


FIGURE 20. SADDLE FIXTURE

3. Complete the slip contacts design to eliminate cable whip disturbances getting to the test specimens.

4. The  $F_{x1}$  test will eventually be considered for inclusion in the ATP to replace the  $F_{I1}$  test. The whole  $F_{I1}$  test procedure is under extensive study as to its validity and could be in trouble to define the parameter to system requirements. If  $F_{x1}$  testing is perfected as planned, the  $F_{I1}$  measurement concerns loses its significance since only one of the parameters need be known from factory calibration.

#### ACKNOWLEDGEMENT:

This project was sponsored by the USAF Space and Missile Systems Organization under Contract F04704-78-C-0005, and was conducted under the direction of Project Officer, Capt. K. R. Wernle.

TITLE: AN EVALUATION OF SENSOR  
FAULT DETECTION AND  
IDENTIFICATION ALGORITHMS  
FOR IMPROVED UTILIZATION  
OF TETRAD CONFIGURED  
STRAPDOWN INS

AUTHORS: RONALD J. HRUBY  
Ames Research Center  
Moffett Field, CA 94035

WILLIAM S. BJORKMAN  
Analytical Mechanics Associates  
Mountain View, AC

RALPH A. CARESTIA  
University of Southern Colorado  
Pueblo, CO 81001

310

AN EVALUATION OF SENSOR FAULT DETECTION AND IDENTIFICATION  
ALGORITHMS FOR IMPROVED UTILIZATION OF  
TETRAD CONFIGURED STRAPDOWN INS

Ronald J. Hruby, William S. Bjorkman\*  
and Ralph A. Carestia\*\*

Ames Research Center

SUMMARY

A tetrad configured strapdown inertial system, which has a minimum of redundancy, can provide a fail-operate redundancy for increased reliability if a sensor failure can be detected and identified. A failure detection and two failure identification algorithms previously tested using wheel gyro tetrad test data are evaluated using test data from a laser gyro tetrad inertial system flown on a UH-1H helicopter and tested on a real time 3-axis motion simulator facility. The performance of the algorithms for step failures when the tetrad is subjected to extraneous oscillatory motion is presented.

\* Analytical Mechanics Associates, Mountain View, California

\*\* University of Southern Colorado, Pueblo, Colorado



## INTRODUCTION

Multiple redundant navigation units are provided in many current commercial and military aircraft in an effort to increase the overall reliability, which of course increases the overall system costs. In reference 1, it is shown that for a laser gyro strapdown system, where individual components, e.g., gyros, accelerometers, are replicated rather than replicating complete navigation systems, it was possible to decrease the cost while maintaining a high level of reliability. The lowest cost can be achieved by using a redundant strapdown system with the least number of operating components. A number of research investigations have been conducted on redundancy management techniques that will minimize the number of sensors required for a given level of reliability. In reference 2, redundancy management techniques were analyzed for 4 (tetrad), 5 (pentad), and 6 (hexad) sensor strapdown systems. These results indicated that fail-operate performance (i.e., continuing to operate with no loss in performance after a gyro failure) was possible as long as five or more sensors were still functional. However, with four sensors functional, only a fail-safe capability was available because the failed sensor could not be identified although it could be detected. The tetrad redundancy management problem was specifically addressed in reference 3. In that study, a failure detection and two failure identification algorithms were developed. As a first step in this evaluation, the algorithms were tested using laboratory data taken from single degree of freedom wheel gyros in a strapdown tetrad configuration that had step failures imposed on it. The results, though encouraging, were limited by the performance of the obsolescent gyros used in the tests. The second step, and the objective of this study was the evaluation of the detection and failure identification algorithms presented in reference 3 using step failures with data measured from a laser gyro tetrad system.

The ring laser gyro tetrad system was of the ortho-skew type (see figure 1) where one sensor is skewed with respect to the three orthogonal sensors, forming equal angles (about 54.735 degrees) with each of the orthogonal sensor's axes. The experimental evaluation was limited to step-type uncompensated bias shifts (step-failures). The ability of the algorithms to detect and identify sensors which have undergone a step failure is a necessary, but not sufficient, condition for their application to aircraft guidance and navigation systems. The performance of the algorithms was evaluated using tetrad sensor data recorded during straight and curved flight paths of a UH-1H research helicopter and sensor data recorded one and two axis sinusoidal motion induced by a three-axis motion simulator. The failure detection and identification results presented in this paper are restricted to gyro failures. Accelerometer failure detection and identification is entirely analogous to that for gyros.

## TETRAD FAILURE DETECTION AND SENSOR IDENTIFICATION ALGORITHMS

The failure detection and identification algorithms for the tetrad strap-down inertial sensor system must detect that a sensor failure has occurred, identify it without error, and remove it from the computational stream. In the ortho-skew configuration, the output of any one sensor can be formulated as a linear combination of the outputs of the other three sensors. This relationship is called parity. Since normal instrument errors and output quantization cause this relationship to be imperfect, a parity residual is defined, (see Appendix A for this development) which takes on a small range of values during normal operation. A failure is indicated when the parity residual exceeds its normal range.

Figure 2 illustrates the failure detection procedure. Time is defined in digital data frames where each data frame  $\Delta$  is  $1/40$  of a second. The output measurement of each instrument is observed as counts where each count has the value  $q$ , which is the gyro quantization. In this paper,  $q$  is  $1.57$  arc-seconds and every measurement readout is in an integer number of counts. A nondestructive readout is used so that any remaining fraction of a count is not lost but is added into the counts for the next time interval. Prior to the failure, figure 2a, the parity residual is computed for each set of four sensor measurements and is summed over a moving window (defined as the parity sum) consisting of a selected number of data frames ( $\tau_d$ ) for comparison with the parity residual detection threshold. The effect on the parity sum of a step change as might result from a sensor failure is shown in figure 2b. The parity residual sum increases in magnitude as a result of the step-change failure, then levels out because the parity residual is summed over only the most recent  $\tau_d$  data frames. If the failure is severe enough to cause the parity residual sum to exceed the detection threshold, the detection logic indicates a failure to the system.

Two failed sensor identification algorithms were investigated, each using prediction in its computation. These algorithms, called the pseudo sensor (PS) algorithm and the constrained fit (CF) algorithm, are complementary. The PS algorithm predicts what a fifth (or pseudo) sensor's output would be, based on the recent past values of all four real sensors. The CF algorithm predicts a sensor's output based on recent past values, but constrained to the other three sensor's output by a parity residual condition placed on the coefficients used for fitting a predictive curve through the recent past values of the sensor's output.

The pseudo sensor failed sensor identification strategy is shown in figure 3. Prior to failure, the pseudo sensor's output is computed from the output of the four real sensors. After a failure is detected, stored past values of the pseudo-sensor's output are used in a least squares fit to predict its future value. This is accomplished over the fit interval  $\tau_f$ . The failure identification interval is  $\tau_i$ , and the situation shown in figure 3 is for a failure of sensor No. 3, one of the orthogonal sensors. Using the four real sensors plus the pseudo sensor, four parity residuals are summed across the isolation interval  $\tau_1$ . The failure causes three of

these sums, those including the failed sensor, to diverge more dramatically from zero than the sum which does not contain the failed sensor (sensor 3 in the example in figure 3). The magnitude of the smallest sum identifies the failed sensor.

The constrained fit failed sensor identification strategy is shown in figure 4. The constrained fit concept is based on the premise that the difference between a sensor's observed and predicted measurements will be greater for the failed sensor than for any of the unfailed sensors in the isolation period  $\tau_i$ . The four measurement residual sums are shown as functions of time in figure 4 for an assumed failure of sensor No. 3. All sums diverge from zero as the result of prediction errors, but the sum for the sensor 3 diverges more rapidly from zero because it has failed.

The effects of sinusoidal frequency, type of motion, and step failure level on the parity residual when used for initial failure detection are evaluated and presented. In addition, the ability of the CF and PS algorithms to identify faulted sensors is evaluated with respect to frequency of motion and step failure level.



## EVALUATION OF TETRAD ALGORITHMS FOR FAILURE DETECTION AND IDENTIFICATION

### Laser Gyro Sensor Test Environment

As noted previously, the failure detection and identification algorithms were tested using prerecorded experimental data. These data samples were generated on a 3-axis motion simulator and during the flight test of The Laser Gyro Tetrad INS in the UH-1H research aircraft. Data was recorded at approximately 40 Hz. See Appendix B for a description of experimental facilities. The step size introduced for a simulated failure varied between 10 counts (1.57 arcseconds/count) and 1000 counts. Four different test data prerecorded samples were used. Three samples included (1) stationary (constant attitude, no local acceleration), (2) single axis 0.1 Hz, (which appears as a ramping input for the test case selected), and (3) two axes, 2 Hz, sinusoidal motion on the pitch/roll orthogonal axes. The fourth sample consisted of UH-1H helicopter flight test data which exhibited harmonic vibrations, at twice the rotor speed, centered at about 10.5 Hz on all axes.

### Prediction of Sensor Output In Identification Interval

As previously noted in this report, failure identification was based on either the constrained fit algorithm or prediction of the output of a fifth sensor which is accomplished by the pseudo sensor algorithm. Because of aircraft motion the predictions always contain errors. These unavoidable errors can lead to erroneous predictions from the constrained fit or the pseudo sensor algorithms in the identification interval. The prediction errors can be expected to increase with increasing lengths of identification interval and higher harmonic frequency components of the aircraft motion.

Table 1, which utilizes a "least squares error" fit algorithm, presents the worst case RMS prediction error for various identification intervals in frame lengths and for data samples from each of the four test environments. Table 1 prediction error data applies to the pseudo sensor and constrained fit algorithms and is presented as a function of the frequency of motion, fit interval, and identification interval for both the linear and parabolic fit orders. Each count represents an attitude change of 1.57 arc-sec, in 1/40 of a second or an equivalent angular rate of  $64^{\circ}/\text{hr}$ . When the prediction error exceeds 30 counts it is defined as a false alarm. The stationary case has the least error. The prediction error increases with increases in the identification interval and as the frequency of motion increases. For example, for the flight test case, a false alarm may occur for identification interval lengths of one frame or greater for either fit order.

The data from Table 1 is plotted in Figure 5 for a 4 frame fit interval and a 3 frame identification interval as a function of frequency. It illustrates the rapid divergence of the prediction error for increasing frequency of motion and suggests that false alarms would occur

for frequencies greater than about 0.30 Hz for the linear fit case and about 0.15 Hz for the parabolic fit case.

#### Failure Detection

A failure condition is indicated when the sum of the parity residuals equals or exceeds the threshold (see Appendix A, equation 10). For example, if the detection threshold was set at 5 counts then a step failure of 2 counts in the skew sensor would cause a failure indication in three data frames because the moving window sum would be 6 counts (which exceeds 5 counts by one). This detection threshold must be high enough to exclude "false alarms" yet low enough to trigger on small but significant failures. For the algorithms used in this study, much smaller failures can be detected than it is possible to isolate. The performance of the failure detection algorithm is shown in Tables 2 and 3 for the four different motion environments already described for Table 1. Table 2 presents the number of data frames which were required to detect various step-failure levels in an orthogonal gyro (the roll gyro) with a  $1/\sqrt{3}$  coefficient in the parity equation when a step failure is introduced sequentially at each of 80 data frames. Table 3 presents the same data for a skew gyro, which has a unit coefficient in the parity equation. The RMS parity residual noise in the four motion environments ranged up to 2.0 counts per data frame. A random count will add or subtract to the ramping input of the detection algorithm causing longer and shorter detection times. False alarms are clearly indicated in the flight data ( $\sim 10.5$  Hz) by the presence of "detected" faults in frame 1 for a step level of 10 counts. A comparison of the results presented in Tables 2 and 3 show the detection algorithm is more sensitive to a failure in the skew gyro than an orthogonal gyro. The increased sensitivity is due to the skew gyro's unit coefficient in the parity equation.

#### Pseudo Sensor Identification Algorithm

The pseudo sensor identification algorithm was evaluated in a stationary, 0.1 Hz, 2 Hz, and UH-1H flight test ( $\sim 10.5$  Hz) motion environment. Step failures ranging from 10 counts to 1000 counts at 80 sequential times (maximum allowed by computer processing) in each sensor for each motion environment were inserted in the recorded data. This represents 320 test cases for the fit type, fit interval, motion frequencies and step levels considered. The results of successful faulted sensor identifications using linear and parabolic fits are shown in table 4 for the pseudo sensor algorithm with 5 and 7 points in the fit interval as a function of step failure level. The stationary case and the 0.1 Hz case show the best results using a linear fit and a 7 point fit interval. The parabolic fit, table 4, shows that success increases with increasing step failure levels.

Figure 6 plots the pseudo sensor identification error as a function of frequency using linear fit versus step failure level in counts for 5 points in the fit interval. Figure 7 shows the error using a parabolic

fit as a function of motion frequency. Clearly the data in both figures illustrate that the pseudo sensor algorithm performance decreases with increasing frequency for both linear and parabolic fits. Comparison between linear and parabolic fit pseudo sensor errors shows better linear fit performance for the stationary, 0.1 Hz, and 10.5 Hz test frequencies. Parabolic fit results are more favorable at 2 Hz. The low relative success rate at these higher frequencies (2 Hz and ~10.5 Hz) is directly related to the occurrence of the prediction errors illustrated in table 1, which shows increasing errors with increasing frequency. The UH-1H flight test data showed the lowest success rate. It combined stationary, ramping, and approximately 10.5 Hz non-random oscillatory motion in three axes. The parabolic fit can be improved for the stationary and 0.1 Hz frequency case by using more points in the fit interval. The apparent anomaly (table 4) of slightly more success at 2 Hz for the parabolic fit than the linear fit is explained by the parabolic prediction error being small for parabolic like motion (2 Hz sinewaves) but large for ramp like motion (0.1 Hz or less).

#### Constrained Fit Identification Algorithm

The constrained fit algorithm was also evaluated in a stationary, 0.1 Hz, 2 Hz, and UH-1H flight test (~10.5 Hz) motion environment in a manner identical to the pseudo sensor algorithm, and the results of successful identifications using linear and parabolic fits for the constrained fit algorithm are presented in table 5. Figure 8 plots the constrained fit error as a function of frequency, with 5 points in the fit interval, using a linear fit versus step failure level in counts. Figure 9 plots the error for a parabolic fit as a function of frequency. Comparison of the identification error data of figure 8 and figure 9 shows that the linear fit is better than the parabolic fit for the stationary, 0.1 Hz, and 10.5 Hz motion environment but the parabolic fit is better at 2 Hz, and table 5 shows that it can be improved with more points in the fit interval. The results show less error for the stationary and 0.1 Hz case but suggest the occurrence of excessive errors for motion of 2 Hz or 10.5 Hz. These results also correlate with the prediction error data in table 1. Table 5 shows that the parabolic fit is more successful than the linear fit at 2 Hz but less successful at the other motion environments. This apparent anomaly is again explained by the parabolic prediction error being smaller for parabolic like motions (2 Hz sine waves) but larger for ramp-like motions (0.1 Hz or less).

#### Comparison of Parabolic and Linear Fits

The linear fit appears to be the best choice for either the pseudo sensor or constrained fit algorithm. Table 1 clearly shows much smaller prediction errors for the linear fit in a flight test environment. The flight test motion used in this study was better approximated by a series of ramp like motions than sinusoidal motions, and a linear fit has a much smaller prediction error for ramp like motions than a parabolic fit. The 10.5 Hz non-random oscillatory motion from the rotor blade is



not sinusoidal and causes both fit types to produce larger errors without predilection for either fit type.

#### Effects of Sensor Resolution on Identification Algorithm Success

A comparison was made between the success of the identification algorithms when applied to laser gyro data and the success achieved on wheel gyro data (reference 3). Figure 10 shows the results of this comparison. A 95% success rate was achieved for the wheel gyro at failure levels of about  $2500^{\circ}/\text{hr}$ . A 95% success level was achieved for the laser gyro on 0.1 Hz motion (the environment studied in reference 3) at failure levels of about  $1250^{\circ}/\text{hr}$ . The comparison should not be viewed as strictly quantitative because of differences in sampling rates between the two inertial sensor systems and differences in test conditions. The results indicate that with the finer resolution of the laser gyros, the minimum step failure level at which a faulted sensor can be identified can be reduced by a factor of about two.

#### CONCLUDING REMARKS

The experimental evaluation of the failure detection algorithms showed a capability to detect all sensor step failures greater than 100 counts (approximately  $1.78^{\circ}/\text{second}$ ) within two data frames (approximately 50 ms) in the identification interval for all test conditions. As a point of reference, the values used for the failure detection threshold in commercial aircraft redundant sensor systems range from about 30 counts to 90 counts.

Both the constrained fit and the psuedo sensor "failed sensor" identification algorithm performances deteriorate with increasing frequency and decreasing step level. The performance deterioration was pronounced for the data from the UH-1H helicopter environment which has a two-per-revolution rotor blade non-random vibration of approximately 10.5 Hz. Using the preceding threshold criteria for failure identification, the performances of both of the failed sensor identification algorithms need to be improved for the helicopter environment.

## APPENDIX A

### TETRAD FAILURE DETECTION AND SENSOR IDENTIFICATION ALGORITHMS DEVELOPMENT

#### Symbol and Variable Conventions

The tetrad reference frame is orthonormal and corresponds to the edges of the box containing the tetrad instrument package. The orthogonal sensor's input axes are (neglecting misalignments) parallel to the axes of the tetrad reference frame. The transformation of coordinates to the tetrad frame from the current body reference frame, in which the tetrad instrument package is mounted, will be denoted  ${}^t_b T$ .

Let  $u_i$  represent a unit vector along the input axis of the  $i^{\text{th}}$  sensor. This vector will be denoted  ${}^t u_i$  when it is expressed in tetrad frame components and  ${}^b u_i$  in the body frame ( ${}^b u_i = {}^b T {}^t u_i$ ). The tetrad frame components of the four sensor axes are denoted by the  $3 \times 4$  matrix,  ${}^t U$ .

$${}^t U = ({}^t u_1 \quad {}^t u_2 \quad {}^t u_3 \quad {}^t u_4) = \begin{pmatrix} 1 & 0 & 0 & \cos \eta \\ 0 & 1 & 0 & \cos \eta \\ 0 & 0 & 1 & \cos \eta \end{pmatrix} \quad (1)$$

The right-most terms are true for the ortho-skew configuration. The angle  $\eta$  is the angle between the skewed sensor's (sensor No. 4) input axis and the axes of each of the orthogonal sensors. The body-frame components of the four sensor axes are:

$${}^b U = ({}^b u_1 \quad {}^b u_2 \quad {}^b u_3 \quad {}^b u_4) = {}^b T {}^t U \quad (2)$$

The sensing-axis unit vectors can be written as a linear combination of the other three. In particular,

$$u_4 = \alpha u_1 + \beta u_2 + \gamma u_3 \quad (3)$$

### Measurement Model

The sensors used in this paper are of the integrating type so that the output measurement is the integral of the sensed input over the sampling time interval,  $\Delta$ .

A gyro, whose sensing axis is  $u_i$ , senses the component of the angular velocity  $\Omega$  which lies along  $u_i$ . More generally, the gyro's measured output is a scaled version of  $u_i \Omega$  which includes bias, quantization, and other effects. The gyro measurement model adopted for this paper is

$$\Delta \theta_i(t) = \left\{ \int_{t-\Delta}^t (b_i + S_i \Omega) d\tau + \tilde{q}_i + \tilde{r}_i \right\} \quad (4)$$

In these equations the notation " $\{ \}$ " means "integer part of,"  $b_i$  is bias,  $S_i$  is the laser gyro's scale factor and compensation vector,  $\tilde{q}_i$  is a quantization error, and  $\tilde{r}_i$  is random error. The quantities  $b_i$  and  $S_i$  are estimated for each sensor from their calibration data. The four gyro outputs are then used to compute an estimate  $\Omega$ . The generic notation used in this paper, where  $m_i$  is the estimated output of the  $i^{\text{th}}$  sensor for phenomenological input vector  $p$ .

The equation

$$m_i = u_i \int p d\tau \quad (5)$$

illustrates, approximately, the relationship between the input ( $p$ ) and sensor's output ( $m_i$ ).

### Transformation to Orthogonal Triad Reference Coordinates

For aircraft sensor measurements to be useful in aircraft guidance and navigation, they must first be transformed from the tetrad reference frame into equivalent orthogonal triad components relative to the aircraft body reference frame.

A least-squares procedure is used in the transformation. See reference 3 for this procedure.



## Failure Detection by Parity Residual Sum Divergence

A relationship exists for any tetrad configuration that relates the measurements from the four like sensors:

$$m_4 = \alpha m_1 + \beta m_2 + \gamma m_3 \quad (6)$$

Equation (6), which follows from equations (3) and (5), states that the output of any sensor can be formulated as a linear combination of the outputs of the other three sensors. This relationship is called parity. The coefficients  $\alpha$ ,  $\beta$ ,  $\gamma$  are called parity coefficients. They can be determined from the tetrad's geometrical configuration. For the ortho-skew configuration,

$$\alpha = \beta = \gamma = \cos \eta = 1/\sqrt{3} \quad (7)$$

More generally,

$$\begin{pmatrix} \alpha \\ \beta \\ \gamma \end{pmatrix} = (\hat{u}_1 \ \hat{u}_2 \ \hat{u}_3)^{-1} \hat{u}_4 \quad (8)$$

Equation (6) never strictly holds in practice, hence a tetrad parity residual,  $\epsilon_5$  is defined as follows:

$$\epsilon_5 = m_4 - \alpha m_1 - \beta m_2 - \gamma m_3 \quad (9)$$

Thus,  $\epsilon_5$  is the difference between the observed  $m_4$  and the  $m_4$  computed in equation (6). For a perfect system,  $\epsilon_5$  would always be zero in the absence of failures. Normal instrument errors and output quantization cause the parity residual to take on a small range of values in normal operation. When a failure occurs, the parity residual exceeds its normal range. Thus, single failures can be detected by monitoring  $\epsilon_5$ . In this study, the parity residual is summed over a specified number of sequential data frames in order to detect small but persistent failures. These sequential data frames are collectively called "accumulation interval for detection" or "detection window" and denoted by  $\tau_d$ . The detection threshold  $d$  is the tolerance on the parity sum. A failure is indicated when the magnitude of the parity sum exceeds the detection threshold as shown in (10).

Failure condition:

$$\left| \sum_{\tau_d} \epsilon_5 \right| \geq d \quad (10)$$

The detection threshold and the length of the detection window determine the level of step failure which can be detected.

The parity coefficients are computed from the best estimates of the orientations of the sensors, but the measurements will be made by the sensors in their actual orientations. The differences between the estimated and actual orientations are misalignment errors. The coefficients, computed as in equation (7), depend on the orientations of all four sensors even though the coefficients multiply only three measurements in the parity residual. A bias-compensation error affects the parity residual in proportion to the coefficient it multiplies. That is, a bias error in sensor No. 4 contributes  $-\gamma\delta$  to the parity residual directly, while a bias error,  $\delta$ , in sensor No. 3 contributes  $-\gamma\delta$  to the parity residual. Thus for the ortho-skew configuration, a bias error of one unit in sensor No. 4 is equivalent to a bias error of  $\sqrt{3}$  units in any one of the other three sensors in its effect on the parity residual. Therefore, biases and scale factor compensation errors can cause false alarms. Random measurement errors which have small means and variances relative to the quantization level will not significantly affect the parity sum.

Failure detection in a tetrad inertial sensor unit is a simple operation of calculation of the parity sum from accumulation of the parity residual. When the magnitude of the parity residual sum exceeds the preset detection threshold, a failure is indicated. The minimum level of step error that can be detected is determined by the number of points in the parity residual sum and the size of the detection threshold.

The apparent time frame of failure can be inferred by summing the parity residual backwards from the time of failure detection until this sum exceeds a preset threshold level. This preset threshold is determined from the dynamic characteristics of the tetrad system and is influenced by uncompensated bias and scale factors as well as the sensor quantization. In this study the preset threshold was set at 5 counts.

#### Failed-Sensor Identification Algorithms

A tetrad strap-down inertial system inherently possesses fail-safe capability by virtue of the failure detection capability just discussed. Extension to fail-operational capability requires one or more reliable algorithms for determining which instrument has failed when the failure-detection scheme indicates a failure has occurred. The development of the two failed-sensor identification algorithms used in this study is presented in the following.

Pseudo sensor Algorithm - If a fifth sensor of each type were available (i.e., a pentad configuration) each of five parity residual equations could combine the measurements of four sensors and exclude one sensor. Thus, extra parity residual equations would be used to identify the faulty sensor. If  $\epsilon_i$  is the parity residual excluding  $m_i$ , the parity residual equations would be of the form:

$$\begin{pmatrix} \epsilon_1 \\ \epsilon_2 \\ \epsilon_3 \\ \epsilon_4 \\ \epsilon_5 \end{pmatrix} = \begin{pmatrix} 0 & -a_{12} & -a_{13} & -a_{14} & 1 \\ -a_{21} & 0 & -a_{23} & -a_{24} & 1 \\ -a_{31} & -a_{32} & 0 & -a_{34} & 1 \\ -a_{41} & -a_{42} & -a_{43} & 0 & 1 \\ -a_{51} & -a_{52} & -a_{53} & -a_{54} & 0 \end{pmatrix} \begin{pmatrix} m_1 \\ m_2 \\ m_3 \\ m_4 \\ m_5 \end{pmatrix} \quad (11)$$

In the pseudo sensor algorithm a predicted fifth sensor with output,  $m_5$ , is used in the first four pentad parity residual equations to identify the failed sensor. Correct identification is limited by the ability to predict  $m_5$ . The fifth parity residual ( $\epsilon_5$ ) is used only for detection. The equation for  $\epsilon_5$  excludes  $m_5$  and may be recognized as the tetrad parity residual defined earlier in equation (9). Pentad (five-sensor) failure identification utilizes the five parity residuals,  $\epsilon_i$ . If sensor  $i$  fails,  $\epsilon_i$  will be smaller than any of the other parity residuals because  $m_i$ , the measurement which is in error due to the failure, enters each of the pentad parity residual equations except the equation for  $\epsilon_i$ . Sensor  $i$  is thus identified as the failed sensor.

In the best orientation, the pseudo sensor's axis is skew to any tetrad axis or to the plane of any two tetrad axes.

In the absence of failures (i.e., prior to failure detection in the tetrad configuration), the pseudo sensor's output,  $m_5$ , may be computed from the measurements of the four real sensors:

$$\begin{aligned} m_5 &= b^u_{55} \int \hat{p} d\tau \\ &= c_{51}m_1 + c_{52}m_2 + c_{53}m_3 + c_{54}m_4 \end{aligned} \quad (12)$$



The coefficients in equations (12) are defined by the geometry of the sensing axes of the real sensors and the sensing axis (i.e.,  $b^u_5$ ) chosen for the pseudo sensor.

$$\begin{pmatrix} c_{51} & c_{52} & c_{53} & c_{54} \end{pmatrix} = b^u_5 \begin{pmatrix} b^u & b^u \end{pmatrix}^{-1} \hat{b}^u \quad (13)$$

After a failure is detected, stored past values of  $m_5$  are used in a least-squares fit to obtain polynomial coefficients with which to predict  $m_5$ .

$$m_5(t) = b_{50} + b_{51}(t - t_0) + b_{52}(t - t_0)^2 + \dots + b_{5p}(t - t_0)^p \quad (14)$$

The least-squares fit should be based on recent data, but should not include data taken after the failure occurred. The interval of time between the apparent time of failure and the time of detection is the isolation interval for identification,  $\tau_i$ . The detection window  $\tau_d$  is greater than or equal to the number of points in the backward sum; otherwise, the failure would not have been detected in  $\tau_d$ . An investigation was made to establish appropriate values of the length  $\tau_f$ , of the fit interval and the polynomial order of the fit, using recorded laser gyro data from laboratory motion simulator, and helicopter flight tests. The motion environment included static, low frequency (ramp), high frequency (2 Hz) and flight motion.

Using data from the fit interval to predict the output of the pseudo sensor in the isolation interval  $\tau_i$ , the first four pentad parity residuals, equation (11), are evaluated. These residuals are summed across  $\tau_i$  and the smallest sum in magnitude is identified as corresponding to the failed sensor.

The situation shown in figure 3 is for a failure of sensor No. 3. The failure is detected at time  $t_d$ . The apparent time of failure is shown as four frames earlier, or  $t_d - d_{4\Delta}$ . Pseudo sensor fit coefficients are computed in the fit interval  $\tau_f$  which includes the fit reference time,  $t_0$ . The four pseudo sensor parity residuals,  $\epsilon_i$ , are summed across the identification interval,  $\tau_i$ . The failure causes three of these sums to diverge more dramatically from zero than does  $\Sigma \epsilon_3$ ;  $\Sigma \epsilon_3$  exhibits some divergence, primarily because of prediction error. The rate of divergence of each of the other parity residual sums is approximately proportional to the failure level times the parity coefficient (equation 11) which multiplies  $m_3$ .

In summary, the pseudo sensor algorithm; uses stored  $m_5$  data computed from equation (12) to calculate coefficients of a polynomial<sup>5</sup>(14) for the estimated pseudo sensor output; extrapolates the polynomial to obtain predicted values of  $m_5$  to be used in the pseudo sensor parity residual sum equations (11); evaluates and integrates the pseudo sensor parity residual sums,  $\Sigma \epsilon_i$ , ( $i = 1, 2, 3, 4$ ) over  $\tau_i$ , identifying the failed sensor as the one whose parity residual sum is smallest in absolute value.

The ability of the pseudo sensor algorithm to correctly identify the failed sensor is limited by the ability to predict the output of the pseudo sensor across the isolation interval. The tendency of prediction errors to grow restricts the length of  $\tau_i$ . Prediction errors will cause the four pseudo sensor parity sums,  $\Sigma \epsilon_1$  through  $\Sigma \epsilon_4$ , to diverge from zero, even in the absence of failures. If the prediction errors are adequately minimized, then one of the parity residual sums ( $\Sigma \epsilon_3$  in figure 3) will not diverge as rapidly as the others, thus making failed-sensor identification possible.

The numerical values of the pseudo sensor parity coefficients depend on the tetrad configuration as well as the relative orientation of the pseudo sensor. It is desirable that all the coefficients  $a_{ij}$  be approximately equal in magnitude.

The ortho-skew pseudo sensor algorithm is therefore unavoidably biased toward selecting some sensors as failed over others because the parity residual-sum divergence rates differ for the same failure level.

Constrained Fit Algorithm - The basic idea behind the constrained fit algorithm is that the measurement residual (i.e., difference between a sensor's observed and predicted measurements in the identification interval  $\tau_i$ ) will be greater for the failed sensor than for any of the unfailed sensors. This strategy, therefore, also requires prediction of sensor output readings in the identification time. Data points in the fit interval  $\tau_f$  are used in a constrained polynomial fit for each sensor. The constraint helps to smooth out noise and quantization error in the individual sensor measurements which might corrupt an unconstrained fit to the measurements. The fit constraint also tends to outweigh the effects of failed data which may lie in the fit interval because three unfailed sensors "out-vote" the failed sensor through the constraint. The apparent point of failure and the identification time are determined by summing the parity residual backward from the point of detection as in the pseudo sensor algorithm. The fit intervals ends at the point before the identification interval begins.

The predicted output value of the  $i^{\text{th}}$  sensor at time (t) is given by

$$\tilde{m}_i(t) = b_{i0} + b_{i1}(t-t_0) + b_{i2}(t-t_0)^2 + \dots + b_{ip}(t-t_0)^p \quad (15)$$

where the coefficients  $b_{ij}$  are evaluated from measured sensor output data in the fit interval. Equations for the  $b_{ij}$ 's are developed in reference 3.

Equation (15) is used to predict each sensor's output in the identification interval. The residuals  $\delta_i$ , which correspond to the difference between the actual sensor output in the identification interval and that predicted by the polynomial coefficients (see equation (16)),

$$\delta_i = m_i(t) - \hat{m}_i(t) \quad (16)$$

are summed across  $\tau_i$ , leading to a largest (absolute) sum for one of the sensors. The largest residual sum identifies the failed sensor.

Figure 4 illustrates the constrained fit algorithm. The measurement residual sums,  $\sum \delta_i$ , are shown as functions of time in the identification interval,  $\tau_i$ . Three of these sums wander away from zero as a result of prediction errors. The fourth, that of sensor No. 3, is shown to diverge more rapidly away from zero. As with the pseudo sensor algorithm, prediction errors can mask the divergence of relatively small failures and cause mistakes in identification of the failed sensor.



## APPENDIX B

### EXPERIMENTAL FACILITIES USED IN STUDY

The Tetrad FO algorithms were tested with real time laser gyro sensor data. The data was generated in the facility shown in figures 11 and 12 and in the UH-1H helicopter which is shown in figure 13. The helicopter flights consisted of straight path and triangular segments near Moffett Field, while the motion simulator tests included stationary, 0.1 Hz, and 2 Hz sinusoidal motion in one or two axis.

#### Motion Simulator Facility Description

The Motion Simulator Facility was developed at Ames Research Center for testing inertial sensor system concepts applicable to strapdown inertial sensors. The facility includes a three-axis gimballed table; two minicomputers; a dual-floppy disk based microcomputer; two digital magnetic tape recorders; a line printer, and other peripherals required for detailed system testing. An adapter plate was built to allow the laser gyro tetrad inertial sensor assembly (ISA) to be installed on the motion simulator. The simulator with the laser gyro ISA is shown in figure 11. Figure 12 shows the minicomputer facility.

The attitude simulator includes an orthogonal three-axis, hydraulic driven gimballed system controlled by an electro-hydraulic servo whose attitude inputs can be derived from V/STOL flight profiles prerecorded on magnetic tape, or by a function generator with sine wave, triangular wave, or ramp outputs at selected frequencies and rates. Monitoring of gimbal angles is accomplished with high resolution linear inductosyn digital shaft encoders whose angular resolution is 2.5 arc seconds. The table is mounted on a concrete base 1.5 meters (5 ft.) in depth, which is in turn supported by 30.5 meter (100 ft.) pilings.

The data acquisition system, schematically shown in figure 14, consists of six time-division multiplexed channels which are used to transmit both digital and analog angular position information from the gimbal axis. The information from the analog encoders is recorded on an analog recording system, while the data from the digital shaft encoders is displayed and recorded on a digital magnetic tape recorder. The copied and formatted magnetic tape data can be analyzed by the central computer facility at Ames when desired. The data analysis program in the minicomputer perform the following functions: parity error computation, sensor cumulative count averaging, gyro error detection, and a comparison of sensor and shaft encoder angular position information. The output of each program can be displayed on a line printer for quick-look analysis.

Sensor data is processed and transmitted to a digital magnetic tape recorder both in the laboratory and in the aircraft by the two computers in the laser gyro flight test system. One computer is used for navigation and guidance computation while the other computer is used for experiments and data acquisition.

TABLE 1 - Least Square Fit RMS Prediction Error (in counts)

Data Source	Identification Interval (frames)	Fit Interval					
		3 frame		4 frame		5 frame	
		linear	parabolic	linear	parabolic	linear	parabolic
FLIGHT TEST 10.5 Hz 175 counts amplitude	0	31	0	62	14	72	36
	1	205	278	178	315	118	279
	2	321	836	198	760	97	536
	3	302	1508	121	1185	36	756
	4	338	2227	220	1686	119	1094
	5	536	3237	352	2482	157	1648
SIMULATED MOTION 2 Hz 450 counts amplitude	0	9	0	21	4	33	9
	1	70	75	83	81	99	81
	2	141	218	157	200	179	181
	3	220	404	243	346	272	302
	4	316	638	345	531	380	456
	5	426	934	460	764	499	651
SIMULATED MOTION 0.1 Hz 20 counts amplitude	0	.693	0	1.105	.359	1.172	.682
	1	3.715	7.364	2.952	6.067	2.485	4.716
	2	4.914	18.507	3.275	12.531	2.899	7.891
	3	5.391	32.476	3.676	19.744	3.300	11.453
	4	7.379	50.796	5.153	30.181	4.260	17.547
	5	9.373	74.333	6.152	43.333	5.055	24.564
SIMULATED MOTION Stationary 0.01-0.02 counts Random noise amplitude	0	.250	0	.279	.143	.350	.173
	1	.911	2.827	.856	1.490	.742	1.304
	2	1.147	6.285	.943	2.767	.751	2.135
	3	1.506	11.742	1.155	4.831	.880	3.464
	4	1.647	18.383	1.239	7.047	.887	4.854
	5	1.990	26.623	1.452	9.943	1.006	6.693



TABLE 2 - Orthogonal Gyro Detection Interval vs Step Failure for Stationary, 0.1Hz., 2Hz., and Flight Test (~10.5Hz) Motion Environments

Detection Threshold is 5 counts or 320 degrees/hr.

Step Failure Level (Degrees/hr)	Stationary			Motion Environment						Flt. Data ~10.5Hz		
	1	2	3	1	2	3	1	2	3	1	2	3
Detection frames												
10.	0	0	0	0	0	0	0	0	0	5	5	5
20.	0	0	0	0	0	0	0	0	0	5	5	5
30.	0	0	0	0	0	0	0	0	0	5	5	5
40.	0	0	0	0	0	0	0	0	1	5	5	4
50.	0	0	0	0	0	0	0	0	2	5	5	4
60.	0	0	0	0	0	0	0	1	4	5	4	4
70.	0	0	0	0	0	0	0	2	5	5	5	4
80.	0	0	0	0	0	0	0	2	6	5	4	4
90.	0	0	0	0	0	1	0	4	7	5	4	4
100.	0	0	0	0	0	2	0	5	8	5	4	4
110.	0	0	0	0	0	3	0	5	11	5	4	6
120.	0	0	3	0	0	4	1	6	12	4	4	6
130.	0	0	3	0	1	5	1	8	12	4	4	9
140.	0	0	13	0	1	9	2	9	15	5	4	15
150.	0	0	13	0	2	19	2	10	16	4	4	20
160.	0	0	21	0	3	22	2	13	17	4	5	21
170.	0	0	21	0	3	28	4	11	23	4	6	26
180.	0	3	35	0	4	37	4	13	23	4	6	32
190.	0	3	35	0	5	44	4	14	29	4	8	31
200.	0	5	52	0	5	50	5	16	26	4	10	32
210.	0	13	46	0	9	53	5	19	25	4	15	31
220.	0	13	57	0	15	49	5	19	27	4	19	34
230.	0	21	50	0	23	45	5	23	31	4	20	38
240.	0	21	57	0	24	45	6	25	29	4	22	42
250.	0	21	57	0	29	47	6	29	27	4	26	42
260.	0	37	43	1	34	43	8	31	27	4	29	40
270.	0	38	42	1	40	39	9	31	28	4	34	38
280.	0	38	42	1	46	33	9	34	26	4	35	39
290.	0	38	42	2	49	29	10	38	23	4	35	39
300.	0	57	23	2	53	25	10	36	27	4	38	36
310.	0	57	23	2	56	22	12	37	27	5	40	33
320.	0	57	23	3	60	17	13	38	26	5	47	26
330.	0	70	10	3	62	15	13	39	26	6	49	24
340.	0	70	10	3	65	12	13	44	22	6	54	19
350.	3	70	7	3	66	11	15	46	18	6	60	13
360.	3	75	2	4	66	10	16	45	19	6	62	11
370.	3	75	2	5	68	7	16	47	17	7	65	7
380.	3	77	0	5	71	4	17	47	16	8	64	7
390.	3	77	0	5	73	2	18	49	13	10	63	6
400.	5	75	0	6	73	1	19	49	12	10	65	4
500.	13	67	0	14	66	0	19	61	0	16	64	0
600.	64	6	0	66	14	0	59	21	0	48	32	0
720.	80	0	0	80	0	0	80	0	0	80	0	0

Cases out of 80 detected in 3rd frame  
 Cases out of 80 detected in 2nd frame  
 Cases out of 80 detected in 1st frame

\* - Approximate counts at indicated degrees/hour failure level

TABLE 3 - Skew Gyro Detection Interval vs Step Failure for Stationary, 0.1Hz., 2Hz., and Flight Test (~10.5Hz) Motion Environments

Detection Threshold is 5 counts or 320 degrees/hr.

Step Failure Level (Degrees/hr)	Motion Environment									Flt. Data ~ 10.5Hz		
	Stationary			0.1Hz			2Hz.					
Detection frames	1	2	3	1	2	3	1	2	3	1	2	3
10.	0	0	0	0	0	0	0	0	1	5	5	5
20.	0	0	0	0	0	0	0	1	1	5	5	4
30.	0	0	0	0	0	0	0	1	2	5	4	4
40.	0	0	0	0	0	0	0	2	4	5	4	4
50.	0	0	0	0	0	0	0	3	8	4	4	4
60.	0	0	0	0	0	1	0	4	9	4	4	7
70.	0	0	2	0	0	7	1	7	12	4	4	10
80.	0	0	10	0	0	12	1	9	13	4	6	17
90.	0	0	23	0	0	18	1	11	20	4	7	27
100.	0	0	23	0	4	24	2	14	18	4	10	34
110.	0	2	41	0	9	32	2	16	23	4	12	33
120.	0	10	49	0	11	43	3	17	31	4	17	41
130.	0	10	57	0	16	53	7	23	28	4	25	36
140.	0	23	54	0	21	54	7	25	31	4	35	36
150.	0	23	57	0	27	50	9	24	34	4	42	31
160.	0	42	38	0	36	43	9	29	33	6	41	31
170.	0	59	21	0	45	35	9	32	35	9	48	24
180.	0	59	21	1	53	26	11	39	26	7	53	10
190.	0	67	13	2	58	20	12	45	22	10	52	17
200.	0	67	13	3	69	8	15	43	22	10	58	12
210.	2	75	3	5	70	5	16	47	17	10	63	7
220.	2	75	3	8	69	3	17	48	15	13	63	4
230.	7	73	0	9	68	3	18	50	12	15	62	3
240.	10	70	0	10	69	1	19	52	9	18	60	2
250.	10	70	0	11	69	0	23	51	6	22	56	2
260.	10	70	0	15	65	0	27	48	5	27	50	3
270.	22	58	0	16	64	0	28	48	4	31	46	3
280.	22	58	0	20	60	0	30	48	2	37	40	3
290.	22	58	0	24	56	0	31	49	0	40	39	1
300.	22	58	0	26	54	0	31	49	0	44	35	1
310.	41	39	0	30	50	0	32	48	0	44	35	1
320.	41	39	0	35	45	0	37	43	0	44	35	1
330.	42	38	0	40	40	0	40	40	0	45	34	1
340.	58	22	0	44	36	0	41	39	0	51	28	1
350.	58	22	0	50	30	0	45	35	0	55	25	0
360.	58	22	0	53	27	0	50	30	0	60	20	0
370.	58	22	0	56	24	0	54	26	0	61	19	0
380.	66	14	0	59	21	0	57	23	0	62	18	0
390.	66	14	0	68	12	0	58	22	0	63	17	0
400.	66	14	0	71	9	0	58	22	0	68	12	0
420.	73	7	0	74	6	0	68	12	0	73	7	0
430.	80	0	0	80	0	0	80	0	0	80	0	0

Cases out of 80 detected in 3rd frame  
 Cases out of 80 detected in 2nd frame  
 Cases out of 80 detected in 1st frame

\* - Approximate counts at indicated degrees/hour failure level

TABLE 4 - Pseudo Sensor Algorithm Success in the Presence of Motion

DATA SOURCE	Step Failure level (counts)	5 frame fit interval		7 frame fit interval	
		linear	parabolic	linear	parabolic
SIMULATED MOTION Stationary 0.1 - 0.2 counts random noise approximate amplitude	10	310*	272	315	293
	25	320	320	320	320
	50	320	320	320	320
	100	320	320	320	320
	200	320	320	320	320
	500	320	320	320	320
	1000	320	320	320	320
SIMULATED MOTION .1 Hz 20 counts peak-to-peak approximate amplitude	10	224	157	222	210
	25	311	275	310	304
	50	320	316	320	320
	100	320	320	320	320
	200	320	320	320	320
	500	320	320	320	320
	1000	320	320	320	320
SIMULATED MOTION 2 Hz 450 counts peak-to-peak approximate amplitude	10	81	94	82	102
	25	91	95	80	117
	50	105	112	96	123
	100	133	145	111	141
	200	207	190	141	174
	500	263	274	225	266
	1000	311	317	300	320
FLIGHT TEST 10.5 Hz 175 counts peak-to-peak approximate amplitude	10	88	81	88	85
	25	88	73	83	82
	50	97	75	86	88
	100	107	87	105	94
	200	129	96	135	125
	500	222	131	220	217
	1000	315	188	316	308

\*NOTE: Each entry represents the number of successful identifications out of 320 samples.



TABLE 5 - Constrained Fit Algorithm Success in the Presence of Motion

DATA SOURCE	Step failure level (counts)	5 frame linear	5 frame fit interval parabolic	7 frame linear	7 frame fit interval parabolic
SIMULATED MOTION	10	320*	313	320	320
	25	320	320	320	320
	50	320	320	320	320
	100	320	320	320	320
	200	320	320	320	320
	500	320	320	320	320
Stationary 0.1 - 0.2 counts random noise approximate amplitude	1000	320	320	320	320
	10	253	181	250	223
	25	318	279	317	315
	50	320	318	320	320
	100	320	320	320	320
20 counts peak-to-peak approximate amplitude	200	320	320	320	320
	500	320	320	320	320
	1000	320	320	320	320
	10	86	83	80	80
	25	93	102	80	80
SIMULATED MOTION .1 Hz 450 counts peak-to-peak approximate amplitude	50	108	127	84	100
	100	118	177	95	117
	200	162	275	128	229
	500	288	320	239	318
	1000	320	320	320	320
FLIGHT TEST 10.5 Hz 175 counts peak-to-peak approximate amplitude	10	80	80	79	82
	25	87	77	89	87
	50	94	82	98	93
	100	111	97	117	110
	200	137	107	147	139
	500	277	158	278	262
	1000	320	236	320	320

\*NOTE: Each entry represents the number of successful identifications out of 320 samples.

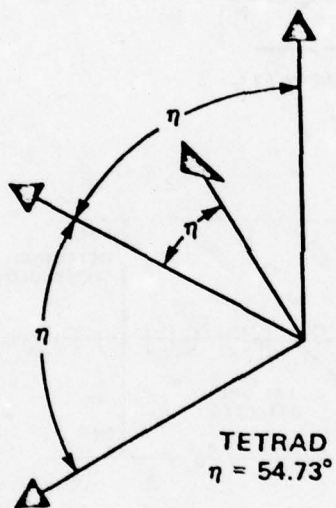
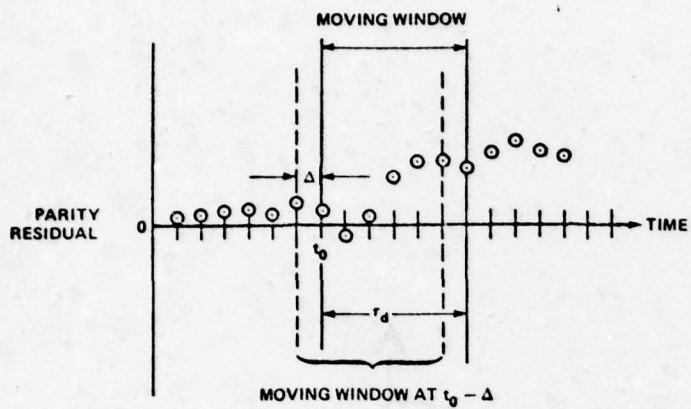
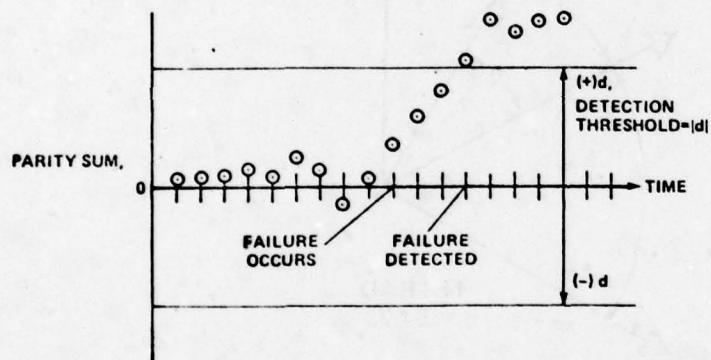


Figure 1.- Ortho-skew tetrad sensor configuration.



2(a)



2(b)

Figure 2 - Tetrad failure detection procedure.



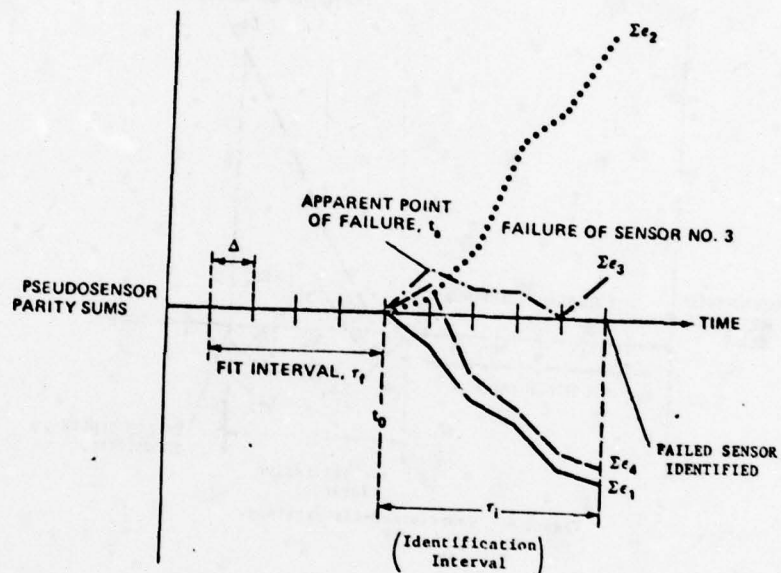


Figure 3.- Pseudosensor strategy.

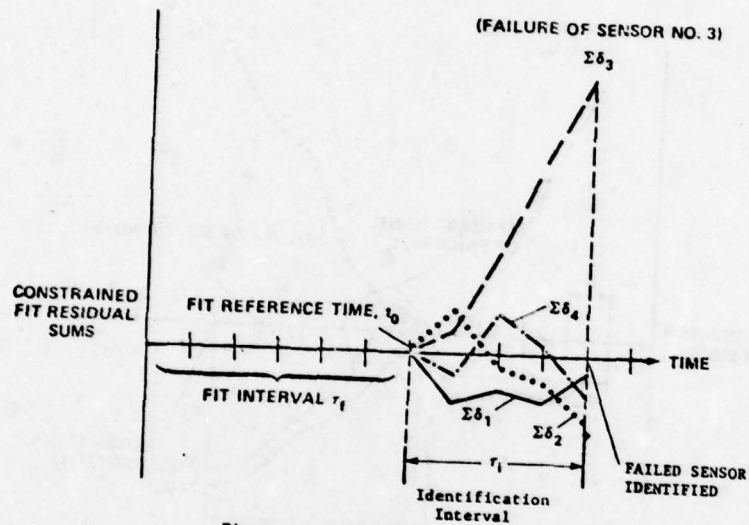


Figure 4.- Constrained-fit strategy.

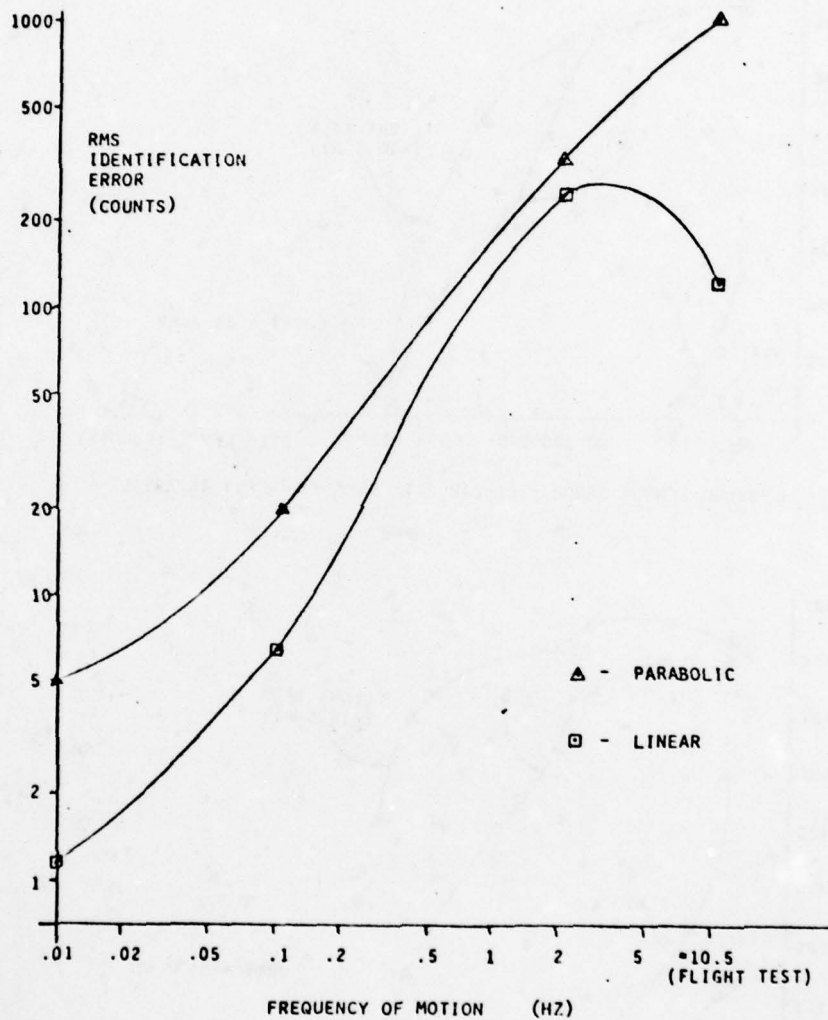


FIGURE 5 - IDENTIFICATION ERROR VS FREQUENCY OF MOTION  
FOR A 3 FRAME IDENTIFICATION LENGTH & A 4 FRAME FIT INTERVAL



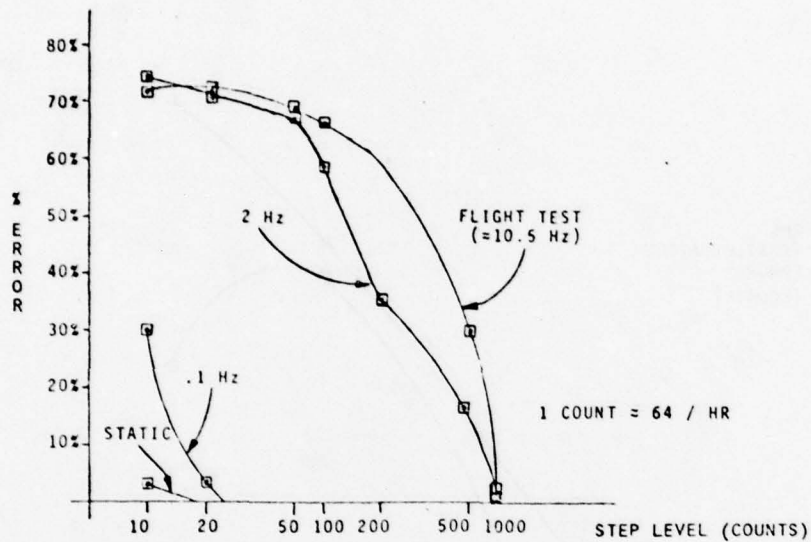


FIGURE 6 - PSEUDO SENSOR ERROR - LINEAR FIT (5 - FRAME FIT INTERVAL)

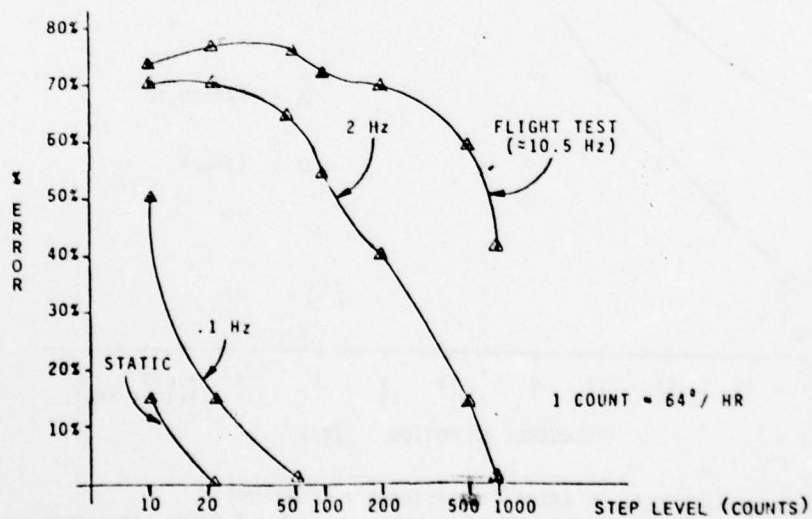


FIGURE 7- PSEUDO SENSOR ERROR - PARABOLIC FIT (5- FRAME FIT INTERVAL)

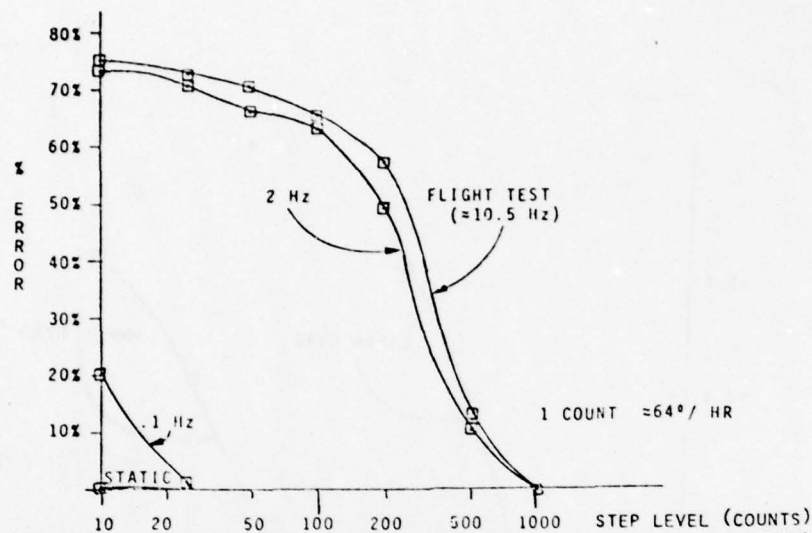


FIGURE 8 - CONSTRAINED FIT ERROR - LINEAR FIT (5 - FRAME FIT INTERVAL)

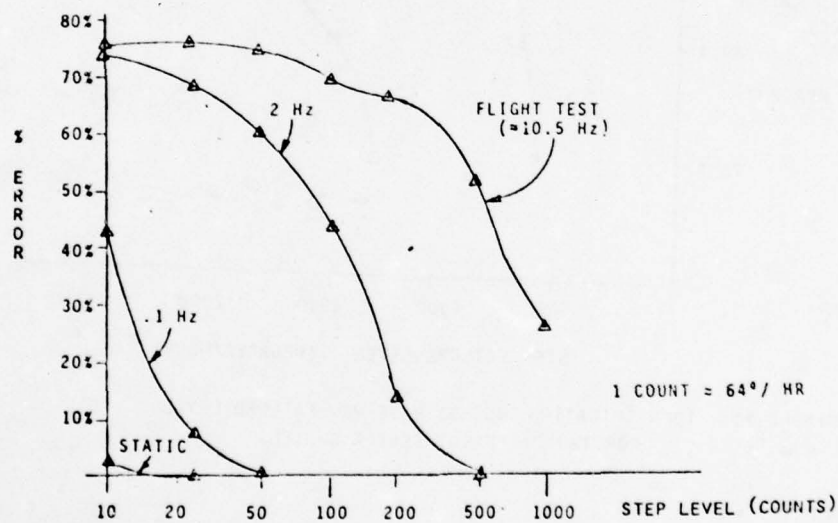


FIGURE 9 - CONSTRAINED FIT ERROR - PARABOLIC FIT (5-FRAME FIT INTERVAL)

AD-A076 567

ARMAMENT DEVELOPMENT AND TEST CENTER EGLIN AFB FL  
PROCEEDINGS OF THE BIENNIAL GUIDANCE TEST SYMPOSIUM (9TH) HELD --ETC(U)  
OCT 79

F/G 17/7

UNCLASSIFIED

ADTC-TR-79-11-VOL-1

NL

5 OF 5

AD  
A076567

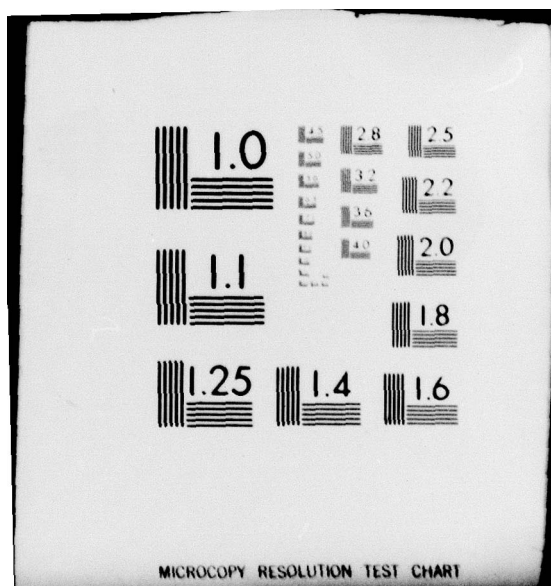


END  
DATE  
FILMED

12-79

DDC





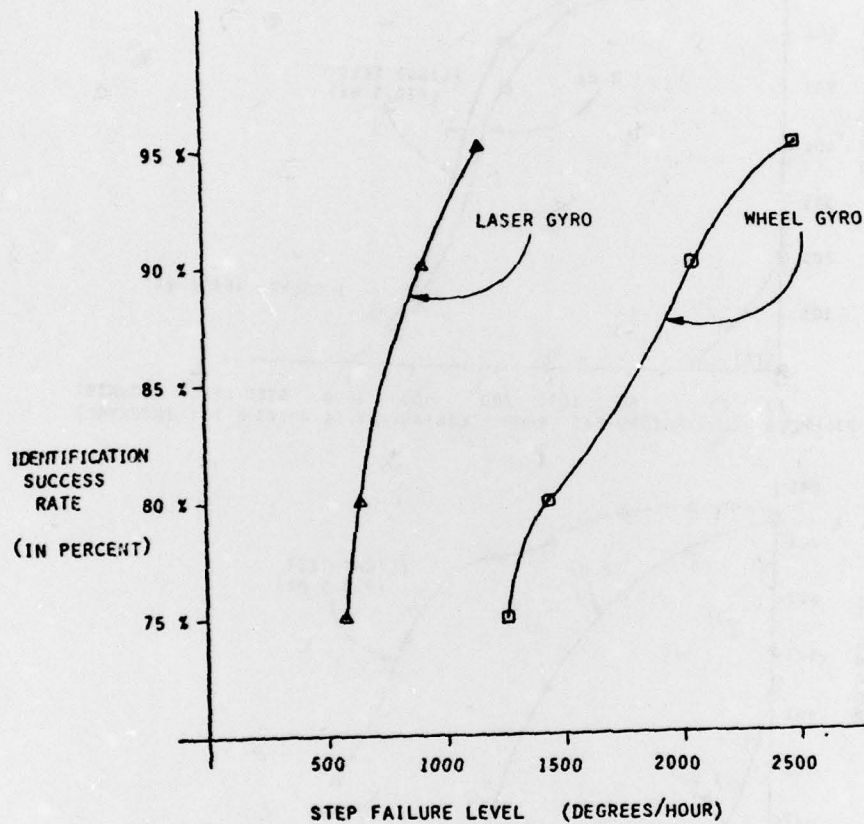


FIGURE 10 - IDENTIFICATION SUCCESS RATE VS. FAILURE LEVEL  
FOR TWO DIFFERENT SENSOR SYSTEMS

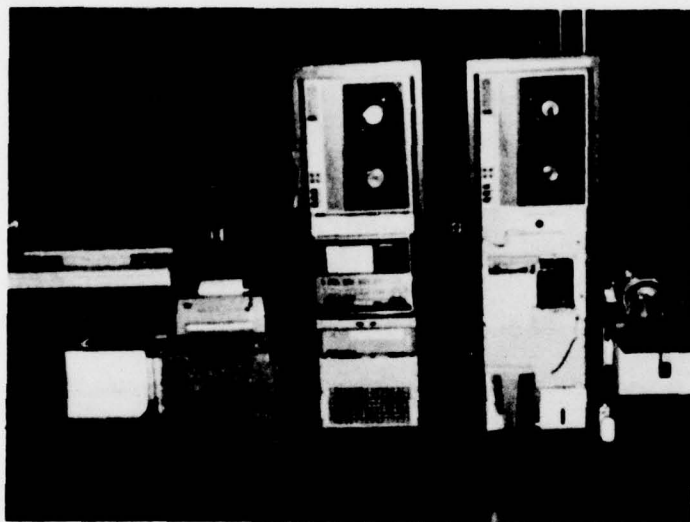


FIGURE 11 - MINICOMPUTER - DATA ACQUISITION SYSTEM



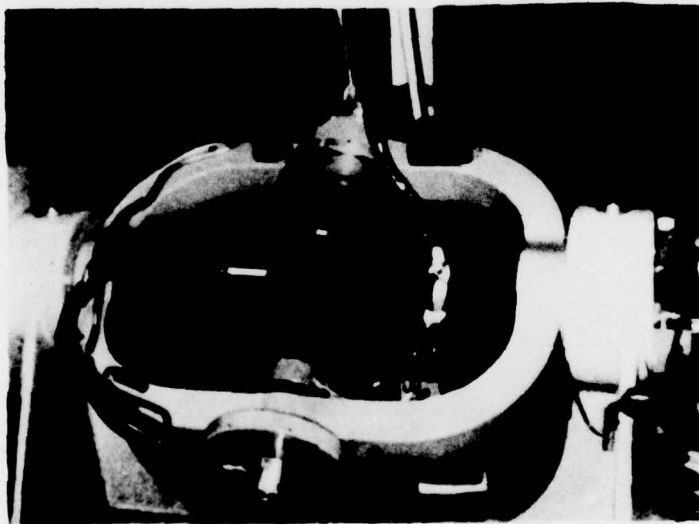


FIGURE 12 - LASER GYRO INERTIAL SENSOR ASSEMBLY  
MOUNTED ON THE MOTION SIMULATOR



FIGURE 13 - ARC UH-1H RESEARCH HELICOPTER

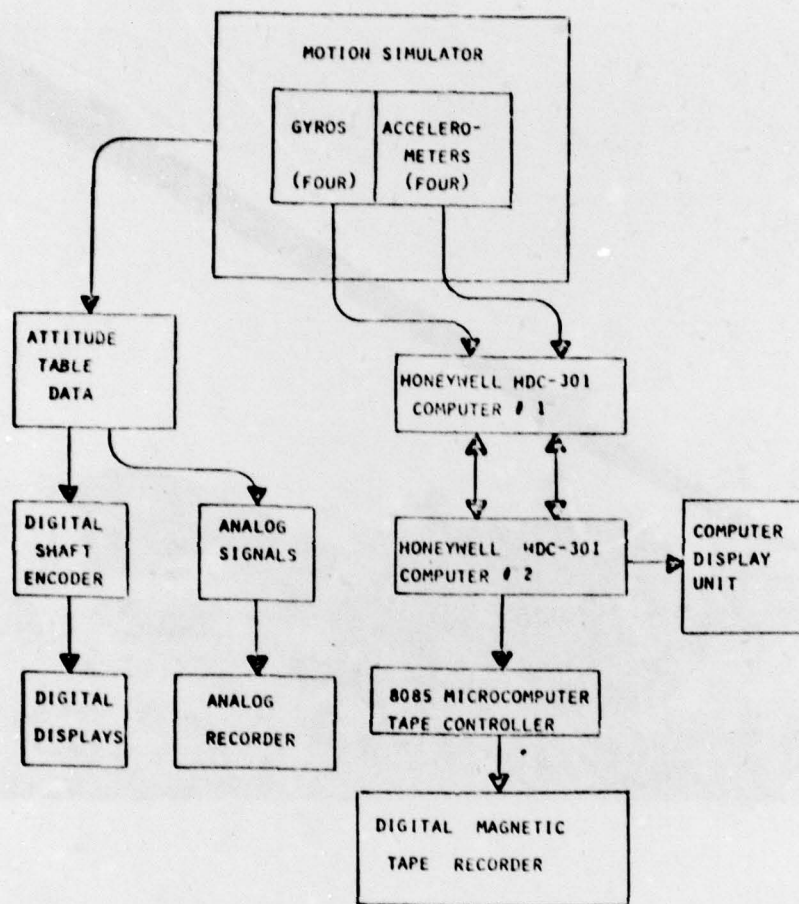


FIGURE 14 - DATA ACQUISITION SYSTEM



# NOTATION

$a_{ij}$	pentad parity coefficients used in the pseudo sensor
$b$	subscript or superscript for "body" frame
$b$	sensor bias error
$b_i$	bias compensation for sensor $i$
$b_{ij}$	polynomial coefficient for sensor $i$ , order $j$ , prefailure
$c_{Si}$	pseudo sensor mapping coefficients, prefailure
$d$	(1) summed parity residual detection threshold value; (2) subscript for "detection"
$i$	(1) subscript for sensor number; (2) subscript for "isolation"; (3) summation index
$j$	index usually used for polynomial order
$n$	angle between the skewed sensor and each mutually orthogonal sensor in the ortho-skew configuration
$m, m(r)$	measurement 4-vector whose elements are $m_i, m_i(r)$ at time $r$
$m, m(r)$	measurement from sensor $i$ at time $r$
$\hat{m}, \hat{m}_i$	estimated or predicted value of $m, m_i$
$n$	number of data points (frames) in the fit interval
$p$	(1) phenomenological input vector ( $\Omega$ or $F$ ); (2) order of a polynomial
$q$	quantization in engineering units per count in sensor output
$q_i$	quantization error in sensor $i$
$r_i$	random or unmodeled error in the output of sensor $i$
$s_i$	scale factor and alignment compensation vector for sensor $i$

$T$	subscript meaning "transposed"
$t_0$	fit reference time
${}^bT_t$	transformation from body to tetrad coordinates
${}^tT_b$	transformation from tetrad to body coordinates
${}^bU, {}^tU$	matrices whose four columns are ${}^b u_i$ or ${}^t u_i$ for $i = 1, 2, 3, 4$
$u_i$	unit vector along the input axis of sensor $i$
${}^b u_i, {}^t u_i$	$u_i$ expressed in the body (b) or tetrad (t) frame
$\epsilon_5$	parity residual which excludes the fifth (pseudo) sensor used for detection of failure
$\alpha$	parity coefficient corresponding to sensor No. 1
$\alpha_{k_c}, \alpha_{k_c}$	parity coefficient of the apparently failed sensor
$\beta$	parity coefficient corresponding to sensor No. 2
$\gamma$	parity coefficient corresponding to sensor No. 3
$\Delta$	measurement sampling interval or time corresponding to one data frame
$\Delta\theta_i(t)$	rotation increment measured by gyro $i$ at time $t$
$\delta_i$	measurement residual of sensor $i$ used in the constrained-fit strategy
$\tau$	(1) time relative to the fit reference time, $t_0$ ; (2) time variable for integration; (3) generic time, as in $m(\tau)$
$\tau_d$	time interval corresponding to the detection window
$\tau_f$	time interval used in a polynomial fit
$\tau_i$	time interval for isolation

$\Omega$	angular velocity
$\{x\}$	integer part of $x$
$\hat{x}$	estimated or predicted value of $x$
$\tilde{x}$	error in estimating $x$
$\epsilon_i, \epsilon_j(\tau)$	tetrad parity residual excluding sensor $i$ in the pseudo sensor configuration
$t$	(1) time; (2) subscript or superscript for "tetrad" frame
$t_a$	apparent time of failure
$t_d$	time of failure detection



#### REFERENCES

1. Eberlein, A. J. and Savage, P. G.: Strapdown Cost Trend Study and Forecast. NASA CR-137585, October 1975.
2. Wilcox, J. C.: Competitive Evaluation of Failure Detection Algorithms for Strapdown Redundant Inertial Instruments. TRW Report No. 18313-6004-RU-00, April 1973 (NAS8-27335).
3. Hruby, R. J.; Bjorkman, W. S.; Schmidt, S. F.; and Carestia, R. A.: A study of Redundancy Management Strategy for Tetrad Strap-down Inertial Systems. NASA TM-78576, February 1979.